# TABULATION OF IMPURITY ABSORPTION SPECTRA - ULTRAVIOLET AND VISIBLE

VOLUME II

M. SPARKS, PRINCIPAL INVESTIGATOR, 213/451-9916

H. VORA

M. FLANNERY

XONICS, INCORPORATED

SANTA MONICA, CALIFORNIA 90401

D D C

APR 10 1978

A

TENTH TECHNICAL REPORT
31 DECEMBER 1977

DISTRIBUTION STATEMENT A

Approved for public release;
Distribution Unlimited

REPORT DOCUMENTATION PAGE		READ INSTRUCTIONS BEFORE COMPLETING FORM
1. REPORT NUMBER	2. GOVT ACCESSION NO.	3. RECIPIENT'S CATALOG NUMBER
4. TITLE (and Subtitle) (6) TABULATION OF IMPURITY ABSORPTION SPECTRA — ULTRAVIOLET AND VISIBLE, VOLUME II.		5. TYPE OF REPORT & PERIOD COVERED Tenth Technical Report, 1 July 1977 through 31 Dec. 1977
		6. PERFORMING ORG. REPORT NUMBER
7. AUTHOR(s) (10) H. Vora, M. Flannery, and M. Sparks		8. CONTRACT OR GRANT NUMBER(s) (15) DAHC 15-73-C-0127, √ DARPA Order-1969
9. PERFORMING ORGANIZATION NAME AND ADDRESS Xonics, Incorporated √ 1333 Ocean Avenue Santa Monica, California 90401		10. PROGRAM ELEMENT PROJECT TASK AREA & WORK UNIT NUMBERS
11. CONTROLLING OFFICE NAME AND ADDRESS Defense Supply Service Room 1D245 - The Pentagon Washington, D.C. 20310		12. REPORT DATE 31 December 1977
		13. NUMBER OF PAGES 328 (12) 328 P.
14. MONITORING AGENCY NAME & ADDRESS(if different from Controlling Office) Defense Advanced Research Projects Agency 1400 Wilson Boulevard Arlington, Virginia 22209		15. SECURITY CLASS. (of this report) Unclassified
		15a. DECLASSIFICATION/DOWNGRADING SCHEDULE

16. DISTRIBUTION STATEMENT (of this Report)

~~This document may be further distributed only with specific prior approval of the Defense Supply Service, Washington, D.C.~~

DISTRIBUTION STATEMENT A

Approved for public release;
Distribution Unlimited

DDC
RECEIVED
APR 10 1978
A

17. DISTRIBUTION STATEMENT (of the abstract entered in Block 20, if different from Report)

18. SUPPLEMENTARY NOTES

19. KEY WORDS (Continue on reverse side if necessary and identify by block number)

impurity absorption, ultraviolet absorption, visible absorption, LiF, NaF, KCℓ, MgF_2, CaF_2, MgO, $Aℓ_2O_3$, SiO_2, silicate glasses, spectra tabulation, laser windows, laser materials

micrometers

20. ABSTRACT (Continue on reverse side if necessary and identify by block number)

The optical-absorption spectra of commonly occurring impurities in several ultraviolet-transparent solids are tabulated and discussed, and the assignments of the absorption bands are reviewed. The wavelength region included extends from the very near infrared, at 1 μm (0.124 eV), through the vacuum-ultraviolet region. The host materials covered are LiF, NaF, KCℓ, MgF_2, CaF_2, MgO, $Aℓ_2O_3$, SiO_2, and silicate glasses. The results are presented in a way useful in locating impurities that absorb at specified wavelengths, in determining the

409 988 JOB

wavelength region in which a specific impurity absorbs, and for general use in several current and envisioned programs, including: reducing the residual optical absorption of materials in order to increase the power of ultraviolet and visible lasers and to increase the resistance of materials to damage by high-intensity radiation in laboratory and space environments; understanding the origin of the residual absorption in order to provide guidance for further improvement of materials and to estimate the expected materials limits set by residual imperfections; and reducing the absorptance of dielectric reflectors and antireflection coatings. The coatings problem is especially important since it is believed that impurities in deposited films is a major factor limiting the absorptance of both types of coatings, and high-power reflectors require the use of dielectric coatings in order to obtain low absorptance. The features of the spectra are summarized in tables and figures. Peak positions, approximate line widths, and when available, the oscillator strengths of all bands are summarized in correlation-type graphs for each material. The intrinsic and extrinsic absorption spectra are categorized according to the type of host material, e.g., alkali halides, alkaline-earth halides, and oxides, and according to the type of impurity, e.g., halogens, H and D centers, OH and OD centers, O, S, Se centers, color centers, radiation-induced defect centers, transition-metal ions, and rare-earth ions. Comparisons of results for various host materials, and also for various impurities, are given in the form of tables and figures whenever possible.

PREFACE

This Tenth Technical Report describes the work performed on Contract Number DAHC15-73-C-0127 on Theoretical Studies of High-Power Ultraviolet and Infrared Materials during the period from 1 July 1977 through 31 December 1977. The work on the current contract is a continuation of that of the previous Contract Number DAHC15-72-C-0129.

In view of the increasing importance of impurity absorption in high-power laser materials for use as windows, this report and the Ninth Technical Report, 30 June 1977, are dedicated to a tabulation of impurity spectra of important materials in the ultraviolet and visible regions. The previous infrared impurity-absorption study, which emphasized the CO_2-laser wavelengths near 10.6 μm, is being updated to include a greater number of impurities, particularly those of importance at other infrared wavelengths. The results, along with the results of our other ongoing programs will be presented in the final report. Previously reported results are not repeated in the present report.

The following investigators contributed to this report:

Dr. H. Vora, consultant, Air Force Materials Laboratory, Dayton, Ohio

Dr. T. G. Stoebe, consultant, University of Washington, Seattle, Wash.

Mr. M. R. Flannery, research assistant

Mr. Eugene Loh, Jr., research assistant

Dr. M. Sparks, principal investigator

Lona Case and Frances Rossiter typed the manuscript and prepared the art work with their usual skill and care.

TABLE OF CONTENTS — VOLUME I*

*Ninth Technical Report, 30 June 1977.

TABLE OF CONTENTS - VOLUME I (Cont.)*

*Ninth Technical Report, 30 June 1977.

TABLE OF CONTENTS — VOLUME II

TABLE OF CONTENTS - VOLUME II (Cont.)

LIST OF ILLUSTRATIONS - VOLUME I*

*Ninth Technical Report, 30 June 1977

LIST OF ILLUSTRATIONS - VOLUME I (Cont.)

LIST OF ILLUSTRATIONS - VOLUME I (Cont.)

LIST OF ILLUSTRATIONS - VOLUME I (Cont.)

LIST OF ILLUSTRATIONS - VOLUME II

LIST OF ILLUSTRATIONS - VOLUME II (Cont.)

LIST OF ILLUSTRATIONS - VOLUME II (Cont.)

LIST OF TABLES - VOLUME I*

*Ninth Technical Report, 30 June 1977.

LIST OF TABLES - VOLUME II

III. ALKALINE-EARTH FLUORIDES

A. Intrinsic Properties of Calcium Fluoride

The intrinsic Urbach ultraviolet absorption edge (which is taken as the frequency at which the absorption coefficient $\beta = 5\,\text{cm}^{-1}$) for calcium fluoride at room temperature is at 10.07 eV (123 nm), according to the absorption spectra[2.1] in Fig. 2.1.* By the same criteria, the intrinsic infrared absorption edge[3.1] of CaF_2 at room temperature is at 0.114 eV (10.87 μm). The American Institute of Physics Handbook[2.7] contains tables of the refractive index of CaF_2 from the ultraviolet, where n = 1.4764 at 5.41 eV (229 nm), to the infrared, where n = 1.3076 at 0.128 eV (9.72 μm).

B. Calcium Fluoride[†]

Coloration of calcium fluoride has been accomplished by additive coloration in calcium vapor, electrolytic coloration, addition of impurity ions, irradiation with X-rays or γ-rays, and bombardment by electrons or neutrons. The spectra vary widely, depending critically on the thermal history, annealing, trace impurities, radiation dose, and exposure to visible or ultraviolet light. Calcium fluoride is much more difficult to color by radiation than are the alkali halides, and the color centers formed are very sensitive to the impurities, quenching rate, and irradiation temperature. Attempts to identify the intrinsic color centers of CaF_2 (as distinct from color centers associated with impurities or impurity transitions) by comparison with the alkali halides resulted in ambiguous identifications of the different spectra in the early literature. Only recently has the problem been resolved.

---

* Volume I, 30 June 1977.

[†] See summary Figures 1.5 and 1.12 of Volume I.

1. <u>O^{--} and S^{--} in CaF$_2$.</u>

A steep rise in the absorption coefficient of CaF$_2$ at wavelengths shorter than 220 nm (5.64 eV) **that** is present before X-irradiation, is generally considered to be indicative of oxygen[3.1a, 3.2] or hydroxyl[3.3] contamination. This peak, shown in Fig. 3.1,[3.3] is far short of the fundamental band-gap absorption edge at 125 nm (9.92 eV)[3.4]. The absorption spectra of typical crystals from three allomorphic groups exhibiting this steep rise are shown in Fig. 3.2 before and after X-irradiation at 300 K, and in Fig. 3.3 after X-irradation at 77 K.[3.5] The dose dependence of room-temperature X-ray coloration is shown in Fig. 3.4 for oxygen-doped crystals. Rauch, et al.,[3.5] have assigned the following impurities to the three spectral groups: I. Y^{3+} and O^{--}, II. O^{--}, and III. S^{--}. The three groups are clearly distinguishable by a combination of their photoluminescence spectra at 77 K after room-temperature X-ray coloration, and their thermoluminescence spectra after low-temperature X-ray coloration.

The so-called UV oxygen absorption at ~200 nm (6.2 eV) is apparently due to some type of oxygen – F$^-$ vacancy complex.[3.2] Burr. et al..[3.6] have shown that when oxygen is compensated by bivalent ions, e.g., Y^{3+}, the UV absorption probably corresponds to a fundamental-band transition locally modified by the impurity ion, similar to the α band in alkali halides, rather than direct excitation of O^{--}. Since X-irradiation leads to the occupation of fluoride vacancies by electrons, a decrease in the UV absorption is expected even though there is partial compensation of this effect by the formation of UV-absorbing V$_K$ centers. This can be seen in the spectrum of the weakly absorbing crystals of Figure 3.4.

Upon room-temperature X-ray coloration, all the crystals develop the characteristic two-band absorption spectra shown in Fig. 3.2. Rauch, et al.,[3.5]
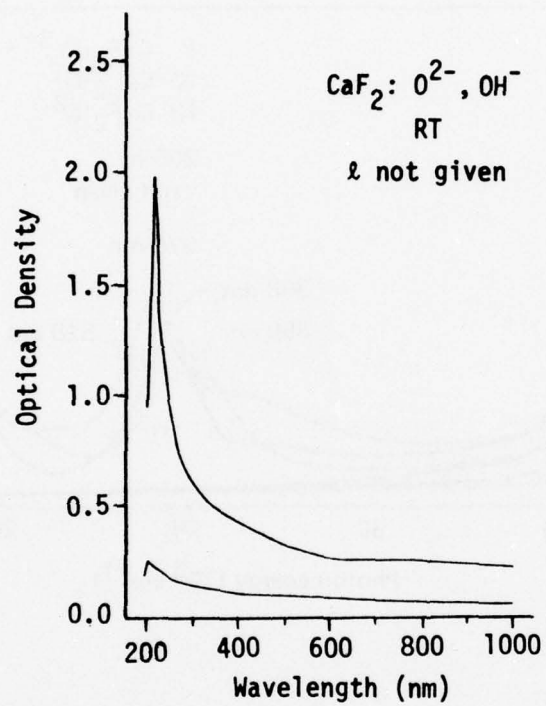
Fig. 3.1. Oxygen and hydroxyl contamination of CaF$_2$:
(a) before thermal treatment, (b) after 3 hours at
765 C in air. [W. Bontinck, Physica 24, 650 (1958).]

Photon energy (eV)

I'   CaF$_2$:(Y^{3+} + O^{2-})
II' CaF$_2$:O^{2-}
III' CaF$_2$:S^{2-}

300 K
ℓ *not given*

Optical density

Photon energy (10^3 cm^{-1})
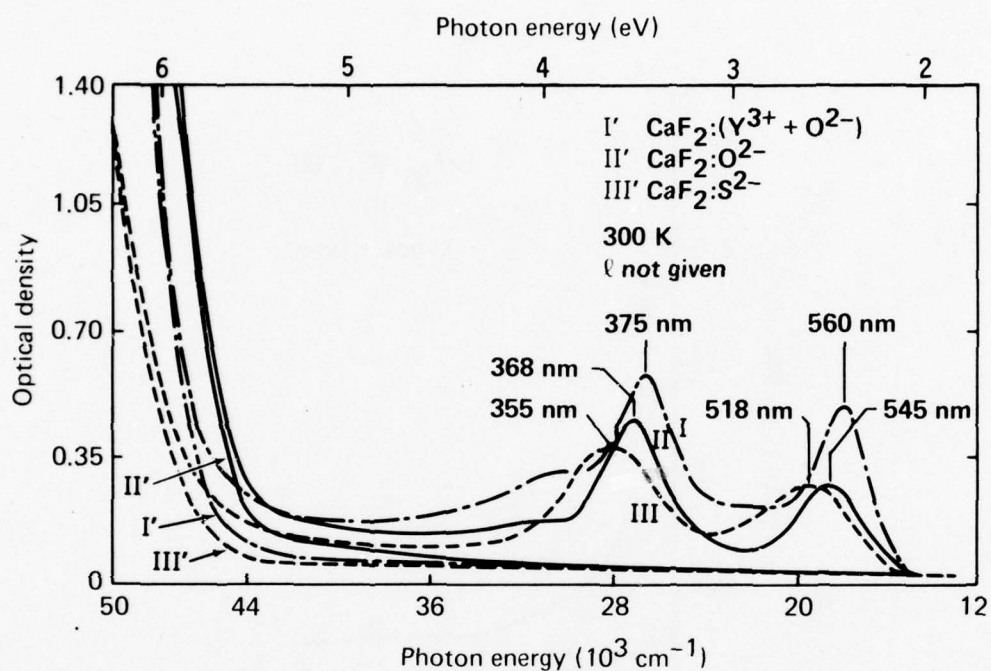
Fig. 3.2.   Absorption spectra of typical doped CaF$_2$ crystals before (primed) and after (unprimed) X irradiation of 4×10^3 R. [R. Rauch, R. Reimann, and G. Schwotzer, Phys. Stat. Sol. (a) 23, 69 (1974).]
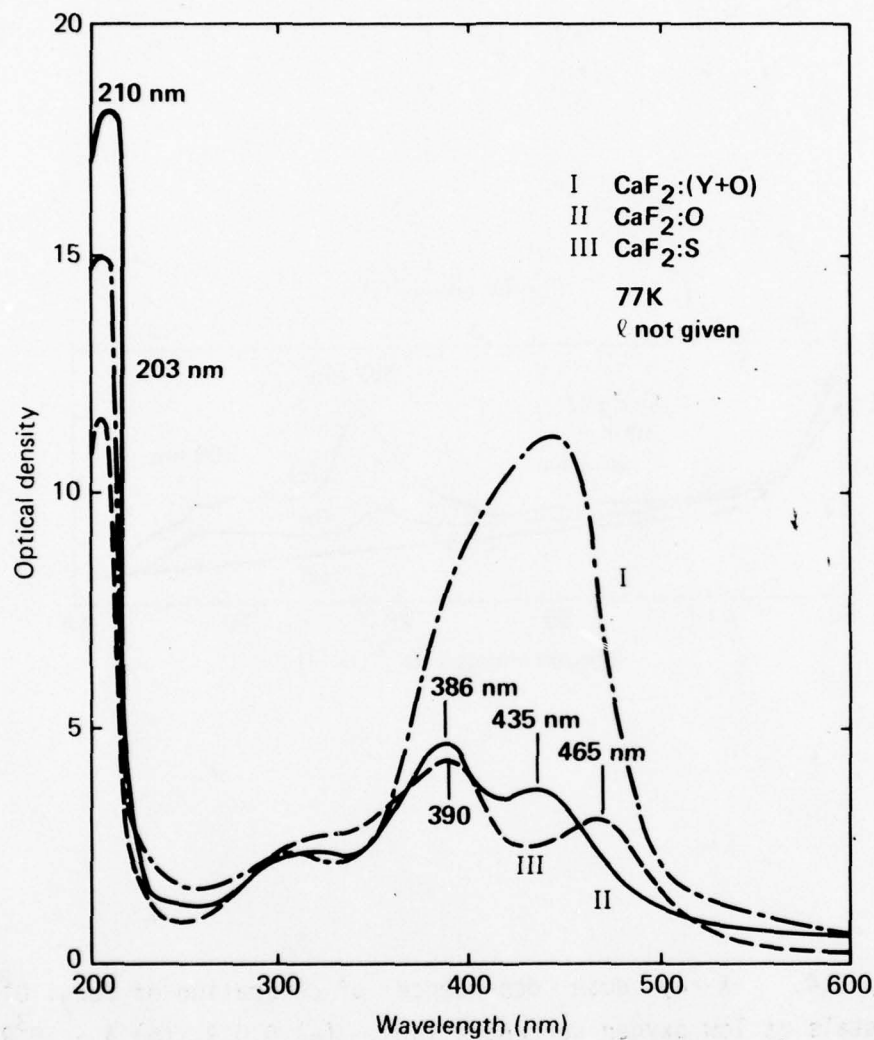
Fig. 3.3. Absorption spectra after X irradiation; I and II ,
7×10^3 R, and III, 4×10^4 R.   [R. Rauch, R. Reimann, and
G. Schwotzer, Phys. Stat. Sol. (a) 23, 69 (1974).]
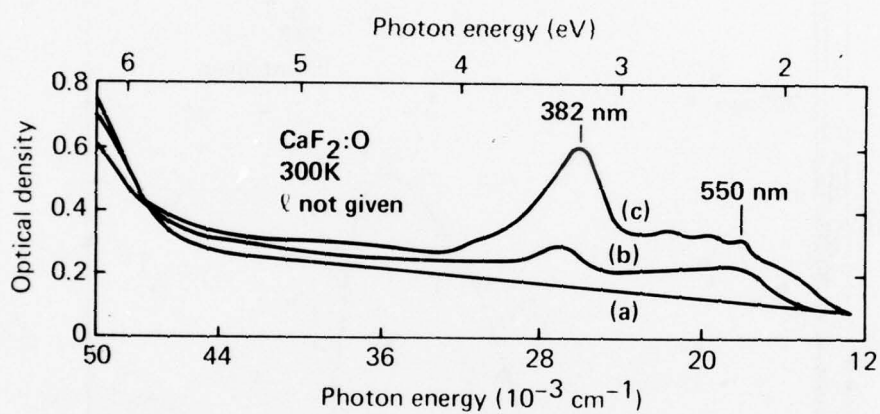
Fig. 3.4.   X-ray dose dependence of coloration of CaF$_2$: O^{2-} crystals at low oxygen concentrations: (a) 0.0 R, (b) 4×10^3R, and (c) 2.5×10^5 R.   [R. Rauch, R. Reimann, and G. Schwotzer, Phys. Stat. Sol. (a) $\underline{23}$, 69 (1974).]

6

apparently assign the high-frequency band at $\sim$ 370 nm (3.35 eV) to F-center absorption, and the low-frequency band at $\sim$ 550 nm (2.25 eV) to absorption by F_2 centers oriented along the $\langle 100 \rangle$ directions. Comparison of the X-ray colored spectrum of impurity-doped CaF_2 with that of additively colored CaF_2 indicates that the low-frequency band in impure CaF_2 is produced by F_2 centers distributed by the presence of the impurity ions. Table 3.1 illustrates the degree of disturbance by a comparison of the shift in the F-center absorption and emission peaks with respect to those of pure CaF_2. The strongly disturbed transitions are due to impurity ions on sites neighboring the F_2 center, while for weakly disturbed F_2 centers the impurity ions are in more distant shells. When stored in the dark the stability of X-ray coloration is quite different for the three groups of crystals. The coloration of the purely oxygen-doped crystals was so unstable that the extinction coefficient decayed to a tenth of its original value in 24 h. In contrast, the optical density of the yttrium-oxygen and sulfur-doped crystals remained virtually unchanged in 24 h, but there were some shifts in the positions of the absorption bands indicating rearrangement of the color centers.

2. Transition-metal ions in CaF_2.

a. Mn^{2+} in CaF_2. The absorption spectrum[3.9, 3.10] of $CaF_2 : Mn^{2+} (3d^5)$ in the ultraviolet and vacuum-ultraviolet regions is shown in Figs. 3.5 and 3.6, respectively. EPR spectroscopy indicates that in CaF_2 the Mn^{2+} ions substitute for the Ca^{2+} ions on their cubic-symmetry lattice sites.[3.11] The crystals used for the absorption spectrum of Fig. 3.5 were clear and transparent with a Mn^{2+} concentration of 180 ppm. The spectrum has three very intense bands at 200 nm (6.2 eV), 185 nm (6.67 eV), and

Table 3.1.   Band maxima of the absorption and emission
transitions of disturbed F$_2$ centers in CaF$_2$. [R. Rauch,
R. Reimann, and G. Schwotzer, Phys. Stat. Sol. (a) 23,
69 (1974).

	Absorption/Emission (nm)	
	Strongly Disturbed	Weakly Disturbed
CaF$_2$ pure [3.7]	520/586	
CaF$_2$:O^{--}	565/684	525/610
CaF$_2$:Na$^+$ [3.8]	615/755	530/620
CaF$_2$:Li$^+$ [3.8]	625/810	530/625
CaF$_2$:S^{--}	500/760	—
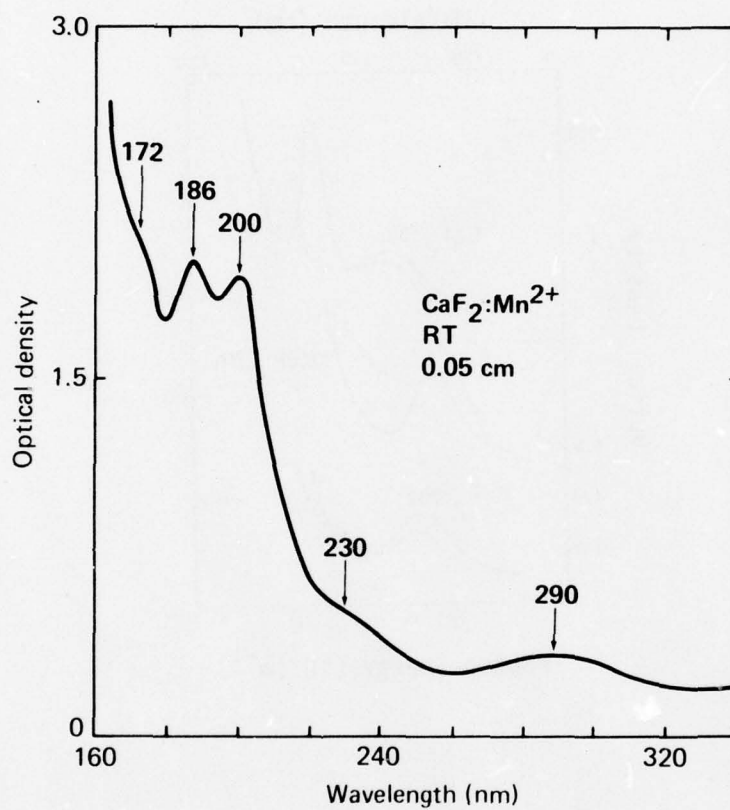
Fig. 3.5. Absorption spectrum of CaF$_2$:Mn^{2+}.   [R. K. Bagai and A. V. R. Warrier, Phys. Stat. Sol. (b) 73, K123 (1976).]

9
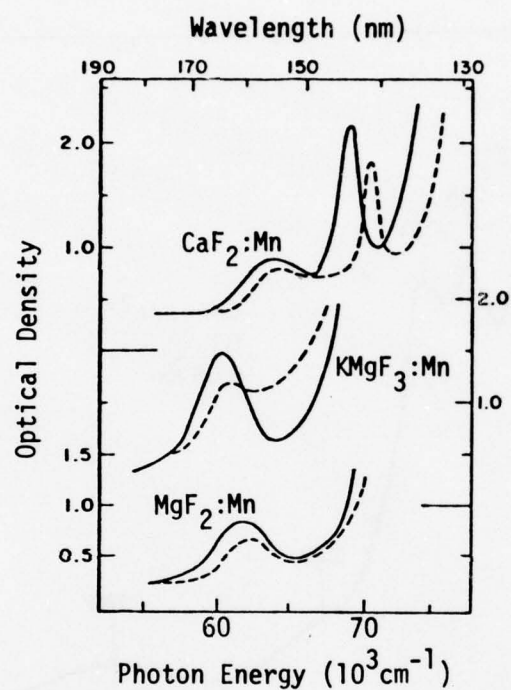
Fig. 3.6. Absorption spectra of Mn^{2+} in different host crystals; solid lines — room temperature, dashed lines — 4.2 K.   CaF$_2$:Mn, ℓ = 1.01 mm, also contains Fe^{2+} with a peak at 145 nm (8.56 eV); KMgF$_3$:Mn, ℓ = 0.46 mm; MgF$_2$:Mn, ℓ = 0.71 mm.   [J. F. Sabatini, A. E. Salwin, and D. S. McClure, Phys. Rev. B11, 3832 (1975).]

172 nm (7.2 eV), a weak shoulder at 230 nm (5.39 eV), and weak bands at 290 nm (4.28 eV) and 400 nm (3.1 eV). The three low-frequency weak bands are assigned to 3d → 3d crystal-field transitions because these transitions are forbidden by parity- and spin-selection rules. The assignment of these transitions has been made in Table 3.2 by comparison with the well resolved and assigned spectra[3.12, 3.13, 3.14] of NaCl:Mn^{2+} and LiF:Mn^{2+}.

The three strong peaks in Fig. 3.5 plus the band in Fig. 3.6 at 156 nm (7.9 eV) are probably due to either intra-ionic 3d → 4p dipole-allowed transitions, or to 2p-valence-band to 3d-impurity-ion charge-transfer transitions in Mn^{2+}. The band at 145 nm (8.56 eV) in Fig. 3.6 is due to similar transitions in Fe^{2+}.

b.   <u>Co^{2+} in CaF$_2$</u>. The absorption spectra[3.10, 3.15, 3.16] of Co^{2+}(3d^7) in CaF$_2$ is shown for the visible region in Figs. 3.7 and 3.9, and for the infrared region in Figs. 3.8 and 3.10. In addition, Fig. 3.11 shows the vacuum-ultraviolet spectrum of Co^{2+} in different host crystals as a function of temperature. The concentration of Mn^{2+} in the samples used for Figs. 3.7 and 3.8 was estimated to be 4500 ppm based on a comparison between the $^4A_{2g} \rightarrow {}^4T_{1g}$ (P) transitions in CaF$_2$: Mn^{2+} and CdF$_2$: Mn^{2+} , assuming identical oscillation strengths in both hosts.   In addition to the triply peaked $^4A_{2g} \rightarrow {}^4T_{1g}$(P) absorption band centered at 2.29 eV (555 nm) in Figs. 3.7 and 3.9, there are three very weak peaks at 2.32 eV (535 nm), 2.44 eV (508 nm) and 2.46 eV (503 nm), probably due to spin-forbidden transitions of the crystal-field-split states of the ^{2}G term. The visible bands shift towards the blue by 0.012 − 0.036 eV, depending on the host lattice, when the crystals are cooled from room temperature to 77 K.

Tabel 3.2. Spectral position [eV] of the 3d → 3d peaks of Mn^{2+} in NaCl, LiF, and CaF$_2$ crystals.

Assignment Crystal	$^4T_{2g}(F)$	$^4A_{2g}(F)$	$^4T_{1g}(D)$	$^4E_g(D)$	$^4T_{2g}(D)$	$^4E_g(G)$	$^4T_{2g}(G)$	$^4T_{1g}(G)$
NaCl [3.13]	5.053	4.860	3.807	3.515	3.348	2.976	2.697	–
LiF [3.14]	5.766	4.593	3.844	3.443	3.147	–	2.639	2.406
CaF$_2$ [3.9]	5.392	4.276	~3.1				–	–
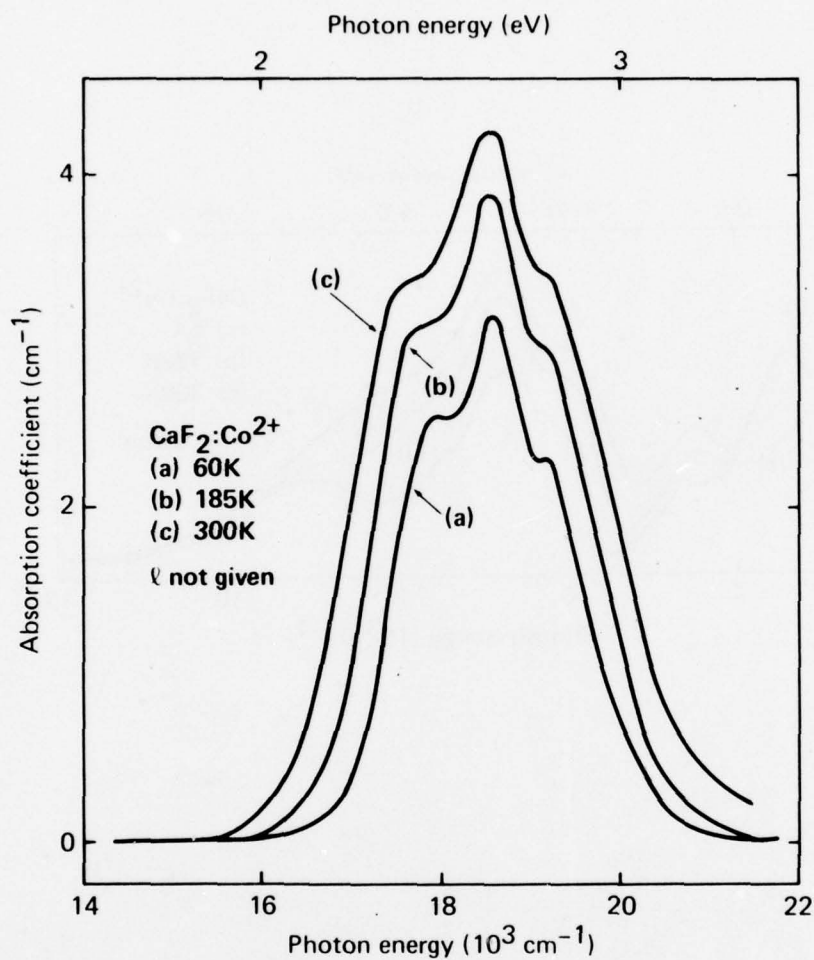
Fig. 3.7. Absorption spectra of CaF$_2$:Co^{2+} in the region of the $^4A_{2g} \rightarrow {}^4T_{1g}(P)$ transition. [G. Schwotzer and W. Ulrici, Phys. Stat. Sol. (b) <u>64</u>, K115 (1974).]
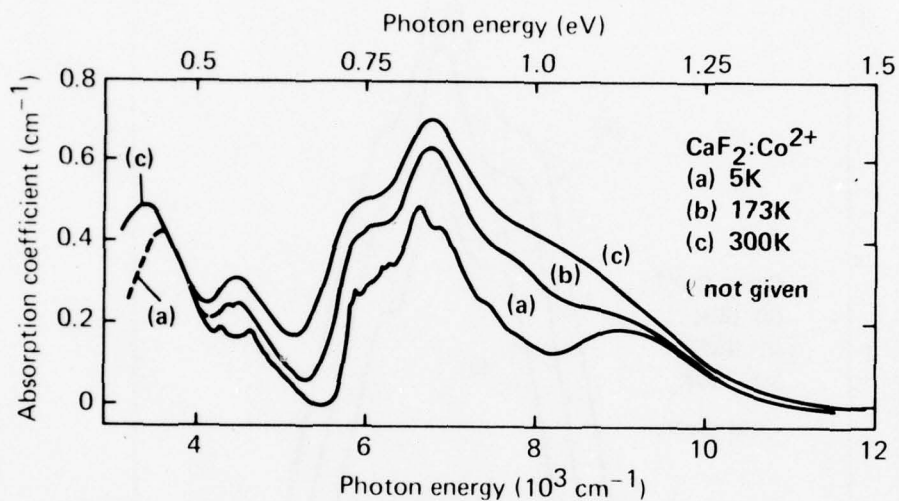
Fig. 3.8. Absorption spectra of CaF$_2$:Co^{2+} in the region of the $^4A_{2g} \rightarrow {}^4T_{1g}$(F) transition (0.66 - 1.05 eV), and the $^4A_{2g} \rightarrow {}^4T_{2g}$(F) transition (0.37 - 0.66 eV). [G. Schwotzer and W. Ulrici, Phys. Stat. Sol. (b) <u>64</u>, K115 (1974).]

14

Photon energy (eV)

2.0   2.5   3.0

Absorption (undefined)

(d)

(c)

(b)

(a) BaF$_2$:Co^{2+}
(b) SrF$_2$:Co^{2+}
(c) CaF$_2$:Co^{2+}
(d) CdF$_2$:Co^{2+}

77K

ℓ not given

(a)

15   18   21   24

Photon energy (10^3 cm^{-1})
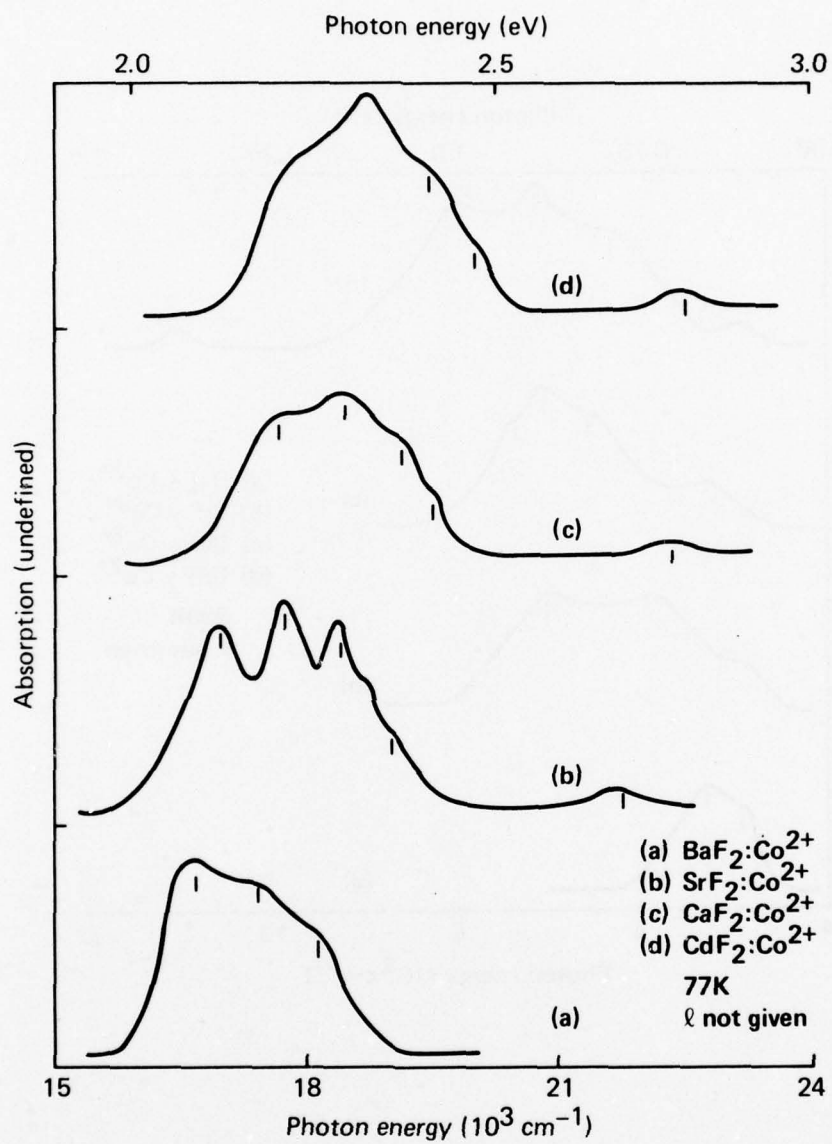
Fig. 3.9. Optical absorption spectra of Co^{2+} in fluoride-type lattices. [A. L. Stolov and Zh. S. Yakovleva, Sov. Phys.-Solid State 10, 1196 (1968).]
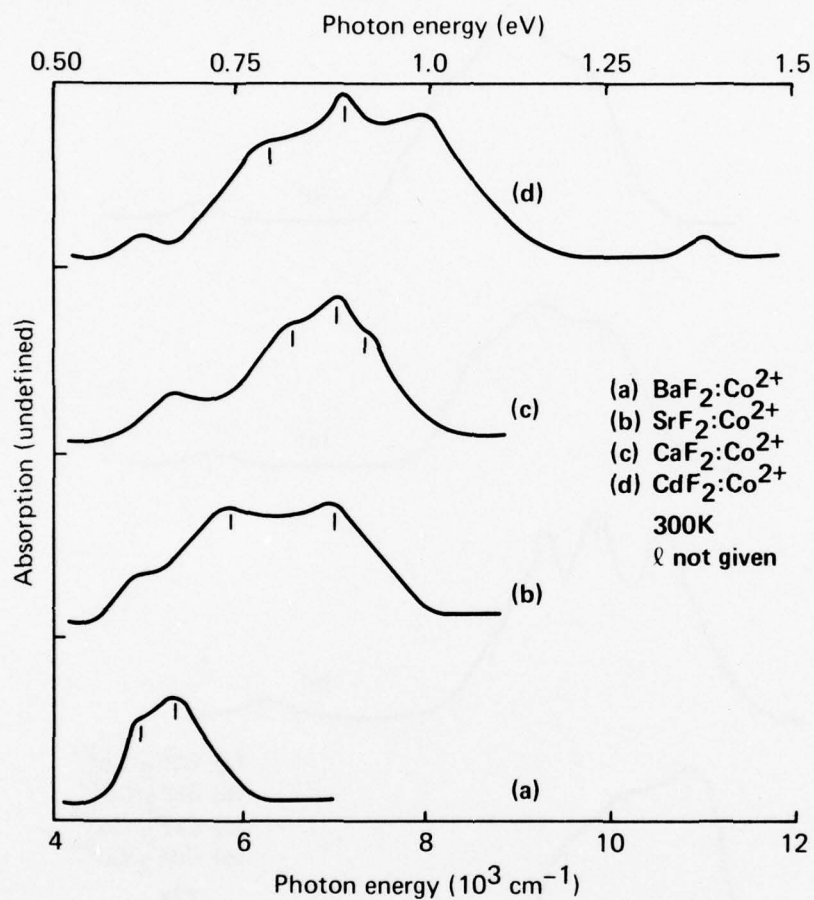
Fig. 3.10. Absorption spectra of Co^{2+} in fluoride-type lattices. [A. L. Stolov and Zh. S. Yakovleva, Sov. Phys.-Solid State 10, 1196 (1968).]
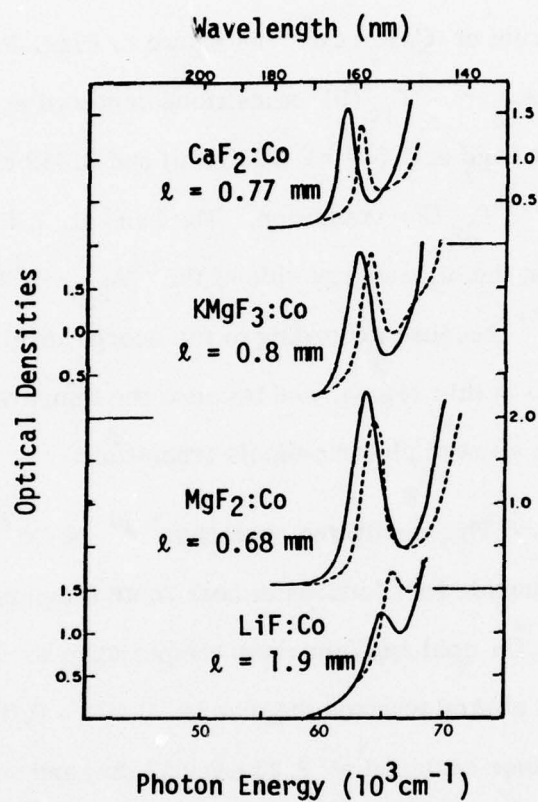
Fig. 3.11. Absorption spectra of Co^{2+} in fluoride-type lattices. [A. L. Stolov and Zh. S. Yakovleva, Sov. Phys.-Solid State 10, 1196 (1968).]

17

The vacuum-ultraviolet band of the 3d → 4s transition at 162 nm (7.63 eV) has an oscillation strength of 3.7×10^{-3} and shifts towards the blue by 0.149 eV on cooling to 4.2 K.

The infrared spectrum of $CaF_2 : Co^{2+}$ as shown in Figs. 3.8 and 3.10 has three bands from the $^4A_{2g} \rightarrow {}^4T_{1g}(F)$ transitions centered at 0.833 eV (1489 nm) and a doublet band at 0.552 eV (2250 nm) and 0.418 eV (2970 nm) assigned to the $^4A_{2g} \rightarrow {}^4T_{2g}(F)$ transition. The band at 1.13 eV (1100 nm), which appears at 5 K on the high-energy side of the $^4A_{2g} \rightarrow {}^4T_{1g}(F)$ transitions, is not due to Co^{2+} because according to the energy level scheme[3.12] no transition is expected in this region, and because the temperature dependence of this band is that of an allowed electric-dipole transition.

c. $\underline{Ni^{2+} \text{ in } CaF_2}$. The absorption spectrum[3.17] of $Ni^{2+}(3d^8)$ in calcium fluoride and cadmium fluoride host lattices at both room temperature and 4.2 K, is shown in Fig. 3.12. On cooling from room temperature to 77 K, the absorption bands narrowed and shifted towards the blue by 0.025 − 0.05 eV. At 4.2 K a series of vibrational lines centered at 2.23 eV (557 nm) and separated by 0.021 eV appeared on the low-energy wing of the CaF_2 absorption curve. Similar structures were not observed in the spectrum of $CdF_2 : Ni^{2+}$. The experimentally observed lines of Ni^{2+} in CaF_2 and CdF_2 are summarized in Table 3.3 together with their transition assignments and the theoretical absorption energies.

3. Rare-earth ions in $\underline{CaF_2}$.

The rare-earth ions have unfilled 4f shells. The effect of the crystal field on the energy levels of the rare-earth ions is smaller than the spin-orbit interactions, partly because the radius of the 4f orbits is small and partly

18

Photon energy (eV)

| 0.5 | 1.0 | 2.0 | 3.0 | 4.0 | 5.0 |

(d) CaF$_2$:Ni^{2+}
(a) RT
(b) 4.2K

(c) CdF$_2$:Ni^{2+}
(c) RT
(d) 4.2K

(b)

(a)

| 3 | 7 | 11 | 15 | 19 | 23 | 33 | 37 | 41 |

Photon energy (10^3 cm^{-1})
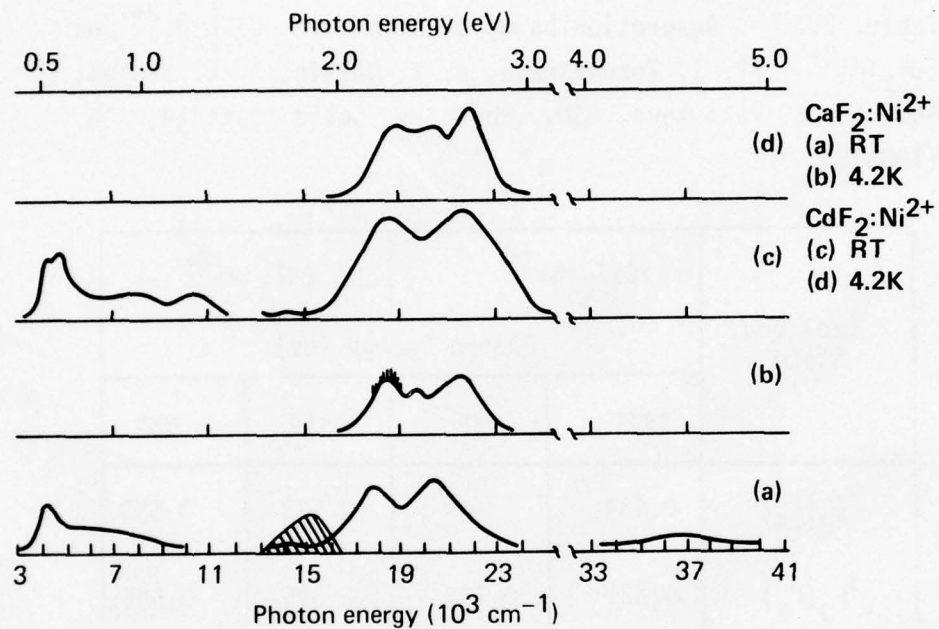
Fig. 3.12. Absorption spectra of Ni^{2+} in CaF$_2$ and CdF$_2$.
Cross-hatched region represents the luminescence spectrum.
[E. I. Zoroatskaya, B. Z. Malkin, A. L. Stolov, and Zh. S.
Yakovleva, Sov. Phys.-Solid State 10, 320 (1968).]

Table. 3.3.   Absorption bands of nickel in $CaF_2:Ni^{2+}$ and $CdF_2:Ni^{2+}$. [E. I. Zoroatskaya, B. Z. Malkin, A. L. Stolov, and Zh. S. Yakovleva, Sov. Phys. — Solid State 10, 320 (1968).]

Excited State	$CaF_2:Ni^{2+}$ Photon Energy (eV)		$CdF_2:Ni^{2+}$	
	calc	exp	calc	exp
$^3F_3(\Gamma_4)$	0.434	–	0.533	0.533
$^3F_3(\Gamma_5)$	0.521	0.533	0.595	0.595
$^3F_2(\Gamma_5)$	0.831	–	0.980	0.992
–	–	–	–	1.302
$^1G_4(\Gamma_5)$	2.220	2.226	2.294	2.319
$^1G_4(\Gamma_4)$	2.387	2.430*	2.455	2.480*
$^1G_4(\Gamma_3)$	2.567	2.572	2.691	2.703

*These bands were observed only at 4.2 K.

because outer, closed-shell 5s and 5p electrons screen the 4f shell. This screening also shields the 4f shell from strong interactions with lattice vibrations, so the typical field splitting of the 4f levels is only about 0.01 eV, and the gross spectral features for a given impurity ion are unusually independent of the host lattice. Thus the 4f → 4f transitions remain very weak and sharp because they are parity-forbidden as in the free-ion case.

The normal oxidation state of all rare-earth compounds is the trivalent state, but with the exception of promethium and lutetium, divalent rare-earth-doped crystals can be grown in the laboratory under chemical or irradiative reducing conditions. In addition, the tetravalent states of cerium, praseodymium and terbium are known to exist, and might occur in crystals grown under reducing conditions.[3.18]

a. Trivalent rare-earth ions in CaF$_2$. The absorption spectra[3.19] of the lowest 4f → 5d transitions in the rare-earth ions are shown in Fig. 3.13. The bands of Gd^{3+} and Lu^{3+} do not appear because their energies are greater than the intrinsic band-gap energy of 9.9 eV in CaF$_2$, and the synthetic element promethium was unavailable for study.

Table 3.4 summarizes the room-temperature transition energy, absorption cross-section, and half-width of the bands in Fig. 3.13. All the trivalent rare-earth ions are stable in CaF$_2$ and have ionic radii compatible with that of Ca^{2+}. Therefore the trivalent rare-earth ions substitute for Ca^{2+} but require some charge compensators, such as interstitial F$^-$, which destroy the perfect cubic symmetry of the lattice site and greatly complicate the crystal-field splitting. There are three irregularities in the lowest 4f → 5d absorption bands of the
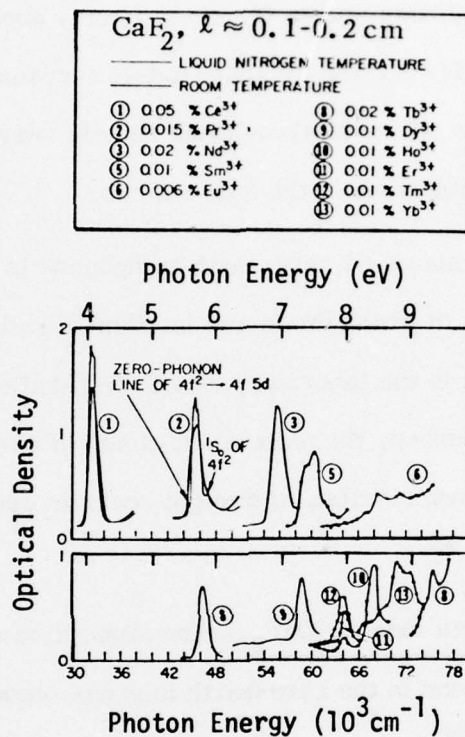
Fig. 3.13. The lowest 4f → 5d absorption band of trivalent rare-earth ions in CaF$_2$ host crystals at room temperature. [E. Loh, Phys. Rev. 147, 332 (1966).]

Table 3.4.   The ground state configurations, transition energies, and absorption cross-sections of the lowest $4f \rightarrow 5d$ band of the trivalent rare-earth ions in CaF_2 at room temperature.   [E. Loh, Phys. Rev. <u>147</u>, 332 (1966).]

Rare earth ion	Ground state of $4f^n$ configuration	Concentration in mole fraction %	Energy of lowest $4f \rightarrow 5d$ transition (eV)	Absorption cross section $10^{-18} cm^2$	Half-width toward low energy (eV)
Ce^{3+}	$4f^1\ ^2F_{5/2}$	0.01	4.03	3.9	0.17
Pr^{3+}	$4f^2\ ^3H_4$	0.015	5.66	5.5	0.21
Nd^{3+}	$4f^3\ ^4I_{9/2}$	0.02	6.94	5	0.21
Pm^{3+}	$4f^4\ ^5I_4$	Not available			
Sm^{3+}	$4f^5\ ^6H_{5/2}$	0.01	7.38	5.5	0.22
Eu^{3+}	$4f^6\ ^7F_0$	0.006	8.50	4.2	0.17
Gd^{3+}	$4f^7\ ^8S$	0.001-10	>9.7		
$(Tb^{4+}$	$4f^7\ ^8S$	< 0.02	9.36	>1.16[a]	0.10)
Tb^{3+}	$4f^8\ ^7F_6$	0.02	5.77	2.7	0.16
Dy^{3+}	$4f^9\ ^6H_{15/2}$	0.01	7.31	2.8	0.17
Ho^{3+}	$4f^{10}\ ^5I_8$	0.01	7.95 (8.44)	1.2 (6.4)	0.14 (0.17)
Er^{3+}	$4f^{11}\ ^4I_{15/2}$	0.01	7.97	2.75	0.14
Tm^{3+}	$4f^{12}\ ^3H_6$	0.01	7.94	3.74	0.17
Yb^{3+}	$4f^{13}\ ^2F_{7/2}$	0.01	8.77	3.2	0.15
Lu^{3+}		0.1	>9.9		

[a]This value is calculated by assuming the concentration of Tb^{4+} equal to that of Tb^{3+}, 0.02%.

23

trivalent rare-earth ions in CaF$_2$. First, the lowest 4f → 5d band of Ho^{3+} at 7.95 eV has an absorption cross-section less than half that of its neighbors Dy^{3+} and Er^{3+}. But the next higher 4f → 5d transition at 8.43 eV, shown in Fig. 3.13 and listed in Table 3.4 in parentheses, has a cross-section more than twice that of its neighbors. Second, in the absorption spectra of Sm^{3+} (4f^5), Eu^{3+}(4f^6), and Yb^{3+}(4f^{13}) the lowest 4f → 5d band is a doublet with separations of 0.125 eV, 0.375 eV, and 0.250 eV, respectively. Possible sources of these peaks are the presence of the corresponding divalent rare-earth ion or two configurations of the 4f^{n-1} electrons in the 4f^{n-1} 5d excited state. Finally in the spectrum of terbium there is an absorption band at 9.35 eV, shown in Fig. 3.13 and listed in Table 3.4 in parentheses, which is probably due to the presence of some tetravalent terbium.

   b. <u>Divalent rare-earth ions in CaF$_2$</u>. The absorption spectra[3.20] of the 4f → 5d transitions of the divalent rare-earth ions, excepting promethium and lutetium, are shown in Fig. 3.14. In addition, the excitation and fluorescence spectra of Tm^{2+} (4f^{13}), Er^{2+}(4f^{12}), Ho^{2+} (4f^{11}), and Dy^{2+} (4f^{10}) are shown in Fig. 3.15. These excitation spectra agree closely with the absorption spectra in most cases. The divalent rare-earth ions are isoelectronic to the trivalent ions of the next larger atomic number. However, the divalent rare-earth ions have a smaller electrostatic interaction with the 5d electrons because of the smaller nuclear charge, thus shifting the 4f → 5d absorption bands from the ultraviolet region, where they occur in the trivalent rare-earth ions, down to the visible and infrared region of the spectrum. The divalent rare-earth ions substitute for the Ca^{2+} ions and require no charge compensation, so the perfect cubic symmetry of the lattice site is preserved, giving a simpler optical spectrum
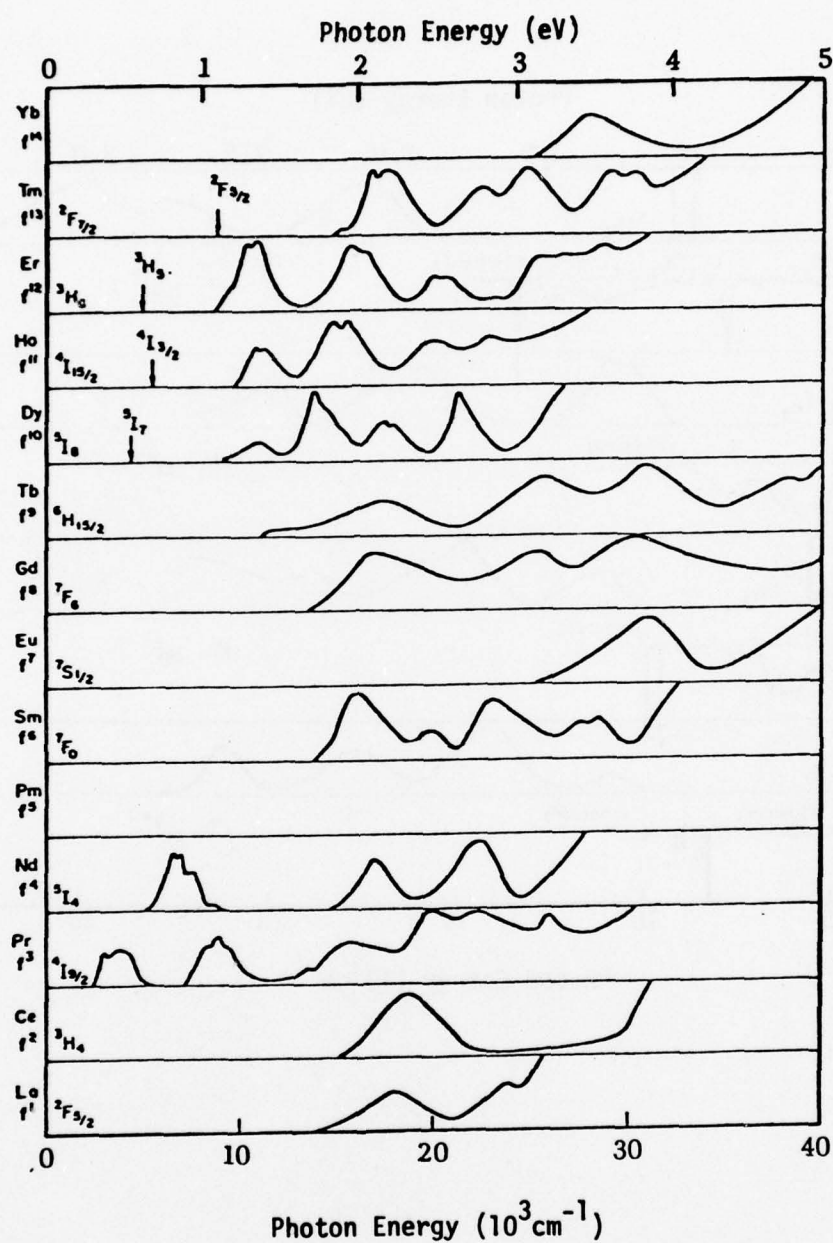
Fig. 3.14. Absorption spectra of the divalent rare-earth ions in CaF$_2$ at room temperature.   [D. S. McClure and Z. J. Kiss, J. Chem. Phys. $\underline{39}$, 3251 (1963).]

Photon Energy (eV)
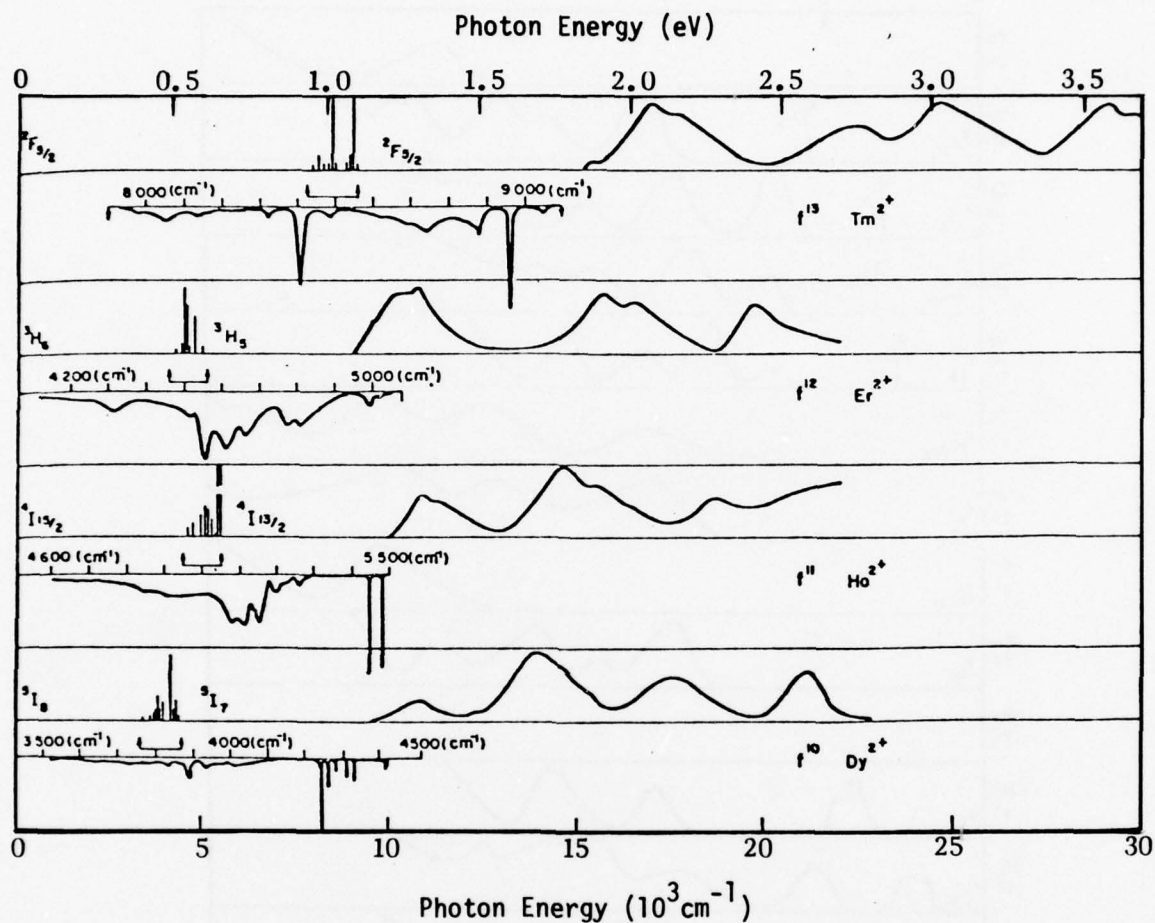
Fig. 3.15. Excitation spectra and fluorescence spectra of Tm^{2+}, Er^{2+}, Ho^{2+}, and Dy^{2+} at 77 K. The fluorescence spectra are f → f transitions as in the figure. [D. S. McClure and Z. J. Kiss, J. Chem. Phys. $\underline{39}$, 3251 (1963).]

than the trivalent ions with very sharp and weak $4f \rightarrow 4f$ transitions. The location of the $4f \rightarrow 4f$ absorptions is shown by the arrows in Fig. 3.14 for Tm^{2+}, Er^{2+}, Ho^{2+}, and Dy^{2+} in CaF_2. The structure of these transitions is difficult to observe in an absorption spectrum, but the structure can be seen in the $4f \rightarrow 4f$ fluorescence spectra shown in Fig. 3.15.

      c.   <u>Photochromic centers in CaF_2</u>. Photochromic centers formed by additive coloration in calcium vapor of CaF_2 doped with La, Ce, Gd, Tb, Lu, and Y, have the visible and ultraviolet spectra[3.21] shown in Figs. 3.16 and 3.17, and the vacuum-ultraviolet spectra[3.22] shown in Figs. 3.18−3.23. Photochromic centers can also be formed in these materials by room-temperature X- or γ-irradiation. These colored crystals possess a photochromic effect whereby their color is reversibly changed upon exposure to light. The effect is produced by a photoreversible electron transfer between a rare-earth ion and a photochromic color center: absorption of ultraviolet light ($\lambda \lesssim 400$ nm) by the photochromic color center transfers an electron to an isolated trivalent rare-earth ion; the process can be reversed thermally or by the absorption of visible light (450 nm $< \lambda < 600$ nm) by the isolated divalent rare-earth ion. The ease with which the reversal occurs is probably associated with the fact that La, Ce, Gd, Tb, and Lu are the only rare earths which are believed to have, like Y, a single d electron in the divalent crystal-field ground state.[3.2] For CaF_2 doped with La, Ce, Gd, or Tb the color changes are stable for a day or more at room temperature. In the photoionized state, the absorption spectrum of the photochromic center below 5 eV (250 nm) is similar in both intensity and structure to the un-ionized state, except that the spectrum is shifted to slightly higher energy.
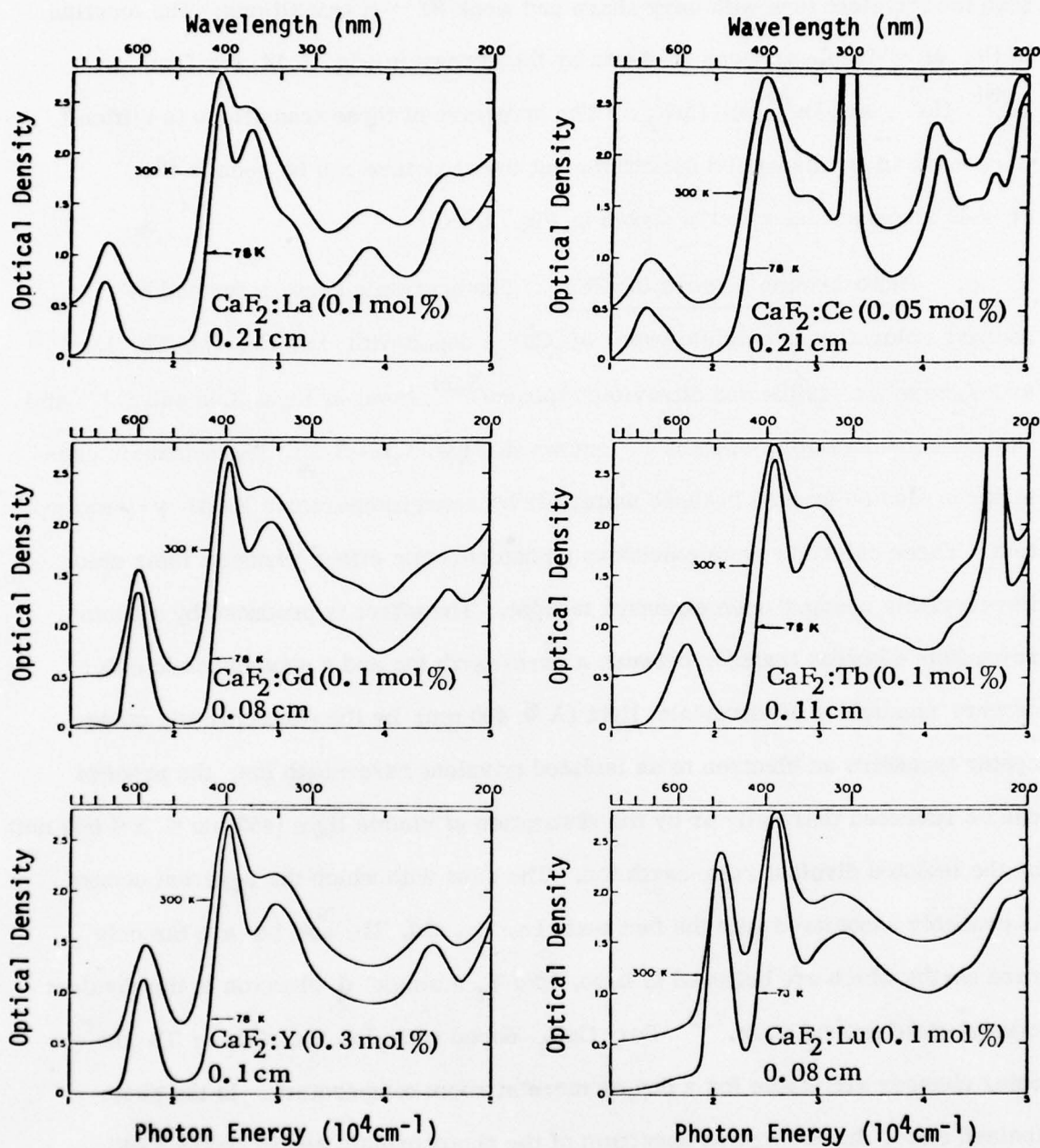
Fig. 3.16. Optical absorption spectrum of additively colored rare-earth-doped CaF$_2$. The 300 K curve has been moved upward by 0.5 OD. The intense absorption bands for Ce and Tb are due to the $4f^u \rightarrow 4f^{u-1}$ 5d transition of the trivalent rare earth and are present before coloration. [D. L. Staebler and S. E. Schnatterly, Phys. Rev. B$\underline{3}$, 516 (1971).]
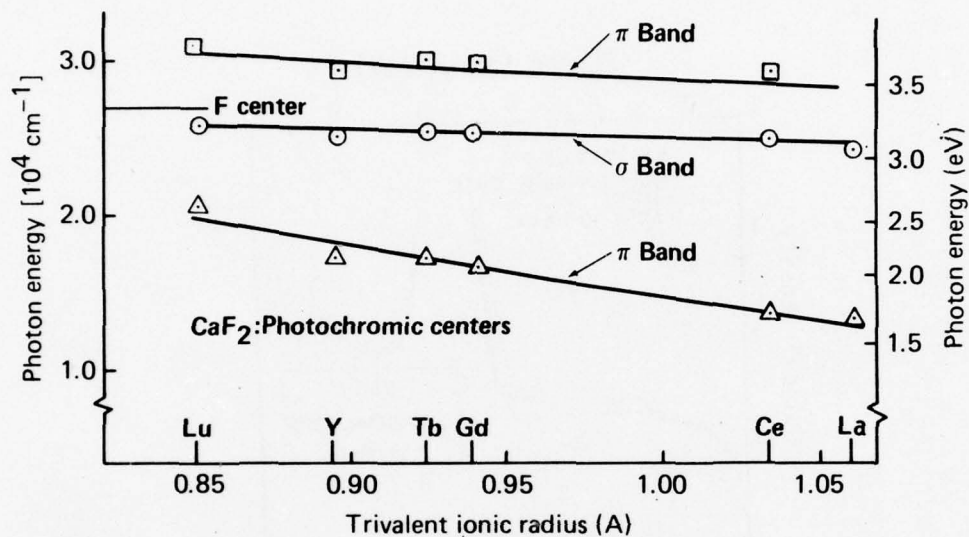
Fig. 3.17. Absorption-band energy as a function of the trivalent ion radius of the impurity. Only the three prominent bands below 4.09 eV are shown.   [D. L. Staebler and S. E. Schnatterly, Phys. Rev. B$\underline{3}$, 516 (1971).]
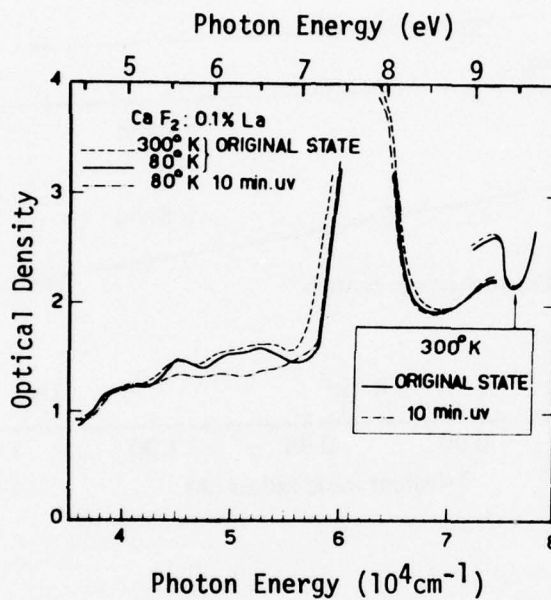
Fig. 3.18. Ultraviolet absorption spectra of photochromic centers in CaF$_2$: 0.1% La. [E. Loh, Phys. Rev. B$\underline{4}$, 2002 (1971).]
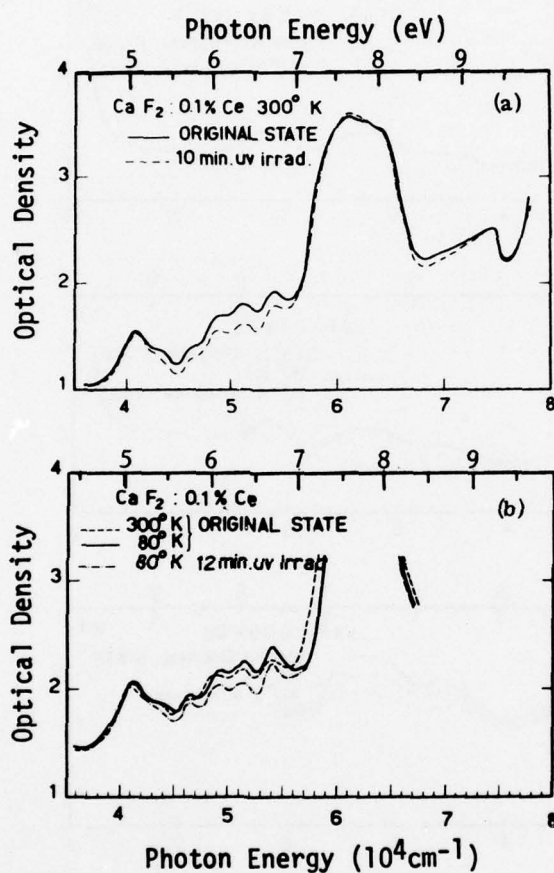
Fig. 3.19. Ultraviolet absorption spectra of photochromic centers in CaF$_2$: 0.1% Ce.   [E. Loh, Phys. Rev. B$\underline{4}$, 2002 (1971).]
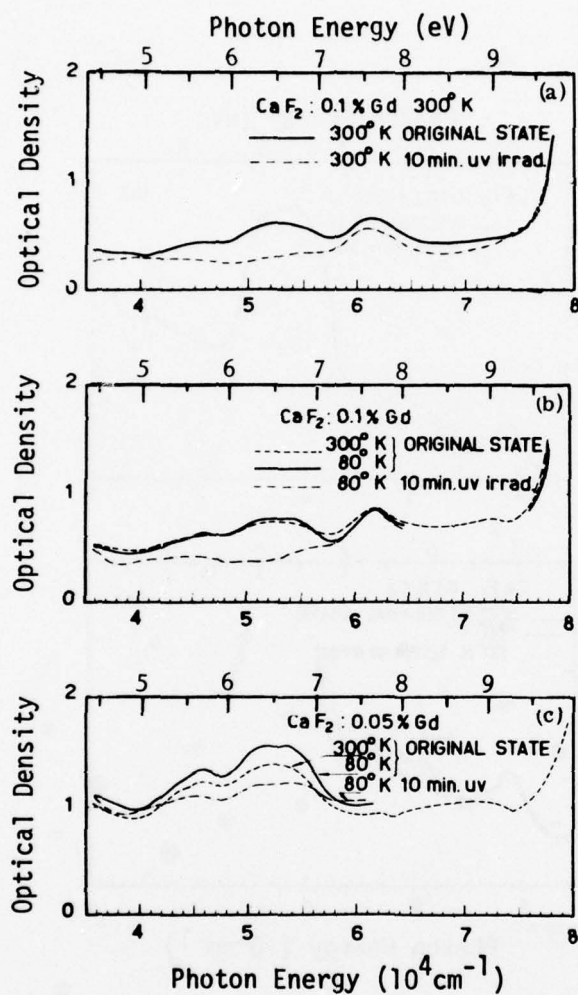
Fig. 3.20. Ultraviolet absorption spectra of photochromic
centers in CaF$_2$:Gd. [E. Loh, Phys. Rev. B$\underline{4}$, 2002 (1971).]
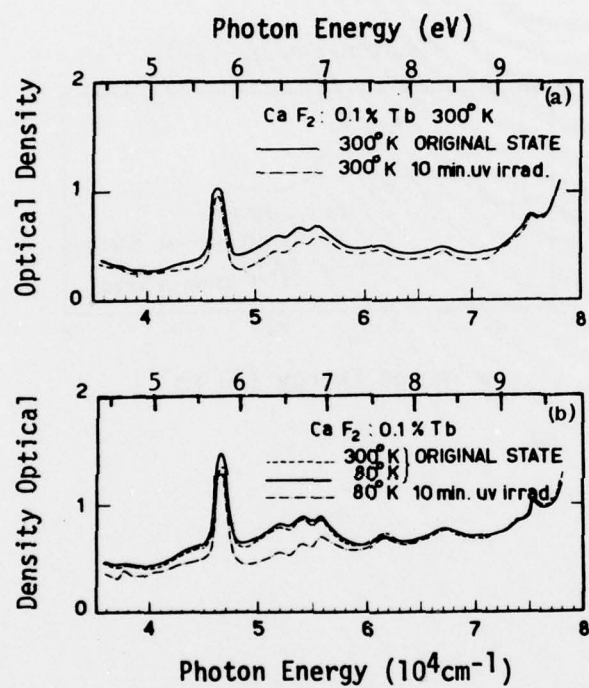
Fig. 3.21. Ultraviolet absorption spectra of photochromic centers in CaF$_2$:0.1% Tb. [E. Loh, Phys. Rev. B4, 2002 (1971).]
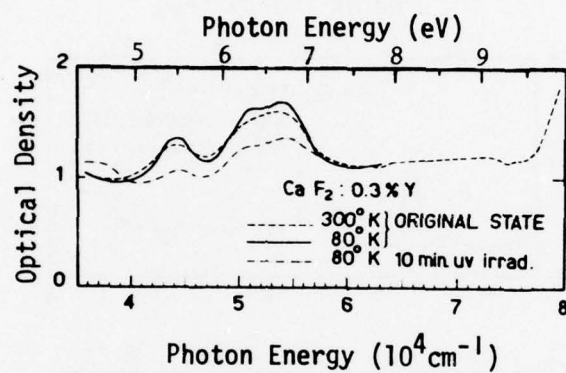
Fig. 3.22. Ultraviolet absorption spectra of photochromic centers in CaF$_2$:0.3% Y.   [E. Loh, Phys. Rev. B$\underline{4}$, 2002 (1971).]
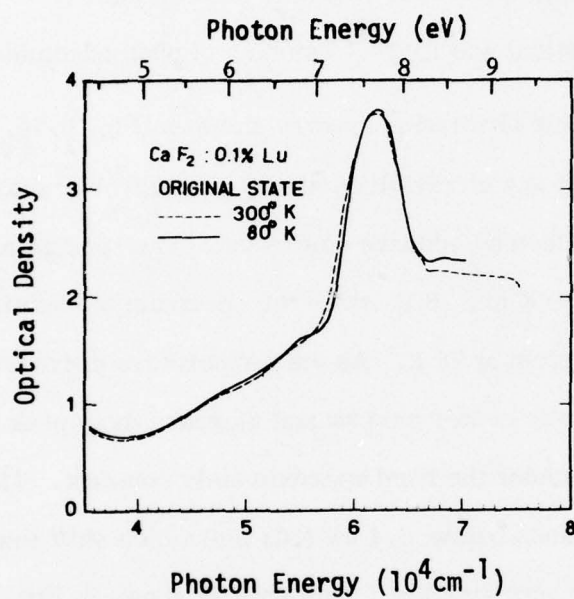
Fig. 3.23. Ultraviolet absorption spectra of photochromic centers in CaF$_2$:0.1% Lu.   [E. Loh, Phys. Rev. B4, 2002 (1971).]

The simplest physical model of a photochromic center is a trivalent-rare-earth ion substituted on a Ca^{2+} site adjacent to a fluorine vacancy that has trapped two electrons, to make a neutral center. Equivalently it can be considered a molecular-like complex of a divalent-rare-earth ion and a nearest-neighbor F center that has two electrons trapped in defect-impurity orbital states.[3.23] This model is consistent with both optical and EPR[3.24] studies of photochromic centers.

The thermally stable absorption spectra shown in Fig. 3.16, i.e., the spectra found after the decay of any ultraviolet-induced photochromic effects, are due to the color centers produced by additive coloration. The spectra are only shown for each impurity at 300 K and 78 K since the spectrum of each impurity at 4 K is identical to its spectrum at 78 K. As the temperature decreases, the individual bands of the photochromic center narrow and increase their peak intensity while keeping the total area under the band approximately constant. The spectra contain three prominent bands below 4.1 eV (302 nm) which shift towards higher energy as the impurity gets smaller. This shift is shown in Fig. 3.17 as a function of the ionic radius of the trivalent impurity obtained from the oxide of the impurity.[3.25] The three bands are identified as electron transitions from the A_1 defect-impurity orbital singlet ground state to the excited singlet (σ band) or doublet (π band) states consistent with the three-fold rotation symmetry of the photochromic center oriented along the $\langle 111 \rangle$ directions. The σ band is the most intense, changes the least as a function of the ionic impurity radius, and approaches the CaF_2 F-band energy (3.22 eV) for the smallest impurity. The assignment of the bands was determined by linear dichroism experiments. Linearly polarized light is selectively absorbed by photochromic centers in

36

particular orientations resulting in a disturbance of the isotropic distribution of centers by either ionizing these centers or reorienting them along another direction.

The ultraviolet and vacuum-ultraviolet spectra[3.22] in Figs. 3.18 – 3.23 include curves for both the thermally stable state and the photo-ionized state of the photochromic centers in CaF$_2$. These samples were obtained by E. Loh from D. L. Staebler, and are apparently some of the same samples used for the spectra in Fig. 3.16. All the impurities have absorption bands between 4.35 eV (286 nm) and 7.07 eV (175 nm) which are probably due to electron transitions between the ground state and higher excited states of the photochromic center, analogous to the L bands of F centers in alkali halides.[3.26] The absorption in this spectral region is particularly sensitive to the state of the photochromic centers, being consistently higher if the photochromic centers are in the thermally stable ground state. At ~7.7 eV (160 nm) there is a prominent peak in all the spectra except the 0.05% Gd-doped CaF$_2$ in Fig. 3.20(c) and the 0.3% Y-doped CaF$_2$ in Fig. 3.22. This peak is characterized by the following properties: (1) the absorption is strong, (2) the peak position of the band is independent of the impurity cation, (3) the absorption is independent of the ionization state of the photochromic centers, (4) the strength of the band appears to depend on the impurity ion and its concentration. The strength and fixed energy of this peak suggest that there is a charge transfer occurring between the photochromic center and a nearby impurity of the same chemical species as that in the photochromic center. For this absorption mechanism, the strength of the band should increase if the impurity ions cluster together. Therefore strong absorption should occur for the larger ions such as La^{3+} and Ce^{3+} which cluster more readily near vacancies at higher impurity concentrations and for

highly annealed samples. The strong 7.7 eV (160 nm) absorption band of the 0.1%
Lu-doped CaF$_2$ in Fig. 3.23 does not appear to fit this pattern because the doping
level is low and Lu^{3+} is the smallest ion in this group. However, this crystal was
grown at Optovac while the others were grown at RCA Laboratories, so a dif-
ferent annealing history could account for the greater clustering and thus greater
absorption relative to the other samples.

4. Actinide ions in CaF$_2$.

The actinide ions are similar to the rare-earth ions in that they both have
unfilled f shells shielded by closed s and p shells which tend to preserve the
free-ion absorption spectrum of the f → f transition even in a crystalline envi-
ronment. However, the large orbital radius of the 5f shell in the actinides
reduces the shielding effect of the $6s^2 6p^2$ electrons below that observed in the
corresponding shells of the rare-earth ions. In general, the spectra of the
actinides are more sensitive to their environment than the spectra of the rare
earths; hence determination of the oxidation state or ground state configuration
of an actinide ion in one host material is not reliably determined by cross-
correlation against the spectrum of the same ion in a known state but in a
different host material. The spectra are further complicated by the pronounced
self-coloration of the crystals or the modification of the impurity oxidation state
produced by the radioactivity of the actinide ions themselves. Thus the colora-
tion history of CaF$_2$ doped with an actinide depends not only on the particular
element present, but also on the isotope number or isotope ratios, and the length
of time since the crystal was grown or underwent high-temperature annealing.

a. $\underline{U^{4+} \text{ and } U^{6+} \text{ in } CaF_2}$. The absorption spectra[3.27] of green, brown, and yellow crystals of CaF_2 doped with $U(5f^3 6d^1 7s^2)$ are shown in Figs. 3.24, 3.25, and 3.26, respectively. The absorption spectrum[3.28] of a deep red crystal of CaF_2:U after γ-irradiation is shown in Fig. 3.34. The oxidation states of uranium in different colored CaF_2 crystals have been subject to question because the oxidation state may change while the CaF_2:U melt is at a high crystal-growing temperature. McLaughlin, et al.,[3.27] have unambiguously identified the oxidation states of uranium in different colored crystals by developing reproducible methods of growing each color of crystal. The oxidation state of the uranium in the crystals was then determined from measurements of the reducing power and total uranium content of the crystals. The upper spectrum in Fig. 3.24 is for green CaF_2:U made from crystalline CaF_2, 2 wt % PbF_2, and 1 wt % UF_4. The spectrum of this crystal is identical to the spectrum of a green crystal produced by Optovac Inc. Hargreaves[3.29] attributed the spectrum to U^{2+}, but chemical analysis of both samples indicates only U^{4+} is present. The spectrum of a brown crystal made from crystalline CaF_2, 2 wt % PbF_2, and 1 wt % UO_2 is shown in Fig. 3.25. Since chemical analysis indicates that only U^{4+} is present, the differences between this spectrum and those of Fig. 3.24 must be accounted for by different methods of charge compensation, since EPR experiments[3.30, 3.31] show that the uranium ions in both crystals are on trigonal sites. When a crystal was grown from powdered CaF_2 plus 1 wt % $UO_2(NO_3)_2 \cdot 6 H_2O$, a yellow crystal containing U^{6+} was formed whose spectrum was identical to the yellow Optovac crystal[3.29] as shown in Fig. 3.26. Chemical analysis of red CaF_2:U crystals indicates U^{3+} is present.
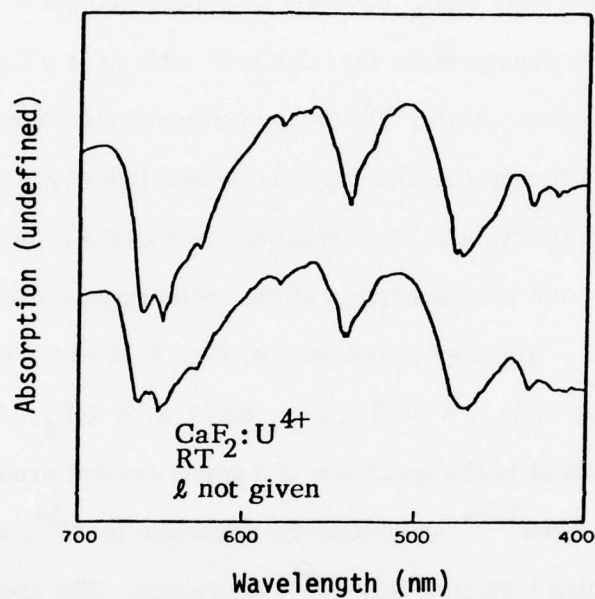
Fig. 3.24. Green crystals of uranium-doped CaF$_2$. Upper trace: absorption spectrum of CaF$_2$: 1% UF$_4$. Lower trace: absorption spectrum of green CaF$_2$ crystals described in Ref. 3.29. [R. McLaughlin, U. Abed, John G. Conway, N. Edelstein, and E. H. Huffman, J. Chem. Phys. 53, 2031 (1970).]
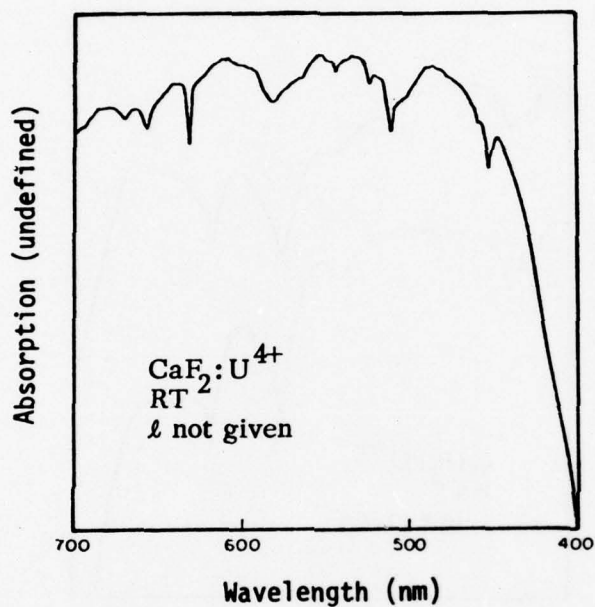
Fig. 3.25.   Absorption spectrum of a brown crystal of
CaF$_2$:1% UO$_2$.   [R. McLaughlin, U. Abed, John G. Conway,
N. Edelstein,   and E. H. Huffman, J. Chem. Phys. 53,
2031 (1970).]

41
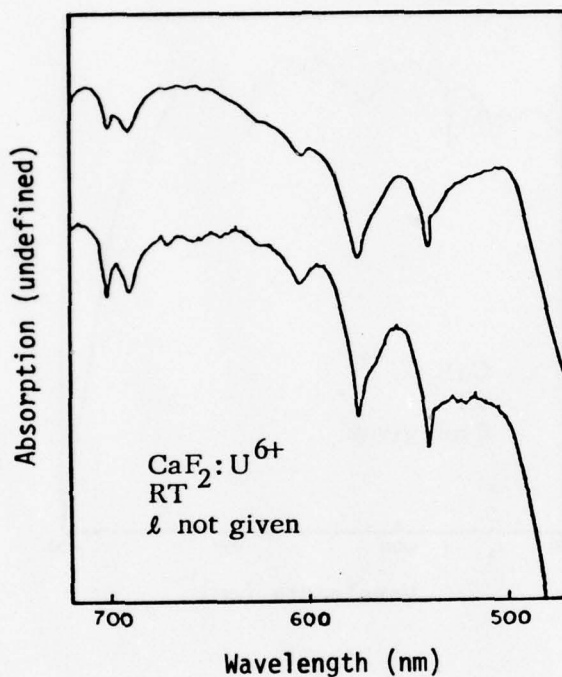
Fig. 3.26. Yellow crystals of uranium-doped CaF$_2$. Upper spectrum: absorption spectrum of CaF$_2$:1% UO$_2$(NO$_3$)$_2$. Lower spectrum: absorption spectrum of yellow crystals described in Ref. 3.29.   [R. McLaughlin, U. Abed, John G. Conway, N. Edelstein, and E. H. Huffman, J. Chem. Phys. 53, 2031 (1970).]

b. $\underline{Np^{3+}\ in\ CaF_2}$. The absorption bands[3.28] of several oxidation states of Np $(5f^4 6d^1 7s^2)$ in LaBr$_3$, CaF$_2$, and in solutions of D$_2$O are shown in Fig. 3.27. The absorption spectra of CaF$_2$:Np^{3+} in the infrared are shown in Figs. 3.28 and 3.29, while the visible spectrum of X-irradiated CaF$_2$:Np^{3+} is shown in Fig. 3.34[3.28]. CaF$_2$ crystals doped with 0.1 − 0.2 wt % ^{237}Np (half-life, 2.2 × 10^6 yr) were light green in color. Np^{3+} was the principal oxidation state present in these crystals, since Np^{4+} and Np^{6+} could be eliminated by comparisons with the ion spectra of Fig. 3.27 while crystal growth conditions precluded the formation of Np^{5+}. When CaF$_2$:Np^{3+} was irradiated at 273 K, it turned a deep blue-green, and an intense absorption band appeared at 580 nm (2.14 eV) in Fig. 3.34. The absorption spectra of CaF$_2$:Np^{3+} is shown before and after X-irradiation in Figs. 3.28 and 3.29. The room-temperature irradiation in Fig. 3.28 decreased the intensities of four Np^{3+} lines and created four new sharp lines which were assigned to Np^{4+}. Apparently the irradiation converted Np^{3+} ions at certain symmetry sites to Np^{4+}. When CaF$_2$:Np^{3+} was X-irradiated at 77 K, only two new Np^{4+} lines appeared, indicating that fewer Np^{3+} symmetry sites could be oxidized at this temperature. In addition, Fig. 3.29 shows several new Np^{3+} lines that appeared from site symmetry changes only during low-temperature irradiation.

· The Np^{4+} produced by radiation, the low-temperature site-symmetry conversion of Np^{3+}, and the broad visible absorption at 580 nm, bleached slightly over a period of months at room temperature. The Np^{4+} structures and the broad visible absorption band could be completely bleached by heating to 400 C, or reduced by 50 percent by prolonged exposure to 300 − 500 nm light.
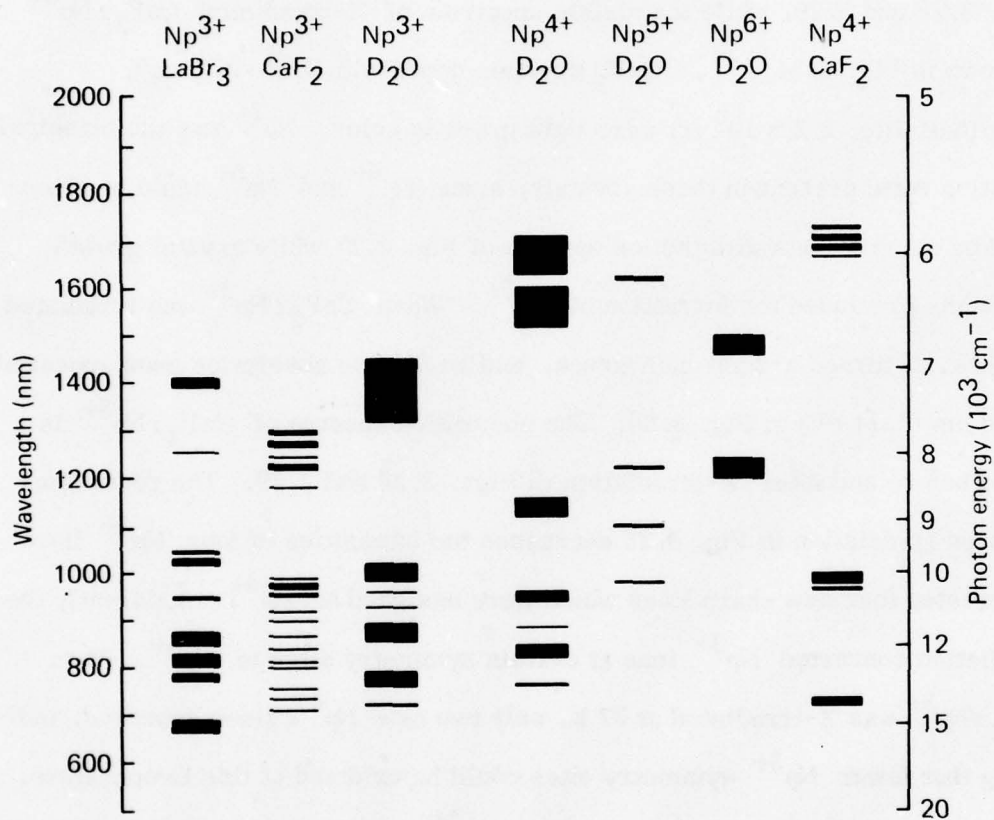
Fig. 3.27. Comparison of the absorption spectra of
Np ions in various media. [J. J. Stacy, N. Edelstein,
and R. D. McLaughlin, J. Chem. Phys. 57, 4980 (1972).]
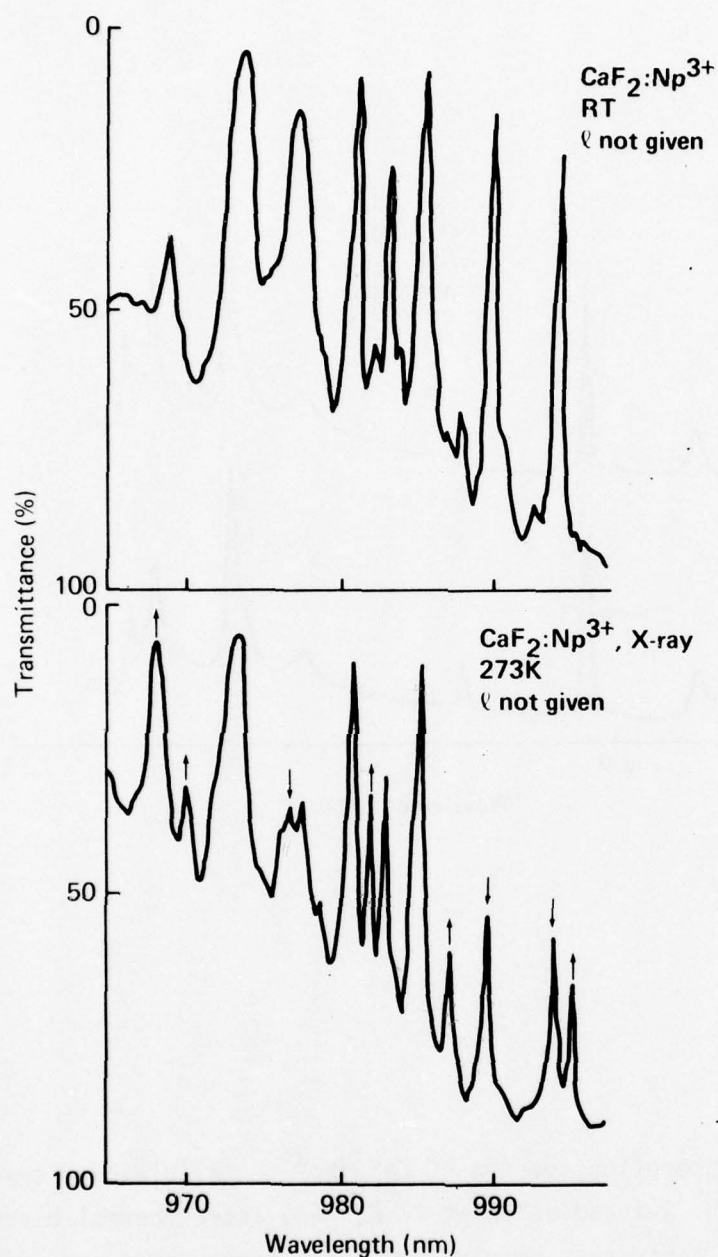
Fig. 3.28. Absorption spectra of CaF$_2$: Np^{3+}: (a) before irradiation, (b) after 10 h irradiation at 273 K. The arrows indicate the absorption lines which increase or decrease upon irradiation. [J. J. Stacy, N. Edelstein, and R. D. McLaughlin, J. Chem. Phys. 57, 4980 (1972).]
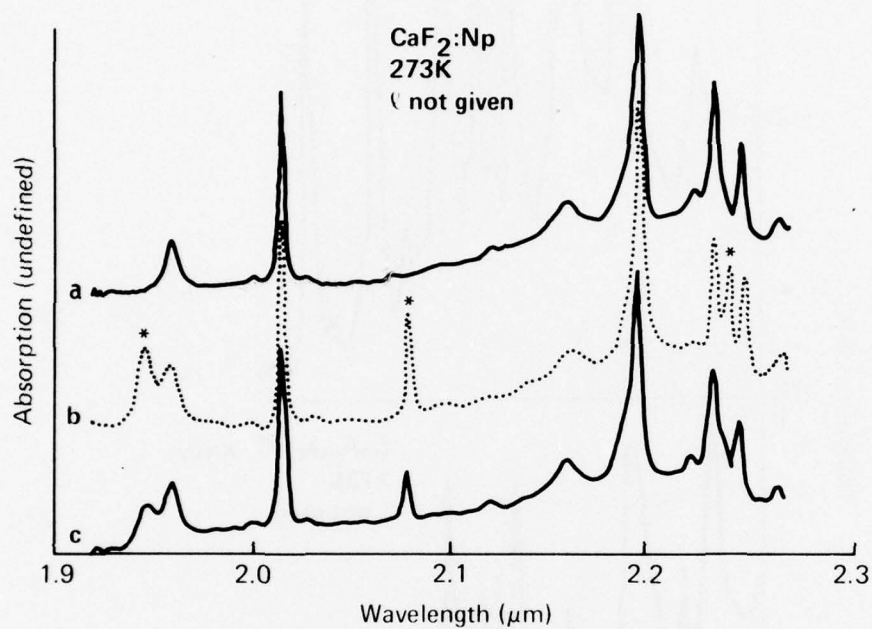
Fig. 3.29. Absorption spectra of CaF$_2$:Np^{3+}: (a) bleached crystal, (b) after 48 h X-irradiation at 77 K, (c) after thermal bleaching to RT. The asterisks denote new lines formed upon irradiation. [J. J. Stacy, N. Edelstein, and R. D. McLaughlin, J. Chem. Phys. 57, 4980 (1972).]

c.   Pu^{3+} and Pu^{4+} in CaF$_2$.   The absorption spectra[3.28, 3.32] of Pu$(5f^6 6d^0 7s^2)$ in CaF$_2$ is shown in Figs. 3.30 and 3.34. The sharp line spectra of Pu^{4+} ions at 77 K in various media is shown in Fig. 3.31, while Table 3.5 lists absorption lines and bands which develop in CaF$_2$:Pu^{3+} by self-irradiation.

CaF$_2$ crystals grown with 0.1 – 0.2 wt% of ^{239}Pu (half-life, 24,360 yr) or ^{238}Pu (half-life, 86 yr) are initially colorless or light blue. Self-irradiation causes the crystals to turn a dark blue color over a period of months in the case ^{239}Pu, or a period of days for ^{238}Pu. The original oxidation state of the plutonium in CaF$_2$ was determined by identifying the center frequencies of three groups of sharp lines with similar groups found by Lämmermann and Conway[3.33] for Pu^{3+} in La(C$_2$H$_5$SO$_4$)$_3 \cdot$ 9 H$_2$O. The comparison is shown in Table 3.6. As self-irradiation of the crystals continues at room temperature, broad bands with half-widths $\sim$0.01 eV ($\sim$ 10 nm) and sharp lines with half-widths $\sim$0.001 eV ($\sim$ 1 nm) develop in the absorption spectrum. The location and strengths of these features are listed in Table 3.5, and the growth of several sharp lines is shown in Fig. 3.30. When self-irradiation occurred at 77 K, the crystals took on a different shade of blue and the sharp line spectra were absent. The radiation-induced sharp line spectra shown in Fig. 3.31 were identified as Pu^{4+} lines by comparison of its spectrum with the solution spectrum of Pu^{4+} and the spectrum of co-precipitated Pu^{4+} and CaF$_2$ in a mineral-oil mull.

The absorption coefficients for CaF$_2$:Pu^{4+} are much stronger than CaF$_2$:Pu^{3+} since very strong Pu^{4+} lines develop with only a small decrease in the Pu^{3+} lines. The broad bands shown in Fig. 3.34 are due to some type of radiation-induced color center in CaF$_2$.
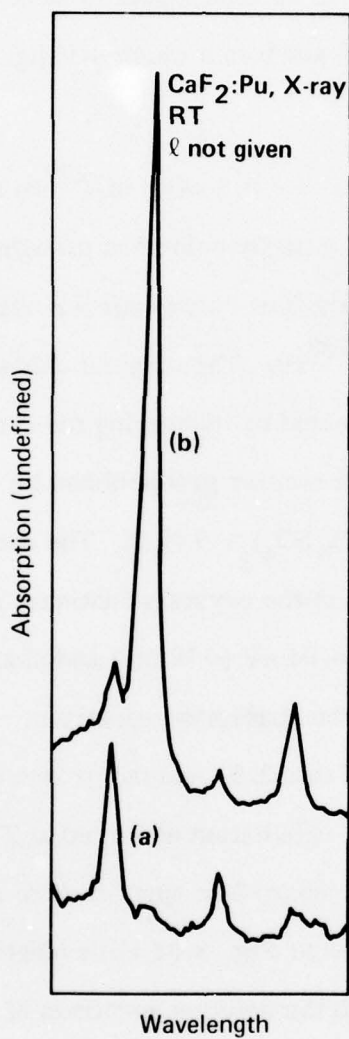
Fig. 3.30.   Absorption spectra of CaF$_2$:Pu: (a) before irradiation, (b) after X-irradiation showing growth of Pu^{4+} lines at 455.4 nm (strong) and 458.4 nm (weak). [R. McLaughlin, R. White, N. Edelstein, and J. G. Conway, J. Chem. Phys. 48, 967 (1968).]

48
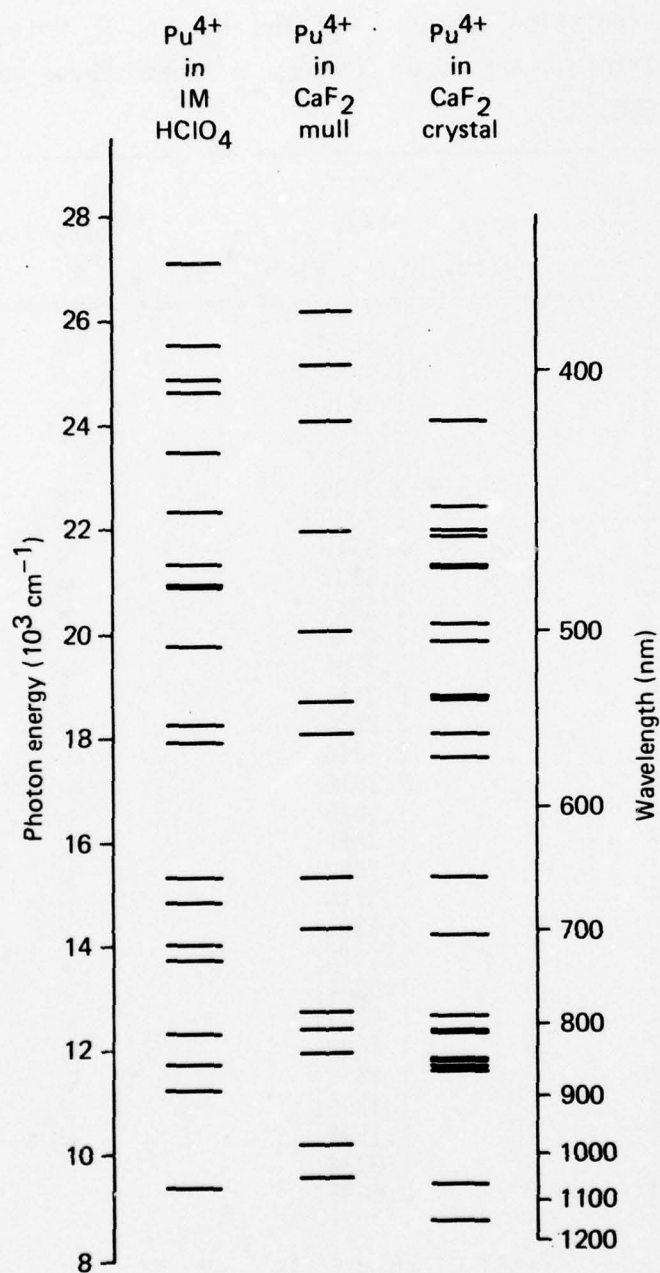
Fig. 3.31.   Sharp line spectra of Pu^{4+} ions at 77 K in various media. [R. McLaughlin, R. White, N. Edelstein, and J. G. Conway, J. Chem. Phys. 48, 967 (1968).]

Table 3.5.   Lines which grow into CaF$_2$:Pu^{3+} crystals due to radiation damage.   [R. McLaughlin, R. White, N. Edelstein, and J. G. Conway, J. Chem. Phys. <u>48</u>, 967 (1968).]

Wavelength (nm)	Energy (eV)	Intensity[a]
	Half-width $\approx 5 \times 10^{-4}$ eV	
414.9	2.9872	m
415.1	2.9859	w
415.4	2.9836	w
446.3	2.7771	w
455.4	2.7217	s
455.9	2.7186	w
458.4	2.7038	w
469.3	2.6410	w
471.2	2.6303	w
495.5	2.5014	w
504.0	2.4592	w
532.3	2.3284	w
534.9	2.3171	w
553.7	2.2384	m
567.4	2.1844	w
567.6	2.1836	w
651.8	1.9016	m
700.6	1.7692	w
702.1	1.7653	w
788.9	1.5710	w
808.8	1.5325	w
809.3	1.5315	w
809.9	1.5304	w
843.1	1.4701	m
844.7	1.4673	w
852.7	1.4535	w
860.8	1.4399	w
1060.0	1.1692	w
1144.0	1.0834	
1850.0	0.6695	
	Half-width $\approx 5 \times 10^{-2}$ eV	
599.8	2.0667	
632.8	1.9588	
657.6	1.8845	
805.7	1.5373	

[a] s, strong; m, moderate; and w, weak.

Table 3.6. Comparison of the centroids of sharp lines of Pu^{3+}. [R. McLaughlin, R. White, N. Edelstein, and J. G. Conway, J. Chem. Phys. $\underline{48}$, 967 (1968).]

	Center of Group (eV)		
La(C$_2$H$_5$SO$_4$) $\cdot$ 9H$_2$O:Pu^{3+}	2.4343	1.9854	1.8542
CaF$_2$:Pu^{3+}	2.4665	1.9826	1.8827
Difference	0.0322	-0.0087	0.0285

d. $\underline{Am^{2+} \text{ and } Am^{3+} \text{ in } CaF_2}$.   The optical absorption spectra of Am^{2+} and Am^{3+} in CaF_2 are shown in Figs. 3.32 and 3.34.[3.28, 3.34, 3.35a] $Am(5f^7 6d^0 7s^2)$ should be the actinide element which is most stable in the divalent oxidation state, since it has additional chemical stability from its half-filled 5f-shell configuration. In addition Eu^{3+}, which is the analog of americium in the lanthanide series, is the most easily reduced rare earth. Initially CaF_2 crystals grown with $0.1-0.2$ wt% ^{241}Am (half-life, 458 yr) or ^{243}Am (half-life, 7370 yr) are light pink or tan, but self-irradiation darkens them to a brown color after weeks or months.

The visible spectrum of self-irradiated CaF_2:Am is shown in Fig. 3.32(a) six weeks after crystal growth. The sharp lines between 525 nm and 490 nm are due to Am^{+3} while the broad peaks are from Am^{+2}. Figure 3.32(b) shows the spectrum of the same crystal after the Am^{2+} has been oxidized back to Am^{3+} by heating for 1h at 500 C. For comparison, Fig. 3.32(c) shows the spectrum of Am^{2+} in a deep reddish-brown, electrolytically reduced crystal subjected to the same heat treatment as the previous crystal. EPR experiments confirm that the divalent americium has the electronic configuration $^8S_{7/2}$ (f^7) and is located on the Ca^{2+} cubic sites.[3.35a] Attempts to find the sharp line spectra expected of Am^{4+} after high radiation doses were unsuccessful.

e. $\underline{Cm^{3+} \text{ and } Cm^{4+} \text{ in } CaF_2}$.   The spectral lines[3.35a] of Cm^{3+} and Cm^{4+} in CaF_2 are shown in Fig. 3.33, and the X-irradiated visible spectrum[3.28] of CaF_2:Cm is shown in Fig. 3.34. CaF_2 crystals grown with $^{244}Cm(5f^7 6d^1 7s^2)$ (half-life, 17.6 yr) are initially pale yellow or colorless, but self-irradiation turns the crystals rose colored after one hour, burgundy after 3−4 h, and
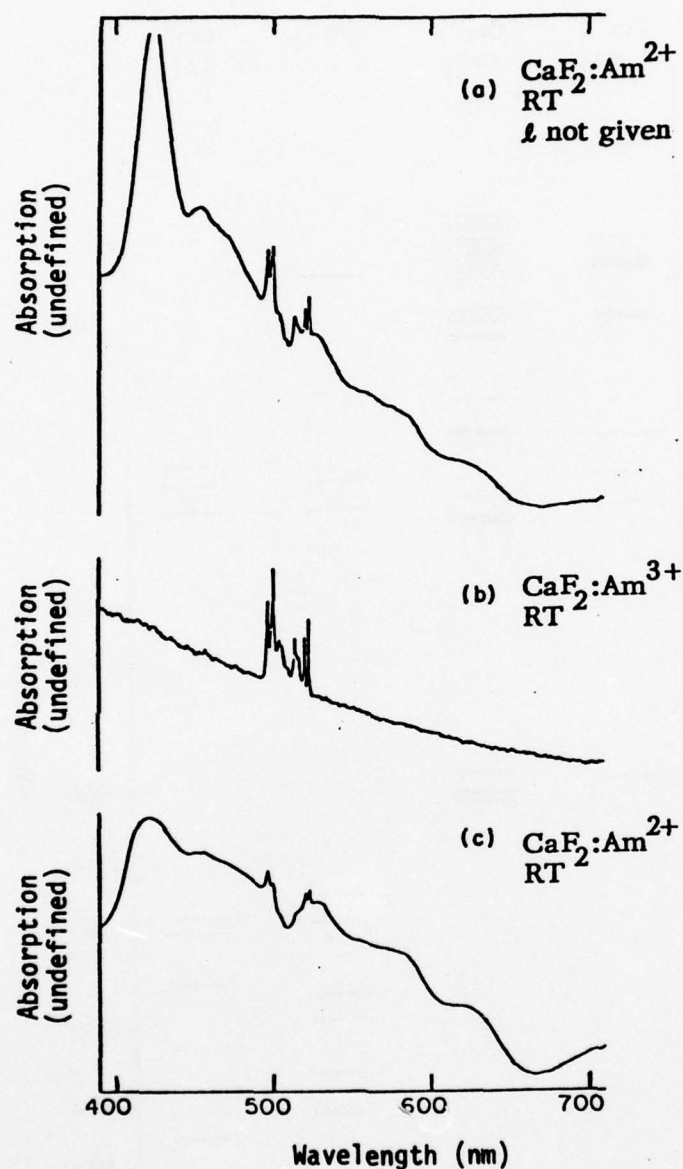
Fig. 3.32. (a) Optical spectrum of a radiation reduced CaF$_2$:Am^{3+} crystal. (b) Optical spectrum of CaF$_2$:Am^{3+} crystal after annealing. (c) Optical spectrum of an electrolytically reduced CaF$_2$:Am^{2+} crystal. [N. Edelstein, W. Easley, and R. McLaughlin, J. Chem. Phys. 44, 3130 (1966).]
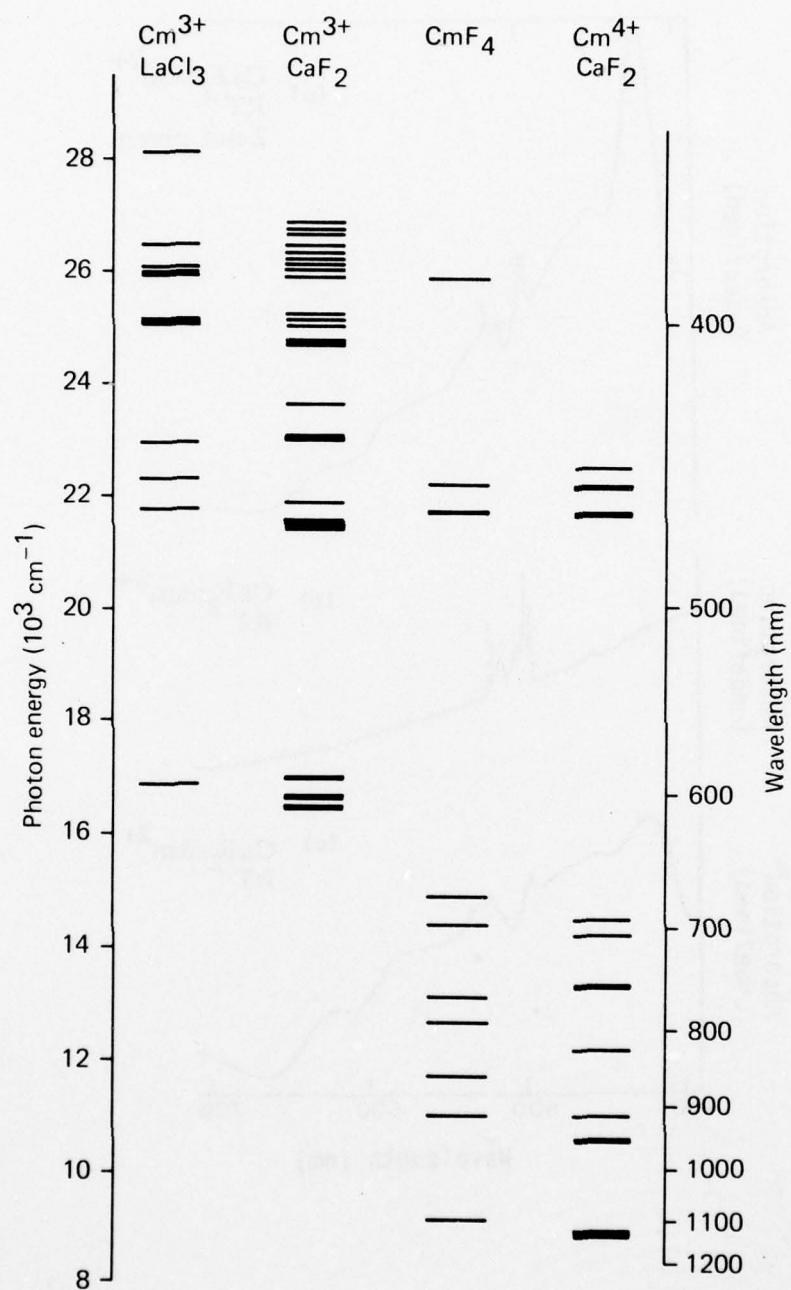
Fig. 3.33. Absorption bands of Cm^{3+} and Cm^{4+} in various matrices.
[N. Edelstein, W. Easley, and R. McLaughlin, Advan. Chem. Ser. 71,
203 (1967).]
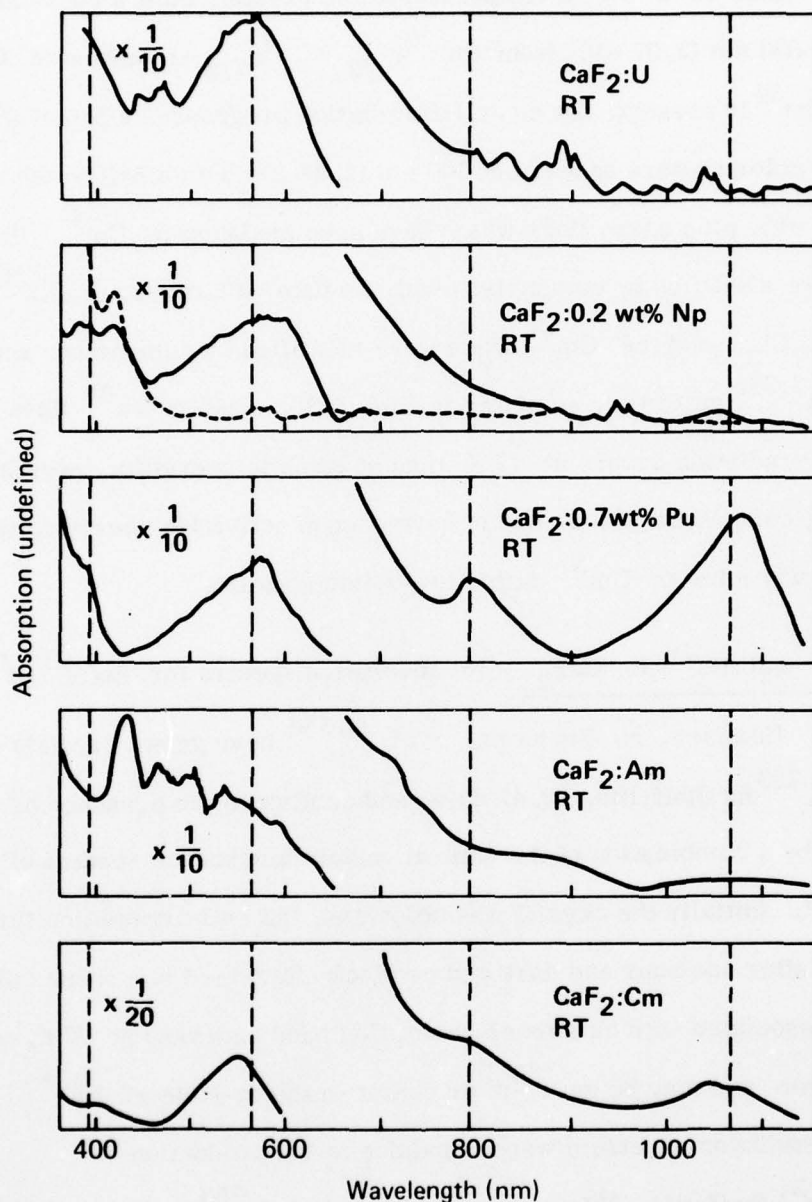
Fig. 3.34.   Broad absorption spectra of color centers in actinide-doped CaF$_2$ after 3 hours of γ irradiation. Dashed lines indicate approximate positions of absorption maxima in Table 3.7. [J. J. Stacy, N. Edelstein, and R. D. McLaughlin, J. Chem. Phys. 57, 4980 (1972).]

finally to black after 15 h. At all temperatures the crystals emit a characteristic orange glow at 600 nm (2.07 eV) from the $^6P_{7/2} \rightarrow {}^8S_{7/2}$ transition of Cm^{3+}. Initially only Cm^{3+} is present, but as self-irradiation progresses a broad absorption band from color centers appears at 500 nm (2.48 eV) with a half-width of ~200 nm (0.25 eV), plus sharp lines which have been assigned to Cm^{4+}. The Cm^{3+} lines were identified by comparison with the data of Gruber, et al.,[3.35b] on Cm^{3+} in LaCl$_3$, and the Cm^{4+} lines were identified by comparison with the data of Keenan[3.35c] on CmF$_4$, as shown in Fig. 3.33. Fewer Cm^{4+} lines appear if self-irradiation occurs at 77 K than at room temperature, possibly because charge-compensating ions do not have enough activation energy to reach as many symmetry sites of Cm^{3+} at the lower temperature.

f. <u>Es^{3+} and Es^{2+} in CaF$_2$.</u> No absorption spectra for Es($5f^{11} 6d^0 7s^2$) were available. However, N. Edelstein, et al.,[3.35d] have grown crystals of CaF$_2$ with ~0.2 wt% ^{253}Es (half-life, 20.47 days) and confirmed the presence of Es^{3+} and Es^{2+} by a combination of the natural radioluminescence spectra of the crystal and EPR. Initially the crystal was colorless, but self-irradiation turned the crystal red after one hour and dark red or black after 3 − 4 h. These color changes were associated with an intense absorption band observed at 77 K, which started at 410 nm and may be an $f^{10}d^1$ or charge-transfer state of Es^{2+}. Changes in the emission spectrum were found due to the production of ^{249}Bk($5f^9 6d^0 7s^2$) (half-life, 314 days) from the decay of ^{253}Es by α emission.

g. <u>Color centers in actinide-doped CaF$_2$.</u> Self-irradiation by alpha particles or γ-irradiation with a ^{60}Co source of actinide-doped CaF$_2$ crystals produces the broad absorption bands shown in Fig. 3.34. These broad bands

are believed to be due to color centers resulting from electron capture at various defect sites, but no reports on these color centers appear in the literature. The maxima of these absorption bands are listed in Table 3.7 for U, Np, Pu, and Cm, which have very similar spectra. The absence of some of the expected peaks in U and Np may be due to less intense absorption or masking by the sharp line spectra of the actinide ion transitions. Similar results are obtained by irradiation at 77 K except that the intensities are less for comparable dosages; Np, Pu, and Cm absorption intensities are reduced by factors of ten, three, and two, respectively.

5.   Color centers in CaF$_2$

The large variety of spectra which have been seen in CaF$_2$ subject to additive, electrolytic, or radiative coloration are summarized in Table 3.8.[3.35e] Some of these spectra[3.36, 3.37, 3.38, 3.39, 3.40] are shown in Figs. 3.35 − 3.40 and Fig. 3.43, plus the more recent spectra of Rauch and Senff[3.41] in Figs. 3.41 and 3.44 and the structure they proposed for color centers in CaF$_2$ in Fig. 3.42.

The original spectra of Mollwo[3.36] were produced by additive coloration of natural crystals of CaF$_2$ with Ca vapor, followed by rapid quenching. The two principal absorptions, the α band at 375 nm (3.31 eV), and the β band at 525 nm (2.36 eV), are always found together. The temperature dependence of the α band resembles that of the F center in the alkali halides, as shown in Fig. 3.36. In addition, the value of the drift mobilities of the α and β band-centers in an electric field, $2 - 5 \times 10^{-4}$ cm^2/V - s for temperatures in the range 650 − 840 C, are the same order of magnitude as that of the F center in alkali halides. Finally Arends,[3.42] and den Hartog and Arends[3.43] have only

Table 3.7.   Wavelengths (nm) of broad absorptions of tripositive ions in CaF$_2$. [J. J. Stacy, N. Edelstein, and R. D. McLaughlin, J. Chem. Phys. <u>57</u>, 4980 (1972).]

U		550		
Np		580		1,050
Pu	380	580	810	1,070
Cm	390	480-540	780	1,060

Table 3.8. Position of absorption peaks in natural and synthetic colored CaF$_2$ crystals. [K. Przibram, Z. Physik 154, 111 (1959).]

Sample															
Smakula (Crystal No. 1)	E			577				395		335				227	
	Ca			570.5				392		338				227	
	Pt			570.5				392							
Smakula (Crystal No. 2)	E	750			550	525			385	337	266				
	Ca		600		550	510			378		270	250			
	Pt		600		550	515			382	338			225		
Smakula (Crystal No. 3)	E	745	600				495		385		265				
Smakula [3.37]	R			580				400		335				~220	
Mollwo [3.36]	Ca					525			375						
Lüty [3.45] High	Ca			587		529		395	381	335					
Low	Ca														
Schulman et al. [3.39]	R			580				400		335				~220	
Helium fired	R				550				380	330					
With NaF addition	R		600			500			380	320					
Bontinck [3.40]	R			580				400		330				225	200
	N							400		330					200
High temp. heating with	Ca					525				340	280				

E = Coloration by 2.5 MeV electrons; Ca = additive coloring with Ca vapor; Pt = electrolytic coloration with Pt cathode; R = irradiation with x-rays; N = neutron bombardment.
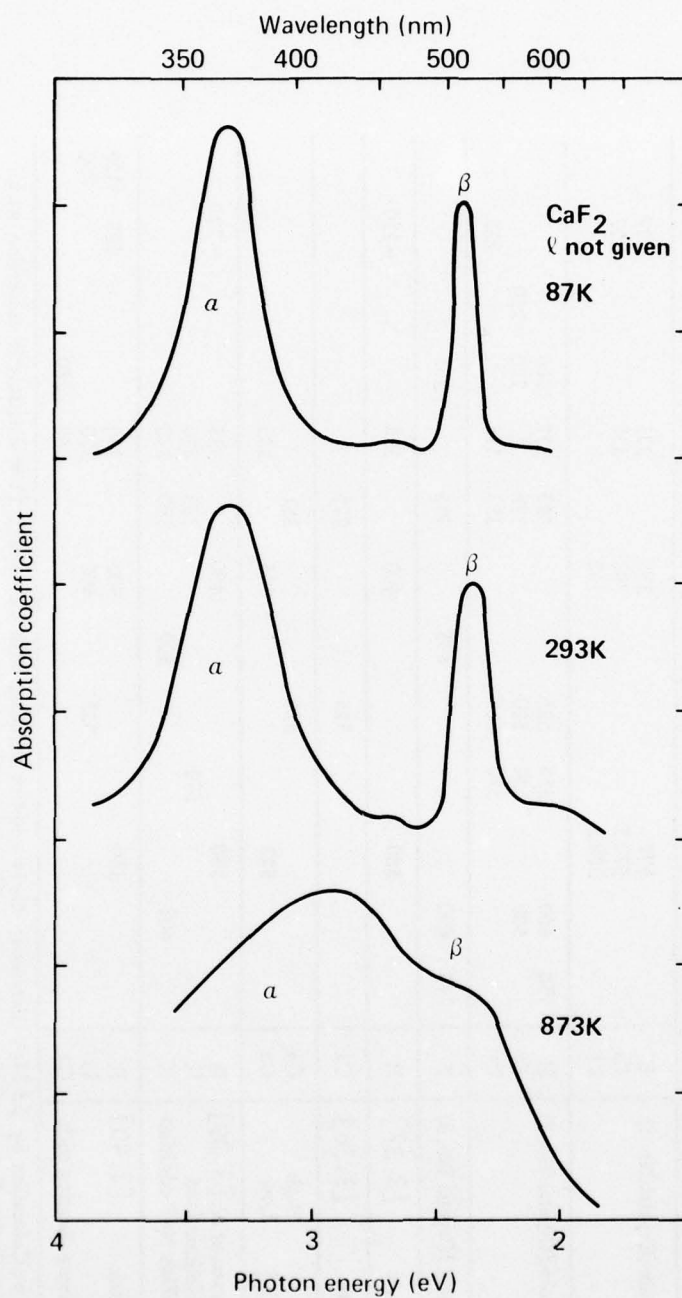
Fig. 3.35. Absorption spectra of additively colored and quenched CaF$_2$ measured at various temperatures. [E. Mollwo, Nach. Gesell. Wiss. Göttingen <u>6</u>, 79 (1934).]
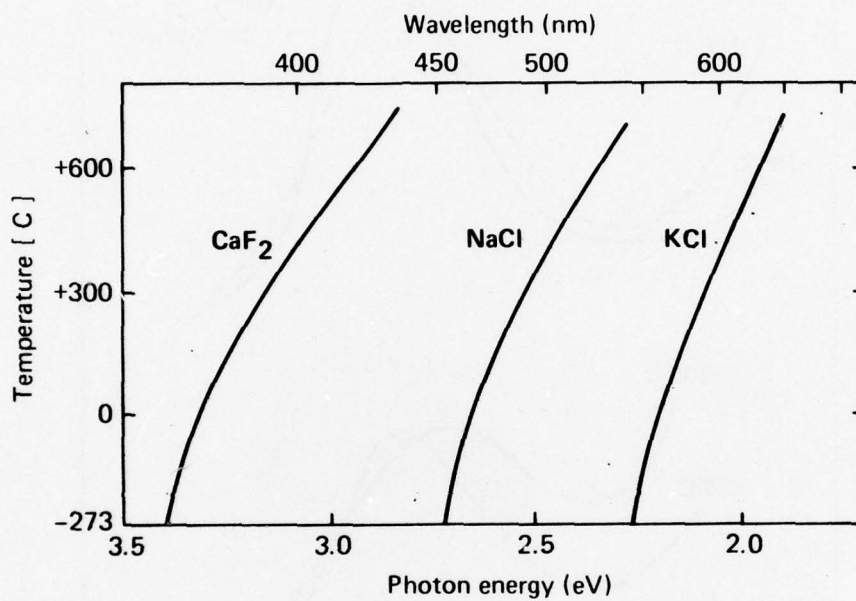
Fig. 3.36.   Temperature dependence of the peak position of the
α band of CaF$_2$ and the F band in KCℓ and NaCℓ. [E. Mollwo, Nach.
Gesell. Wiss. Göttingen <u>6</u>, 79 (1934).]
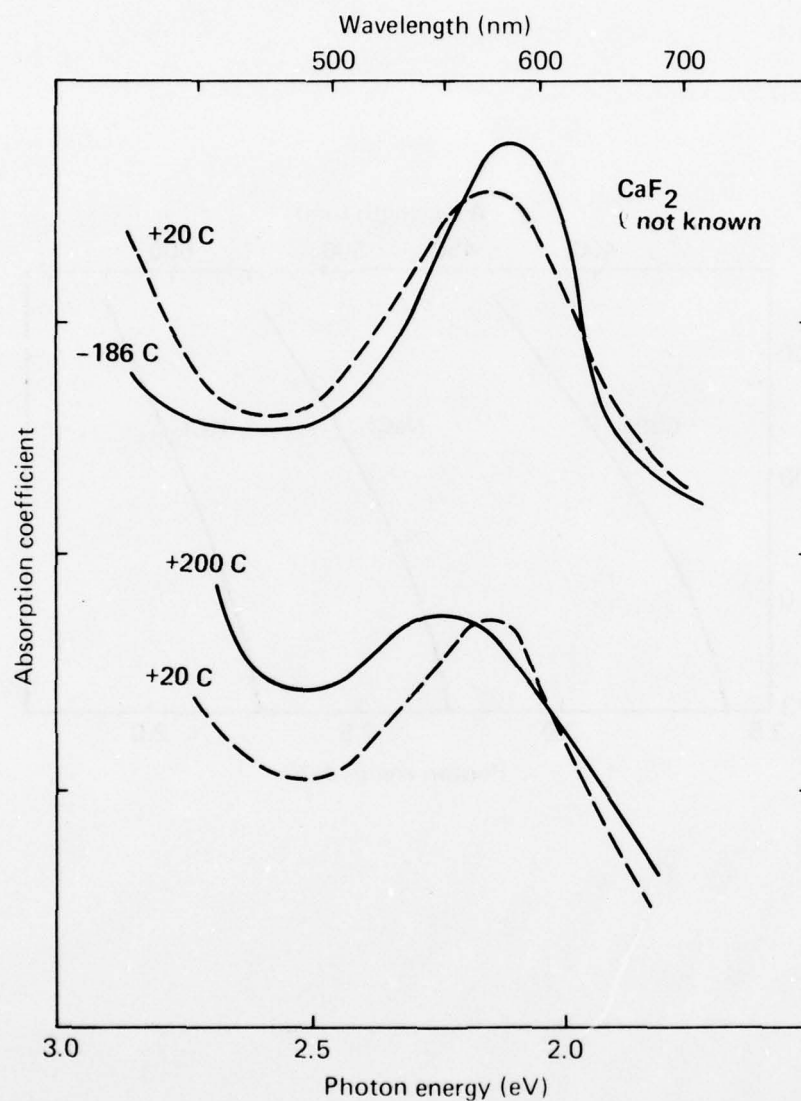
Fig. 3.37. Absorption spectra of additively colored and slowly quenched CaF$_2$ measured at various temperatures. [E. Mollwo, Nach. Gesell. Wiss. Göttingen 6, 79 (1934).]
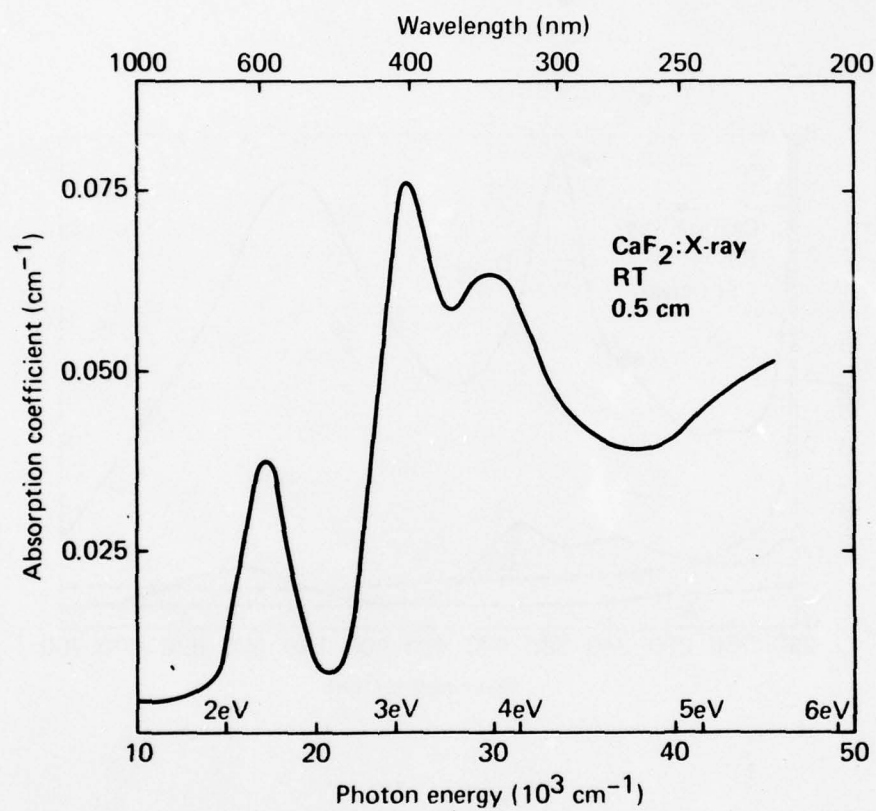
Fig. 3.38. Absorption spectrum of CaF$_2$ colored by X irradiation.
[A. Smakula, Phys. Rev. 77, 408 (1949).]
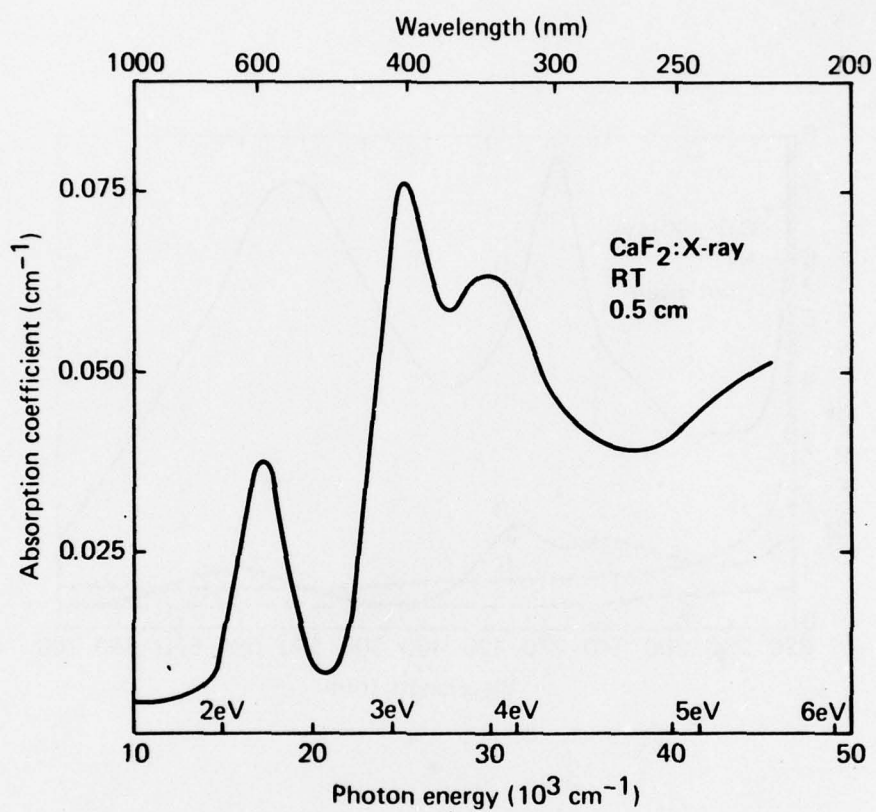
Fig. 3.38. Absorption spectrum of CaF$_2$ colored by X irradiation. [A. Smakula, Phys. Rev. 77, 408 (1949).]
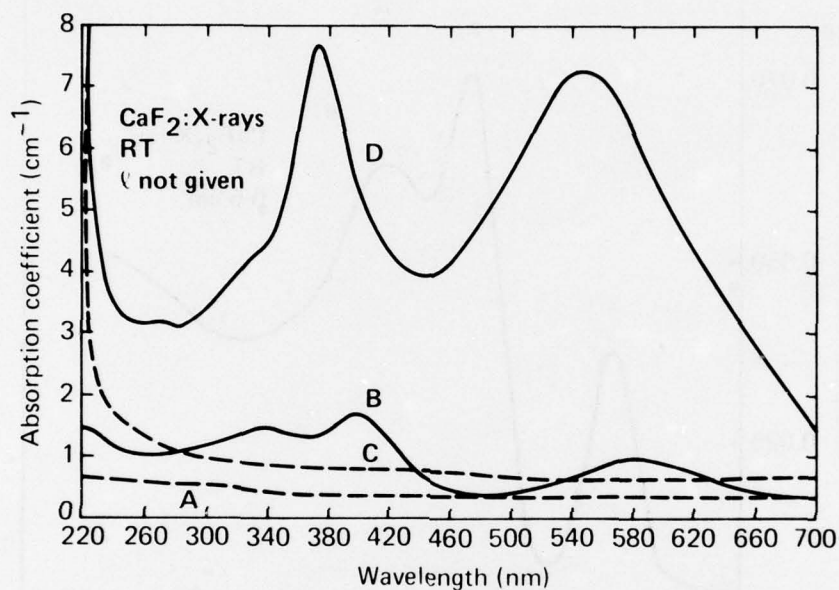
Fig. 3.39.   Absorption spectra of CaF$_2$:   A — original crystal;
B — original crystal after X irradiation;   C — crystal heat-
treated at 1200 C in He; D — crystal from C after X irradiation.
[J. H. Schulman,   R. J. Ginther, and R. D. Kirk, J. Chem. Phys.
20, 1966 (1952).]
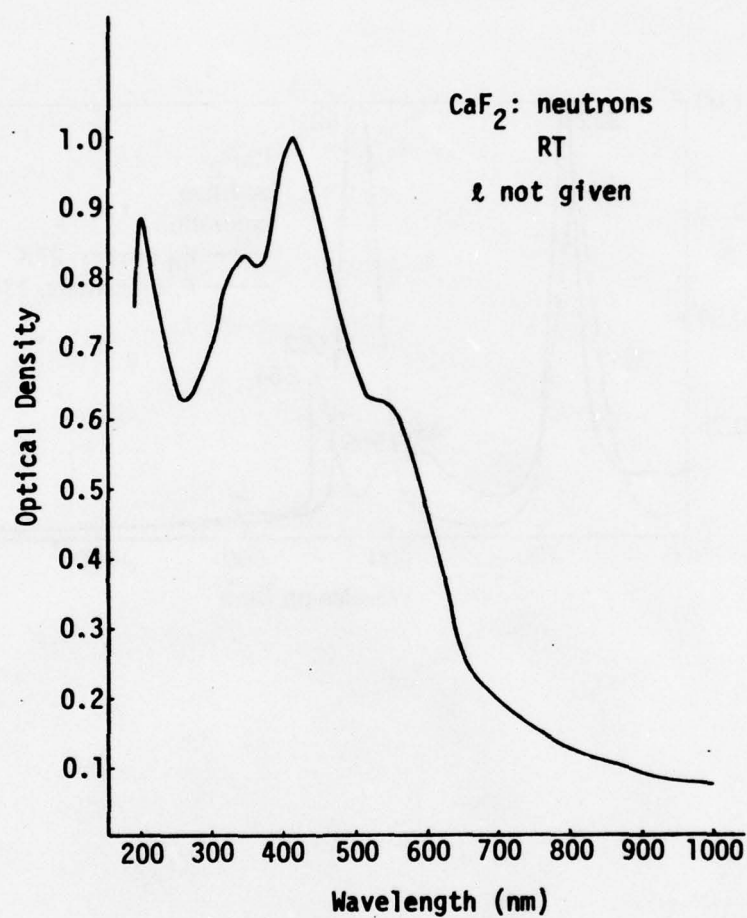
Fig. 3.40. Absorption spectrum of CaF$_2$ irradiated with neutrons.
[H. Bontinck, Physica 24, 639 (1958).]
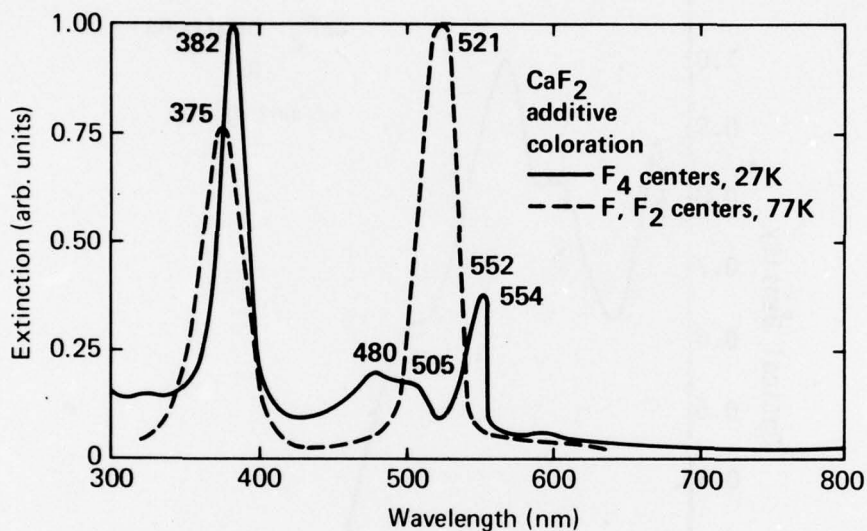
Fig. 3.41. Additively colored CaF$_2$. Solid curve: absorption
spectrum of pure CaF$_2$ with F$_4$ centers (Ref. 3.47). Dashed
curve: Mollwo absorption spectrum of natural (Y-doped) CaF$_2$
with F and F$_2$ centers (Ref. 3.36). [R. Rauch and I. Senff,
Phys. Stat. Sol. (a) 26, 537 (1974).]
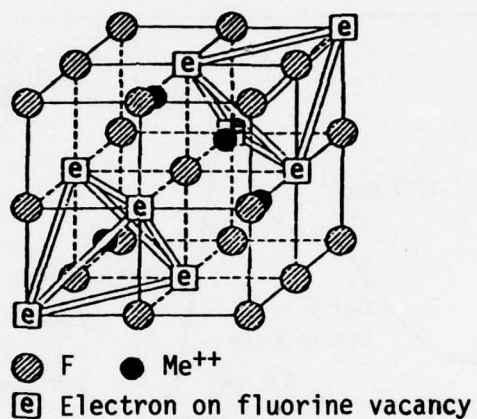
Fig. 3.42. Fluorite-type lattice showing the two variants of tetrahedral F$_4$ centers. The configuration in the upper right-hand corner is the most probable. [R. Rauch and I. Senff, Phys. Stat. Sol. (a) 26, 537 (1974).]
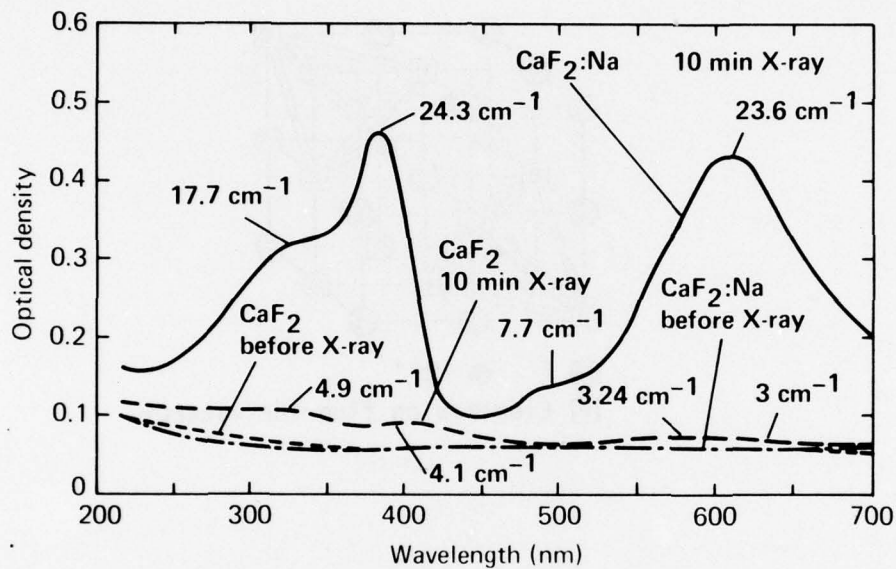
Fig. 3.43. The effect of Na$^+$ ion impurity on the X-ray coloration sensitivity of CaF$_2$. [J. H. Schulman and R. J. Ginther, J. Opt. Soc. Am. 43, 1818 A (1953).]

68
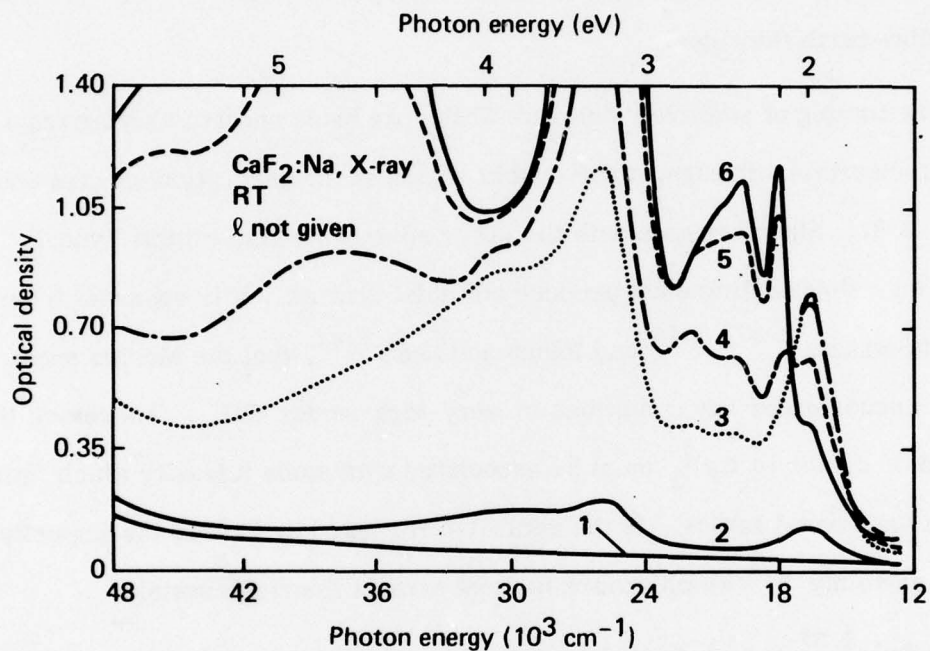
Fig. 3.44. X-ray coloration of low concentrations of Na$^+$
ions in CaF$_2$. (1) original Na$^+$-doped crystal; (2) 1 min
X-irradiation; (3) 15 min; (4) 30 min; (5) 60 min; and
(6) 90 min. [R. Rauch and I. Senff, Phys. Stat. Sol. (a)
26, 537 (1974).]

detected F centers by ESR experiments in additively colored crystals which exhibited the Mollwo spectrum in Fig. 3.35. Therefore the Mollwo spectrum is a combination of the absorptions of F and F$_2$ (an aggregate of two adjacent F centers along a [100] direction) centers, which are always formed simultaneously in alkaline-earth fluorides.

Slow cooling of additively colored CaF$_2$ produces spectra varying from general absorption throughout the visible region to the absorption spectra shown in Fig. 3.37. Since crystals with the latter spectrums also exhibit Tyndall scattering, slow cooling must produce colloidal centers. It is apparent from the work of Smakula,[3.37, 3.44] and Rauch and Senff[3.41], that the Mollwo spectrum does not occur under any conditions in very high-purity CaF$_2$. Therefore the isolated F center in CaF$_2$ must be associated with some impurity which "pins" them in the crystal lattice. In the natural CaF$_2$ used by Mollwo the impurity is almost certainly Y^{3+} which occurs in most natural fluorite crystals.

Smakula[3.37] found an entirely different spectrum shown in Fig. 3.38 for X-irradiated, high-purity synthetic CaF$_2$. Very high X-ray doses were required to produce this four-band spectrum which had no bands in common with the Mollwo spectrum. Lüty[3.45] found that similar spectra could be produced by additive coloration, regardless of the quenching rate, as long as the excess Ca was restricted to small values, i.e., the additive coloration temperature had to be low (500 – 600 C). At higher additive coloring temperatures, slow quenching produced a four-band spectrum superimposed on a broad colloidal-type absorption, while rapid quenching produced Mollwo's two-band spectrum. Smakula[3.44] later found that very high-purity CaF$_2$ always produces the four-band spectrum when

colored by electron beam, X-irradiation, electrolytic coloration or additive coloring (regardless of the quench rate). Bontinck[3.40] confirmed these results for X-irradiation and additive coloring, but found the unique spectrum shown in Fig. 3.40 for neutron bombardment which contains the β band at 525 nm (2.36 eV) and the three high-frequency bands of the four-band spectrum.

Karras[3.46], and Görlich, et al.,[3.47, 3.48] found an entirely different color-center spectra characterized by a strong band at 382 nm (3.25 eV), a narrow band at 550 nm (2.25 eV), and two weaker bands at 480 nm (2.58 eV) and 500 nm (2.48 eV) – after additive coloration of CaF$_2$. This spectrum[3.41] is shown in Fig. 3.41 compared to the Mollwo spectrum. This type of spectrum is found in high-purity crystals which lack any ESR signal. Rauch and Senff[3.41] proposed tetrahedral complexes of four F centers to account for the strongest line at 382 nm. Fig. 3.42 shows the two possible variants of these centers: the most likely variant had four electrons on fluoride sites surrounding an interstitial site, while the other possible configuration has four electrons on fluoride vacancies surrounding a Ca^{2+} site.

    a.   <u>Subtractively colored CaF$_2$</u>. The spectra[3.38, 3.41] of CaF$_2$ subtractively colored with Na^+ are shown in Figs. 3.43 and 3.44. If an Na^+ ion is substituted for a Ca^{2+} ion in CaF$_2$, electrical neutrality requires that either an interstitial Na^+ ion or a F^- ion vacancy be formed. Either of these entities should constitute an electron trap which enhances the X-ray colorability of the pure crystal. Although Schulman and Ginther[3.38] found the spectrum in Fig. 3.43 which is quite different from the additively colored spectrum, Karras and Ullmann[3.49] were able to obtain spectra nearly identical to those in

Fig. 3.41, except for some weak bands directly attributable to the dopants (Li, Na, K). The absorption spectrum[3.50] of CaF$_2$ subtractively colored by X-rays at 37 K is shown in Fig. 3.54 together with the spectra of room-temperature X-irradiated CaF$_2$: Li, CaF$_2$: Na, and CaF$_2$: K. Rauch and Senff[3.41] found that for high sodium concentrations [($> 10^{-2}$ mol %)], X-irradiation always produced the two-band Mollwo spectrum of Fig. 3.41. They found the same spectrum for low sodium concentrations during the initial stages of X-irradiation, but as the dose was increased the spectrum was converted to a superposition of the two- and four-band spectra, as shown in Fig. 3.44.

b. <u>H and F bands in CaF$_2$</u>. The absorption spectra[3.51] of CaF$_2$ containing H and F centers is shown in Figs. 3.45 and 3.46. In Fig. 3.45 the absorption spectrum of CaF$_2$ additively colored with Ca vapor at 750 C is compared to the absorption spectrum of CaF$_2$ X-irradiated and measured at 4 K without intermediate warmup. The strong band at 377 nm (3.29 eV) in the irradiated spectrum must be due to isolated F centers since neither the impurities nor the F centers could migrate at such a low temperature. Tanton, et al.,[3.51] also found F bands in SrF$_2$ and BaF$_2$ at 442 nm (2.81 eV) and 611 nm (2.03 eV), respectively. In addition to the F band, Tanton, et al.,[3.51] identified a band at 314 nm (3.95 eV) as the H band because it grew under X-irradiation and thermally bleached (as shown in Fig. 3.46) at the same rate as the F band. Similar bands were found in SrF$_2$ and BaF$_2$ at 325 nm (3.82 eV) and 364 nm (3.41 eV), respectively.
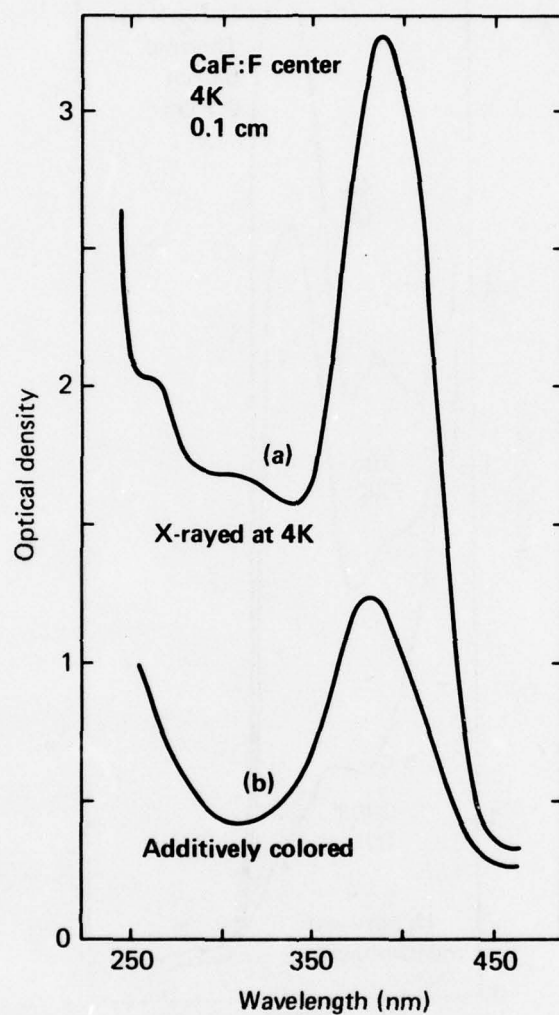
Fig. 3.45.   Optical absorption spectrum of F centers in CaF$_2$
produced by (a) X irradiation and by (b) additive coloration.
[G. A. Tanton, R. A. Shatas, J. E. Williams, and Ambuj Mukerji,
J. Chem. Phys. 49, 5532 (1968).]
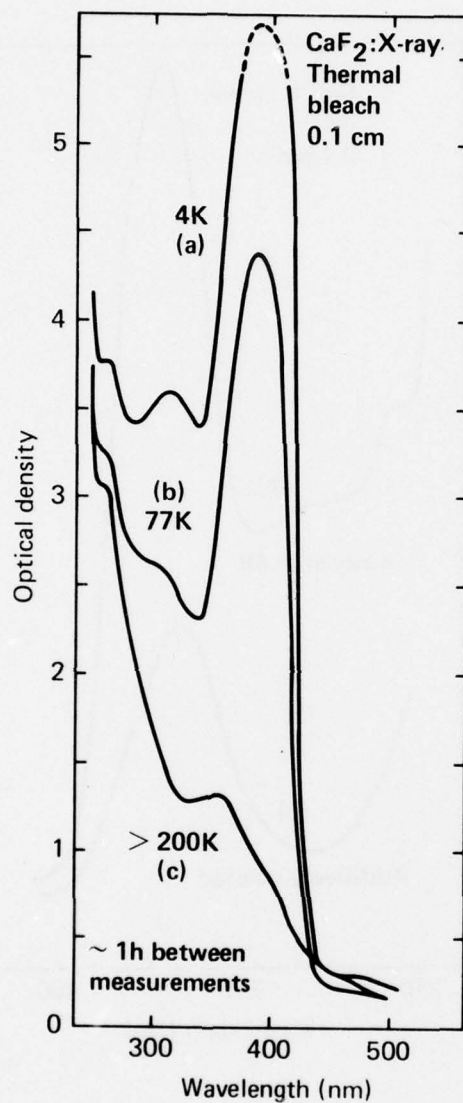
Fig. 3.46. Thermal bleaching of the 377 nm F band and the 3.14 nm H band produced by X irradiation of CaF$_2$ at 4 K.   [G. A. Tanton, R. A. Shatas, J. E. Williams, and Ambuj Mukerji, J. Chem. Phys. 49, 5532 (1968).]

c. <u>M and M^+ centers in CaF_2</u>. In CaF_2, the F center is a fluorine vacancy which has trapped an electron, while the M center[3.52] consists of two nearest neighbor F centers along a [100] crystallographic direction, as shown in Fig. 3.47. The M center has three distinct optical dipole moments appropriate to its D_{2h} point symmetry group. The transition moment for the M band lies along the [100] axis containing the vacancies and corresponds to a transition from the $^1\Sigma_g^+$ ground state to a $^1\Sigma_u^+$ excited state as shown in Fig. 3.48. The other two moments for the higher energy M_F bands lie along the $\langle 110 \rangle$ directions perpendicular to the vacancy axis and correspond to transitions from the $^1\Sigma_g^+$ ground state to the $^1\Pi_u$ excited states. The M and M_F bands shown in Fig. 3.49 lie at 519 nm (2.39 eV) and 366 nm (3.39 eV), respectively, since the crystal-field is too weak to split the M_F band. The crystal used in this spectrum was additively colored and then quenched at a moderate rate in liquid nitrogen to form M centers exclusively. Slower quench rates allow large aggregates of F centers to form, and more rapid quench rates form F and M centers in equal concentrations. The spectrum in Fig. 3.49 also contains a shoulder at 390 nm (3.18 eV) due to M centers, a very small F band at 376 nm (3.30 eV) which can only be distinguished by dichroic measurements, an F_3^- aggregate band at 677 nm (1.83 eV), and small peaks at 550 nm (2.25 eV) and 600 nm (2.07 eV) probably due to impurity-color-center complexes.

The dichroism between [001] and [010] polarized light is shown in Figs. 3.50 and 3.51 for the M and M_F bands, respectively, of additively colored CaF_2. The (a) curves give the dichroism of the crystal after the M centers have been aligned along the [001] direction with [001] polarized
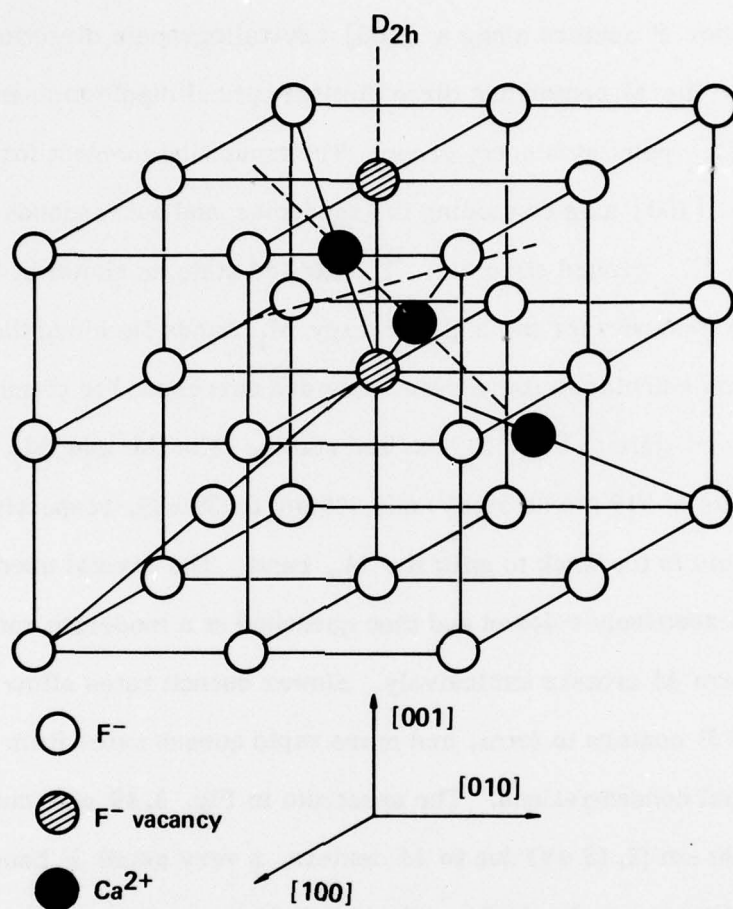
Fig. 3.47. Model of the CaF$_2$ lattice showing two fluorine vacancies along the [001] axis forming an M center. The dashed lines represent the directions of the optical dipole moments of the M center. [W. C. Collins, Phys. Stat. Sol. (b) 56, 291 (1973).]
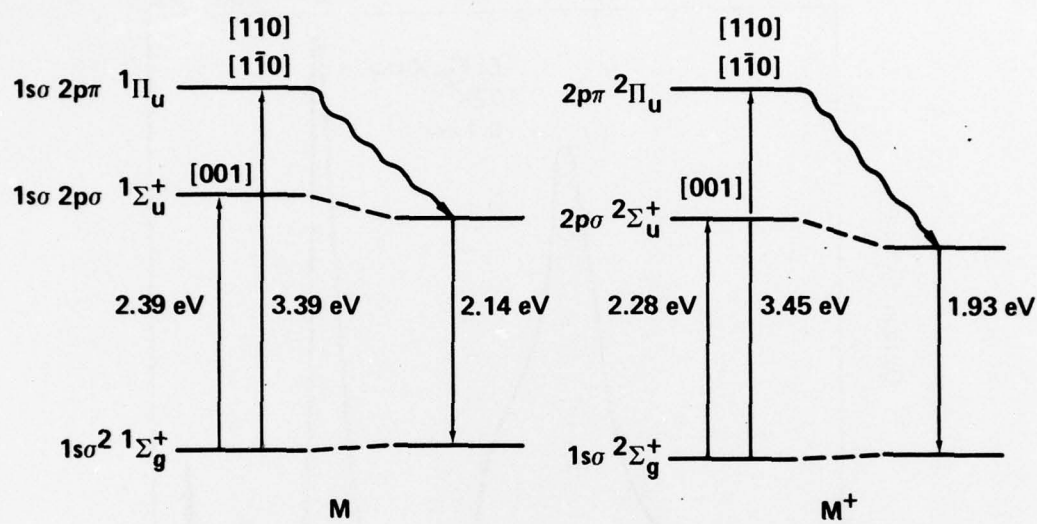
Fig. 3.48.   Comparison of the energy level diagrams for the M and M$^+$ centers aligned with the [001] axis in CaF$_2$. The direction of the dipole moment, electron configuration, and symmetry orbital is shown for the M and M$_F$ band absorptions. [W. C. Collins, Phys. Stat. Sol. (b) 56, 291 (1973).]
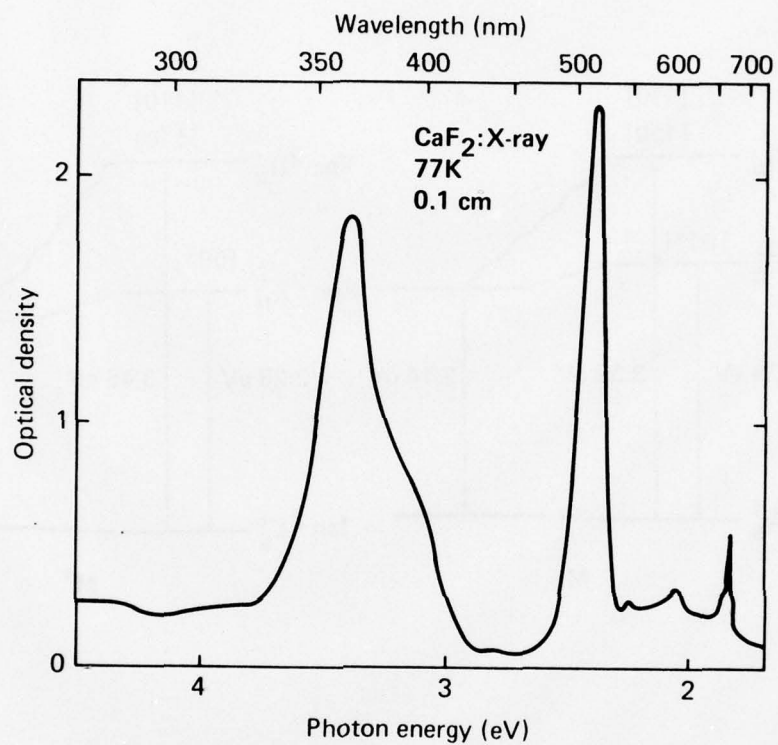
Fig. 3.49. Absorption spectrum of additively colored CaF$_2$ showing the two strong M-center absorption bands at 519 and 366 nm. [W. C. Collins, Phys. Stat. Sol. (b) 56, 291 (1973).]
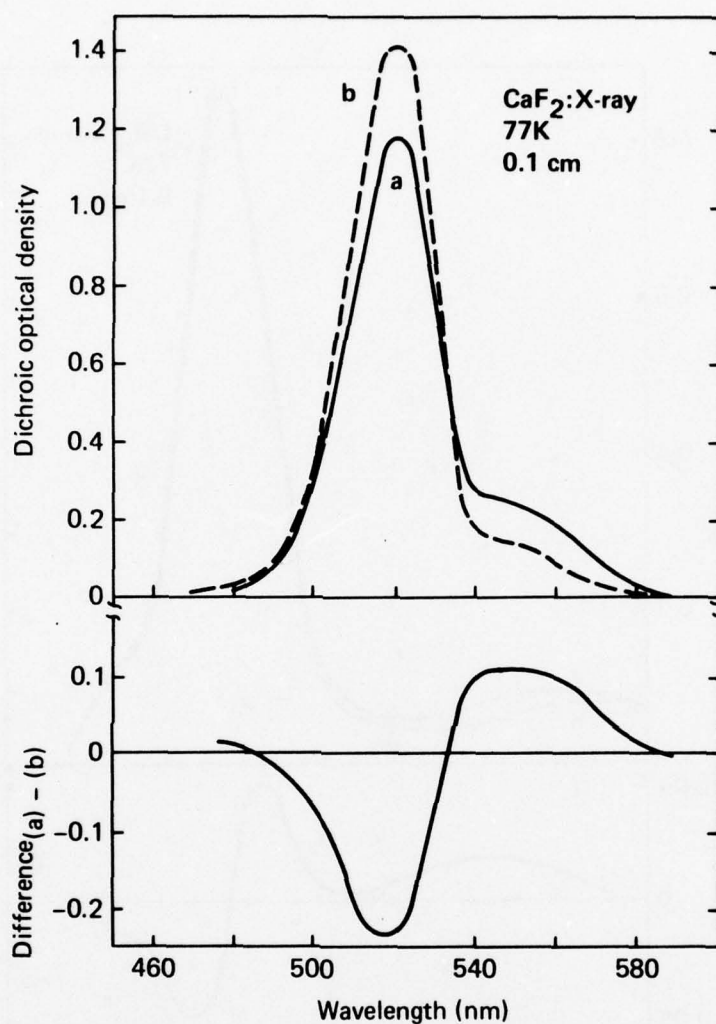
Fig. 3.50.   Dichroism in the M-band region: (a) after alignment of M centers in additively colored CaF$_2$ with [001] polarized ultraviolet light and (b) after subsequent bleaching with visible light.   The change in dichroism is shown by the lower curve. [W. C. Collins, Phys. Stat. Sol. (b) 56, 291 (1973).]
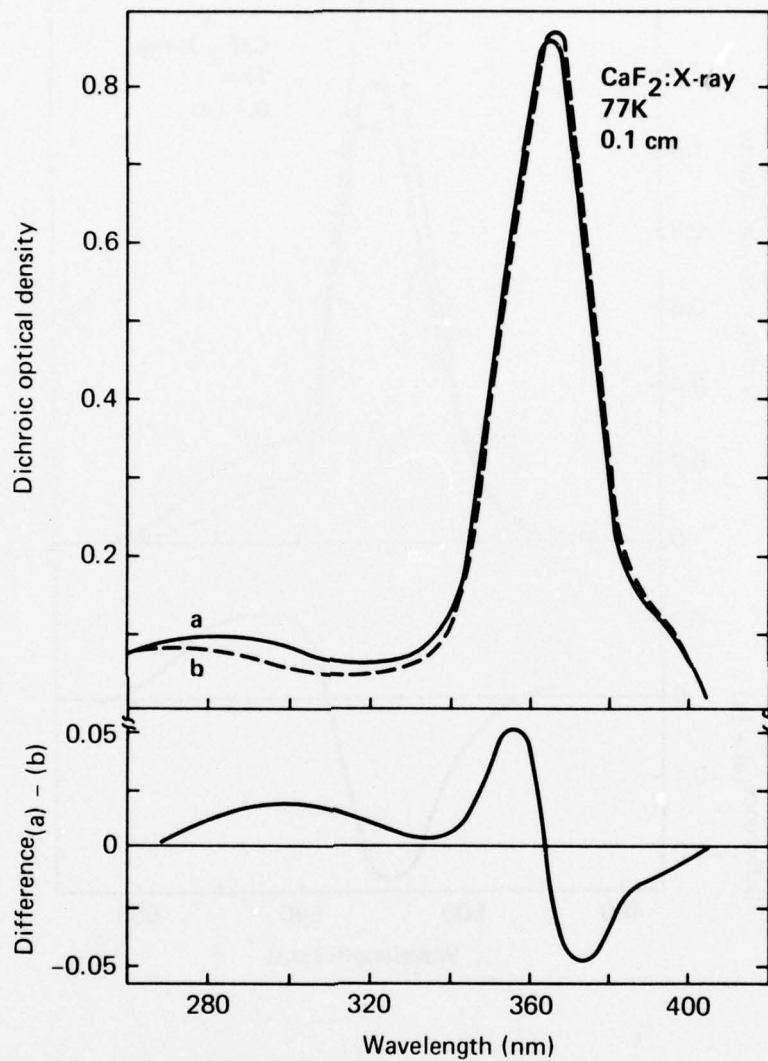
Fig. 3.51.   Dichroism in the M$_F$-band region: (a) after alignment of M centers in additively colored CaF$_2$ with [001] polarized ultraviolet light and (b) after subsequent bleaching with visible light.   The change in dichroism is shown by the lower curve.   [W. C. Collins, Phys. Stat. Sol. (b) 56, 291 (1973).]
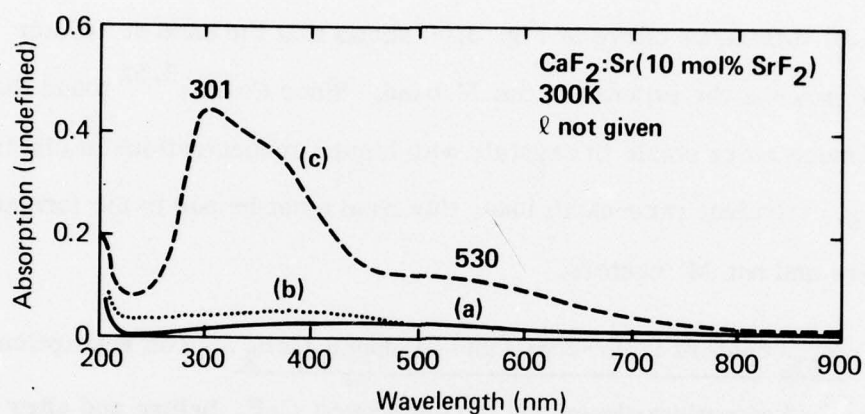
Fig. 3.52.   Absorption spectra of CaF$_2$:Sr: (a) before X
irradiation; (b) after 3×10^4R; and (c) after 8×10^4R,
$T_R = T_M = 84$ K.   [P. Görlich and P. Ullmann, Phys. Stat.
Sol. (b) 50, 577 (1972).]

ultraviolet light. This ultraviolet light may also ionize the M center to form M$^+$ centers, or ionize other centers or impurities to provide electrons to form M' centers. The (b) curves give the dichroism after the crystal has been bleached with intense visible light which should neutralize any M$^+$ or M' centers. The (a) – (b) difference curve in Fig. 3.50 shows that the band at 545 nm (2.28 eV) grows at the expense of the M band. Since Collins[3.52] found that this band was much more stable in crystals with higher concentrations of electron traps, e.g., trivalent rare-earth ions, this band must be due to the formation of M$^+$ centers and not M' centers.

d. F_{AE} centers in Sr-doped and Ba-doped CaF$_2$. The absorption spectra[3.50] of strontium-doped and barium-doped CaF$_2$ before and after X-irradiation are shown in Figs. 3.52 and 3.53. By analogy with F$_A$ centers in alkali halides, the color centers formed in these crystals are designated as F_{AE} centers, where the index AE (alkaline earth) indicates that one of the four Ca^{2+} lattice cations tetrahedrally surrounding an F center has been replaced by a foreign alkaline-earth cation. For comparison, Görlich and Ullmann[3.50] gave the spectra in Fig. 3.54 of CaF$_2$ and BaF$_2$ after additive coloration, sub- tractive coloration by X-irradiation at 37 K, and after room-temperature X-irradiation of Li- , Na- , and K-doped crystals. Görlich and Ullmann[3.50] imply that since the maximum absorption for low-temperature X-irradiated CaF$_2$:Sr occurs at 301 nm (4.12 eV) and that for CaF$_2$:Ba occurs at 315 nm (3.94 eV), there is probably some similarity between the F_{AE} centers in these crystals and some of the centers formed by low-temperature subtractive color- ation by X-irradiation of pure CaF$_2$, because there is a strong shoulder at ~310 nm (4.00 eV) on the F–center peak.
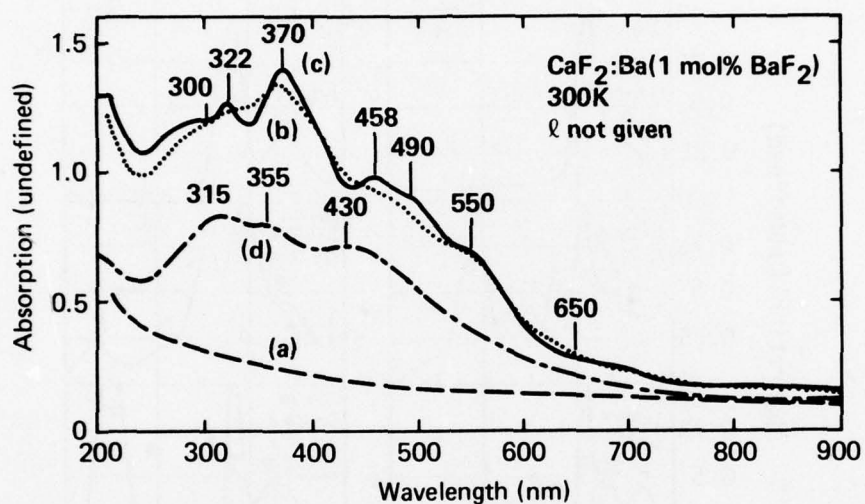
Fig. 3.53.   Absorption spectra of CaF$_2$:Ba :   (a) before X-irradiation; (b) after 3×10^4R;   (c) after 3×10^4R, T_n = 48 K; and (c) after 10^3R, T_R = T_M = 84 K.   [P. Görlich and P. Ullmann, Phys. Stat. Sol. (b) <u>50</u>, 577 (1972)].
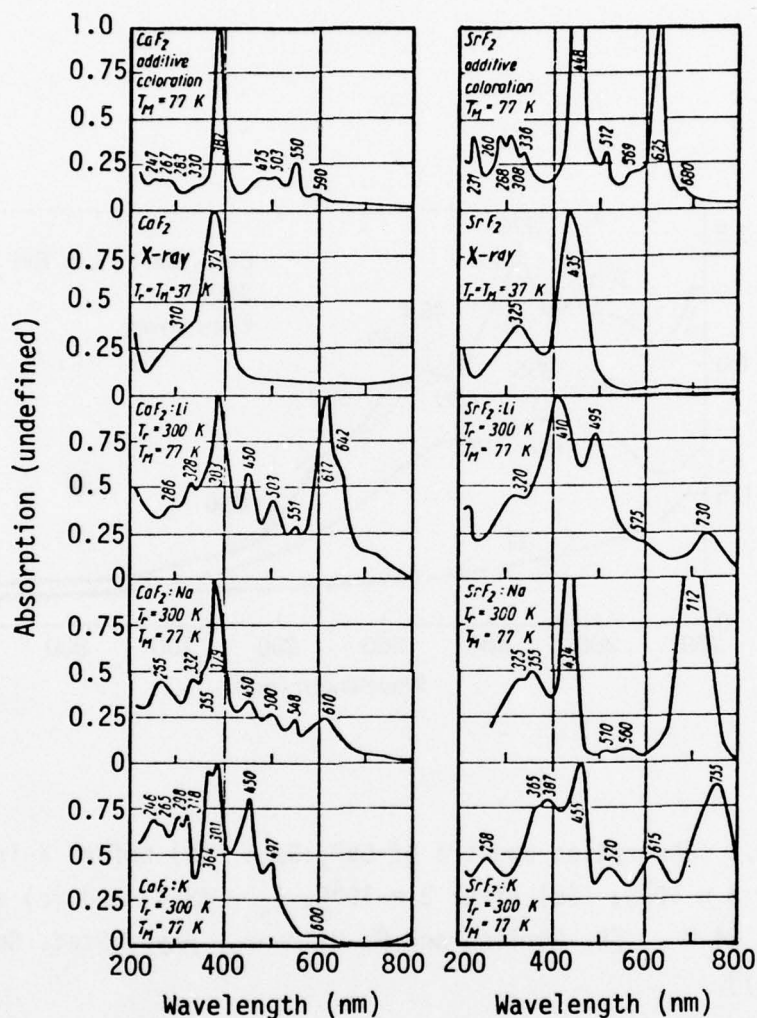
Fig. 3.54. Comparison of the absorption spectra of CaF$_2$ and SrF$_2$ crystals after additive coloration, subtractive coloration by X-irradiation, and X-irradiated Li-, Na-, and K-doped crystals. [P. Görlich and P. Ullmann, Phys. Stat. Sol. (b) 50, 577 (1972).]

e.   Self-trapped hole in CaF_2. The self-trapped hole, V_K center, or fluorine molecular ion has been found in CaF_2:Tm crystals by Hayes and Twidell[3.53].   The V_K centers are produced by X-irradiation of CaF_2:Tm at 80 K, and they decay at 138 K with the emission of luminescence.   ESR experiments confirm that the fluorine molecular ion lies with its axis along a cube edge where the fluorine neighbor distance, 0.273 nm, is least.   Hayes and Twidell[3.53] reported one optical absorption band at 350 nm (3.54 eV) but did not give a spectrum.   There appears to be no subsequent confirmation in the literature of the self-trapped hole in CaF_2.

f.   Color centers in CaF_2:Mn^{2+}.   The absorption spectra[3.54] of pure and manganese-doped CaF_2 crystals before and after X-irradiation are shown in Figs. 3.55 and 3.56, respectively.   In addition to the specified manganese content of the crystals, they all contained approximately 3 ppm of oxygen. Prior to X-ray coloration, the pure and manganese-doped CaF_2 crystals exhibited an absorption coefficient $\beta = 1 \text{ cm}^{-1}$ which increased somewhat at shorter wavelengths as shown in Fig. 3.55.   It can be seen that the CaF_2:5 mol % Mn crystal has developed a weak absorption band near 400 nm (3.10 eV) and increased absorption on approaching 220 nm (5.64 eV).   This increase in absorption in CaF_2 at short wavelengths is characteristic of oxygen or sulfur contamination (see Sec. III-B.1).

The absorption spectra of the samples in Fig. 3.55 after X-ray coloration is shown in Fig. 3.56.   At low concentrations the manganese impurity merely enhances the colorability of CaF_2, while at high concentrations (e.g., in the 5 mol % Mn samples) new bands are formed at 420 nm (2.95 eV) and 300 nm (4.13 eV).   The 1 mol % Mn sample shows a well developed band at
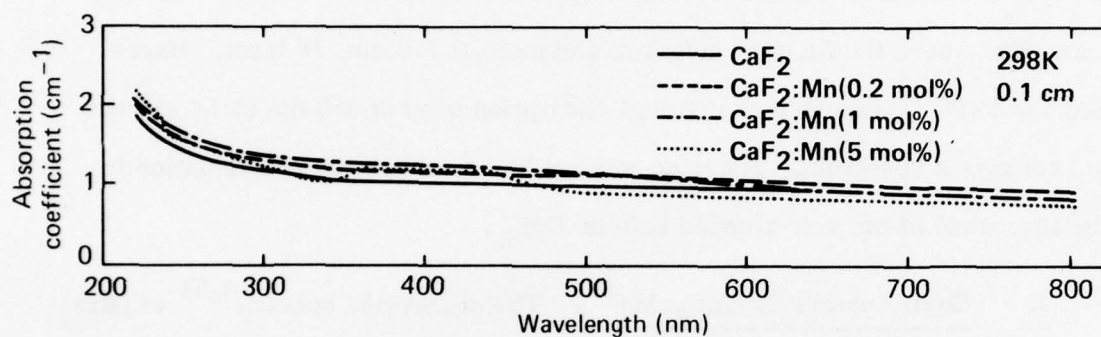
Fig. 3.55. Absorption spectrum of pure and manganese-doped CaF$_2$
crystals prior to X-irradiation.   [M. D. Agrawal and K. V. Rao,
Phys. Stat. Sol. (a) $\underline{3}$, 153 (1970).]
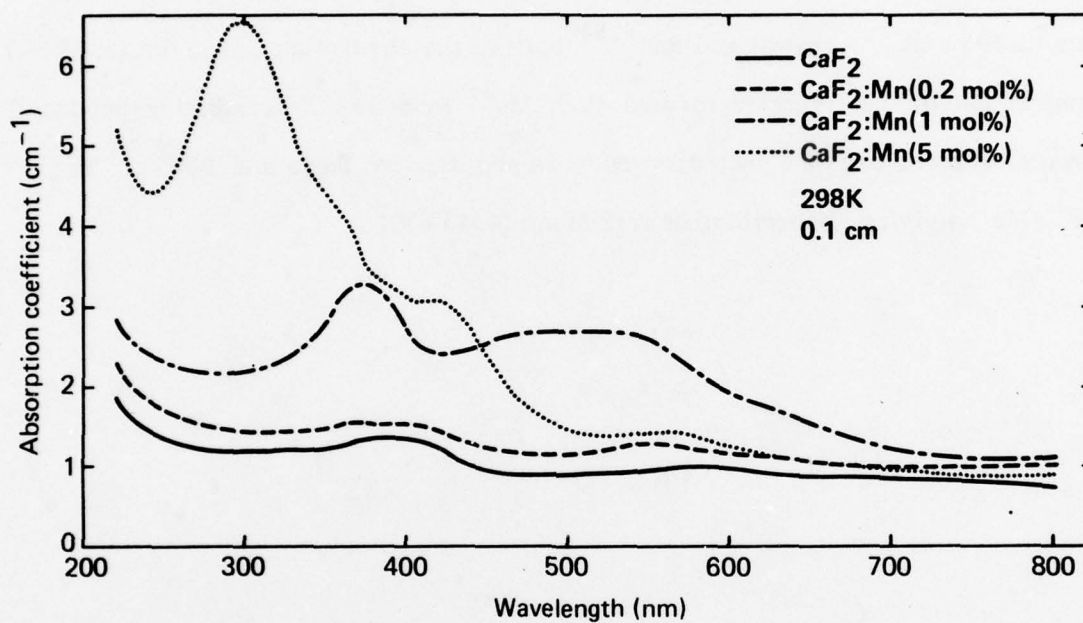
Fig. 3.56. Absorption spectrum of X-irradiated pure and manganese-doped CaF$_2$. [M. D. Agrawal and K. V. Rao, Phys. Stat. Soī. (a) 3, 153 (1976).]

375 nm (3.31 eV) identifiable as F centers in association with Mn impurity atoms, plus bands at 480 nm (2.58 eV) and 550 nm (2.25 eV) which are probably aggregates of F centers associated with Mn impurity atoms. In the 5 mol % Mn sample the F band has shifted to 360 nm (3.44 eV) because of lattice distortion incurred when the smaller radius Mn^{2+} ion (0.091 nm) is substituted for the Ca^{2+} ion (0.106 nm).   Agrawal and Rao[3.54] believe the absorption at 300 nm (4.13 eV) may be due to Mn^0 centers formed when Mn^{2+} ions trap X-irradiation-produced free electrons, because such centers were reported by Ikeya and Itoh[3.55] in KCl: Mn as giving absorptions near 280 nm (4.43 eV).

C. Magnesium Fluoride*

Magnesium fluoride crystallizes in the rutile structure, rather than
the CaF$_2$ structure as for most alkaline-earth halides. It is tetragonal,
with lattice parameters a = 0.4623 nm and c = 0.3052 nm. One of the attrac-
tive features of MgF$_2$ is its low solubility in water (0.013 g/100g of H$_2$O).
This value of solubility is lower than that of any fluoride except CaF$_2$.
This is of great significance because many fluorides tend to lose their
transmission through a reaction with moisture present in the air. Hunter[3.56]
and Canfield, et al.,[3.57] observed very little aging of evaporated MgF$_2$
films when they were exposed to air for prolonged times.

Figure 3.57 shows the transmittance of an optically polished high-
purity crystal of MgF$_2$ (sample thickness = 1.51 mm), before and after elec-
tron irradiation, in the region from 110 to 300 nm (11.3 to 4.13 eV).[3.58]
The absorption edge corresponding to β = 5 cm^{-1} [i.e., T $\simeq$ exp(-5)(0.151)
= 0.47] in the unirradiated crystal is seen at 118 nm (10.5 eV). This
value is dependent on the purity and the orientation of the crystal, since
MgF$_2$ is anisotropic. The birefringence of MgF$_2$ is shown in Fig. 3.58.[3.59]

The intrinsic infrared-absorption edge for MgF$_2$, corresponding to
β = 5 cm^{-1} for light propagation along the c-axis of the crystal, is at
0.138 eV (9.01 μm).[3.60] The refractive index of MgF$_2$ between 178.0 and
706.5 nm (6.97 and 1.76 eV) is tabulated in the American Institute of
Physics Handbook.[3.61] With decreasing photon energy over this spectral
range, the index decreases from 1.43975 to 1.37599 for the ordinary ray,
and from 1.45365 to 1.38771 for the extraordinary ray.

---

*See summary Figures 1.4 and 1.11 of Volume I.
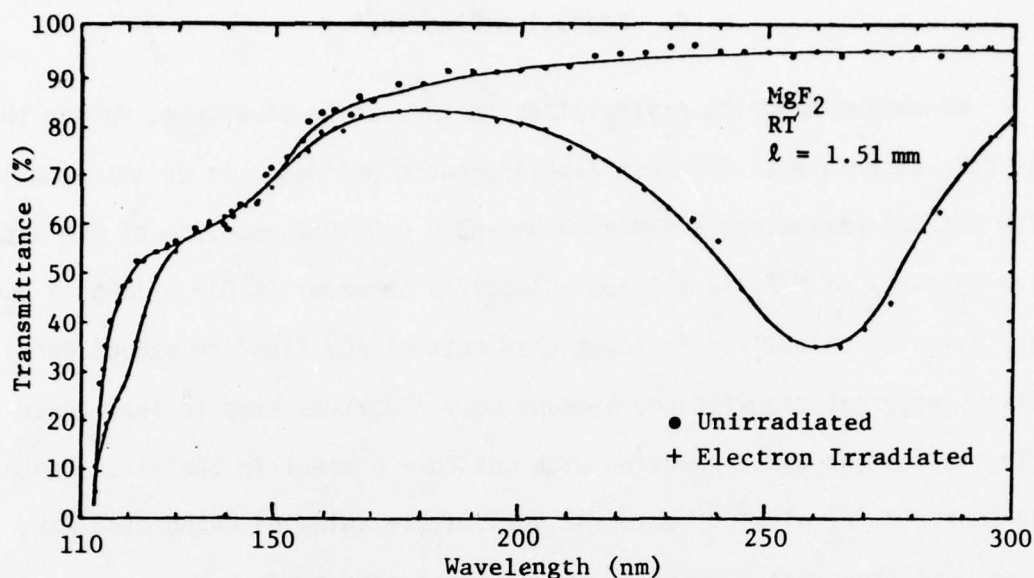
Fig. 3.57. Transmittance of MgF$_2$ before and after irradiation by 10^{14} electrons/cm^2 at 1.0 MeV and at 2.0 MeV. [D. F. Heath and P. A. Sacher, Appl. Optics $\underline{5}$, 937 (1966).]
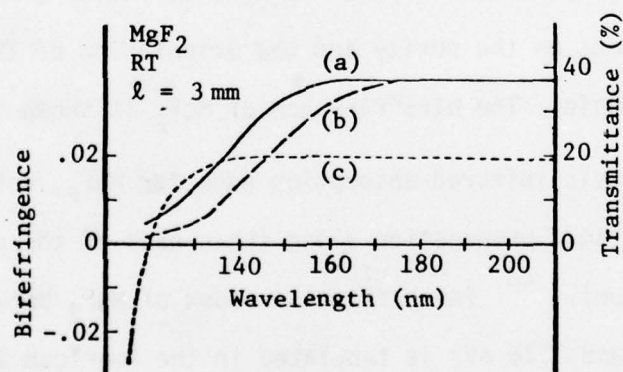
Fig. 3.58. Optical properties of magnesium fluoride. (a) is polarized perpendicular to the optic axis; (b) is polarized parallel to the optic axis. Maximum transmittance for each component is 50%. Accuracy is +3%. Curve (c) is the birefringence. [W. C. Johnson, Rev. Sci. Instr. $\underline{35}$, 1375 (1964).]

Sec. III-C MgF$_2$

1. <u>Temperature dependence of the transmittance limit of MgF$_2$ and
some other VUV materials</u>. The short-wavelength transmittance limit of
various vacuum-ultraviolet window materials has been found to be temperature
dependent[3.62,3.63,3.64,3.65,3.66]; in general, as the temperature decreases
materials transmit to shorter wavelengths, and the slope of the transmit-
tance as a function of wavelength becomes steeper. This feature is illus-
trated in Fig. 3.59, which is a transmittance-versus-wavelength plot of a
1 mm thick polished MgF$_2$ crystal at 83, 200 and 296 K.[3.65] A decrease in
cutoff wavelength λ_{co} (defined arbitrarily as that wavelength at which the
transmittance could just be measured, usually 0.1 - 0.5 percent) from 113.2
to 109.7 nm (10.95 to 11.30 eV) is seen as the temperature is lowered from
296 to 83 K. At 83 K, the MgF$_2$ sample shows anomalously low transmittance
at longer wavelengths, apparently due to the condensation of residual atmos-
phere in the cryostat on the crystal surfaces.[3.65]

Figure 3.60 shows the temperature dependence of λ_{co} for a number of
vacuum-ultraviolet materials.[3.65] Except for LaF$_3$, λ_{co} for all materials
shifts to shorter wavelengths as the temperature is lowered; depending on
the material, the shift varies between 4 and 8 nm over the temperature
range 373 to 10 K, with BaF$_2$ showing the largest shift. In LaF$_3$, no shift
in λ_{co} with temperature is seen; Hunter and Malo[3.65] indicate that the
anomalous behavior of LaF$_3$ could be attributed to its low purity. In Fig.
3.60, the + marks in the case of BaF$_2$ refer to measurements made on cleaved
samples, while the other data points are from polished samples. The short
solid and the dashed lines in this figure show the results of earlier inves-
tigators, Laufer, et al.,[3.63] and Davis[3.64], respectively.
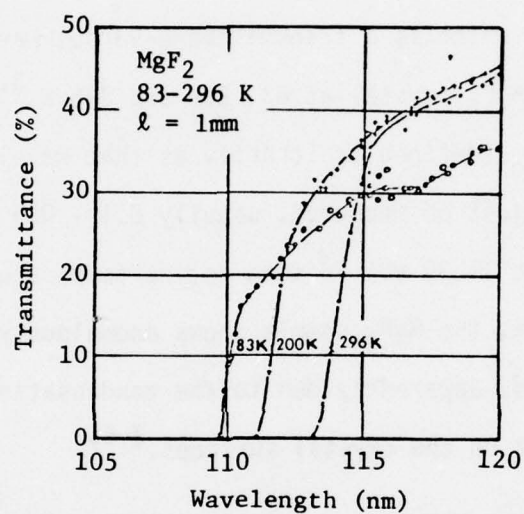
Fig. 3.59. Temperature dependence of the absorption
edge of MgF$_2$. [W. R. Hunter and S. A. Malo, J. Phys.
Chem. Solids 30, 2739 (1969).]
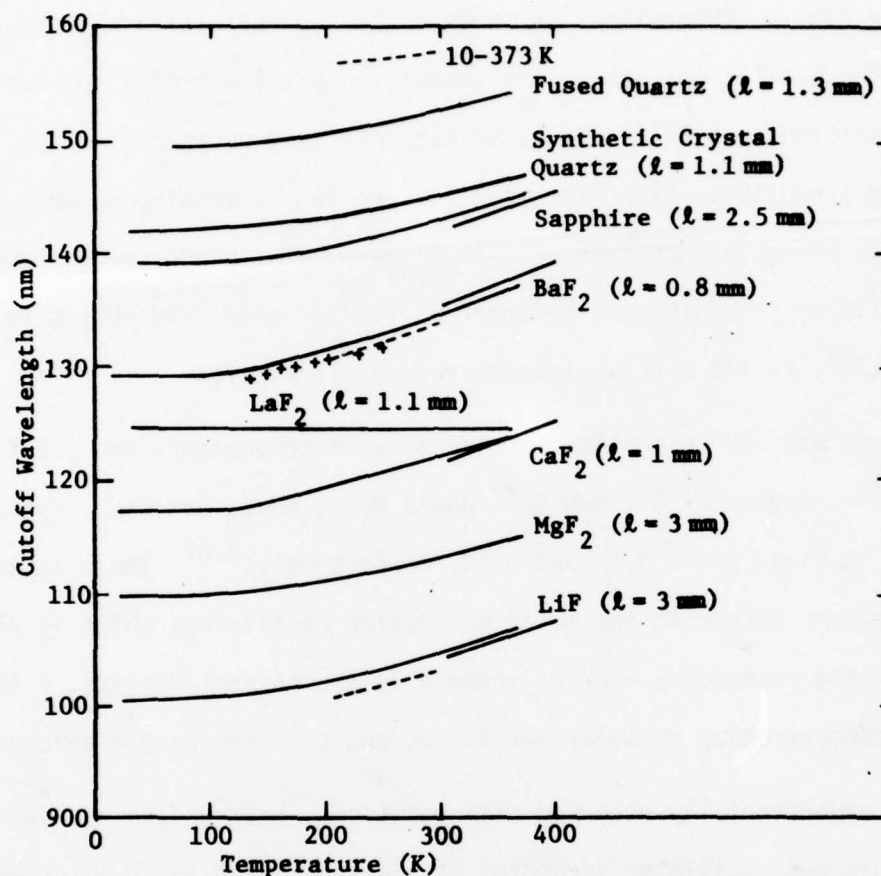
Fig. 3.60. The temperature dependence of the short wavelength transmittance limit of various vacuum-ultraviolet materials. [W. R. Hunter and S. A. Malo, J. Phys. Chem. Solids 30, 2739 (1969).]

2. <u>Transition metal ions in MgF_2</u>. As in other ionic crystals, the incorporation of transition-metal ions into the MgF_2 lattice gives rise to several absorption bands over a wide spectral range. The low-energy transitions give rise to absorptions in the visible and near infrared, and correspond to the excitations within the transition-metal d orbitals. Many of these transitions are difficult to detect optically because of their low oscillator strengths, which vary from 10^{-7} to 10^{-5} depending on whether the transitions are spin-forbidden or spin-allowed. The high-energy transitions have oscillator strengths of the order of 10^{-3} or more, and they give rise to absorptions in the ultraviolet and vacuum ultraviolet.

The UV and VUV absorption spectra at room temperature and 4.2 K of Mn^{2+}-, Fe^{2+}-, and/or Ni^{2+}-, and Co^{2+}-doped MgF_2, $KMgF_3$ and CaF_2 crystals are shown in Figs. 3.61, 3.62 and 3.63, respectively.[3.67] The ε in the figure captions refers to the molar extinction coefficient which is determined from the relation $\varepsilon = p/c\ell$, where p is the optical density, c is the impurity concentration in moles per liter, and ℓ is the sample thickness.

The experimentally observed peak positions, half-widths, extinction coefficients and oscillator strengths of high-energy (5 to 10 eV or 248 to 129 nm) absorption bands of various transition-metal ions in fluoride host crystals are summarized in Table 3.9.[3.67] Sabatini, et al.,[3.67] have assigned some of these absorption bands to 3d to 4s excitation of the transition-metal impurity. These transitions have three important characteristics: (i) Their oscillator strengths have moderate values, of the order of 10^{-3} at room temperature, which decrease on cooling (Table 3.9). (ii) Their spectral positions after crystal-field corrections are near those of 3d to 4s free-ion transitions. (iii) Their transition energies
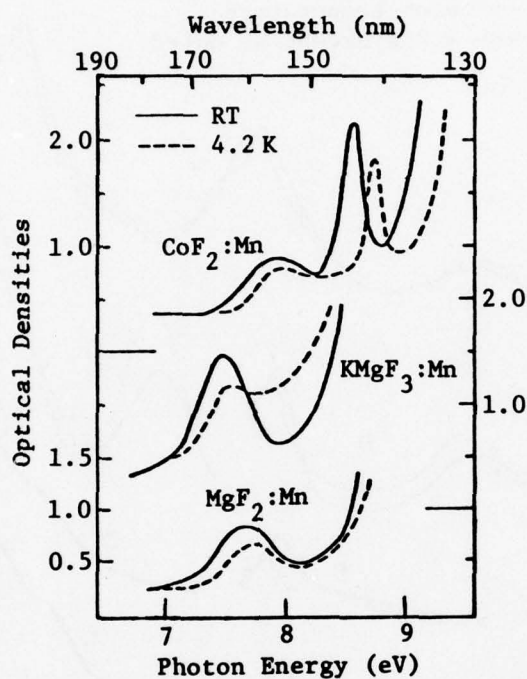
Fig. 3.61. Vacuum-ultraviolet spectra of Mn^{2+} in different host crystals; KMgF$_3$:Mn, 0.46 mm thick, ϵ = 27.3 × O.D.; MgF$_2$:Mn, 0.71 mm thick, ϵ = 110 × O.D.; CaF$_2$:Mn, 1.01 mm thick, containing both Mn^{2+} and Fe^{2+}, ϵ = 260 × O.D. for Mn^{2+} and 870 × O.D. for Fe^{2+}. [J. F. Sabatini, A. E. Salwin, and D. S. McClure, Phys. Rev. B $\underline{11}$, 3832 (1975).]
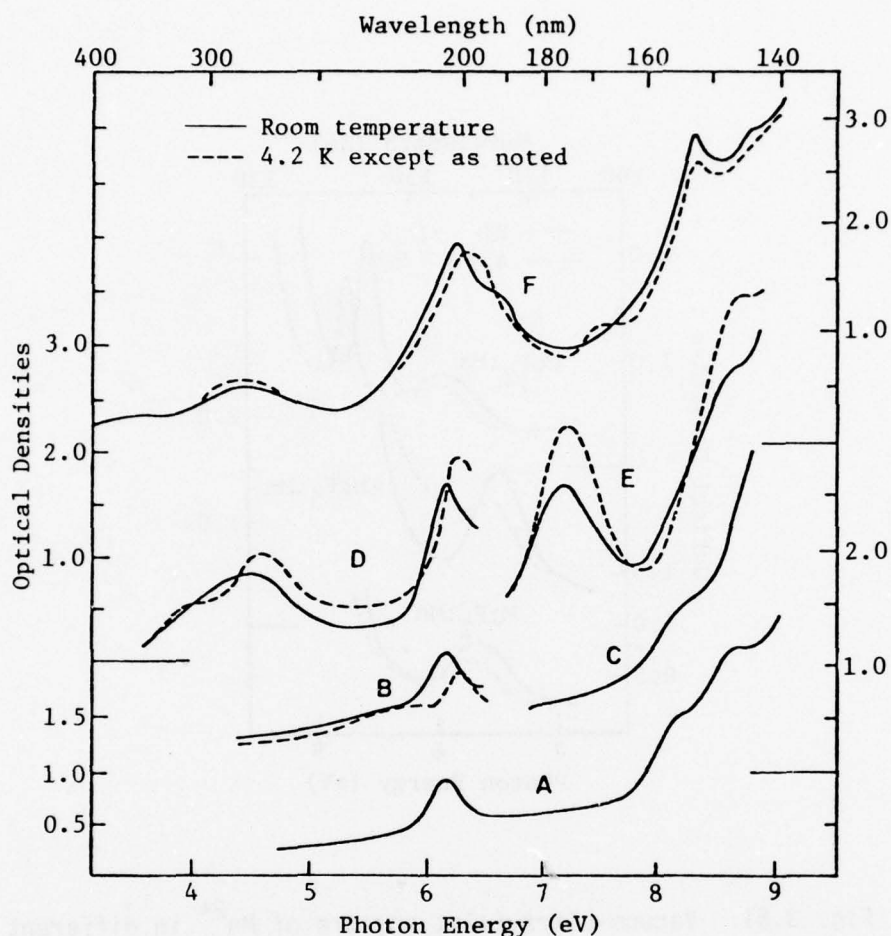
Fig. 3.62. Ultraviolet spectra of crystals containing Fe^{2+} and/or Ni^{2+}. (a) KMgF$_3$:Fe (B), 3.51 mm thick, $\varepsilon = 128 \times$ O.D.; (b) KMgF$_3$:Fe (Optovac), 563 mm thick, $\varepsilon = 82 \times$ O.D. for those features due to Fe^{2+}; (c) KMgF$_3$:Ni (Dietz), 0.97 mm thick, $\varepsilon = 28 \times$ O.D. for any features due to Ni^{2+}; (d) KMgF$_3$:Fe (Hukin), 12.78 mm thick; $\varepsilon = 36 \times$ O.D. for those features due to Fe^{2+}, dashed line 77 K; (e) KMgF$_3$:Ni (Guggenheim), 0.89 mm thick, containing both Ni^{2+} and Fe^{2+}; (f) MgF$_2$:Fe, 0.57 mm thick; $\varepsilon = 56 \times$ O.D. [J. F. Sabatini, A. E. Salwin, and D. S. McClure, Phys. Rev. B <u>11</u>, 3832 (1975).]
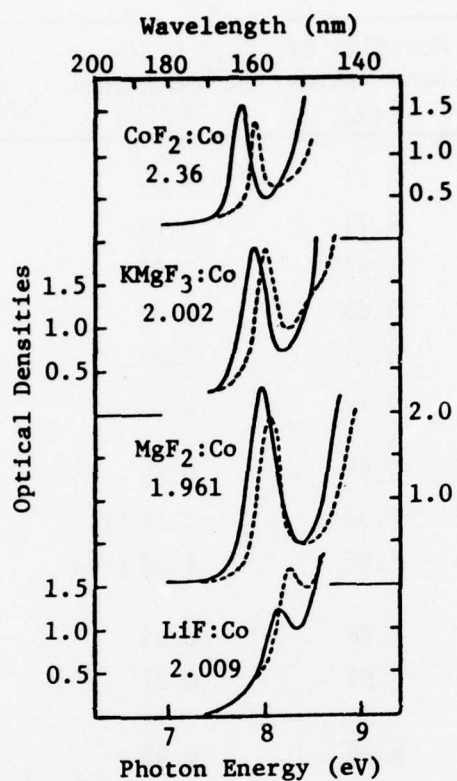
Fig. 3.63.   Vacuum-ultraviolet spectra of Co^{2+} in different host
crystals with crystal metal-fluorine distances in Å indicated,
solid lines — room temperature, dashed lines — 4.2 K, KMgF$_3$:Co,
0.80 mm thick, ϵ = 31 × O.D.; MgF$_2$:Co, 0.68 mm thick, ϵ = 15 × O.D.;
CaF$_2$:Co, 0.77 mm thick, ϵ = 320 × O.D.;   LiF:Co, 4.90 mm thick,
ϵ = 100 × O.D.   [J. F. Sabatini, A. E. Salwin, and D. S. McClure,
Phys. Rev. B 11, 3832 (1975).]

97

Table 3.9. Absorption bands of the transition-metal ions in fluoride host crystals from 5 to 10 eV. [J. F. Sabatini, A. E. Salwin, and D. S. McClure, Phys. Rev. B 11, 3832 (1975).]

System	Temperature (K)	Position of Band Maxima (eV)	Full Width at Half-maximum (eV)	Extinction Coefficient (liters/mol-cm)	Oscillator Strength
$KMgF_3$:V	300	4.71	0.87	13	3.9×10^{-4}
	77	4.71	0.87	14	4.1×10^{-4}
	300	5.64	0.62	49	1.1×10^{-3}
	77	5.68	0.43	39	5.9×10^{-4}
	300	8.11	0.87	770	2.3×10^{-2}
	4.2	8.16	0.74	1100	2.8×10^{-2}
$KMgF_3$:Cr	300	5.75	0.62	9.2	2.0×10^{-4}
	300	7.32	1.12 (?)	130	5.0×10^{-3}
	4.2	7.32	1.24 (?)	156	6.8×10^{-3}
$KMgF_3$:Mn	300	7.46	0.43	25	3.7×10^{-4}
	4.2	7.51	0.31	18	1.9×10^{-4}
$KMgF_3$:Fe	300	6.08	0.55	40	7.5×10^{-4}
	4.2	6.08	0.55	40	7.5×10^{-4}
			0.56	112[a]	2.3×10^{-3}
	300	7.94	0.56	3400[b]	6.5×10^{-2}
				160[a] (?)	2.6×10^{-3}
	300	8.43	0.43	4900[b] (?)	7.3×10^{-2}
$KMgF_3$:Co	300	7.76	0.25	40	3.5×10^{-4}
	4.2	7.87	0.21	40	2.9×10^{-4}
$KMgF_3$:Ni	300	7.94	0.74 (?)	28	7.3×10^{-4}
MgF_2:Mn	300	7.64	0.52	61	1.1×10^{-3}
	4.2	7.75	0.56	45	8.8×10^{-4}
MgF_2:Co	300	7.85	0.37	35	4.5×10^{-4}
	4.2	7.96	0.25	28	2.5×10^{-4}
CaF_2:Co	300	7.63	0.24	450	3.7×10^{-3}
	4.2	7.77	0.16	380	2.1×10^{-3}

[a]Assuming band to be an Fe transition.   [b]Assuming band to be an Ni transition.

are dependent on the temperature and the lattice constant of the host; they increase on cooling and when the lattice constant is reduced (Fig. 3.63 and Table 3.9).

Numerous peaks are seen in the ultraviolet absorption spectra of Fe^{2+}-doped fluoride host crystals (Fig. 3.62). Their assignments were made difficult by the presence of F centers, Ni^{2+} and other background impurities in the crystals.

The site symmetry of Fe^{2+} in MgF$_2$ lattice is D$_2$h. The crystal-field splitting of the 3d^6 orbital of the Fe^{2+} ion in this symmetry is shown in Fig. 3.64.[3.68] The spin-allowed transitions labeled 1 and 2 in the figure give rise to two broad absorption bands in the near infrared. These bands peak at 1026 nm (1.209 eV) and 959.7 nm (1.292 eV) at room temperature, but shift to 1220 nm (1.017 eV) and 938.5 nm (1.319 eV) at 6 K. At low temperatures, the zero-phonon line and the multiphonon sideband structures are also observed (Fig. 3.65). At 6 K, the zero-phonon line appears at 1360 nm (0.913 eV) with a half-width of 2.3×10^{-3} eV, and is assigned to the transition from the |±2> spin doublet of the A$_1$ ground state to the |±2> spin doublet of the B$_3$ state (transition labeled 3 in Fig. 3.64). On heating from 6 K to 59 K, the structure of the multiphonon sideband becomes less prominent, the intensity of the zero-phonon line decreases, and a new line appears on the low-energy side of the zero-phonon line at 1363 nm (0.910 eV), as shown in Fig. 3.66. This line has been assigned to the transition between the |-1> spin states of the A$_1$ ground state and the B$_3$ orbital' (transition 3 in Fig. 3.64).

The low oscillator strengths of many spin-forbidden intra-d-shell transitions can be increased by up to 3 orders of magnitude by irradiation,
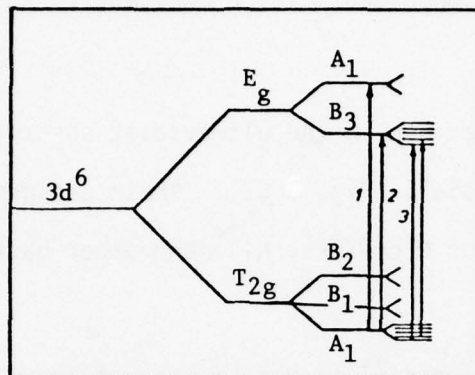
Fig. 3.64. Crystal field splitting of the 3d^6 orbital of Fe^{2+} in D$_{2h}$ symmetry. [U. Dürr and R. Weber, Solid State Comm. 14, 907 (1974).]
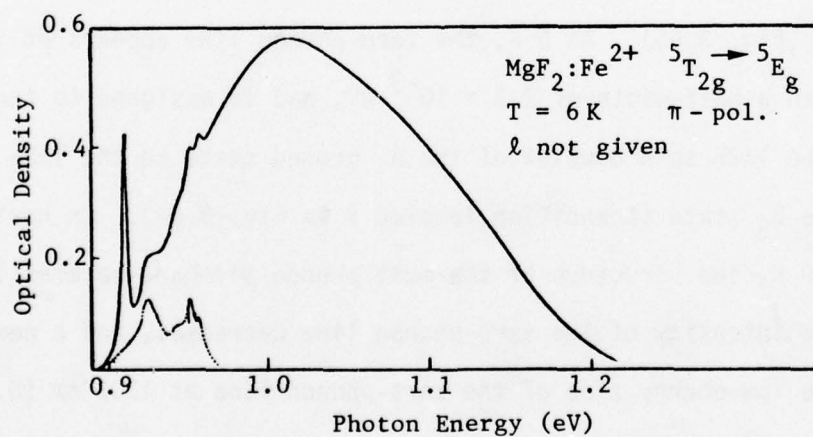
Fig. 3.65. Absorption spectrum and one-phonon portion MgF$_2$:Fe^{2+}. [U. Dürr and R. Weber, Solid State Comm. 14, 907 (1974).]
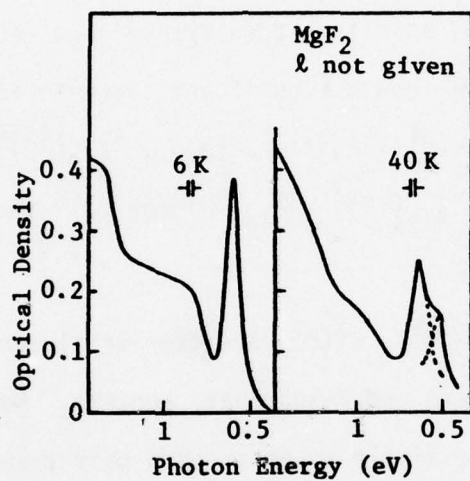
Fig. 3.66. Absorption spectrum of MgF$_2$:Fe^{2+} between
0.905 and 0.955 eV at 6 K and 40 K.   [U. Dürr and
R. Weber, Solid State Comm. 14, 907 (1974).]

as shown in Fig. 3.67 for crystals of MgF$_2$:2 atomic percent Co, MgF$_2$:0.75 atomic percent Ni, and MgF$_2$:0.05 atomic percent Mn.[3.69] In the figure the optical spectra before irradiation are labeled a and those after a γ-ray exposure of 10^7 R are labeled b. The possible assignments for various transitions, their peak positions and oscillator strengths before and after γ-ray irradiation are listed in Tables 3.10 and 3.11.[3.69] After irradiation the previously spin-forbidden transitions (e.g., all the transitions for Mn^{2+} impurity) show a significant increase in oscillator strength, while spin-allowed transitions (e.g., $^4T_{1g}(^4F) \rightarrow {}^4T_{2g}(^4F)$, $^4T_{1g}(^4F) \rightarrow {}^4A_{2g}(^4F)$, and $^4T_{1g}(^4F) \rightarrow {}^4T_{1g}(^4P)$ for Co^{2+} impurity) show little change in intensity.

Irradiation of MgF$_2$ doped with transition-metal ions produces various defects, including F centers and F-aggregate centers. Many of these defects have high mobility and are likely to be trapped near transition-metal sites. Detailed optical studies on the absorption and emission of 3d impurity ions in MgF$_2$ have led Yun, et al.,[3.70] to suggest that the radiation-induced enhancement of the spin-forbidden transitions is due to the exchange interaction between the 3d electrons and color centers.

3. <u>Radiative coloration of MgF$_2$</u>. Radiation-induced defects in MgF$_2$ have not been studied as extensively as in alkali halides. Early studies of the optical properties of irradiated MgF$_2$ led to a tentative assignment of the absorption band near 260 nm to F centers and the bands near 320 and 376 nm to M-center absorption.[3.71] The F center in an alkali-halide lattice has an octahedral symmetry, and its excited state is triply degenerate. In the MgF$_2$ lattice, the F center is expected to give rise to a broadened absorption band because its C$_{2v}$ symmetry can lift the degeneracy of the

102
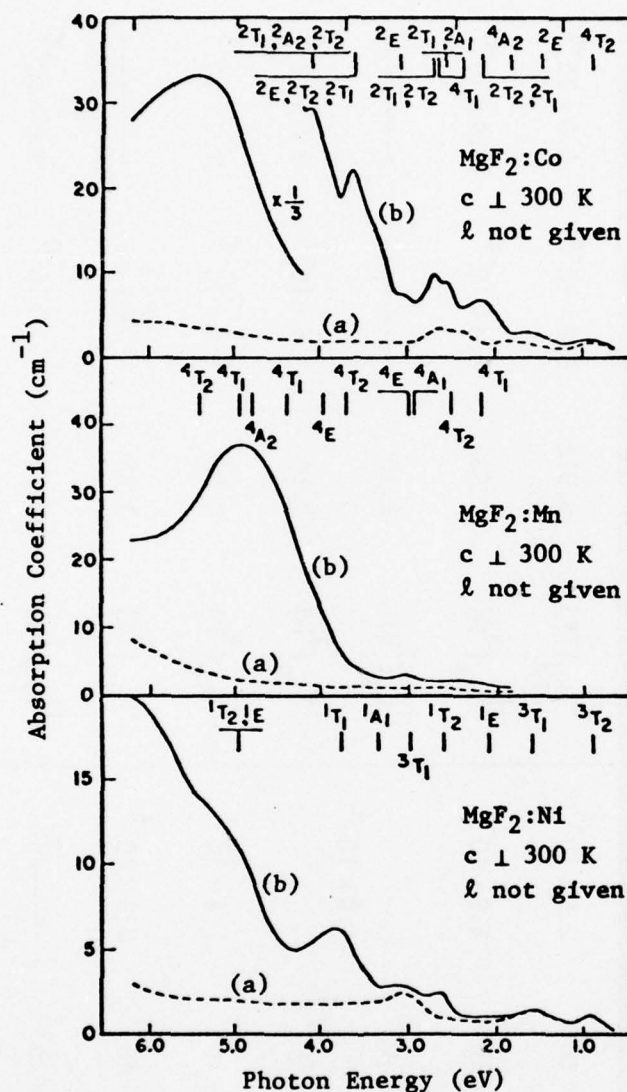
Fig. 3.67. Room-temperature absorption spectra illustrating the enhancement of the spin-forbidden transitions for Co^{2+}, Ni^{2+}, and Mn^{2+} impurity ions in MgF$_2$. Spectra labeled (a) represent the absorption in unirradiated crystals while the curves labeled (b) show the absorption following γ irradiation. [L. A. Kappers, S. I. Yun, and W. A. Sibley, Phys. Rev. B $\underline{29}$, 943 (1972).]

Table 3.10. Mn^{2+} and Ni^{2+} transitions in MgF$_2$ crystals. [L. A. Kappers, S. I. Yun, and W. A. Sibley, Phys. Rev. B $\underline{29}$, 943 (1972).]

	MgF$_2$:Mn				MgF$_2$:Ni		
Assignment (O_h) $^6A_{1g}(^6S) \rightarrow$	Peak Position (eV)	Oscillator Strength Before Irradiation	After Irradiation	Assignment (O_h) $^3A_{2g}(^3F) \rightarrow$	Peak Position (eV)	Oscillator Strength Before Irradiation	After Irradiation
$^4T_{1g}(^4G)$	2.13	3.3×10^{-7}	2.6×10^{-5}	$^3T_{2g}(^3F)$	0.918	6.9×10^{-6}	6.3×10^{-6}
$^4T_{2g}(^4G)$	2.58	2.7×10^{-7}	2.9×10^{-5}	$^3T_{1g}(^3F)$	1.63	8.6×10^{-6}	9.4×10^{-6}
$^4A_{1g}(^4G)$ $^4E_g(^4G)$	2.99	$\{1.9\times10^{-7}$ $1.1\times10^{-7}\}$	1.0×10^{-4}	$^1E_g(^1D)$	2.10	------	------
$^4T_{2g}(^4D)$	3.71	2.0×10^{-7}	1.4×10^{-5}	$^1T_{2g}(^1D)$	2.64	1.8×10^{-7}	8.8×10^{-6}
$^4E_g(^4D)$	3.95	2.9×10^{-7}	2.8×10^{-5}	$^3T_{1g}(^3P)$	3.02	1.9×10^{-5}	1.7×10^{-5}
$^4T_{1g}(^4P)$	4.35	3.3×10^{-7}	------	$^1A_{1g}(^1G)$	3.35	------	------
$^4A_{2g}(^4F)$	4.71	------	------	$^1T_{1g}(^1G)$	3.73	$<4.1\times10^{-8}$	3.5×10^{-5}
$^4T_{1g}(^4F)$	4.96	------	------	$^1T_{2g}(^1G)$ $^1E_g(^1G)$	4.96	$<3.4\times10^{-7}$	1.5×10^{-5}
$^4T_{2g}(^4F)$	5.40	------	------				

Table 3.11. Co^{2+} transitions in MgF$_2$ crystals. [L. A. Kappers, S. I. Yun, and W. A. Sibley, Phys. Rev. B $\underline{29}$, 943 (1972).]

Assignment (O_h) $^4T_{1g}(^4F) \rightarrow$	Peak Position (eV)	Oscillator Strength	
		Before Irradiation	After Irradiation
$^4T_{2g}(^4F)$	0.912	3.0×10^{-6}	3.4×10^{-6}
$^2E_g(^2G)$	1.46	2.5×10^{-8}	1.5×10^{-6}
$^4A_{2g}(^4F)$	1.82	1.6×10^{-6}	1.5×10^{-6}
$^2T_{2g},^2T_{1g}(^2G)$	2.15	8.4×10^{-8}	1.0×10^{-5}
$^4T_{1g}(^4P)$	$\begin{cases} 2.38 \\ 2.68 \end{cases}$	2.1×10^{-5}	2.1×10^{-5}
$^2T_{1g}(^2H)$ $^2A_{1g}(^2G)$	2.55	---------	3.6×10^{-6}
$^2T_{1g},^2T_{2g}(^2H)$	2.70	---------	4.8×10^{-6}
$^2E_g(^2H)$	3.09	2.9×10^{-8}	1.5×10^{-6}
$^2T_{1g}(^2P)$ $^2E_g,^2T_{2g}(^2D)$	3.63	$< 6.4 \times 10^{-8}$	3.2×10^{-5}
$^2T_{1g},^2A_{2g}(^2F)$ $^2T_{2g}(^2F)$	4.07	$< 6.5 \times 10^{-8}$	6.1×10^{-5}

excited state.[3.72] M centers with four different symmetries, C$_2$h, C$_2$v, D$_2$h and C$_1$ are possible in the MgF$_2$ lattice, as shown in Fig. 3.68.[3.73]

The transmittance spectrum of an electron-irradiated MgF$_2$ crystal is shown in Fig. 3.57.[3.58] Two absorption bands are seen: a strong band at 260 nm (4.77 eV), presumably due to F centers, and a considerably weaker band at 120 nm (10.3 eV), presumably due to the β bands (exciton perturbed by an F center).

Optical absorption spectra of neutron-irradiated MgF$_2$ crystals are shown in Fig. 3.69.[3.74] Again, two bands are seen, the F band near 4.8 eV (260 nm) and the band at 10.6 eV (117 nm) near the fundamental absorption edge. Since the F band and the 10.6 eV band could be bleached simultaneously with the F light (Fig. 3.69), and since the optical density of the F band varied linearly with that of the 10.6 eV band during the course of bleaching experiments (Fig. 3.70), the 10.6 eV band was assigned to the β band, the exciton perturbed by an F center.

The effects of irradiation temperature, radiation intensity, and background impurity content on the colorability of MgF$_2$ have been studied in some detail by Sibley and Facey.[3.72] In this work, MgF$_2$ crystals from three commercial sources, the Harshaw Chemical Co., Alpha Inorganics and Optovac Corporation, were used. Their background impurity contents are indicated in Table 3.12. Both unoriented and oriented samples were used in this work; the two orientations used are indicated by C$_{\parallel}$, where the sample face is parallel to the c-axis and C$_{\perp}$, where the specimen face is perpendicular to the c-axis.

Figure 3.71 shows the absorption spectra of γ-irradiated MgF$_2$ crystals in the spectral range 177 to 620 nm. The F-center band near 260 nm (4.77 eV) and a
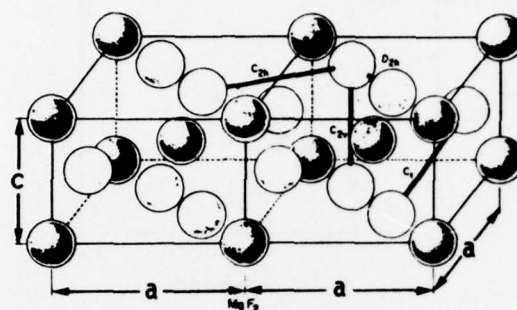
Fig. 3.68. MgF$_2$ lattice. The four possible M-center configurations are shown by the solid lines.   [O. E. Facey and W. A. Sibley, Phys. Rev. B $\underline{2}$, 1111 (1970).]
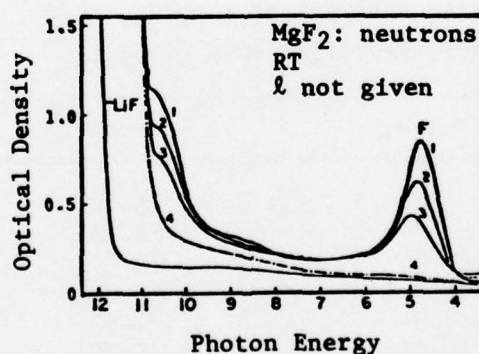
Fig. 3.69.   Absorption spectra of neutron-irradiated MgF$_2$ crystals. 1. Before bleaching (n-irradiated for 5 hrs).   2. Bleached for 1 hr. 3. Bleached for 1 + 3.5 hrs. 4. Unirradiated. [T. Tsuboi, R. Kato, and M. Nakagawa, J. Phys. Soc. Japan $\underline{25}$, 645 (1968).]
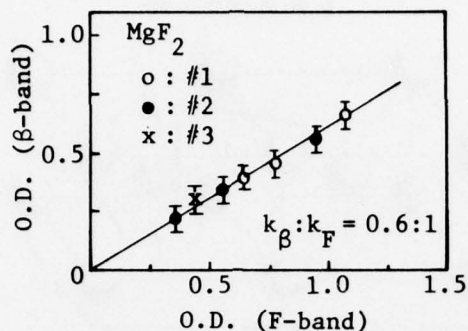
Fig. 3.70. Relation between the optical densities, O.D., of 10.6 eV- and F-bands. Specimen #1: neutron irradiated for 7 hours, then optically bleached for 1 hour and 1 + 2 hours, #2: irradiated for 5 hours, then bleached for 1 hour and 1 + 3.5 hours, #3: irradiated for 3 hours. [T. Tsuboi, R. Kato, and M. Nakagawa, J. Phys. Soc. Japan 25, 645 (1968).]

Table 3.12. Impurity analyses of samples (μg/g). [W. A. Sibley and O. E. Facey, Phys. Rev. 174, 1074 (1968).]

Element	Harshaw	α Inorganic	Optovac
Al	2-10	5-10	•••
Ba	< 1	< 1-10	•••
Ca	≤ 20	8	•••
Co	≤ 10	4	•••
Cr	< 1-9	< 1-50	45
Cu	10-40	5,20	•••
Fe	< 4	< 4-10	150-180
K	3	8	•••
Mn	1	3-50	•••
Na	< 10	< 10	69
Mo	< 10-60	< 10-55	•••
Pb	< 10	< 10	•••
Si	100	< 10	•••
Zn	< 100	< 100	•••

108
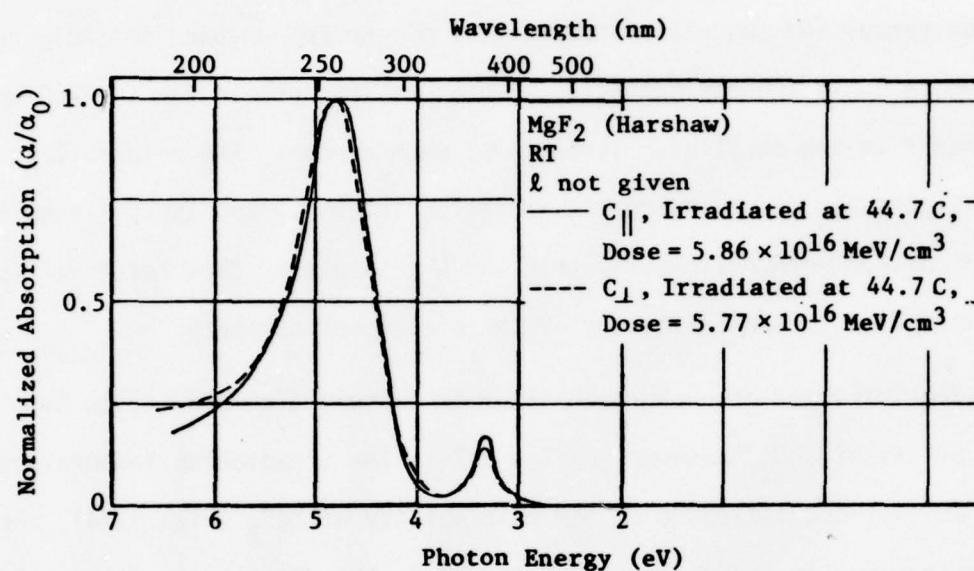
Fig. 3.71. Absorption spectra of two samples of MgF$_2$ cut with different orientations and irradiated to about the same γ dose. [W. A. Sibley and O. E. Facey, Phys. Rev. <u>174</u>, 1074 (1968).]

smaller M-center band near 376 nm (3.30 eV) are seen, and the orientation dependence of the peak position of the band near 260 nm is apparent.

Figure 3.72 shows a plot of energy absorbed by the sample during irradiation versus the absorption coefficient of the 260 nm band or the product $n_F f$, where n_F is the concentration of centers responsible for the 260 nm band and f is the oscillator strength of each center. The colorability of MgF$_2$ is strongly dependent on the radiation intensity and the $C_{||}$ samples can be colored more efficiently than the $C_\perp$ samples. This latter effect was attributed to the anisotropy of the oscillator strength.

The influence of background impurity content (Table 3.12) on the colorability of MgF$_2$ is shown in Fig. 3.73. The irradiation temperature also has a strong influence on the colorability of MgF$_2$ (Fig. 3.74). As the temperature is increased from 5 to 300 K, the efficiency of the coloration first decreases, reaching a minimum between 80 and 200 K, and then increases again at higher temperatures.

The irradiation temperature and intensity have a marked influence on the structure of the absorptions near 376 nm, as illustrated in Fig. 3.75. In this figure the solid absorption curve was obtained from a crystal which was electron-irradiated with intensity 1.2×10^{12} MeV/cm^2 at 300 K, and the dashed absorption curve was obtained from a crystal which was electron-irradiated at 273 K with the same intensity but for a shorter period of time. Two different kinds of centers, one causing absorption peaking near 370 nm (3.35 eV) and the other near 400 nm (3.10 eV), are apparent.

Figure 3.76 shows that a straight-line relationship is observed when the total area under the 370 and 400 nm bands is plotted against the square of the total area under the 260 nm band. A straight-line relationship is
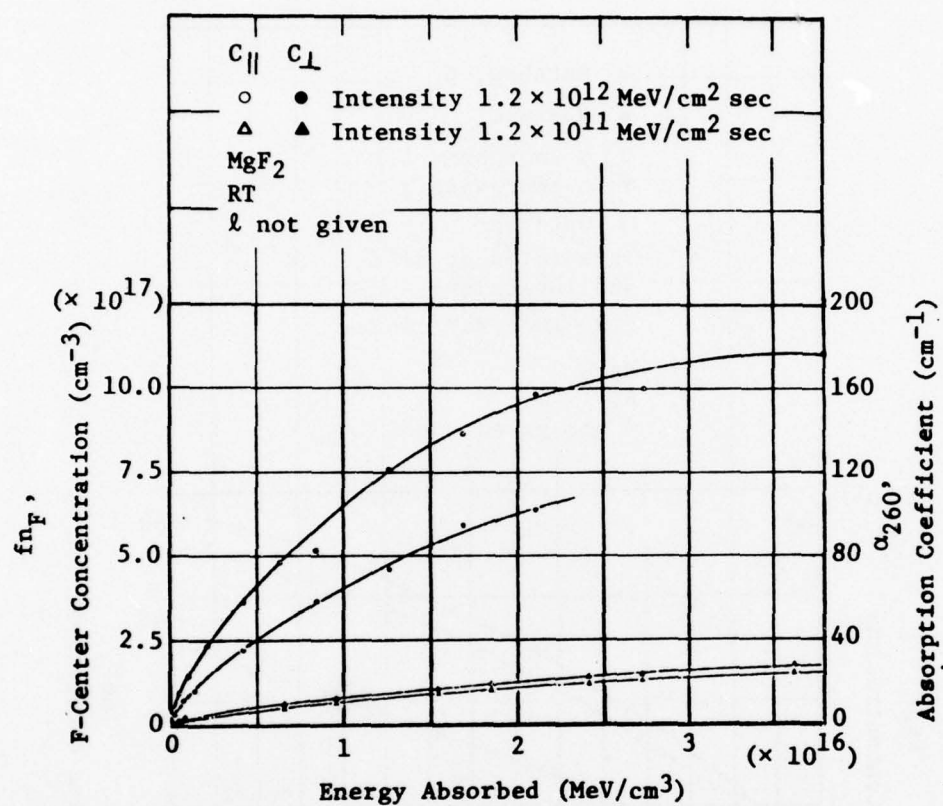
Fig. 3.72 Effect of radiation intensity on the room-temperature colorability of MgF$_2$. [W. A. Sibley and O. E. Facey, Phys. Rev. **174**, 1074 (1968).]
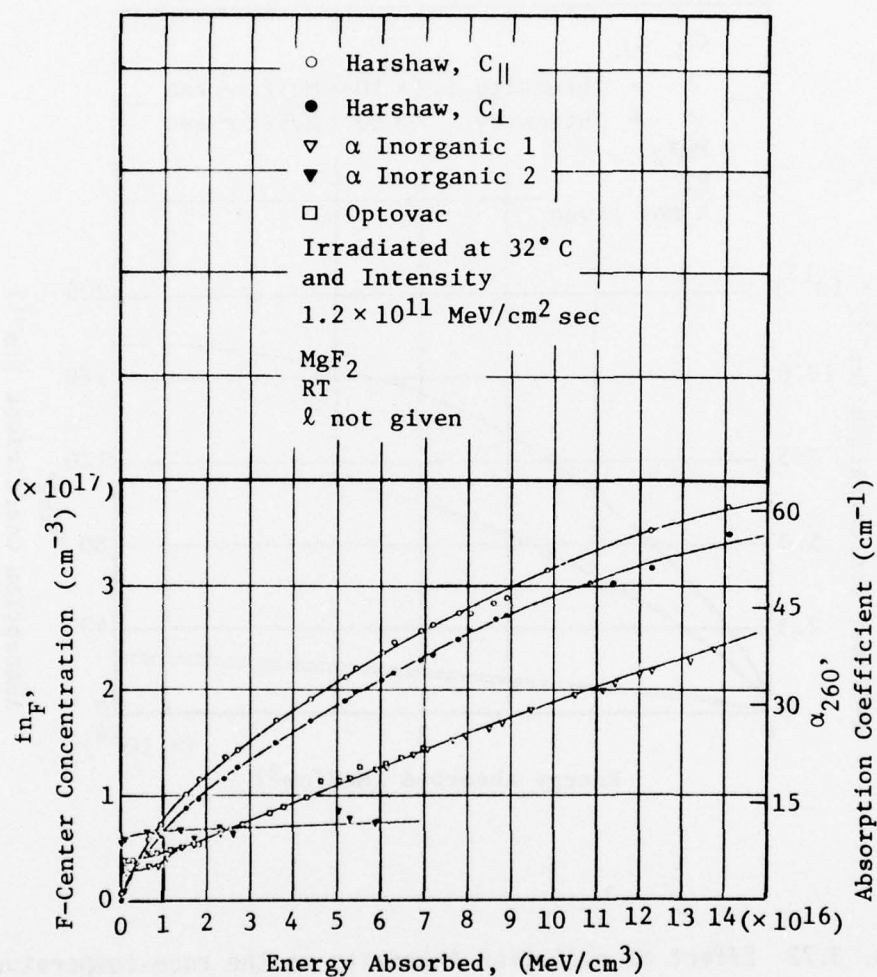
Fig. 3.73. Colorability, at one irradiation temperature and intensity, of samples obtained from a number of different commercial sources. [W. A. Sibley and O. E. Facey, Phys. Rev. 174, 1074 (1968).]
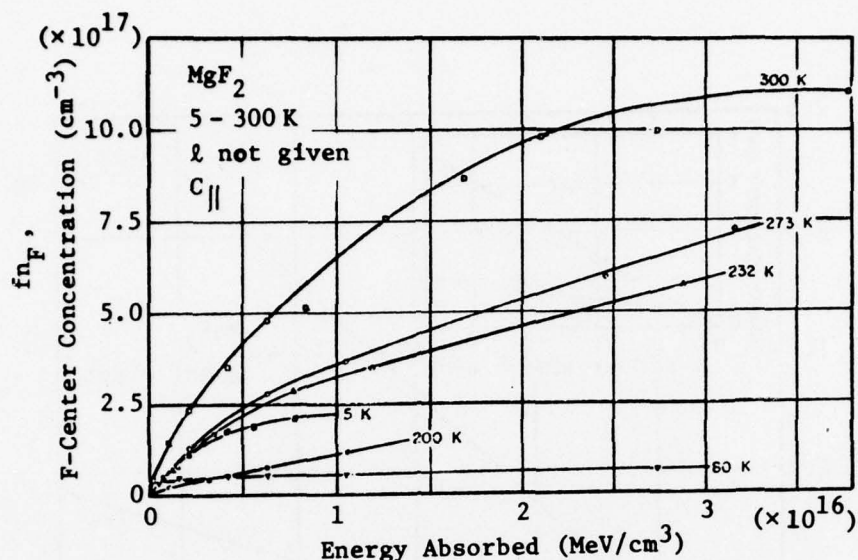
Fig. 3.74. Plot of the F-center concentration versus energy absorbed as a function of irradiation temperature. The data were taken on Harshaw samples at a fixed radiation intensity of 1.2×10^{13} MeV/cm^2 sec. [W. A. Sibley and O. E. Facey, Phys. Rev. 174, 1074 (1968).]
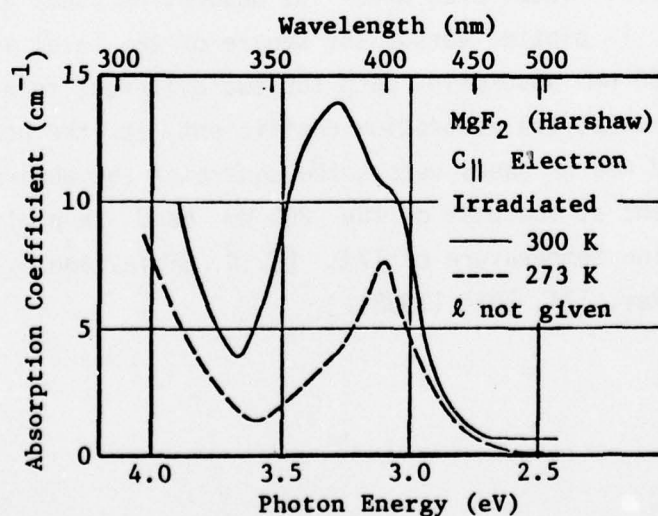
Fig. 3.75. Plot of the absorption coefficient versus photon energy for one sample irradiated at two different temperatures. [W. A. Sibley and O. E. Facey, Phys. Rev. 174, 1074 (1968).]
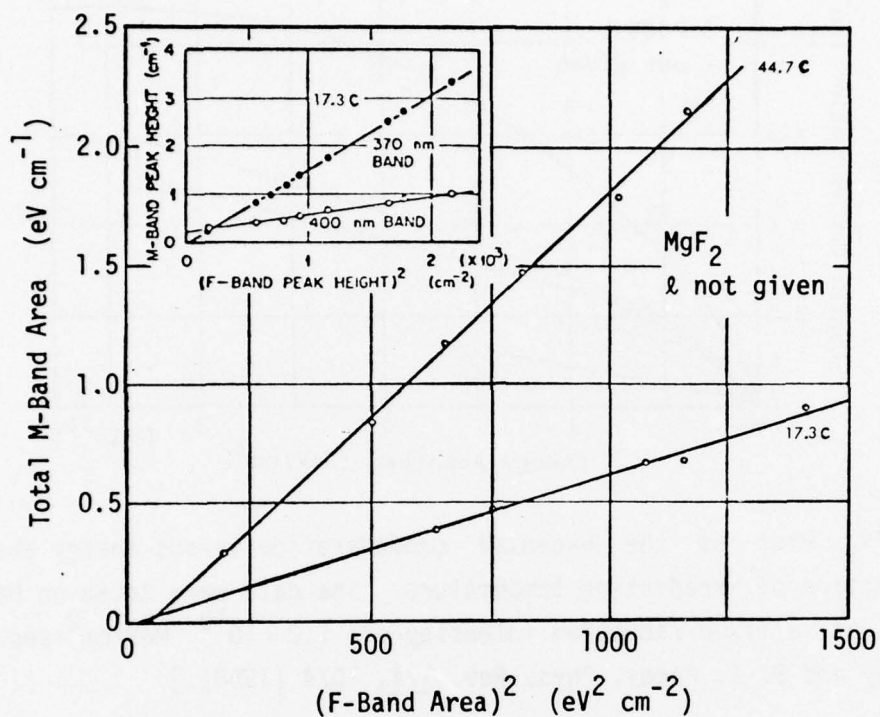
Fig. 3.76. Total area under the absorption bands at 370 and
400 nm is plotted versus the square of the total area under
the 260 nm absorption band for two different temperatures.
In the inset the absorption coefficient at the peak of the
370 and 400 nm bands versus the square of the absorption co-
efficient at the peak of the 260 nm band is plotted for a
radiation temperature of 17 C. [W. A. Sibley and O. E. Facey,
Phys. Rev. 174, 1074 (1968).]

also observed when the intensity of the peak of the 370 nm or 400 nm absorption band is plotted against the square of the intensity of the 260 nm band, as shown in the inset of Fig. 3.76. Since it has been shown earlier that the concentration of M centers in KCℓ varies linearly with the square of the F-center concentration, Sibley and Facey[3.72] assigned the 260 nm band to F centers and the 370 nm and 400 nm bands to two different configurations of the M centers.

Additional work has established that the 370 nm absorption band is caused by M centers with C_2h symmetry, $M(C_2h)$, and the 400 nm band is caused by $M(C_1)$ centers (Fig. 3.68).[3.73, 3.75]

The excitation of the 370 nm (3.35 eV) band gives rise to an emission band peaking at 420 nm (2.96 eV). At low temperatures, narrow line transitions are observed on the low-energy side of the absorption band and on the high-energy side of the emission band (Fig. 3.77).[3.73] These narrow line transitions have a mirror symmetry about the zero-phonon line, observed at 387.3 nm, and have been assigned to transitions involving the lattice vibration modes. The energy difference in wave numbers between the zero-phonon line in absorption and emission and the other sharp lines, and the possible lattice-mode assignments, are indicated in Table 3.13.

4. <u>Additive coloration of MgF$_2$</u>. MgF$_2$ crystals can be additively colored by heating in Mg vapor.[3.76] The optical absorption spectrum of such a crystal is shown by the dashed line in Fig. 3.78. Two bands are seen, an unpolarized band at 370 nm (3.35 eV) and a broad band near 250 nm (4.96 eV). Both of these bands have been attributed to vacancy clusters.[3.76] When an additively colored crystal is cooled to liquid-helium temperature, fine line structure appears on the low-energy side of the 370 nm band, as shown in
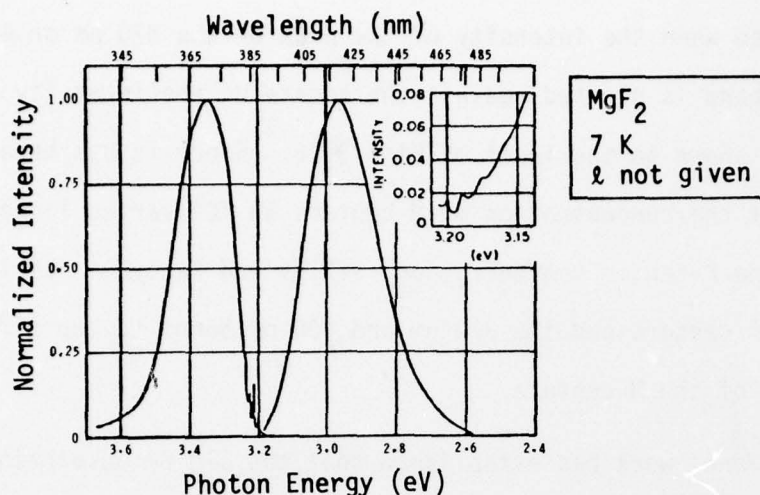
Fig. 3.77. Normalized absorption and emission at 7 K of the M(C$_{2h}$) center. The sharp line structure is evident for absorption, but is so weak in the case of the luminescence that it is shown in the inset with the scale expanded. [O. E. Facey and W. A. Sibley, Phys. Rev. B $\underline{2}$, 1111 (1970).]

Table 3.13. Narrow-line transitions in MgF$_2$. [O. E. Facey and W. A. Sibley, Phys. Rev. B $\underline{2}$, 1111 (1970).]

Absorption			Luminescence			Lattice mode Assignment
Peak position		Energy difference	Peak position		Energy difference	
(nm)	(eV)	(eV)	(nm)	(eV)	(eV)	(eV)
387.3	3.20		387.0	3.20		
385.7	3.21	0.013	388.5	3.19	0.013	0.011(Γ_5) or 0.015(X_2)
384.5	3.22	0.023	390.2	3.18	0.026	0.022(Γ_6), 0.026(X_1), or 0.023(Z_2)
382.7	3.24	0.038	392.0	3.16	0.040	0.037(Γ_{10}), 0.040(Γ_3), or 0.037(X_3)
380.8	3.26	0.055	393.5 (?)	3.15	0.052	0.054(Γ_4), 0.056(X_1), 0.055(X_2), 0.055(Z_2), or 0.056(Γ_6)

116
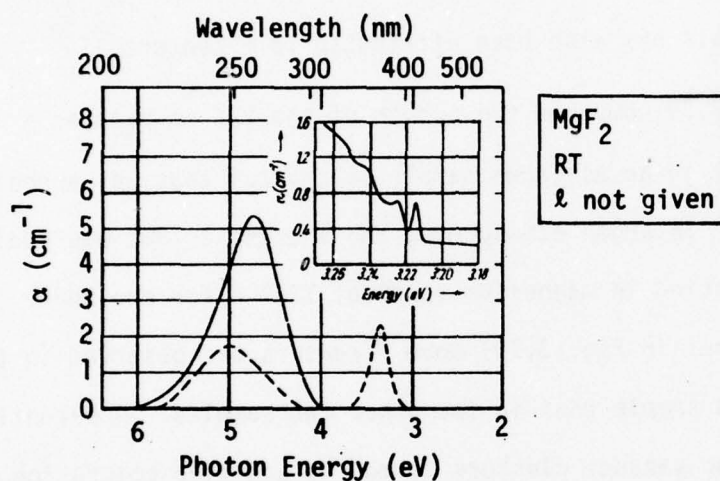
Fig. 3.78. Plot of the absorption coefficient versus photon energy for an MgF$_2$ crystal additively colored at 1200 C and 740 torr before γ-irradiation and following a γ-dose of 2.4×10^{15} MeV/cm^3. The inset shows the sharp line spectra which appear at 4 K on the low-energy side of the unpolarized 370 nm band. [W. E. Vehse, O. E. Facey, and W. A. Sibley, Phys. Stat. Sol. (a) 1, 679 (1970).]

the inset of Fig. 3.78. The solid line in the figure shows the optical absorption spectrum of an MgF$_2$ crystal which was irradiated after additive coloration. The absorption band at 265 nm (4.68 eV) grows at the expense of the 250 and 370 nm bands, and its optical properties have been found to be similar to the 265 nm band observed in irradiated MgF$_2$ crystals (with no prior additive coloration). Therefore the 265 nm band in additively colored crystals has also been attributed to F centers.[3.78]

Figure 3.79 compares the growth of the 265 nm band as a function of γ-ray exposure in an as-grown sample, a crystal that was annealed at 1200 C for one hour in argon atmosphere, and a crystal that was additively colored by heating in magnesium vapor at 1200 C for one hour. At low exposures (inset in Fig. 3.79) more F centers are observed in the additively colored sample than in the other two samples. Apparently, irradiation breaks up vacancy clusters formed by additive coloration and converts them into isolated F centers.

MgF$_2$ crystals have also been additively colored by heating in Aℓ vapor.[3.76] In this case, F centers are produced directly without any need for subsequent irradiation.
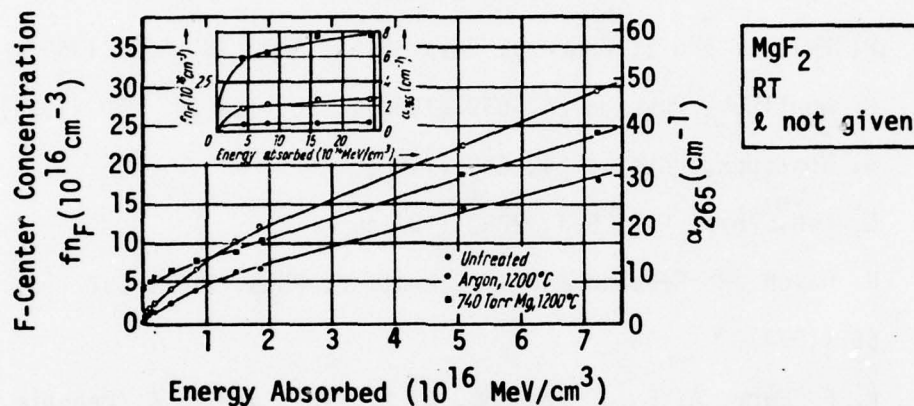
Fig. 3.79. Colorability of an additively colored MgF$_2$
crystal as compared with the colorability of similar
crystals heated in an inert atmosphere.   An untreated
crystal is shown for reference.   [W. A. Vehse, O. E.
Facey, and W. A. Sibley, Phys. Stat. Sol. (a) 1, 679
(1970).]

REFERENCES

3.1   H. G. Lipson, B. Bendow, L. Skolnik, S. S. Mitra, and N. E. Massa, in <u>Proceedings of the Fifth Annual Conference on Infrared Laser Window Materials</u>, Las Vegas, Nevada, 1-4 December 1975. (Defense Advanced Research Projects Agency, February 1976), p. 889.

3.1a   P. Feltham and I. Andrews, Phys. Stat. Sol. <u>10</u>, 203 (1965).

3.2   W. Bontinck, Physica <u>24</u>, 639 (1958); Physica <u>24</u>, 650 (1958).

3.3   W. Bontinck, Physica <u>24</u>, 650 (1958).

3.4   E. Loh, Phys. Rev. B <u>4</u>, 2002 (1971).

3.5   R. Rauch, R. Reimann and G. Schwotzer, Phys. Stat. Sol. (a) <u>23</u>, 69 (1974).

3.6   K. F. Burr, A. E. J. Strange, R. G. King, and L. G. Penhale, Phys. Lett. A <u>24</u>, 44 (1967).

3.7   J. H. Beaumont and W. Hayes, Proc. Roy. Soc. A <u>309</u>, 41 (1969).

3.8   R. Rauch, Internat. Conf. Luminescence, Leningrad 1972, in: Izv. Akad. Nauk. SSSR, Ser. fiz. <u>37</u>, 595 (1973).

3.9   R. K. Bagai and A. V. R. Warrier, Phys. Stat. Sol. (b) <u>73</u>, K 123 (1976).

3.10   J. F. Sabatini, A. E. Salwin, and D. S. McClure, Phys. Rev. B <u>11</u>, 3832 (1975).

3.11   J. M. Baker, B. Bleaney, and W. Hayes, Proc. Roy. Soc. A <u>247</u>, 141 (1958).

3.12   W. Ulrici, Phys. Stat. Sol. (b) <u>64</u>, K 115 (1974).

3.13   A. Mehra, Phys. Stat. Sol. <u>29</u>, 847 (1968).

3.14   S. C. Jain and G. D. Sootha, Phys. Stat. Sol. <u>22</u>, 505 (1967).

3.15   G. Schwotzer and W. Ulrici, Phys. Stat. Sol. (b) $\underline{64}$, K 115 (1974).

3.16   A. L. Stolov and Zh. S. Yakovleva, Soviet Phys. - Solid State $\underline{10}$, 1196 (1968).

3.17   E. I. Zoroatskaya, B. Z. Malkin, A. L. Stolov, and Zh. S. Yakovleva, Sov. Phys. - Solid State $\underline{10}$, 320 (1968).

3.18   William S. C. Chang, Principles of Quantum Electronics, Addison-Wesley, 1969, p. 151.

3.19   E. Loh, Phys. Rev. $\underline{147}$, 332 (1966).

3.20   D. S. McClure and Z. J. Kiss, J. Chem. Phys. $\underline{39}$, 3251 (1963).

3.21   D. L. Staebler and S. E. Schnatterly, Phys. Rev. B $\underline{3}$, 516 (1971).

3.22   E. Loh, Phys. Rev. B $\underline{4}$, 2002 (1971).

3.23   R. Casanova Alig, Phys. Rev. B $\underline{3}$, 536 (1971).

3.24   C. H. Andrews and E. S. Sabisky, Phy. Rev. B $\underline{3}$, 527 (1971).

3.25   R. D. Sharmon and C. T. Prewill, Acta. Cryst. B $\underline{25}$, 925 (1969).

3.26   Fritz Luty, in Physics of Color Centers, ed. by W. B. Fowler (Academic Press, New York, 1968), p. 181.

3.27   R. McLaughlin, U. Abed, John G. Conway, N. Edelstein, and E. H. Huffman, J. Chem. Phys. $\underline{53}$, 2031 (1970).

3.28   J. J. Stacy, N. Edelstein, and R. D. McLaughlin, J. Chem. Phys. $\underline{57}$, 4980 (1972).

3.29   W. A. Hargreaves, Phys. Rev. $\underline{156}$, 331 (1967).

3.30   S. D. McLaughlan, Phys. Rev. 1$\underline{50}$, 118 (1966).

3.31   R. S. Title, P. P. Sorokin, M. J. Stevenson, G. D. Peltit, J. E. Scardefield, and J. R. Lankard, Phys. Rev. $\underline{128}$, 62 (1962).

3.32   R. McLaughlin, R. White, N. Edelstein, and John G. Conway, J. Chem. Phys. $\underline{48}$, 967 (1968).

3.33   H. Lämmermann and J. Conway, J. Chem. Phys. $\underline{38}$, 259 (1963).

3.34   N. Edelstein, W. Easley, and R. McLaughlin, J. Chem. Phys. $\underline{44}$, 3130 (1966).

3.35a   N. Edelstein, W. Easley, and R. McLaughlin, Advan. Chem. Ser. $\underline{71}$, 203 (1967).

3.35b   J. B. Gruber, W. R. Cochran, J. G. Conway, and A. Nicol, J. Chem. Phys. $\underline{45}$, 1423 (1966).

3.35c   T. K. Keenan, J. Am. Chem. Soc. $\underline{83}$, 3719 (1961).

3.35d   N. Edelstein, John G. Conway, D. Fujita, W. Kolbe, and R. McLaughlin, J. Chem. Phys. $\underline{52}$, 6425 (1970).

3.35e   K. Przibram, Z. Physik $\underline{154}$, 111 (1959).

3.36   E. Mollwo, Nach. Gesell. Wiss. Göttingen $\underline{6}$, 79 (1934).

3.37   A. Smakula, Phys. Rev. $\underline{77}$, 408 (1949), $\underline{91}$, 1570 (1953).

3.38   J. H. Schulman and R. J. Ginther, J. Opt. Soc. Am. $\underline{43}$, 1818 A (1953).

3.39   J. H. Schulman, R. J. Ginther, and R. D. Kirk, J. Chem. Phys. $\underline{20}$, 1966 (1952).

3.40   H. Bontinck, Physica $\underline{24}$, 639 and 650 (1958).

3.41   R. Rauch and I. Senff, Phys. Stat. Sol. (a) $\underline{26}$, 537 (1974).

3.42   J. Arends, Phys. Stat. Sol. $\underline{7}$, 805 (1964).

3.43   H. W. den Hartog and J. Arends, Phys. Stat. Sol. $\underline{22}$, 131 (1967).

3.44   A. Smakula, Z. Physik $\underline{138}$, 276 (1954).

3.45   F. Lüty, Z. Physik $\underline{134}$, 596 (1953).

3.46   H. Karras, Phys. Stat. Sol. $\underline{1}$, 68 (1961).

3.47   P. Görlich and H. Karras, Proc. Internat. Conf. Semicond. Phys., Prague 1960, p. 698.

3.48   P. Görlich, H. Karras, and R. Lehmann, Phys. Stat. Sol. $\underline{3}$, 98 (1963).

3.49   H. Karras and P. Ullmann, Jenaes Jahrbuck. 1969/70, VEB Gustav Fisher Verlag, Jena, 1970, p. 1.

Sec. III-References

3.50   P. Görlich and P. Ullmann, Phys. Stat. Sol. (b) $\underline{50}$, 577 (1972).

3.51   G. A. Tanton, R. A. Shatas, J. E. Williams, and A. Mukerji,
        J. Chem. Phys. $\underline{49}$, 5532 (1968).

3.52   W. C. Collins, Phys. Stat. Sol. (b) $\underline{56}$, 291 (1973).

3.53   W. Hayes and J. W. Twidell, Proc. Phys. Soc. (London) $\underline{79}$, 1295
        (1962).

3.54   M. D. Agrawal and K. V. Rao, Phys. Stat. Sol. (a) $\underline{3}$, 153 (1970).

3.55   M. Ikeya and N. Itoh, Proc. Internat. Conf. Sci. and Tech. Non-
        metallic Crystals, New Delhi, 1969, p. 48.

3.56   W. R. Hunter, Optica Acta $\underline{9}$, 255 (1962).

3.57   L. R. Canfield, G. Hass, and J. E. Waylonis, Appl. Optics $\underline{5}$,
        45 (1966).

3.58   D. F. Heath and P. A. Sacher, Appl. Optics $\underline{5}$, 937 (1966).

3.59   W. C. Johnson, Rev. Sci. Instr. $\underline{35}$, 1375 (1964).

3.60   T. F. Deutsch, J. Phys. Chem. Solids $\underline{34}$, 2091 (1973).

3.61   American Institute of Physics Handbook, Third Edition, D. E. Gray,
        ed., McGraw-Hill, New York, 1972, pp. 6-35.

3.62   A. R. Knudsen and J. E. Kupperian, J. Opt. Soc. Am. $\underline{47}$, 440 (1957).

3.63   A. H. Laufer, J. A. Pirog, and J. R. McNesby, J. Opt. Soc. Am.
        $\underline{55}$, 64 (1965).

3:64   R. J. Davis, J. Opt. Soc. Am. $\underline{56}$, 837 (1966).

3.65   W. R. Hunter and S. A. Malo, J. Phys. Chem. Solids $\underline{30}$, 2739 (1969).

3.66   T. Tomiki and T. Miyata, J. Phys. Soc. Japan $\underline{27}$, 658 (1969).

3.67   J. F. Sabatini, A. E. Salwin, and D. S. McClure, Phys. Rev. B $\underline{11}$,
        3832 (1975).

3.68   U. Dürr and R. Weber, Solid. State Comm. $\underline{14}$, 907 (1974).

3.69   L. A. Kappers, S. I. Yun, and W. A. Sibley, Phys. Rev. B $\underline{29}$,
        943 (1972).

3.70   S. I. Yun, L. A. Kappers, and W. A. Sibley, Phys. Rev. B 8, 773 (1973).

3.71   R. F. Blunt and M. I. Cohen, Phys. Rev. 153, 1031 (1967).

3.72   W. A. Sibley and O. E. Facey, Phys. Rev. 174, 1074 (1968).

3.73   O. E. Facey and W. A. Sibley, Phys. Rev. B 2, 1111 (1970).

3.74   T. Tsuboi, R. Kato, and M. Nakagawa, J. Phys. Soc. Japan 25, 645 (1968).

3.75   O. E. Facey and W. A. Sibley, Phys. Rev. 186, 926 (1969).

3.76   W. E. Vehse, O. E. Facey, and W. A. Sibley, Phys. Stat. Sol. (a) 1, 679 (1970).

IV. OXIDES AND GLASSES[*]

A. Silicon Dioxide and Some Silicate Glasses

Silicon dioxide (SiO_2) exists in both crystalline and non-crystalline forms. It melts at 1710 C and cn cooling sets to a transparent glass — the non-crystalline form — which is often referred to as silica glass, vitreous silica, fused silica or simply as silica. Its structure is basic to various silicate glasses.

Crystalline SiO_2 can be prepared in the laboratory and is also found as a mineral in three basic structures — quartz, tridymite, and cristobalite. Each of these three polymorphic forms can exist in two or three subsidiary forms. The most stable forms are low (or α) quartz below 573 C, high (or β) quartz 573 to 867 C, high tridymite 867 to 1470 C, and high cristobalite 1470 to 1710 C.

The basic structural unit in all known forms of silicon dioxide consists of an SiO_4 tetrahedron in which each silicon atom is surrounded by four tetrahedrally located oxygen atoms. Crystalline SiO_2 consists of a three-dimensional network of SiO_4 tetrahedron joined so that each oxygen atom is common to two tetrahedra. Different ways of combining tetrahedral groups with all corners shared correspond to the different polymorphic forms of SiO_2.

The same tetrahedral SiO_4 structure exists in glassy silica, which, however, lacks long-range periodicity. Schematic two-dimensional representations of crystalline and glassy SiO_2 are shown in Fig. 4.1.[4.1]

---

[*]See summary Figures 1.8, 1.9, and 1.13 of Volume I.

(a)   (b)
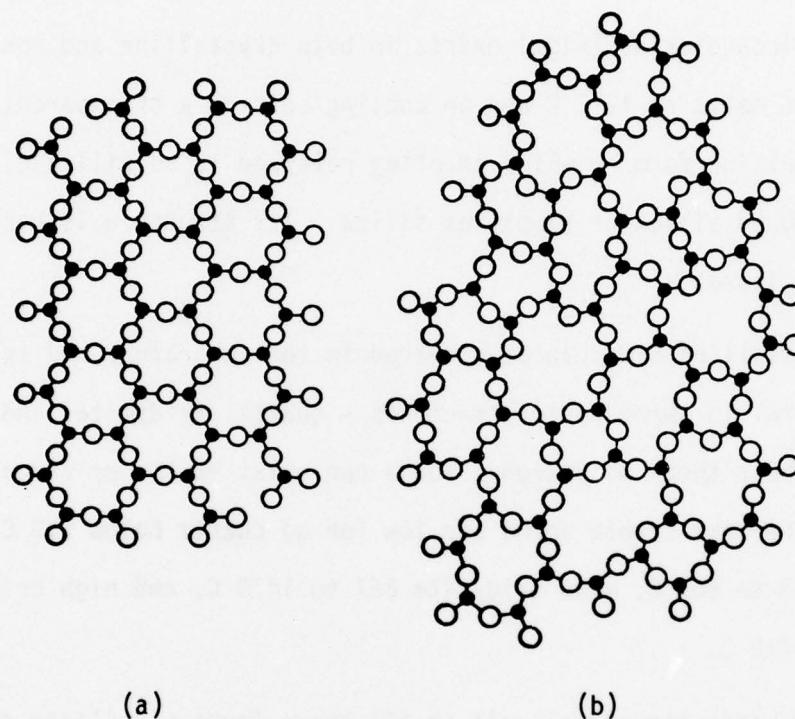
Fig. 4.1. Two-dimensional representation of (a) crystalline and (b) glassy SiO$_2$. [J. I. Slaughter, in _Ceramics for Advanced Technologies_, J. E. Hove and W. C. Riley, eds., Wiley, New York, 1965, pp. 218-250.]

In fused silica and α-quartz the Si-O bond distance is approximately 0.161 nm. The Si-O-Si bond angle, which may vary in fused silica, is 144° in α-quartz.

Some of the material which has been selected for this section as pertinent to the present report has been discussed in greater detail in review articles by Lell, et al.[4.2] and Sigel.[4.3]

1.   Some common impurities in SiO_2.   Alkali oxides, aluminum and hydrogen are common impurities in SiO_2.   Considerations of the oxygen-to-silicon ratio indicate that the non-bridging oxygens, that is oxygen bonded to only one silicon, will be generated by the presence of alkali oxide. In SiO_2, the oxygen-to-silicon ratio of two requires that each oxygen be bonded to two silicon atoms forming an infinite three-dimensional network. As Na_2O, for example, is added, the Na^+ can be accommodated in the interstices of the structure, as shown in Fig. 4.2.[4.4] This results in an increase in the O:Si ratio, which will require that the infinite network be broken at several points corresponding to oxygen ions bonded to single silicon. Hydrogen, like alkali ions, also generates non-bridging oxygen in the SiO_2 network.

Aluminum normally substitutes for silicon in the SiO_2 structure, but since it is trivalent, aluminum has to accept an additional negative charge which in turn is compensated by an alkali ion in its vicinity. Aluminum addition to alkali-doped SiO_2 leads to a decrease in the concentration of non-bridging oxygens.

2.   Fundamental and common impurity-related UV absorption in SiO_2. The positions of the ultraviolet absorption edges of high-purity quartz,

● Si^{4+} ○ O^{2-} ◉ Na$^+$
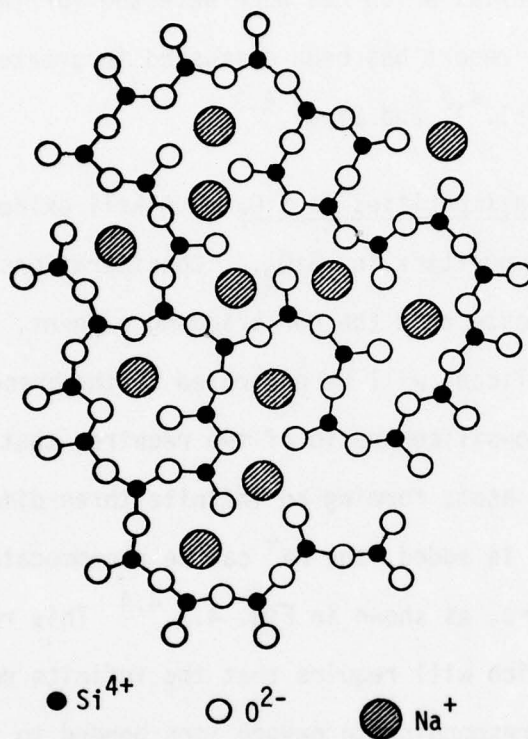
Fig. 4.2.   Schematic representation of modified silicate
network.   [W. D. Kingery,   in Introduction to Ceramics,
Wiley, New York, 1960, pp. 140-160.]

fused silica, and a sodium silicate (2 SiO_2 - 1 Na_2O) glass are shown in Fig. 4.3.[4.3] The absorption edge, corresponding to $\beta = 5$ cm^{-1}, is seen at approximately 148 nm (8.38 eV) for quartz, at 168 nm (7.38 eV) for fused silica, and at 236 nm (5.25 eV) for the sodium-silicate glass. The observed shift of the absorption edge of fused silica relative to quartz is believed to be due to the distribution of Si-O-Si bond angles in fused silica. Notice that the absorption tail in quartz or silica is much steeper than that in sodium-silicate glass.

Reflectance spectra in the region of 6 - 14 eV (207 - 89 nm) of crystalline and glassy SiO_2 are shown in Fig. 4.4.[4.3] The similarity in the spectra of both materials suggests that the absorption arises from the electronic transitions characteristic of the SiO_4 tetrahedron.

Optical attenuation in a high-purity glass, in what is normally the transparent region below the fundamental absorption edge, occurs because of scattering and absorption. Variations in the local dielectric constant and the local electric field are associated with the random molecular structure of glass. The dielectric-constant variation contributes to the scattering, and the electric-field variation contributes to the absorption. The scattering and absorption losses in high-purity silica and soda-lime-silicate glasses are shown in Fig. 4.5 and Fig. 4.6. Pinnow and co-workers[4.5] conclude that the observed absorption loss with photon energy from 1 to 7 eV (1239.8 to 177.1 nm), as shown in Fig. 4.6, is due to an intrinsic mechanism associated with local field variations. Note that this exponential rise of β in the transport region (Fig. 4.6) is much less steep than that of the Urbach absorption tail (Fig. 4.3), which occurs just off scale to the right in Fig. 4.6.
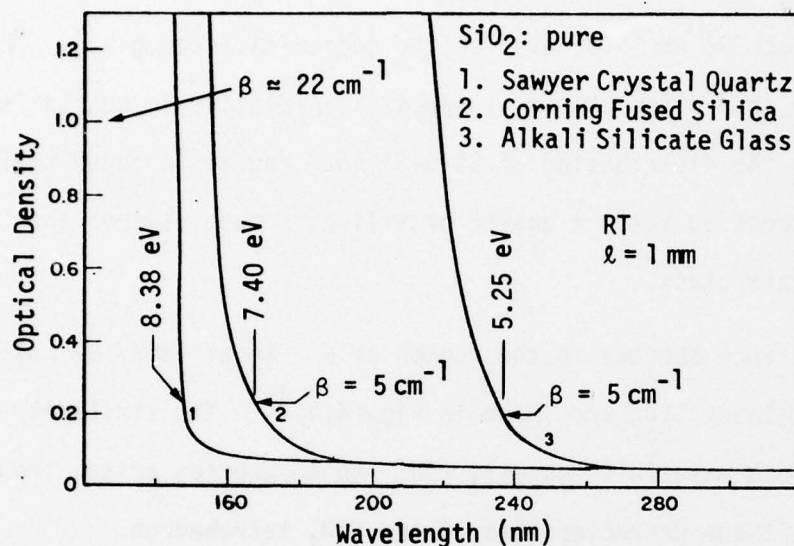
Fig. 4.3.   Ultraviolet absorption edges of high-purity
(1) crystalline quartz, (2) fused silica, and (3) NRL
2 SiO$_2$ - 1 Na$_2$O glass.   Note the narrowing of the band
gap and the decrease in the steepness of the absorption
edge in going from quartz to silica to sodium silicate
glass.   [G. H. Sigel, Jr., J. Non-Crystalline Solids,
13, 372 (1973/74).]
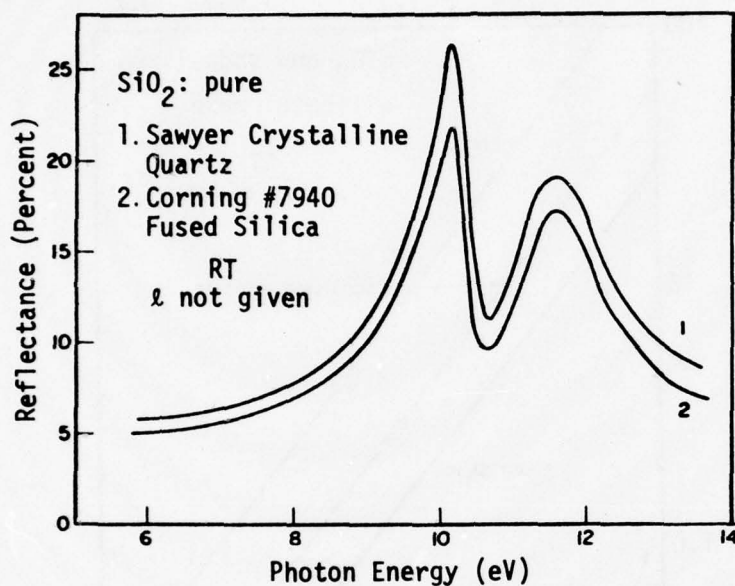
Fig. 4.4. Reflectance spectra of high-purity (1) crystalline quartz and (2) of fused silica showing the lowest energy peaks at 10.2 eV and 11.5 eV above the absorption edge. Additional peaks were observed at higher energies. [G. H. Sigel, Jr., J. Non-Crystalline Solids, 13, 372 (1973/74).]

131
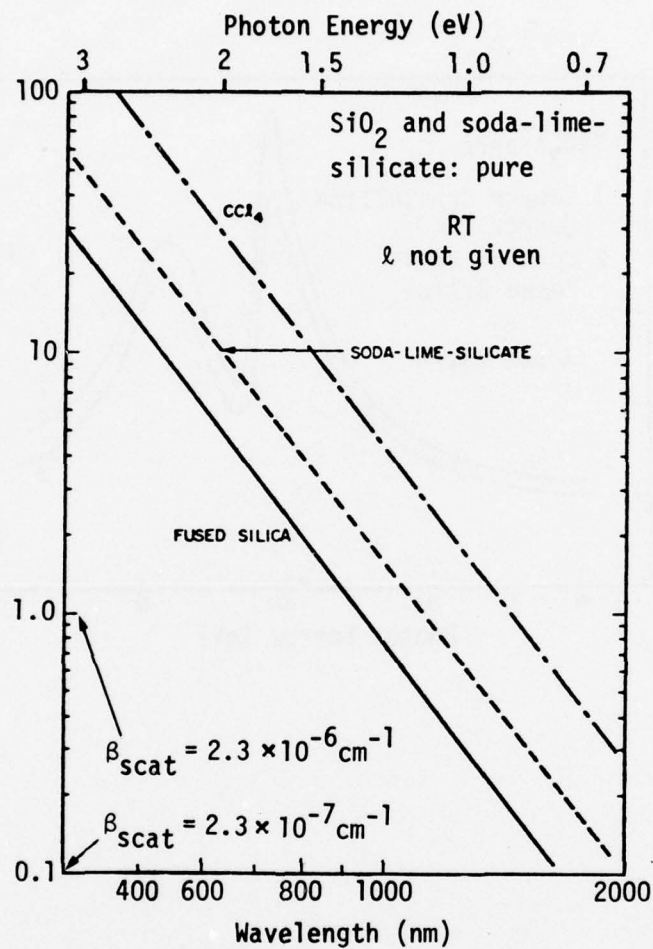
Fig. 4.5. Intrinsic scattering loss of fused silica, soda-lime-silicate, and for comparison, the liquid CCℓ_4. [D. A. Pinnow, T. C. Rich, F. W. Ostermayer, Jr., and M. DiDomenico, Jr., Appl. Phys. Lett. 22, 527 (1973).]
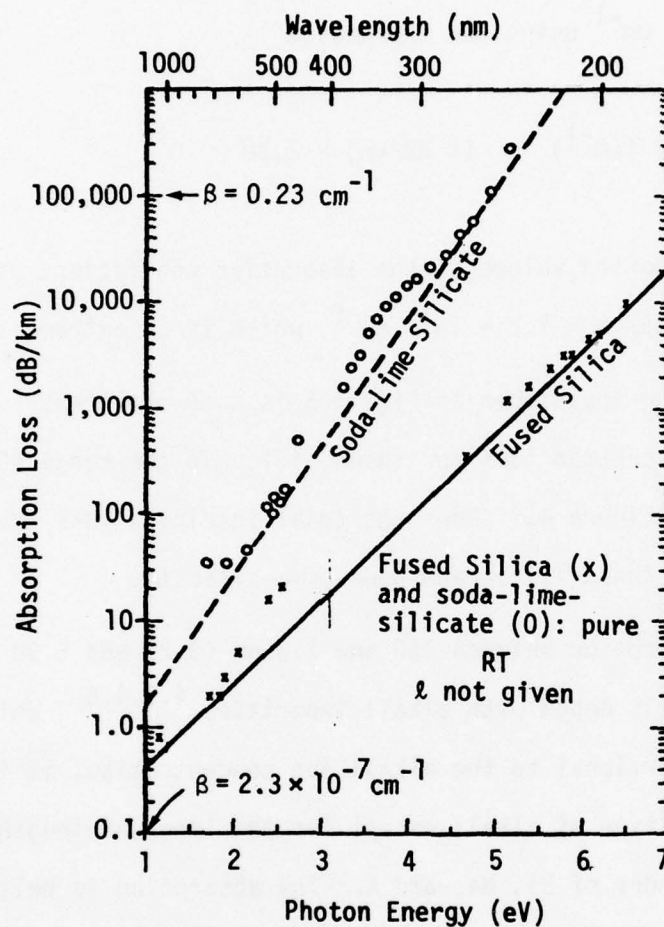
Fig. 4.6.   Intrinsic absorption loss for fused silica and
soda-lime-silicate.   These curves represent lower bounds
for all experimental absorption data.   Shown are some of
the experimental data points used to develop these curves.
The rather broad gap in data for fused silica in the range
of 2.5—4.5 eV is due to the limitations in sensitivity and
wavelength of the measurement techniques.   [D. A. Pinnow,
T. C. Rich, F. W. Ostermayer, Jr., and M. DiDomenico, Jr.,
Appl. Phys. Lett. 22, 527 (1973).]

The absorption loss (X) in dB/km can be converted into an absorption coefficient (β) in cm^{-1} using the expression

$$\beta \ (cm^{-1}) \ = \ (X \ dB/km) \times 2.30 \times 10^{-6}$$

Notice that the reported values of the absorption coefficient in Fig. 4.6 are as low as 0.8 dB/km $\simeq$ 1.8×10^{-6} cm^{-1}, which is an extremely low value.

The scattering loss shown in Fig. 4.5 is somewhat greater (from 20 to 100 %) than the absorption loss for fused silica in the range 400 to 1000 nm (3.1 to 1.24 eV). Figure 4.7 shows the total intrinsic loss from scattering and absorption for fused silica and soda-lime-silicate.

A strong absorption between 150 and 210 nm (8.27 and 5.90 eV) is observed when silica is doped with alkali impurities.[4.3,4.6] While this absorption is proportional to the alkali ion concentration, it is relatively independent of the type of alkali except for the long wavelength tail, which increases in the order of Li, Na, and K. The absorption is believed to be associated with non-bridging oxygens because it decreases when an aluminum addition is made to alkali-doped silica, as shown in Fig. 4.8. Sigel[4.3] reports that the substitutional aluminum alone does not produce any ultraviolet absorption in silica in amounts up to 0.5 percent.

Reflectance spectra of two silicate glasses of high alkali content are shown in Fig. 4.9.[4.3] The energies of the reflectance peaks in these and some other silicate glasses and in pure SiO_2 are listed in Table 4.1.[4.3] In the spectral range 7 - 15 eV (177 - 83 nm), the reflectance peaks in these systems are seen to occur at 8.5, 9.3, 10.2, and 11.5 eV. The 11.5 eV peak is believed to be associated with a band-to-band transition
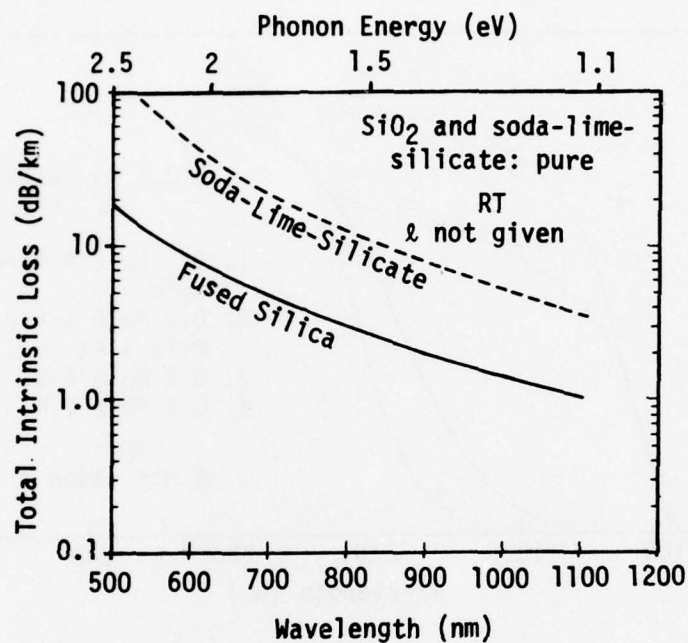
Fig. 4.7. Total intrinsic loss, which is the sum of the absorption and scattering losses, in fused silica and soda-lime-silicate. [D. A. Pinnow, T. C. Rich, F. W. Ostermayer, Jr., and M. DiDomenico, Jr., Appl. Phys. Lett. 22, 527 (1973).]
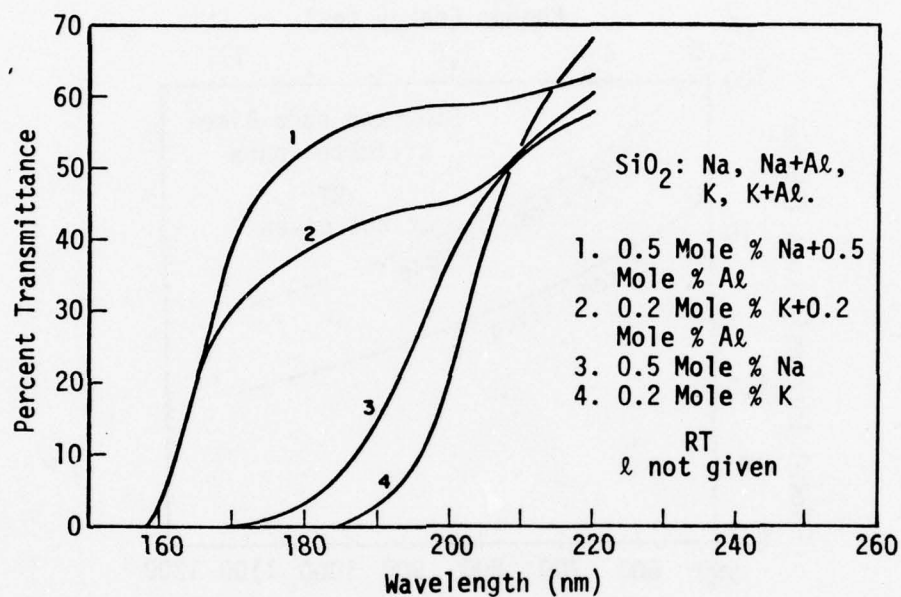
Fig. 4.8. Effect of aluminum addition on the ultraviolet transmittance of alkali-doped SiO$_2$. Samples co-doped with aluminum and alkali showed weaker absorption in the 200–300 nm region, probably because of the reduction of non-bridging oxygens by aluminum-alkali pairing in the network. [G. H. Sigel, Jr., J. Non-Crystalline Solids 13, 372 (1973/74).]
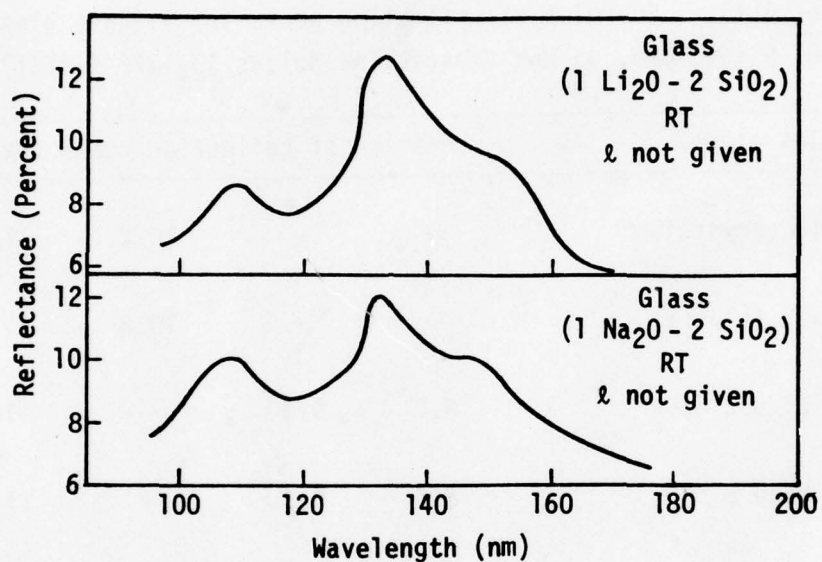
Fig. 4.9.   Reflectance spectra of two binary silicate glasses.   Note the similarity of the spectra regardless of the alkali type, as well as tailing of the low energy band. [G. H. Sigel, Jr.,   J. Non-Crystalline Solids 13, 372 (1973/74).]

Table 4.1.   Energies of reflection peaks in silicate glasses.
[G. H. Sigel, Jr., J. Non-Crystalline Solids 13, 372 (1973/74).]

Glass type	Location of reflection peaks (eV)			
SiO_2(crystal)	–	–	10.2	11.5
SiO_2 (glassy)	–	–	10.2	11.5
1 Li_2O–2 SiO_2	8.5	9.3	–	11.5
1 Na_2O–2 SiO_2	8.5	9.3	–	11.5
1 Na_2O–3 SiO_2	8.5	9.3	–	11.5
1 Na_2O–6 SiO_2	–	9.0[a]	–	11.5
1 Na_2O–1 CaO–5 SiO_2	8.5	9.3	–	11.5
1 Na_2O–1 Al_2O–3 SiO_2	8.5	–	10.2	11.5

[a] This broad peak appears to result from contributions from 8.5 and 9.3 eV peaks.

138

characteristic of the SiO_4 tetrahedron because it appears in all silicate glasses irrespective of composition. The lowest energy peak at 8.5 eV in alkali-silicate glasses has been assigned to non-bridging oxygens because it occurs at the same position irrespective of the alkali type. The appearance of this peak in an alkali-silicate glass apparently shifts its absorption edge to lower energy relative to that of SiO_2 (Fig. 4.3).[4.3]

Figure 4.10 shows the transmittance spectra near the ultraviolet cut-off edge of a number of commercial (Corning and Amersil) glasses.[4.7]

Optical absorption spectra of several high-purity silicate glasses are shown in Fig. 4.11.[4.3] The approximate values of absorption coefficient (β) shown in Fig. 4.11 were obtained by subtracting the measured optical density at 280 nm, 0.05, from the optical density measured at shorter wavelengths. For example, a measured optical density of 0.6 for a 0.1 cm thick sample corresponds to $\beta = 2.30 \times 10 \times (0.6 - 0.05) = 12.7$ cm^{-1}.

3.   <u>Impurity absorption in silicate glasses</u>. The presence of transition and rare-earth metals in a silicate glass can produce charge-transfer absorptions in the ultraviolet region which are so strong that a few parts per million of impurity can be detected in a 2 mm thick sample. In a specimen of conventional thickness (1 - 10 mm), the presence of these impurities results in an edge shift. Fig. 4.12 illustrates the effect of Fe^{3+} impurity on the ultraviolet transmission of 3 SiO_2 - 1 Na_2O glass.[4.3]

The valence state, and hence the optical absorption, of a transition-metal ion depends on whether the glass is melted in an oxidizing or reducing atmosphere. The presence of Fe^{3+} in high-purity silicate glasses melted in an oxidizing atmosphere appears to be a serious problem. By selecting

139
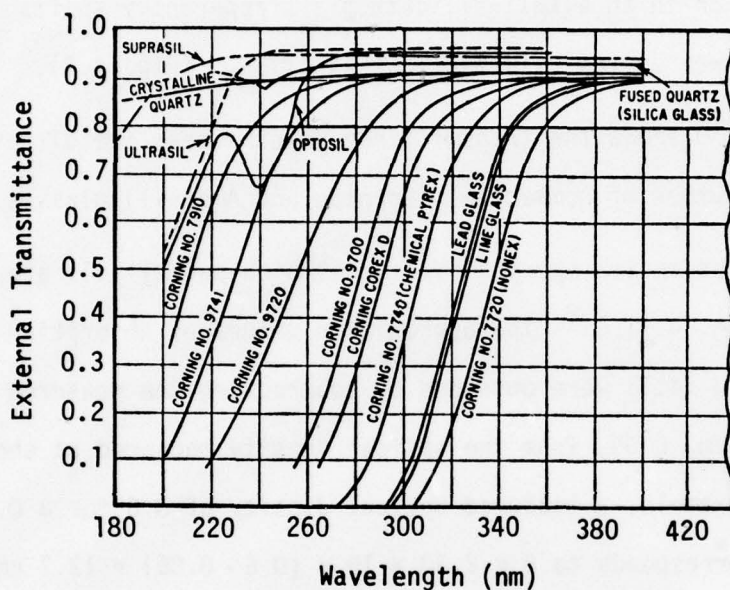
Fig. 4.10.   Transmittance spectra, showing the onset of
optical absorption, of several Corning and Amersil glasses.
[American Institute of Physics Handbook, Third Edition,
McGraw-Hill, New York, 1962, p. 6-94.]
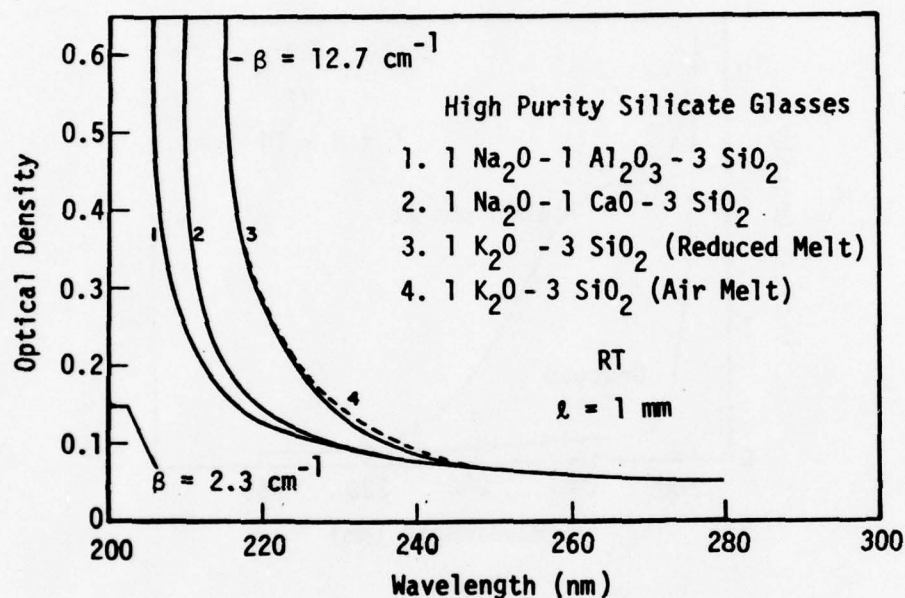
Fig. 4.11. Optical absorption edges of several typical high-purity silicate glasses. The slight difference between the air- and reduced-melted potassium silicate glass absorptions is due to the presence of about 1 ppm of iron impurity. [G. E. Sigel, Jr., J. Non-Crystalline Solids 13, 372 (1973/74).]
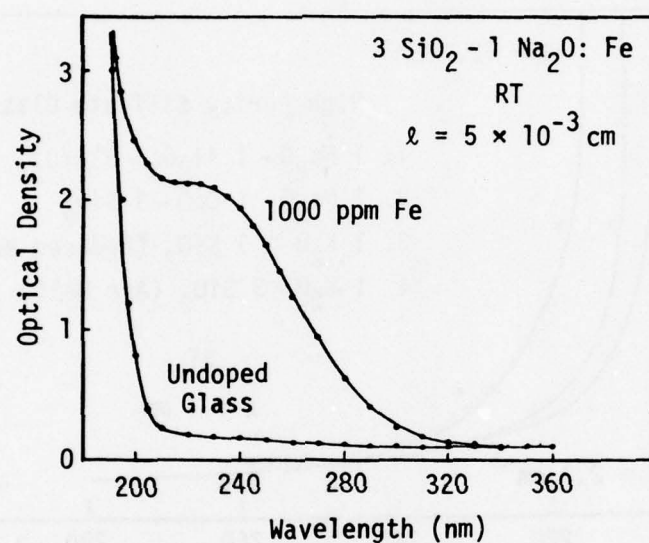
Fig. 4.12.   Optical absorption spectra of undoped and
iron-doped 3 SiO$_2$ - 1 Na$_2$O glass melted in an oxidizing
atmosphere.   [G. H. Sigel, Jr.,   J. Non-Crystalline
Solids 13, 372 (1973/74).]

high-purity starting materials and by taking proper precautions during preparations, Sigel[4.3] was able to reduce the level of iron contamination in silicate glasses to a very low value (less than 0.5 ppm in the case of 1 Na_2O - 3 SiO_2 glass). For such pure glasses, the ultraviolet absorptions of the air-melted and reduced-melted glasses were nearly the same (Fig. 4.11).

Optical absorption spectra of 1 Na_2O - 3 SiO_2 glass containing varying concentrations of copper ions and melted in either a reducing (CO - CO_2) or an oxidizing (air) atmosphere are shown in Fig. 4.13 and Fig. 4.14, respectively.[4.8] The absorption band seen near 235 nm (5.28 eV) in the glass sample, melted in a reducing atmosphere and containing 100 ppm of copper (Fig. 4.13), is believed to be due to Cu^{2+} ions since, for a given copper concentration, the band is more intense in the sample melted in the oxidizing atmosphere (Fig. 4.14).

Sigel[4.3] found that at a few ppm concentration levels, Fe^{2+} or Fe^{3+} in silicate glasses absorbs more strongly than any of the following impurities: aluminum, copper, platinum, titanium, calcium, magnesium, cerium, gallium, indium, thallium, and water vapor. Titanium at a concentration of 25 −50 ppm gave rise to an absorption band near 200 nm (6.20 eV), while Ca and Mg in large quantities did not show any absorptions at energies below that of the alkali absorption. Thus, for equivalent alkali content, the absorption edges of an alkali silicate glass and of the alkali-alkaline earth silicate glass are nearly at the same position.

4. <u>Optical absorption in irradiated SiO_2</u>. During exposure to ionizing radiation, a large number of electrons and holes are generated within a material. Most of these electrons and holes recombine within a
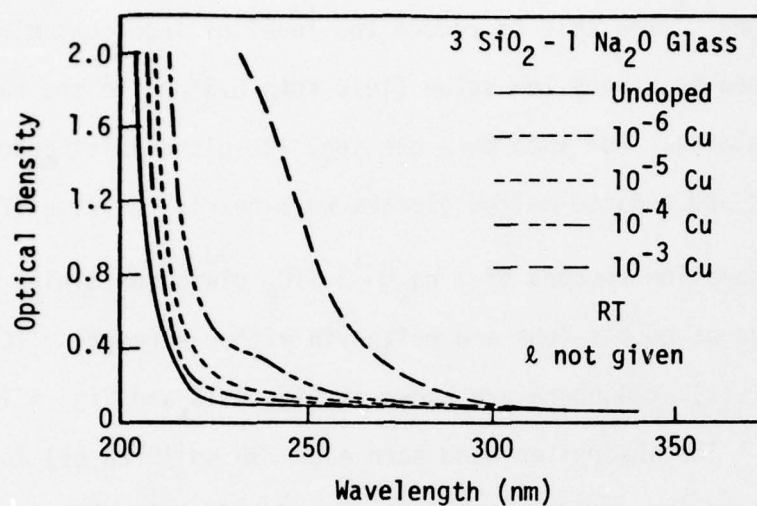
Fig. 4.13. Absorption spectra of copper-doped glasses
melted in a reducing atmosphere.   [R. J. Ginther and
R. D. Kirk, J. Non-Crystalline Solids 6, 89 (1971).]
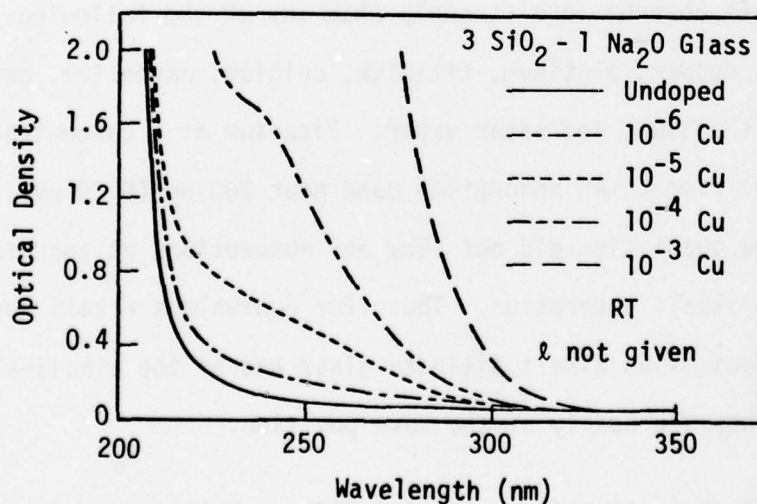
Fig. 4.14. Absorption spectra of copper-doped glasses
melted in air. [R. J. Ginther and R. D. Kirk, J. Non-
Crystalline Solids 6, 89 (1971).]

short period of time; however, some may become trapped at impurities and lattice defects present in the material, giving rise to observed coloration.

SiO_2 can be made with very low concentrations of metallic impurities. Such material is highly resistant to coloration and doses of 10^7 R or more are required to produce appreciable coloration. This level of exposure is approximately two orders of magnitude more than that required for comparable coloration in less pure materials.[4.2]

In a γ-irradiated sample of pure silica, Levy[4.9] was able to resolve the observed absorption in the range 200 - 350 nm (7.2 - 3.54 eV) into four Gaussian components with peaks at 282 nm (4.4 eV), 248 nm (5.0 eV), 230 nm (5.4 eV), and 212 nm (5.8 eV), as shown in Fig. 4.15. (This figure is from Lell, et al.,[4.9a] which is a simplified version of a similar figure by Levy.[4.9])

The bands near 212 nm (5.8 eV) and 230 nm (5.3 eV) are also observed in irradiated synthetic quartz. Weeks and Nelson[4.10] have shown that these absorptions are due to the same types of centers in both quartz and silica. These centers have been associated with trapped electrons, and for this reason they are referred to as E'-centers; E_1' for the center with absorption at 212 nm (5.8 eV) and E_2' for the center with absorption at 230 nm (5.3 eV).[4.11,4.12] A proposed model for the E_2'-center is shown in Fig. 4.16,[4.2] where the rectangle around a complete molecular unit signifies an SiO_2 vacancy.

The absorption band near 212 nm (5.8 ev) is also referred to as the C-band. Nelson and Crawford,[4.13] observing that the band is formed more readily in fused silica than in quartz, have suggested that the 212 nm (5.8 eV) band in glassy silica is formed by simple ionization of the Si-O bond with consequent charge delocalization on the silicon and oxygen.
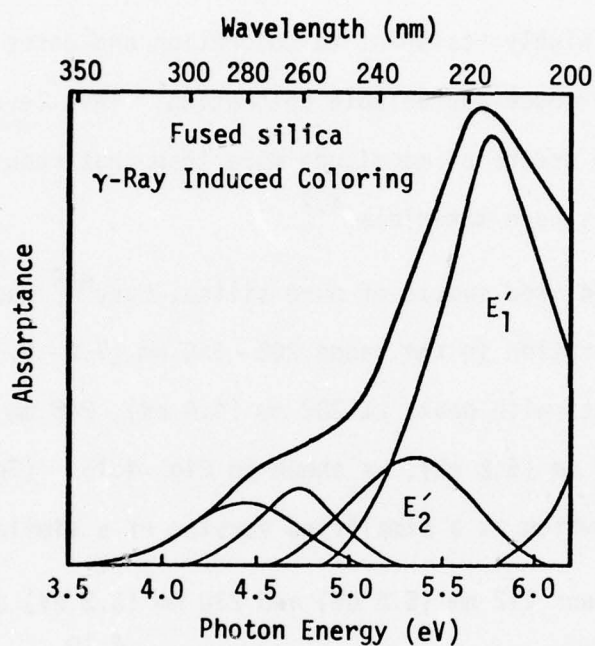
Fig. 4.15. Absorption spectrum of irradiated fused silica
resolved into individual bands.   [E. Lell, N. J. Kreidl,
and J. R. Hansler, in Progress in Ceramic Science, Vol. 4,
J. E. Burke, ed., Pergamon Press, New York, 1966, pp. 1-94;
the data from P. W. Levy, J. Phys. Chem. Solids 13, 287
(1960).]
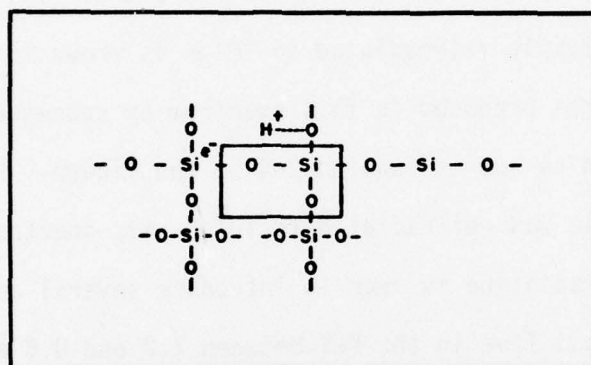
Fig. 4.16. Model of the E$_2'$ center. [E. Lell, N. J. Kreidl, and J. R. Hansler, in Progress in Ceramic Sicence, Vol. 4, J. E. Burke, ed., Pergamon Press, New York, 1966, pp. 1-94.]

Absorption spectra of pure silica γ-irradiated to various doses are shown in Fig. 4.17.[4.6]   Note the radiation bleaching, that is, a decrease in absorption with increasing dose, for the absorption band near 4.0 eV (310 nm), and the influence of thermal history on the colorability of fused silica.

The absorption spectrum in the range 1 to 8.5 eV (1240 to 146 nm) of a synthetic quartz sample γ-irradiated to 10^9 R is shown in Fig. 4.18, curve 1.[4.14]   Changes produced in this spectrum by subsequent thermal treatments are shown by curves labeled 2-4 in the figure. Following thermal bleaching, the sample was reirradiated to 10^9 R: its spectrum is labeled 5 in Fig. 4.18. γ-irradiation is seen to introduce several absorption bands in α-quartz; at least five in the VUV between 7.2 and 8.6 eV (172 - 144 nm), and at least three in the visible and UV with peaks at 2.5 eV (496 nm), $\sim$ 3.5 eV (354 nm), and 5.4 eV (230 nm).

The effect of electron irradiation on the transmittance of high-purity (Dynasil optical grade) fused silica is illustrated in Fig. 4.19.[4.15] The presence of the C-band near 215 nm (5.8 eV) is apparent in the irradiated sample. Heath and Sacher[4.15] indicate that another band, referred to as the E band, with its maximum lying between 160 and 167 nm (7.75 and 7.42 eV), is also present in the irradiated sample.

Transmittance spectra of electron-irradiated, sapphire- (Aℓ_2O$_3$-) shielded glasses are shown in Figs. 4.20 - 4.23.[4.15] Figs. 4.20 and 4.21 demonstrate that the sapphire shield can be used successfully to protect high-purity (Corning 7940 and Dynasil 1850A) fused silica against coloration from electron irradiation.
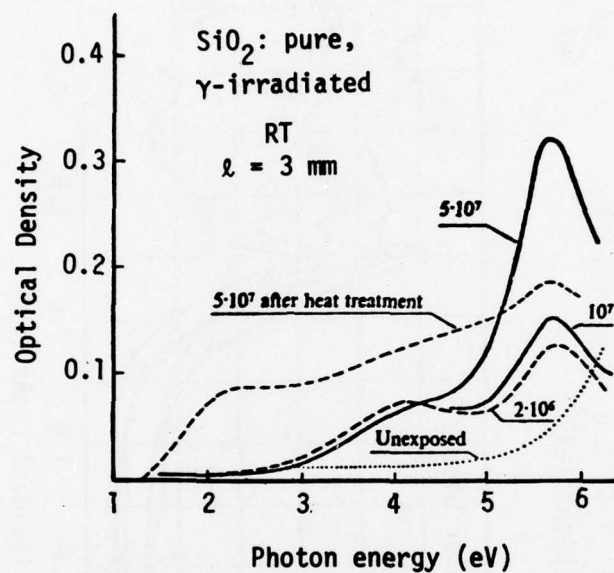
Fig. 4.17. Absorption spectra of undoped fused silica unexposed and exposed to various doses, and exposed to 5×10^5 rad after heat treatment (1 h at 900 C in air). [E. Lell, Phys. Chem. Glasses $\underline{3}$, 84 (1962).]
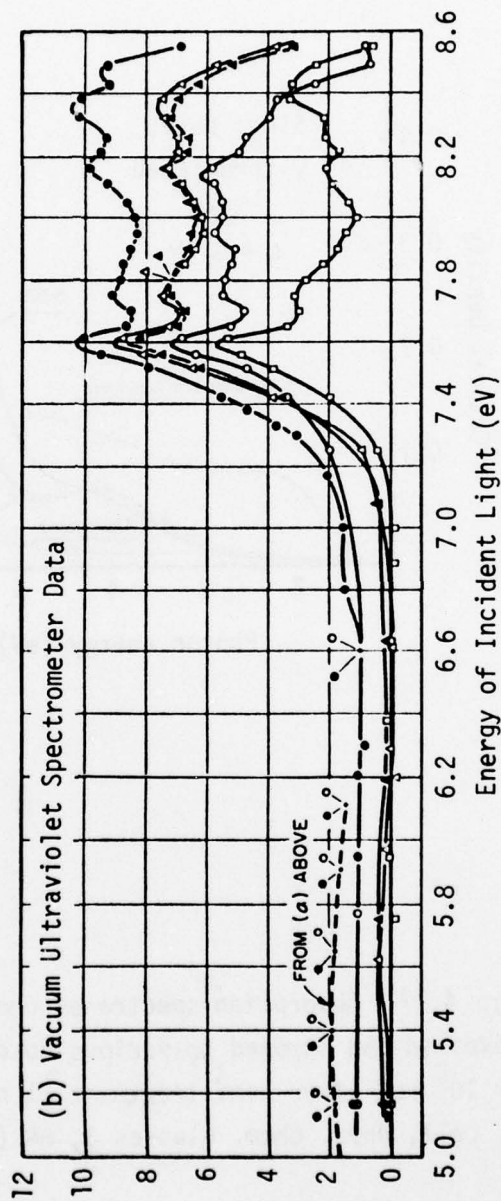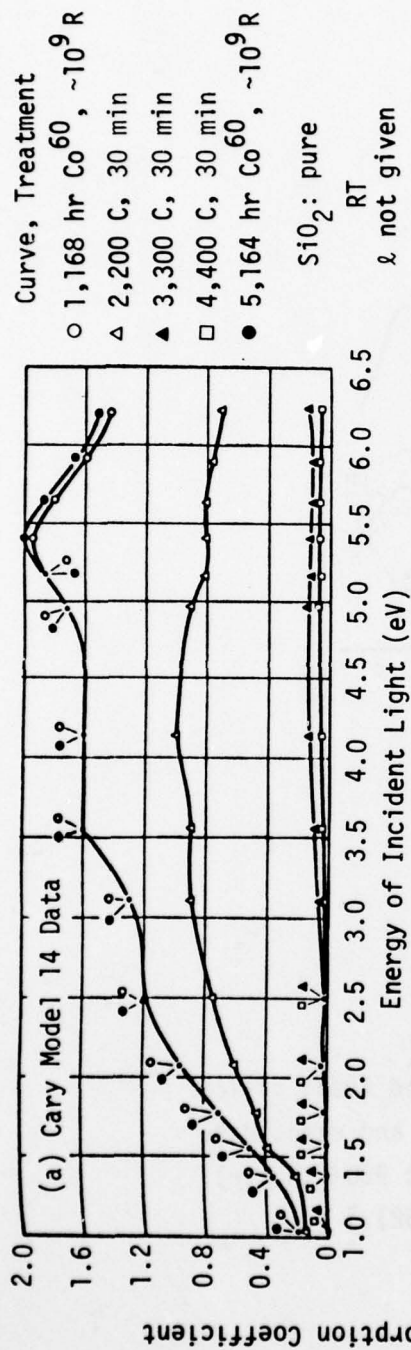
Fig. 4.18. Optical absorption of α-quartz crystal as a function of irradiation and thermal treatment. The c axis of the crystal was parallel to the direction of light propagation; $\alpha_{initial}$ is the absorption of the as-received crystal. [R. A. Weeks, J. Am. Ceram. Soc. 53, 176 (1970).]
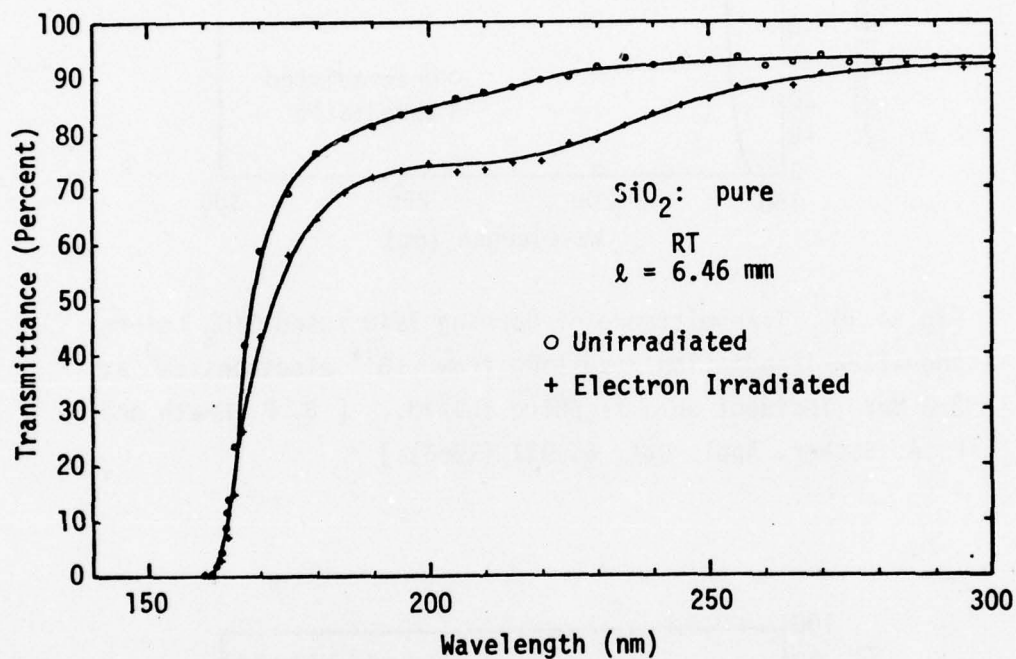
Fig. 4.19.   Transmittance of fused SiO$_2$ before and after
irradiation by 10^{11} electrons/cm^2 at 1.0 MeV and at 2.0 MeV.
[D. F. Heath and P. A. Sacher, Appl. Opt. <u>5</u>, 937 (1966).]
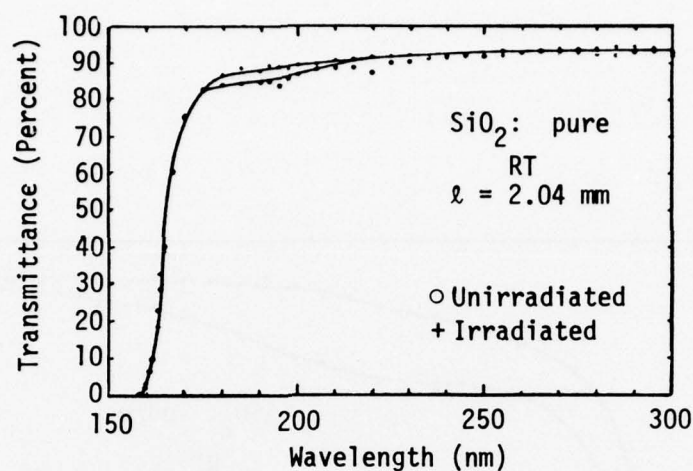
Fig. 4.20. Transmittance of Corning 7940 fused SiO$_2$ before and after irradiation resulting from 10^{14} electrons/cm^2 at 2.0 MeV incident on a sapphire shield.   [D. F. Heath and P. A. Sacher, Appl. Opt. 5, 937 (1966).]
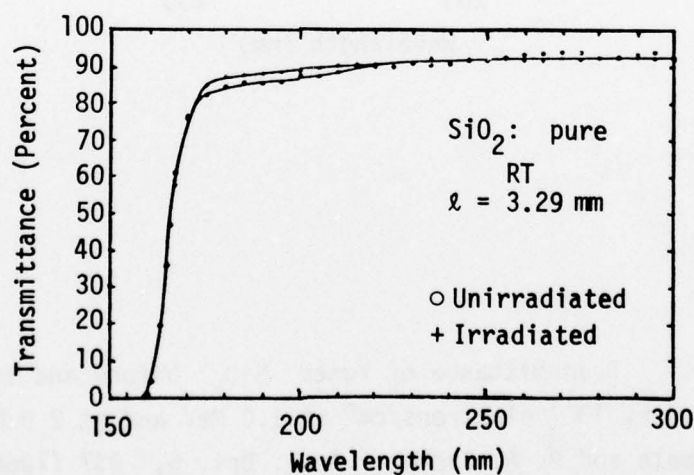
Fig. 4.21. Transmittance of Dynasil 1850A fused SiO$_2$ before and after irradiation resulting from 10^{14} electrons/cm^2 at 2.0 MeV incident on a sapphire shield.   [D. F. Heath and P. A. Sacher, Appl. Opt. 5, 937 (1966).]
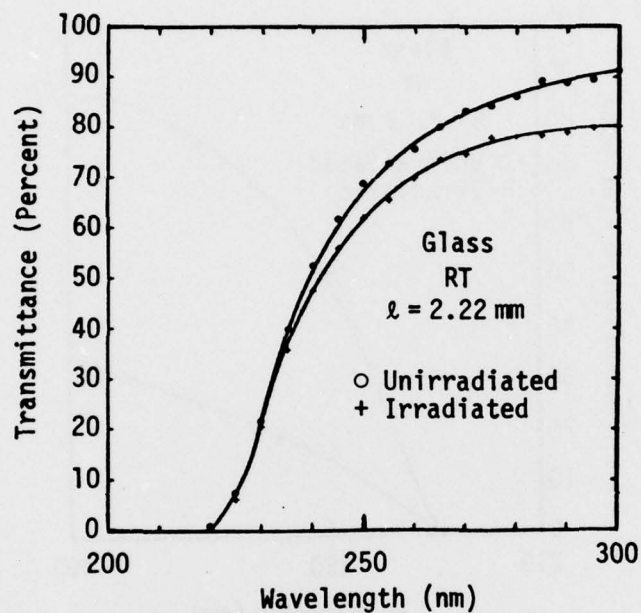
Fig. 4.22. Transmittance of Corning 9-54 (Vycor) before and after irradiation resulting from 10^{14} electrons/cm^2 at 2.0 MeV incident on a sapphire shield.   [D. F. Heath and P. A. Sacher, Appl. Opt. 5, 937 (1966).]
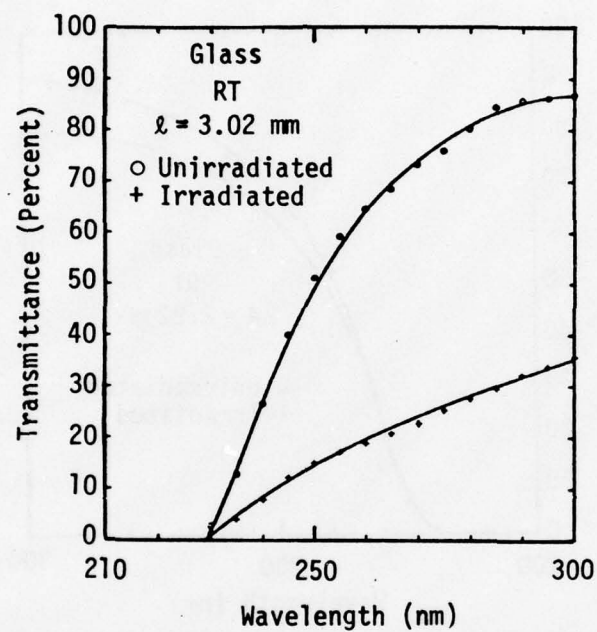
Fig. 4.23. Transmittance of Corning 7-54 before and after irradiation resulting from 10^{14} electrons/cm^2 at 2.0 MeV incident on a sapphire shield.   [D. F. Heath and P. A. Sacher, Appl. Opt. 5, 937 (1966).]

5. <u>Aluminum-alkali system</u>. The effects of aluminum and alkali additions on the colorability of fused silica have been studied in detail by Lell[4.6] and, later on, by Sigel,[4.3] who extended absorption measurements in the VUV to 8 eV (155 nm). Some of the following figures have been taken from Lell's paper. In these figures, the concentrations of impurities are given in mol percent added, without correction for vaporization. A significant difference can exist between the impurity concentrations added to, and detected in the fused silica, as indicated by the data in Table 4.2.[4.6]

Optical absorption spectra of irradiated samples of alkali-doped silica are shown in Fig. 4.24.[4.3] Characteristic features of the absorptions are the band at 7.6 eV (163 nm) and the E_1' and E_2' bands which overlap to produce a compound band between 5 and 6 eV (248 and 207 nm). Sigel[4.3] found that the intensity of the E_2' band at 235 nm (5.3 eV) was proportional to alkali concentrations ranging from 0.01 to 0.5 percent. This observation led him to suggest that the E_2' center is more complex than suggested earlier (Fig. 4.16) and that it might involve alkali in addition to non-bridging oxygens and protons. Sigel also suggests that the E_2' center might be a characteristic defect of alkali silicate glass rather than silica.

Since the 7.6 eV (163 nm) band is also observed in high-purity silica, and since its intensity is relatively insensitive to the variations in alkali content, the band is believed to be due to a defect characteristic of the Si-O network.

Absorption spectra of γ-irradiated, alkali-doped fused silica are shown in Fig. 4.25.[4.6] Before irradiation, an absorption band near

Table 4.2. Flame-photometric determination of
alkali in doped silica. [E. Lell, Phys. Chem.
Glasses 3, 84 (1962).]

mol. % added	mol. % detected in fused silica
0.2 Li	0.014 Li
0.2 Li 0.2 Aℓ	0.035 Li
0.2 Li 0.2 Ga	0.03 Li
1.0 Li 1.0 Aℓ	0.7 Li
0.2 Na	0.04 Na
0.2 Na 0.2 Aℓ	0.12 Na
0.5 Na 0.5 Aℓ	0.3 Na
0.5 K	0.08 K
0.2 K 0.2 Aℓ	0.074 K
0.5 K 0.5 Aℓ	0.185 K
Undoped	0.004 Na 0.001 Li

Fig. 4.24.   Optical absorption spectra of X-irradiated (exposure $\simeq 10^6$R), alkali-doped fused silica showing the E$_2'$ and E$_1'$ bands at 5.4 and 5.8 eV and the hole band at 7.6 eV. [G. H. Sigel, Jr., J. Non-Crystalline Solids 13, 372 (1973/74).]

157
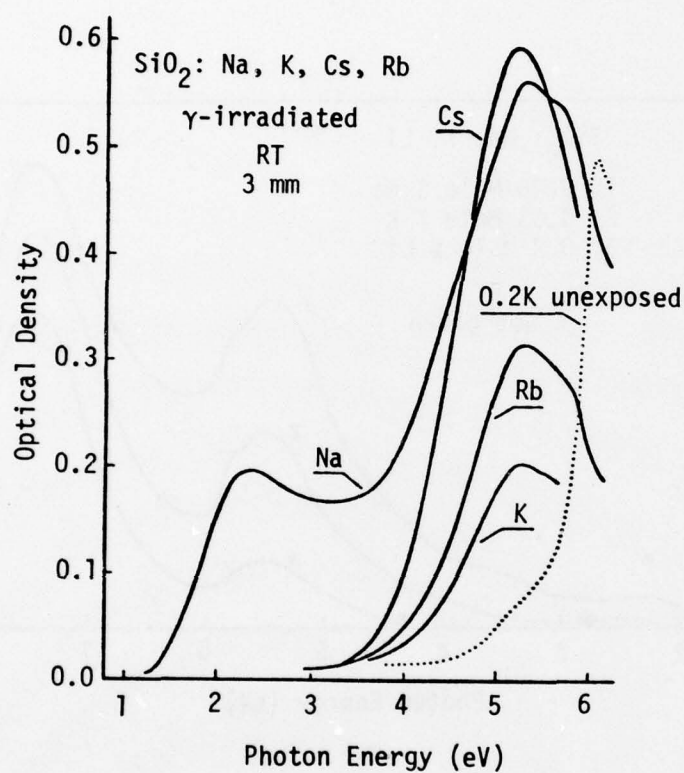
Fig. 4.25. Absorption spectra of alkali-doped fused silica γ-irradiated to 10^7 rad. The dotted line curve is representative for unexposed fused silica doped with alkali. The specimens are doped with 0.2% Na and 0.5% K, Rb, and Cs. [E. Lell, Phys. Chem. Glasses $\underline{3}$, 84 (1962).]

205 nm (6.05 eV) was observed in K-, Rb- or Cs-doped silica, as shown by the dotted curve in Fig. 4.25. In addition to the composite band near 5 eV (248 nm), which was observed in irradiated samples of all alkali-doped silica, a band near 2.3 eV (539 nm) was observed in a sample of Na-doped silica (Fig. 4.25). Lell attributed this band to the 0.01 percent aluminum (impurity) which was detected in this particular sample.

Optical absorption spectra of irradiated fused silica co-doped with aluminum and alkali is seen to be the appearance of several absorption bands between 1 and 5 eV (1240 and 248 nm) upon irradiation. In Fig. 4.26 notice that the peak position of the absorption band near 4.0 eV (310 nm) is dependent on the type of alkali; it shifts to lower energy as the atomic number of alkali increases. This band is believed to be associated with electrons trapped at lattice defects in the material.

The absorption band seen near 2.3 eV (540 nm) in Figs. 4.26 and 4.27 is not readily observed if fused silica is doped only with Aℓ (Fig. 4.28); the simultaneous presence of aluminum and alkali is required for its appearance, while its intensity is determined by that component which is present in lower concentration and by the type of alkali. Electron spin resonance studies have established that the 540 nm (2.3 eV) band arises from holes trapped at imperfections in silica. A similar type of defect gives rise to absorption bands near 460 and 620 nm (2.7 and 2.0 eV) in smokey quartz, and in irradiated samples of natural and synthetic quartz (Fig. 4.29). Sigel[4.3] observed similar absorption bands, at much lower intensity levels, in irradiated high-purity silicate glasses containing less than 1 ppm Aℓ (Fig. 4.30). This observation led him to postulate that the presence of Aℓ in SiO_2 may simply result in an increase in the oscillator strengths of

SiO$_2$: Al + Li, Al + Na, Al + K,
Al + Cs, Al + Rb
γ-irradiated
RT
l = 1 mm
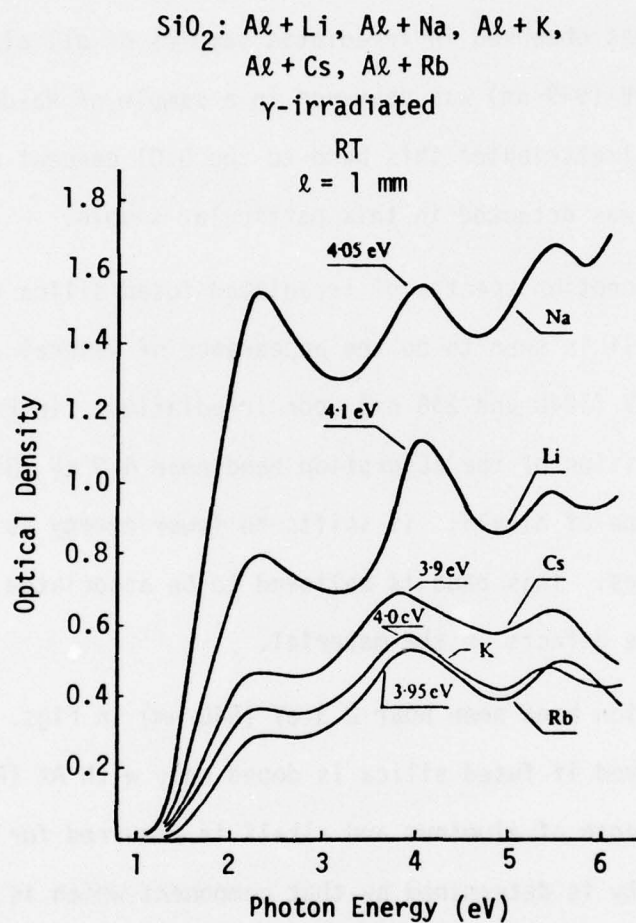
Fig. 4.26.   Absorption spectra of fused silica doped with
0.2% Al and 0.2% of the various alkalis and γ-irradiated
to 10^7 rad.   The position of the band at 4 eV depends on
the type of alkali.   The energy of the absorption maximum
is indicated. [E. Lell, Phys. Chem. Glasses 3, 84 (1962).]

160
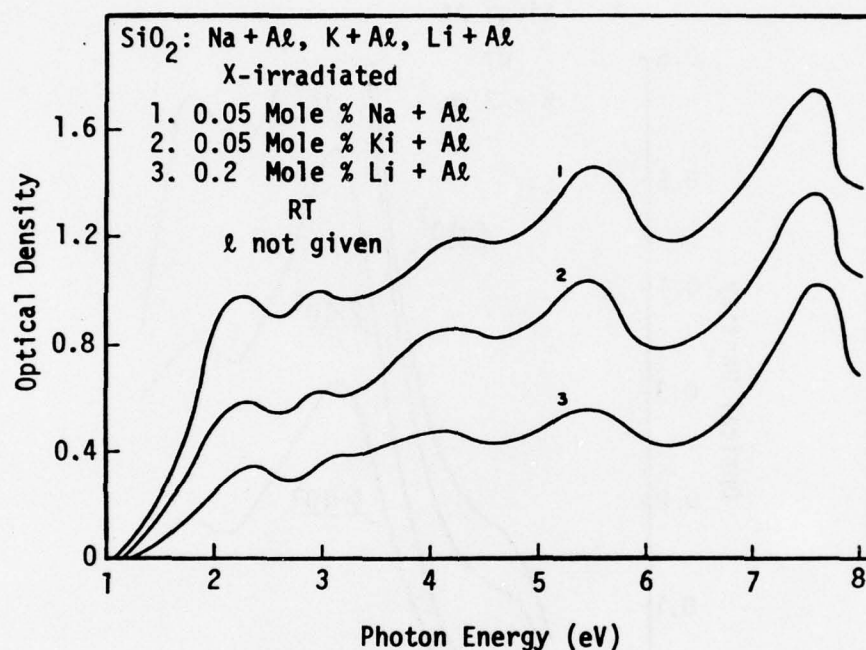
Fig. 4.27. Optical absorption of X-irradiated ($\simeq 10^6$R) fused silica co-doped with aluminum and alkali. The increase in the visible absorption when aluminum is present may arise from an increase in oscillator strength rather than the production of many more defect centers. [G. H. Sigel, Jr., J. Non-Crystalline Solids 13, 372 (1973/74).]

161
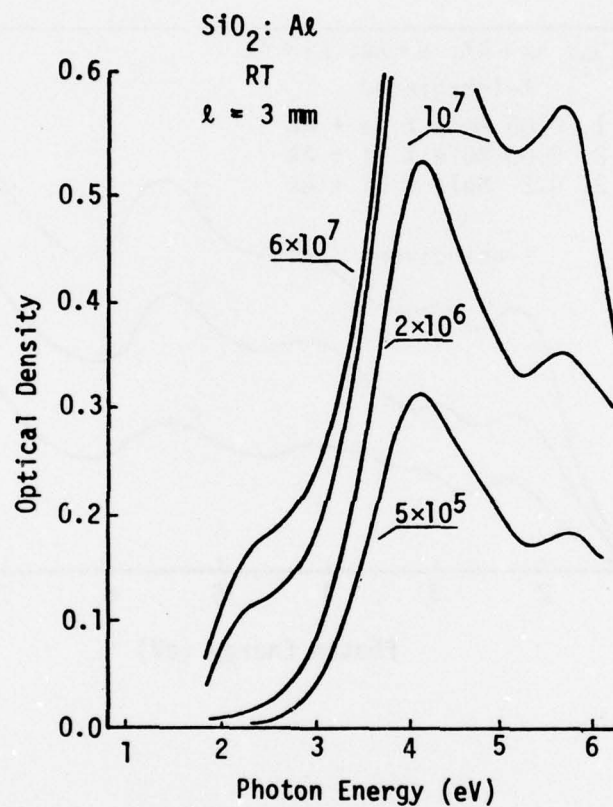
Fig. 4.28. Absorption spectra of fused silica doped with 2.0% Aℓ and γ-irradiated to various doses (rad). [E. Lell, Phys. Chem. Glasses $\underline{3}$, 84 (1962).]
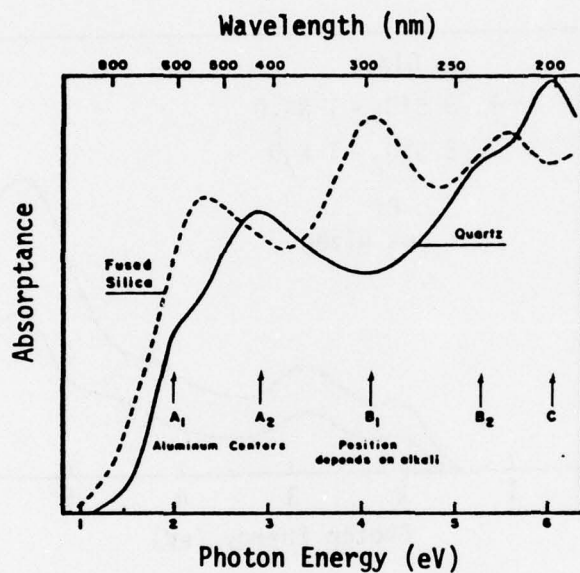
Fig. 4.29. Comparison of irradiated fused silica and irradiated quartz. [E. Lell, N. J. Kreidl, and J. R. Hansler, in Progress in Ceramic Science, Vol. 4, J. E. Burke, ed., Pergamon Press, New York, 1966, pp. 1-93.]
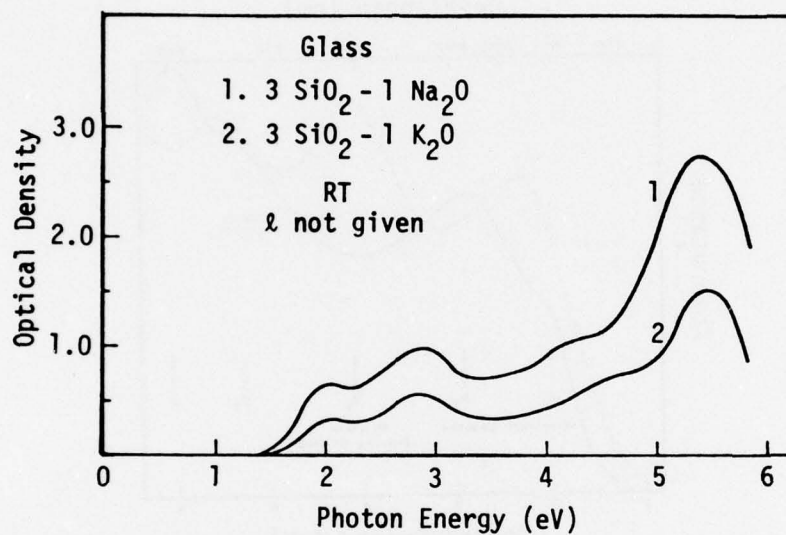
Fig. 4.30.   Optical absorption spectra of two X-irradiated, air-melted, high-purity silicate glasses.   The strong band at 5.4 eV is attributed to E_2' centers which may be a major electron trap in alkali silicate glasses. [G. H. Sigel, Jr., J. Non-Crystalline Solids 13, 372 (1973/74).]

the visible bands and that the basic hole center involves a hole trapped at a non-bridging oxygen which can be bonded to either a silicon or an aluminum.

Optical absorption spectra at various exposure levels are shown in Fig. 4.31 for fused silica doped with 0.2 percent Li and 0.2 percent Aℓ, and in Fig. 4.32 for fused silica doped with 0.2 percent Cs and 0.2 percent Aℓ.[4.6]   Figure 4.33 shows the resolution of the spectrum of fused silica doped with 0.2 percent Li and 0.3 percent Aℓ and γ-irradiated to 2×10^6 rad. The peak positions and the half-widths of resolved Gaussian components are listed on Table 4.3.

6.   <u>Gallium-lithium system</u>. Optical absorption spectra of fused silica doped with various amounts of Ga and Li and γ-irradiated to several exposure levels are shown in Fig. 4.34.[4.6]   The presence of Ga in unexposed silica gives rise to a strong absorption band at 224 nm (5.54 eV), as shown by the dotted curve in Fig. 4.34. In the figure it is seen that the coloration increases with increasing amounts of impurities added, and that at least two bands with peaks near 245 nm (5.05 eV) and 539 nm (2.3 eV) are present in the irradiated samples.

7.   <u>Transient radiation effects in SiO$_2$ and silicate glasses</u>. So far, only a few studies on the transient radiation effects in SiO$_2$ and silicate glasses have been made and short-lived coloration in both the visible and ultraviolet has been reported.[4.3,4.16,4.17]

In pure SiO$_2$ the only transient coloration observed is in the ultraviolet centered near 215 nm (5.77 eV).[4.3]   Figure 4.35 compares the permanent (solid-line) and transient (points) colorations produced in this material by electron irradiation. The 215 nm (5.77 eV) band is the E_1'
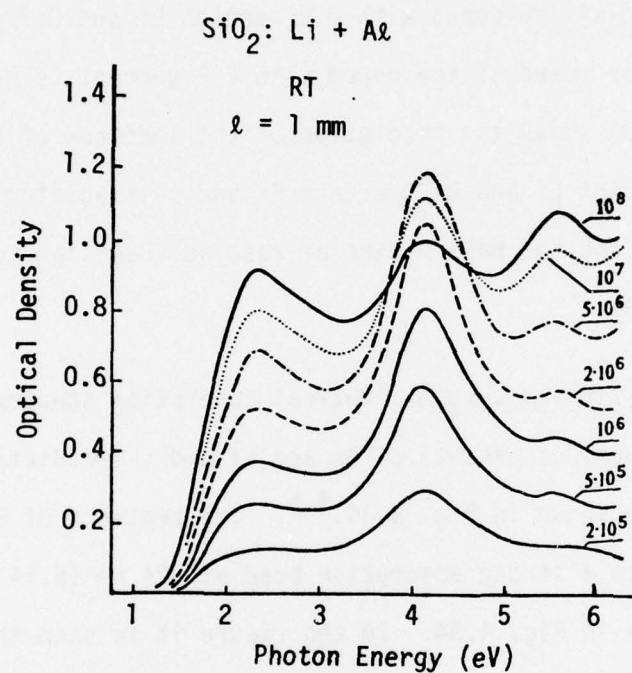
Fig. 4.31. Absorption spectra of fused silica doped
with 0.2% Li and 0.2% Al and γ-irradiated to various
doses (rad).   [E. Lell, Phys. Chem. Glasses $\underline{3}$, 84
(1962).]

166
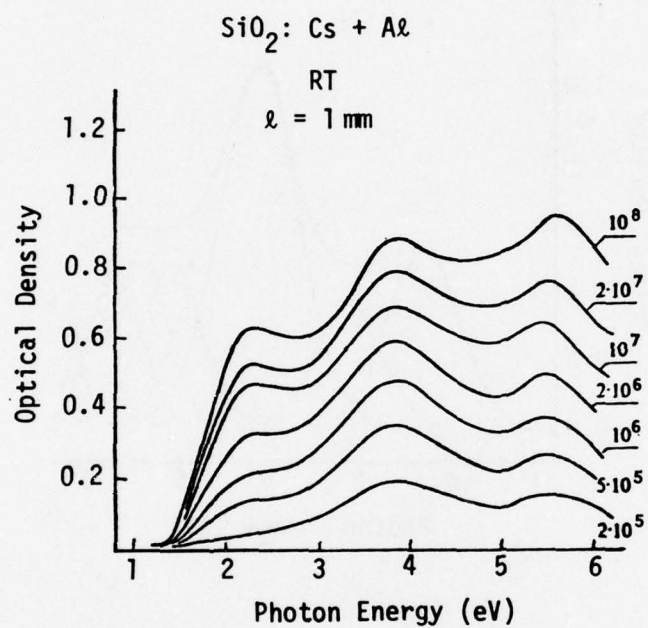
Fig. 4.32. Absorption spectra of fused silica doped with 0.2% Cs and 0.2% Aℓ and γ-irradiated to various doses (rad).   [E. Lell, Phys. Chem. Glasses $\underline{3}$, 84 (1962).]
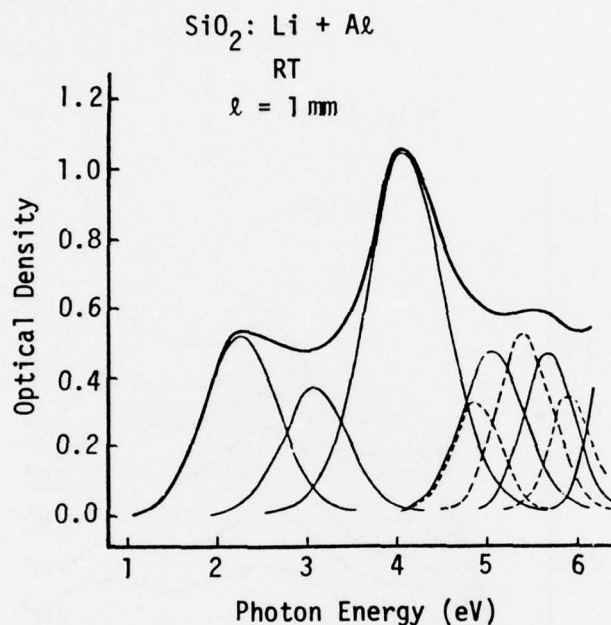
Fig. 4.33. Resolution of an absorption spectrum into individual Gaussian bands. Resolved is the absorption curve for fused silica doped with 0.2% Li and 0.2% Aℓ exposed to 2×10^6 rad. The three bands in broken lines with absorption maxima at 4.88, 5.46, and 5.74 eV are an alternative solution for the two bands with maxima at 5.08 and 5.70 eV. The three remaining bands show maxima at 4.10, 3.08, and 2.25 eV. [E. Lell, Phys. Chem. Glasses $\underline{3}$, 84 (1962).]

Table 4.3.   Absorption maxima and widths of individual absorption bands in irradiated doped fused silica. [E. Lell, Phys. Chem. Glasses $\underline{3}$, 84 (1962).]

	Absorption Maximum (eV)	Wavelength (nm)	Full Width at Half Maximum (eV)
1	2.25	550	0.94
2	3.08	402	0.83
3	4.10	302	1.02
4	5.08	244	0.94
5	5.70	217	0.64
4a	4.88	254	0.96
5a	5.46	227	0.92
6a	5.74	216	0.86

SiO$_2$: Ga, Li

RT

ℓ = 1 mm
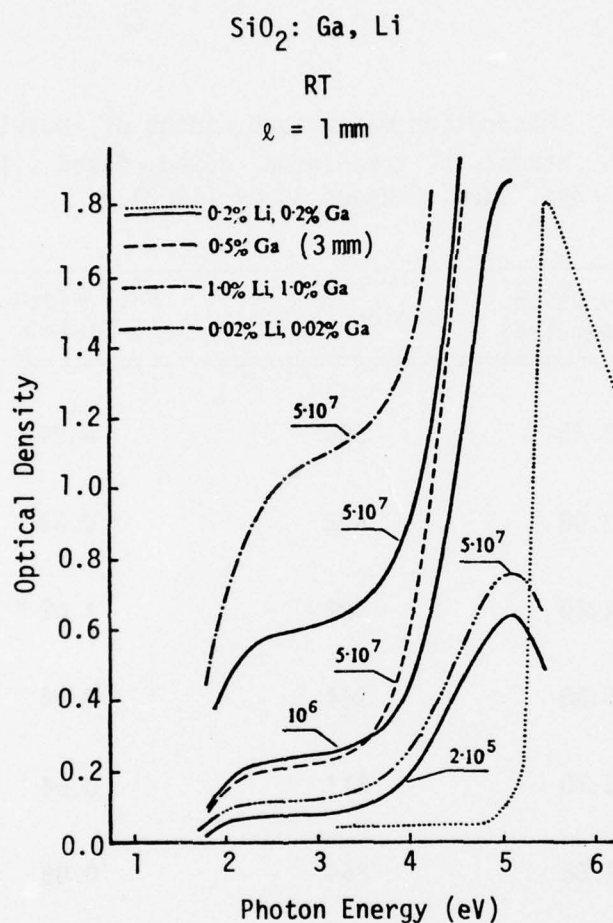
Fig. 4.34. Absorption spectra of fused silica doped with various amounts of Ga and Li and exposed to various doses (rad).   The dotted curve is representative for unexposed Ga-containing fused silica.   [E. Lell, Phys. Chem. Glasses 3, 85 (1962).]
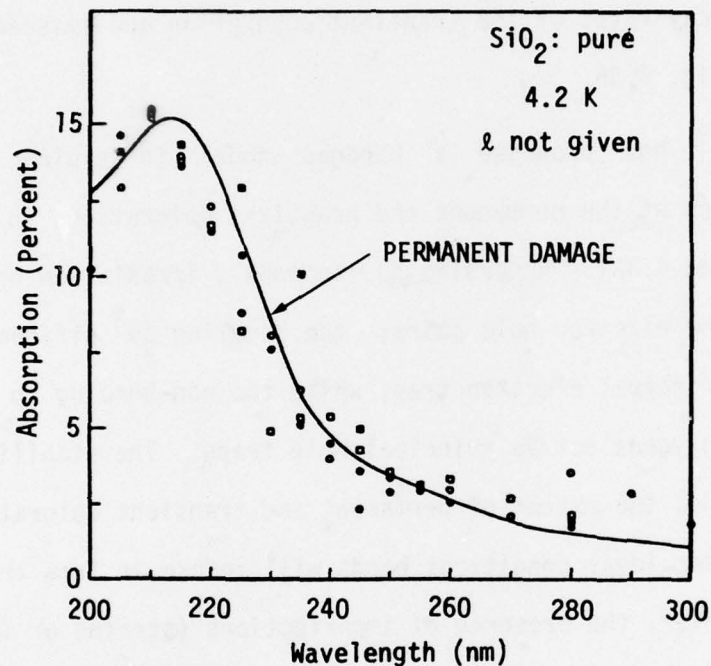
Fig. 4.35. A comparison of the permanent damage (solid line)
observed in Corning 7943 silica (after Arnold and Compton)
with the transient coloration (points) measured immediately
after the electron pulse irradiation.   The band near 215 nm
is the E$_1'$ band. [G. H. Sigel, Jr., J. Non-Crystalline Solids
<u>13</u>, 372 (1973/74).]

171

band, which had been assigned earlier to electrons trapped on dangling silicon orbitals.

The transient UV coloration due to electron-pulse irradiation is accompanied by an intense luminescence centered near 450 nm (2.76 eV). At 4.2 K, the decay rates of the transient absorption and emission are similar, as shown in Fig. 4.36.

Sigel[4.3] has proposed a bandgap model to explain the observed characteristics of the permanent and transient colorations in pure SiO_2 (Figs. 4.37 and 4.38). According to the model, irradiation breaks up Si-O bonds, creating electron-hole pairs; the dangling sp^3 silicon orbital serves as a principal electron trap, while the non-bonding p orbitals of non-bridging oxygens act as principal hole traps. The stability of these traps determines the extent of permanent and transient colorations in the material. Under ideal conditions bonds will reform in less than a few milli-seconds; however, the presence of imperfections (strains or impurities) could prevent bond reformation, giving rise to permanent coloration.

In SiO_2, Sigel postulates the existence of two kinds of hole traps, one of which H_d contributes to the observed emission (Fig. 4.38). The radiative process results when holes are thermally activated out of H_d traps into the valence band for migration to, and eventual recombination at, E′ sites. However, since the observed emission intensity is not proportional to the time derivative of the observed absorption intensity (Fig. 4.36), it is suggested that most of the electrons in E′ sites might annihilate by non-radiative recombination with holes in H_n sites. Since optical excitation at 215 nm produces neither bleaching nor photo current, the excited state E^* of the E′ center is shown below the conduction band edge in Fig. 4.38.
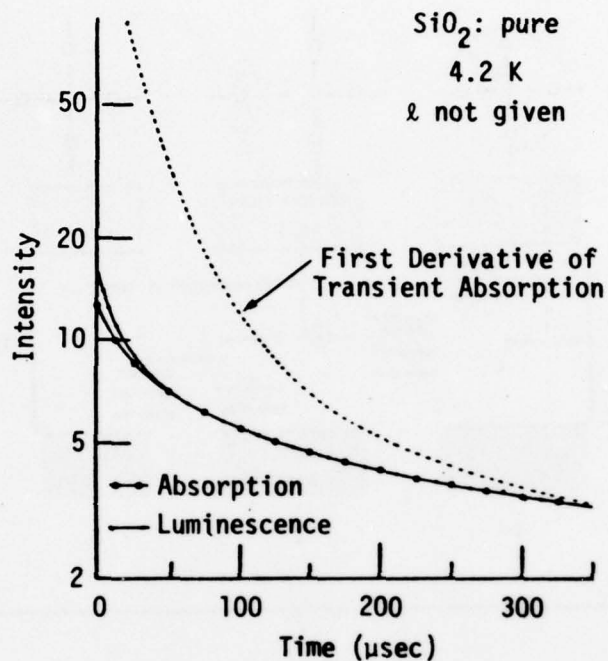
Fig. 4.36.   The decay rate of the transient absorption and emission at 4.2 K.   The luminescence would follow the dotted curve if the annihilation of each absorbing center resulted in radiative emission.   [G. H. Sigel, Jr., J. Non-Crystalline Solids 13, 372 (1973/74).]
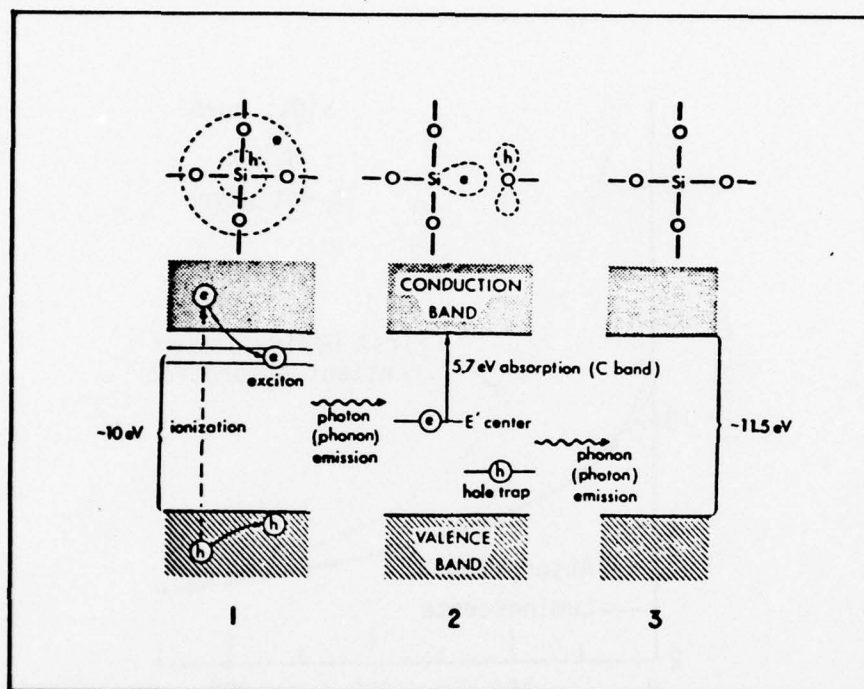
Fig. 4.37. Schematic diagram of postulated steps involved in the formation and annihilation of transient E' center. The impinging radiation can ionize an Si-O band, resulting in the formation of a defect pair which eventually recombine to heal the damage.   [G. H. Sigel, Jr., J. Non-Crystalline Solids 13, 372 (1973/74).

174
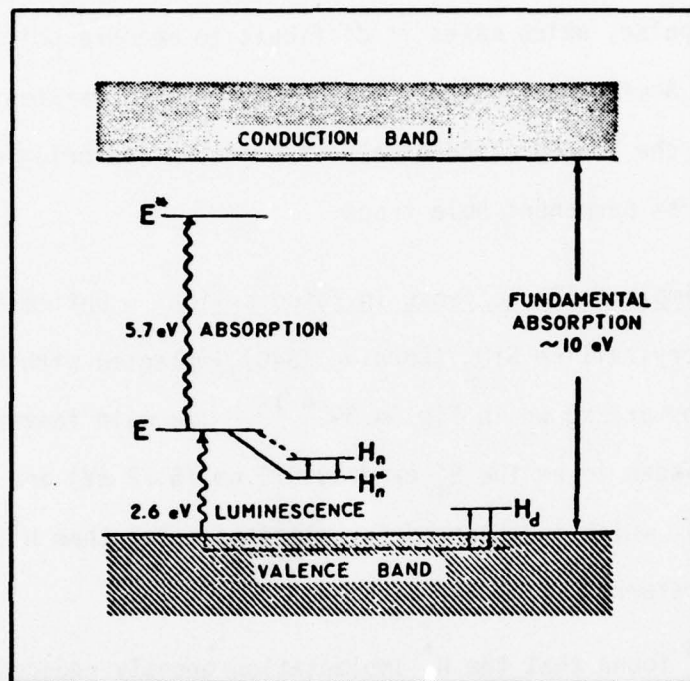
Fig. 4.38. Proposed band-gap model of the transient radiation effects in SiO$_2$, permitting both radiative and non-radiative recombination of holes with E' centers. [G. H. Sigel, Jr., J. Non-Crystalline Solids 13, 372 (1973/74).]

Pulsed electron irradiation of alkali-doped SiO$_2$ and high-purity silicate glasses also produces short-lived coloration. However, contrary to the situation in pure SiO$_2$, silicate glasses show substantial permanent coloration per pulse, which makes it difficult to measure point by point across a band. According to Sigel, this behavior is consistent with the hypothesis that the introduction of alkali produces non-bridging oxygens which can serve as permanent hole traps.

8.   <u>Ion-implantation effects in fused silica.</u> Optical absorption spectra of non-crystalline SiO$_2$ (Corning 7940) implanted with H$^+$, He$^+$, Ar$^+$, Kr$^+$, and Xe$^+$ ions are shown in Fig. 4.39.[4.18] The main features of the absorptions are seen to be the E$_1'$ band at 215 nm (5.77 eV) and a band at 245 nm (5.06 eV), which is observed for all ions other than H$^+$. This 245 nm band is referred to as the B$_2$ band.

Arnold[4.18] found that the H$^+$ implantation greatly reduced the B$_2$-band intensity produced by prior or subsequent implantation of fused silica with heavier ions. The effect of H$^+$ implantation on the absorption spectrum of an Xe$^+$ implanted silica is shown in Fig. 4.40.

In Table 4.4 the total ion energy is partitioned into electronic and nuclear interaction events for a 250 keV accelerating potential. The data in Table 4.4 and the observation that for heavier ions, the intensity of the B$_2$ band increases with increasing ion mass for a given ion fluence led Arnold to suggest that the defect giving rise to this absorption is generated by ion energy going into displacement processes.

In some impure SiO$_2$, a band at 245 nm (5.06 eV) is observed before irradiation or implantation; the band has been assigned to a center

Fig. 4.39. Optical aborption in fused silica (Corning 7940)
implanted with H$^+$, He$^+$, A$^+$, Kr$^+$, and Xe$^+$ ions. The curves
have been displaced vertically for clarity. Relative values
of absorption can be obtained by normalizing all curves to
zero optical density at 350 nm.   [G. W. Arnold, IEEE Trans.
Nucl. Sci. 20, 220 (1973).]
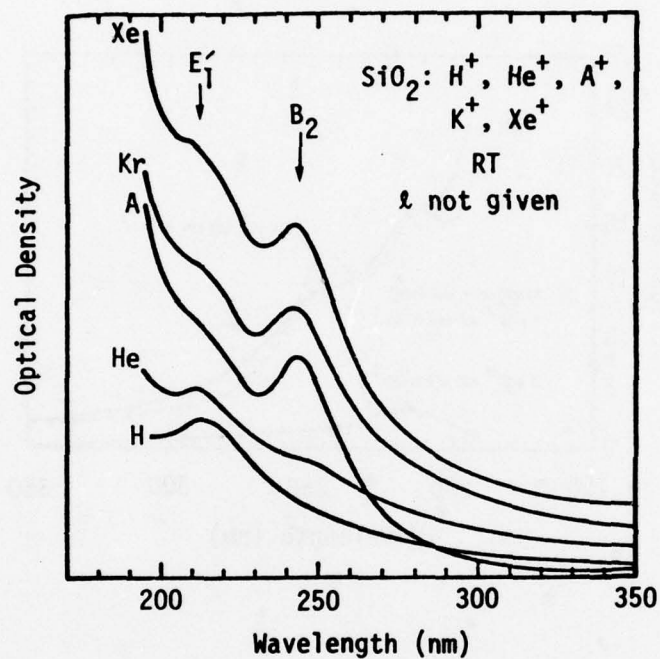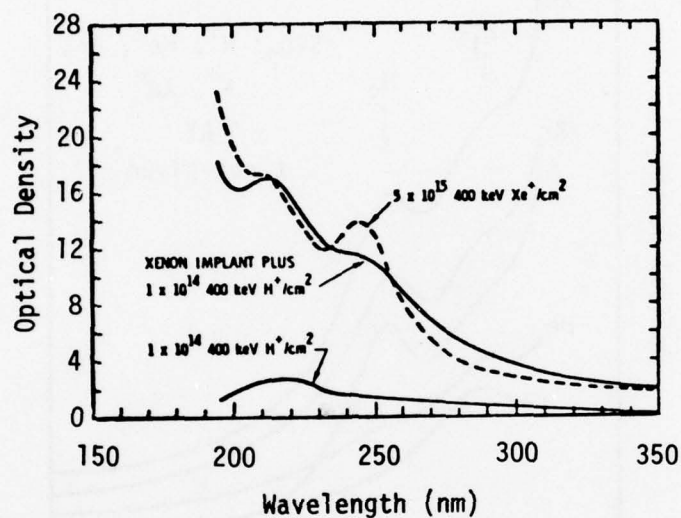
Fig. 4.40. Optical absorption in fused silica (Corning 7940) which was first implanted with 5×10^{15} 400 keV Xe^+ ions/cm^2 and then with 1×10^{14} 400 keV H^+ ions/cm^2. Bottom curve shows absorption in a similar sample implanted with 1×10^{14} 400 keV H^+ ions/cm^2. [G. W. Arnold, IEEE Trans. Nucl. Sci. 20, 220 (1973).]

Table 4.4. Partition of 250 keV accelerating energy
into electronic (ε) and nuclear (ν) interaction pro-
cesses for various ions. [G. W. Arnold, IEEE Trans.
Nucl. Sci. 20, 220 (1973).]

Ion	ν (keV)	ε (keV)
H$^+$	0.6	249.4
He$^+$	6.5	243.5
O$^+$	67.6	182.4
A$^+$	158.4	91.6
Kr$^+$	208.3	41.7
Xe$^+$	221.7	28.3

consisting of a trivalent impurity (e.g., Al^{3+}) substituting for Si^{4+} and an adjacent oxygen vacancy. The identical spectral positions of this band and the implantation-induced B_2 band led Arnold to suggest that the B_2 band is associated with an oxygen vacancy, produced by displacement processes, which has trapped the binding electrons of two adjacent silicon atoms. Proposed models for the centers responsible for the 215 nm (5.77 ev) band, the 245 nm (5.06 eV) impurity band, and the B_2 band are shown in Fig. 4.41.[4.18]

$\equiv Si-O^{\oplus}\ ^{\bullet}Si\equiv$ 215 nm BAND:$C(E_1)$ BAND

$\equiv Si^{\bullet}\ \square\ Al\equiv$ 245 nm IMPURITY BAND

$\equiv Si^{\bullet}\ \square\ ^{\bullet}Si\equiv$ 245 nm DAMAGE BAND:B_2 BAND
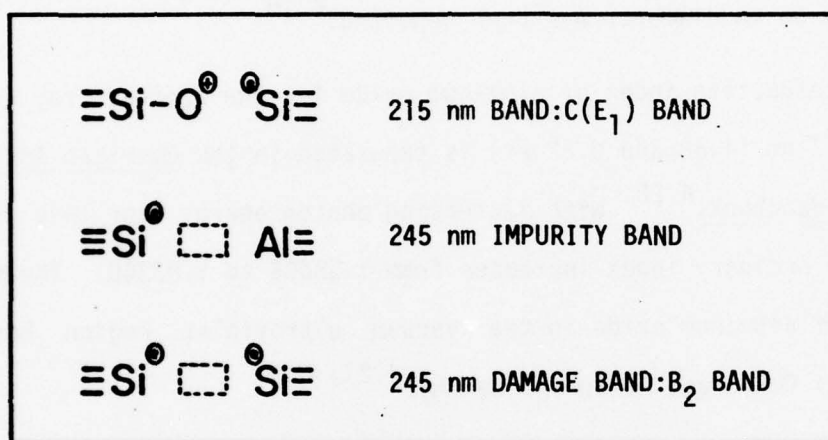
Fig. 4.41. Proposed models for the 215 nm absorption band, the 245 nm impurity band, and the 245 nm (B_2) damage band. [G. W. Arnold, IEEE Trans. Nucl. Sci. 20, 220 (1973).]

B. Aluminum Oxide *

Aluminum oxide (Al$_2$O$_3$), also known as alumina, corundum, or sapphire, is more resistant to moisture and to mechanical damage than are the alkali halides and alkaline-earth halides. In spite of its high melting point (2050 C), successful growth of good optical quality sapphire crystals as large as 25 cm in diameter has been reported.[4.19]

The refractive index of aluminum oxide for the ordinary ray between 265 and 5577 nm (4.68 and 0.22 eV) is tabulated in the American Institute of Physics Handbook.[4.20] With increasing photon energy over this spectral range, the ordinary index increases from 1.58638 to 1.83360. The bire-fringence of aluminum oxide in the vacuum ultraviolet region has been discussed by Chandrasekharan and Damany.[4.21, 4.22]

The intrinsic infrared-absorption edge for aluminum oxide, corre-sponding to $\beta = 5$ cm^{-1}, for light propagation along the c-axis of the crystal, is at 6,000 nm (0.21 eV or 6 μm).[4.23]

The absorption coefficient near the fundamental absorption edge of pure Al$_2$O$_3$ is shown in Fig. 4.42.[4.24] Note the steep rise in β at the absorption edge and the rather long secondary tail, with large β, up to several hundred cm^{-1}, extending into the nominally transparent region. Since the range of β in Fig. 4.42 is not sufficiently great, an accurate estimate of the Urbach absorption edge corresponding to $\beta = 5$ cm^{-1} cannot be made because the extrapolation would have to be made from the absorption data which include contributions from the secondary tail.

---

*See summary Figures 1.7 and 1.14 of Volume I.
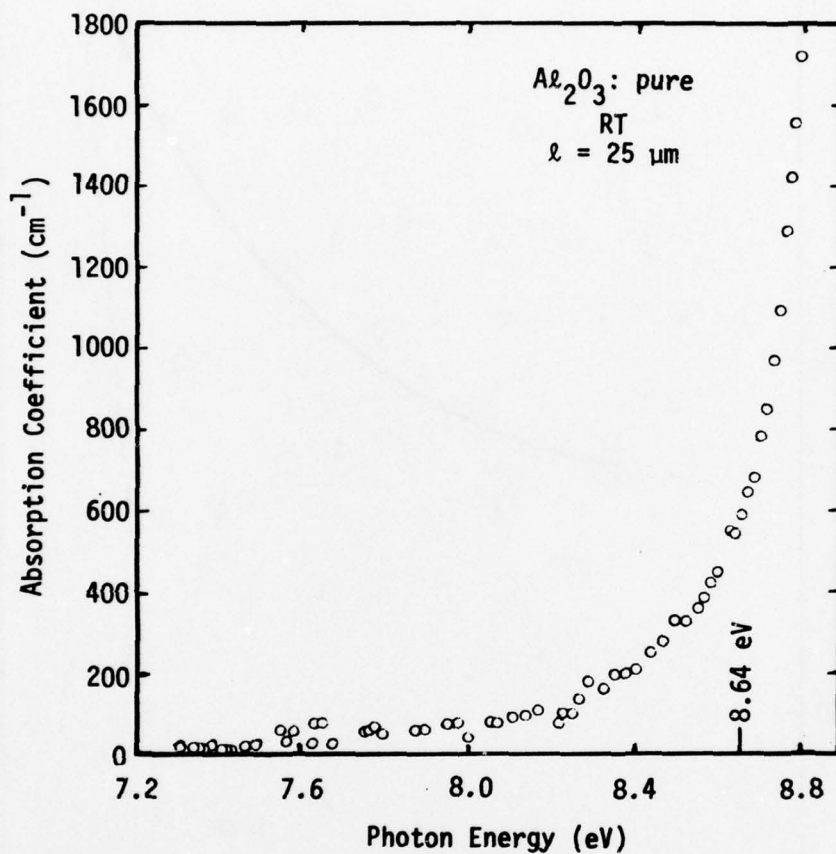
Fig. 4.42(a).   Absorption coefficient of pure $A\ell_2O_3$, showing the sharp rise in the absorption coefficient at the absorption edge near 8.64 eV and the rather long and strong secondary absorption tail extending to approximately 7.2 eV.   [H. H. Tippins, Phys. Rev. B 1, 126 (1970).]

183
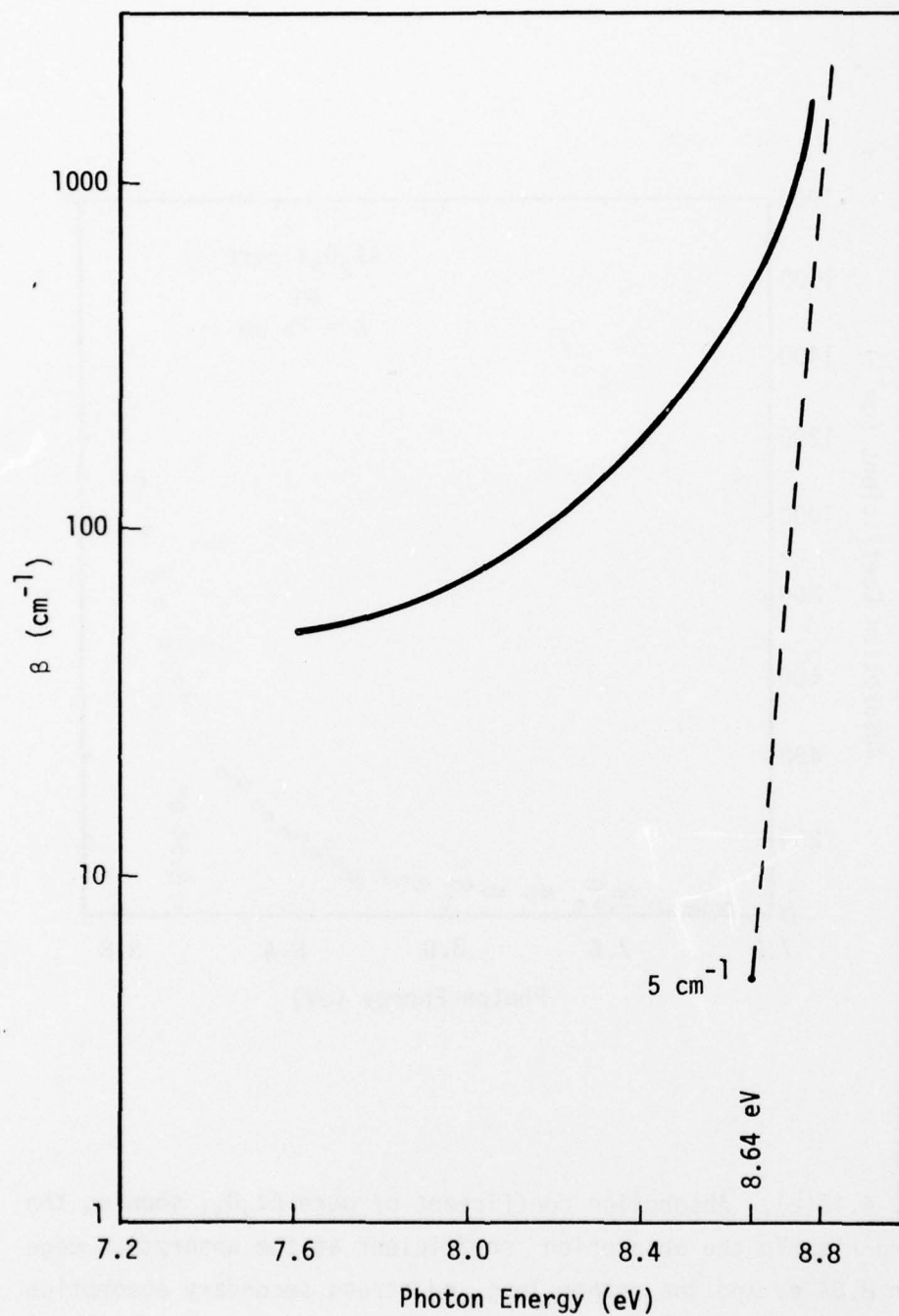
Fig. 4.42(b).   Replot of the average β from Fig. 4.42(a) on an
exponential scale showing that β is not exponential. The dashed
exponential curve through 5 cm^{-1} is an extrapolation from the
high absorption region, β > 1000 cm^{-1}.

The transmittance near the short-wavelength cutoff, before and after electron irradiation, of a UV-grade optically polished Al_2O_3 is shown in Fig. 4.43.[4.25] This figure defines the cutoff at 8.64 eV (143.5 nm) more sharply than in the preceding figure and also demonstrates the high resistance of sapphire to transmittance loss from high-energy electron irradiation.

1. <u>Transition-metal ions in Al_2O_3</u>. Aluminum oxide has a rhombohedral-hexagonal crystal structure in which an Al atom is surrounded by a trigonally distorted octahedron of oxygens. Aluminum fills two-thirds of the octahedral sites, and while its true site symmetry is C_3, the site group C_{3v} may be retained for many purposes.[4.26]

The Laporte selection rule, which requires that the parities of the final and initial states be different and, thus, forbids intra-d-shell transitions in cubic crystals, is relaxed in aluminum oxide because there is no center of symmetry at the positive-ion site in its lattice. The observed oscillator strengths of the spin-allowed d-d transitions of the transition-metal ions in aluminum oxide are of the order of 10^{-4}.

Because of its non-cubic crystal structure, many of the absorption bands associated with lattice defects or impurities in Al_2O_3 are anisotropic.

A detailed analysis of the polarized optical absorption spectra due to intra-d-shell transitions of several first-group transition-metal ions in aluminum oxide has been made by McClure.[4.26] This analysis indicates that the vibrational-electronic contribution to band strength is quite small at low temperatures but increases rapidly at high temperatures, that the surroundings of an ion are distorted in some electronic states, and that the impurity ion, while it substitutes for Al, probably occupies a position
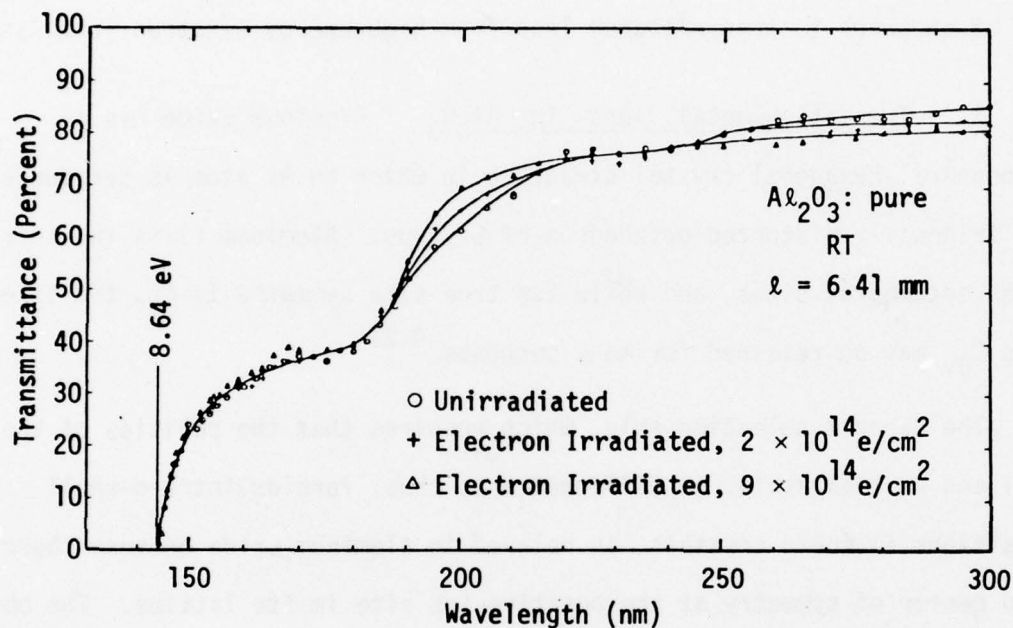
Fig. 4.43. Transmittance spectra of Al_2O_3, showing the absorption edge at 143.5 nm and the relatively small effect of electron irradiation from 2×10^{14} electrons/cm^2 at 1.0 MeV and 9×10^{14} electrons/cm^2 at 2.0 MeV. [D. F. Heath and P. A. Sacher, Appl. Opt. 5, 937 (1966).]

displaced by about 0.01 nm from the Al site in the c direction toward the empty octahedral site.

Table 4.5 summarizes the possible assignments, polarizations, centroid positions, Dq values and oscillator strengths (f-numbers) of the intra-d-shell transitions of Ti^{3+} through Ni^{3+} observed in aluminum oxide at 77 K. Three-part symbols, such as ^2T_2tE, are used in the table to specify electronic states. Here $^2T_2$ refers to the cubic-field parent, t the strong-field configuration, and E the trigonal-field representation.

The polarized absorption spectra at 77 K of Ti^{3+}, V^{3+}, Cr^{3+}, Mn^{3+} and Co^{3+}, and at 35 K of Ni^{3+}, in aluminum oxide are shown in Fig. 4.44 through Fig. 4.49.

At 77 K and below, McClure[4.26] observed fine structures in the polarized spectra of all first-group transition-metal ions from V^{3+} through Ni^{3+}. These were identified as vibrational structures, and most of the observed vibrational intervals were found to be characteristic of the aluminum oxide lattice. The assignments of the Al_2O_3 lattice vibrations are listed in Table 4.6.[4.27] The first strong-band vibrational structures of Co^{3+}, V^{3+}, and Cr^{3+} in corundum are shown in Figs. 4.50 through 4.52, respectively. The sharp line structure in the Cr^{3+} band is highly polarized perpendicular to c, but in the V^{3+} band the structure appears with about the same intensity in both polarizations, and while several vibrational modes appear in the Co^{3+} absorption, only one mode is present in Cr^{3+} and V^{3+} absorptions. The observed progression of 200 cm^{-1} intervals in the T_2 bands of V^{3+} and Cr^{3+} was assigned to an E_u mode of the aluminum oxide (Table 4.6). McClure concludes that the ground states and the first excited states are similar in

Table 4.5. Summary of ground- and excited-state assignments, Dq values, centroids of strong bands (ν in eV) and f-numbers ($f \times 10^4$) of observed intra-d-shell transitions of trivalent ions in Al_2O_3 at 77 K. [D. S. McClure, J. Chem. Phys. $\underline{36}$, 2757 (1962).]

State	Ti	V	Cr	Mn	Fe	Co	Ni
ground	^2T_2tE	$^3T_1t^2A_2$	$^4A_2t^3A_2$	$^5Et^3eE$	$^6A_1t^3e^2A_1$	$^1A_1t^6A_1$	$^2Et^6eE$
1st exc.	$\underline{^2E}$	$\underline{^3T_2et}$	$\underline{^4T_2et^2}$	$\underline{^5T_2t^2e^2}$	$\underline{^4T_1t^4e}$	$\underline{^1T_1t^5e}$	?
//ν	2.517	2.171	2.288	2.554		1.952	2.083
ν	2.288						
f	0.432	0.279	1.30	1.77		0.27	3.3
$\perp\nu$	2.517	2.160	2.232	2.319		1.907	2.021
ν	2.288						
f	0.132	0.360	4.80	2.67		0.87	4.5
2nd exc.	$\cdots$	$\underline{^3T_1et}$	$\underline{^4T_1et^2}$	$\cdots$	$\underline{^4T_2}$	$\underline{^1T_2t^5e}$	
//ν		3.091	3.125		2.133	2.873	
f		5.61	10.16			1.05	
$\perp\nu$		3.138	3.026		2.207	2.827	
f		1.60	5.88			0.60	
3rd exc.	$\cdots$	$\underline{^3A_2e^2}$	$\underline{^4T_1e^2t}$		$\underline{^4A_1},\underline{^4Et^3e^2}$		
//ν		3.874	4.886		3.195		
f			1.3				
$\perp\nu$			4.836		3.203		
f			1.2				
Dq cm^{-1}	0.2362	0.2170	0.2251	0.2414	0.2046	0.2269	
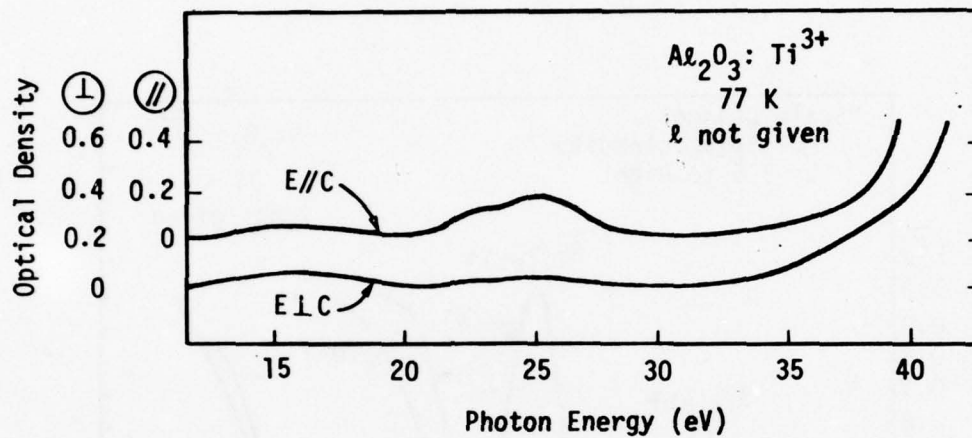
Fig. 4.44. Absorption spectrum of Ti^{3+} in Al_2O_3.
[D. S. McClure, J. Chem Phys. <u>36</u>, 2757 (1962).]
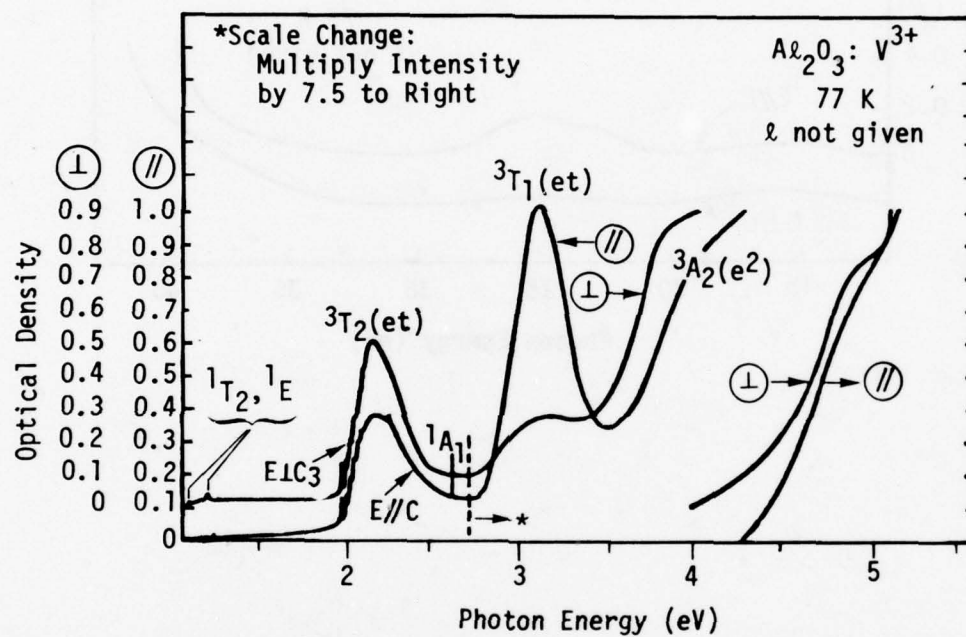
Fig. 4.45. Absorption spectrum of V^{3+} in Al_2O_3.
[D. S. McClure, J. Chem. Phys. <u>36</u>, 2757 (1962).]
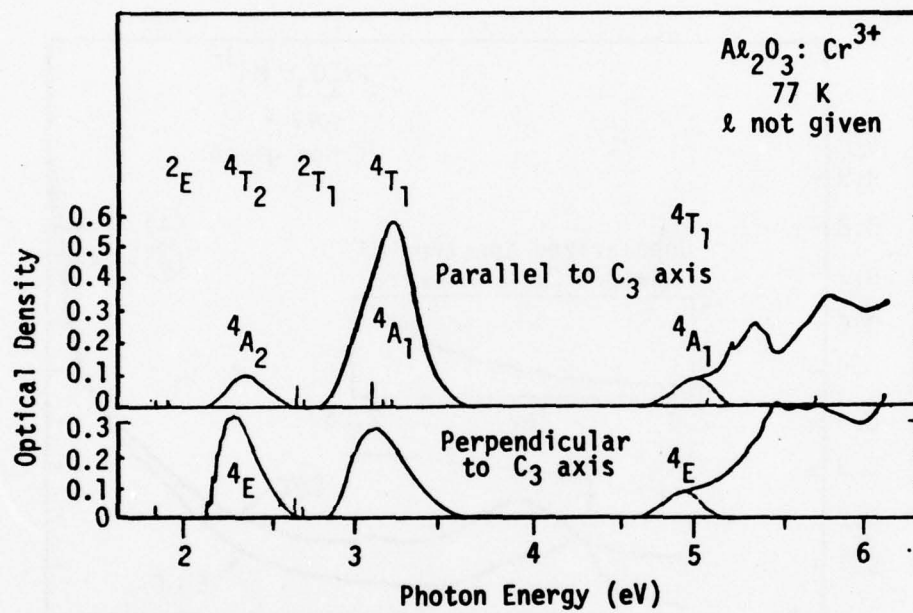
Fig. 4.46. Absorption spectrum of Cr^{3+} in $Aℓ_2O_3$.
[D. S. McClure, J. Chem. Phys. <u>36</u>, 2757 (1962).]
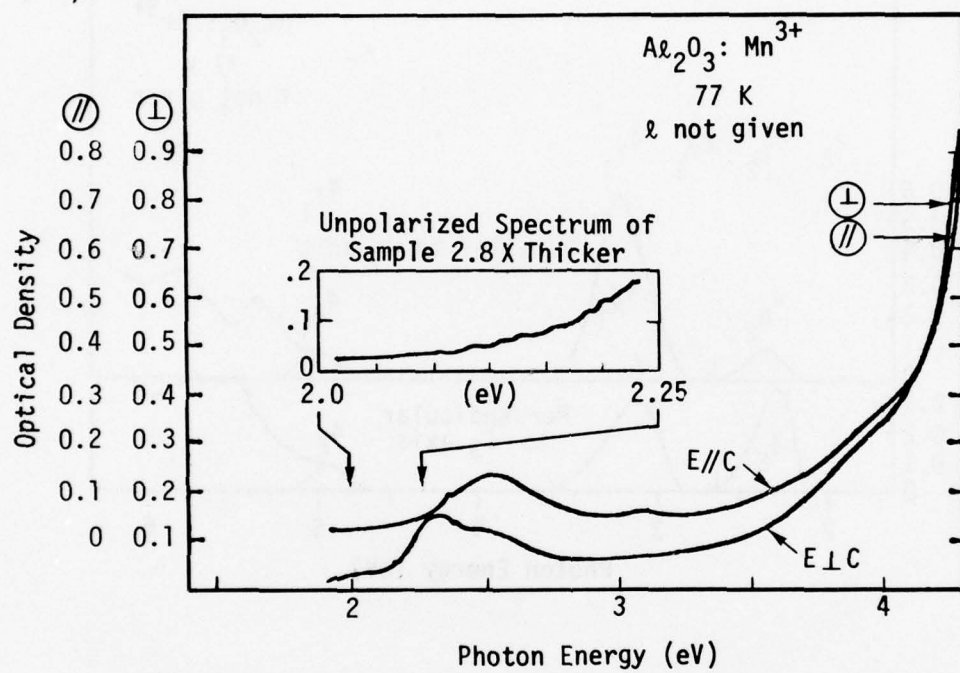
Fig. 4.47. Absorption spectrum of Mn^{3+} in $A\ell_2O_3$.

[D. S. McClure, J. Chem. Phys. <u>36</u>, 2757 (1962).]
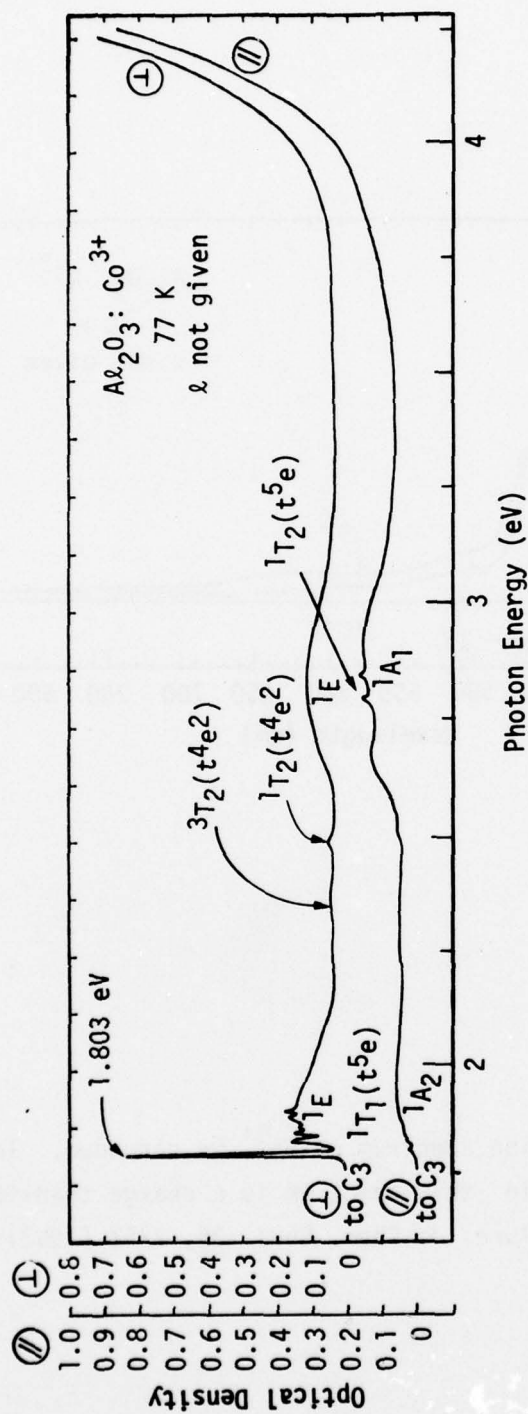
Fig. 4.48. Absorption spectrum of Co^{3+} in Al_2O_3. [D. S. McClure, J. Chem. Phys. 36, 2757 (1962).]
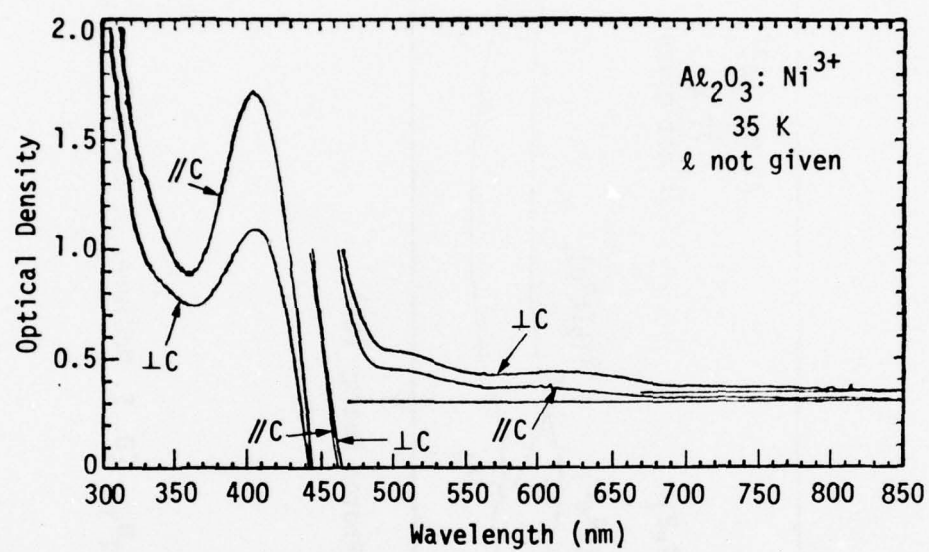
Fig. 4.49. Absorption spectrum of Ni^{3+} in corundum. The high-energy band in this spectrum is a charge transfer band. [D. S. McClure, J. Chem. Phys. <u>36</u>, 2757 (1962).]

Table 4.6.   Vibrations of aluminum oxide.   Symmetry classification D_{3d}.   [R. S. Krishnan, Proc. Indian Acad. Sci. 26A, 450 (1947).]

Rep'n	Number of Modes	Activity		Observed Frequencies (cm^{-1})				
		Raman	IR					
A_{1g}	2	+		578	751			
A_{1u}	3							
A_{2u}	2		+	244	847			
A_{2g}	2							
E_u	4		+	194	328-55	434	909	
E_g	5	+		375	417	432	450	642
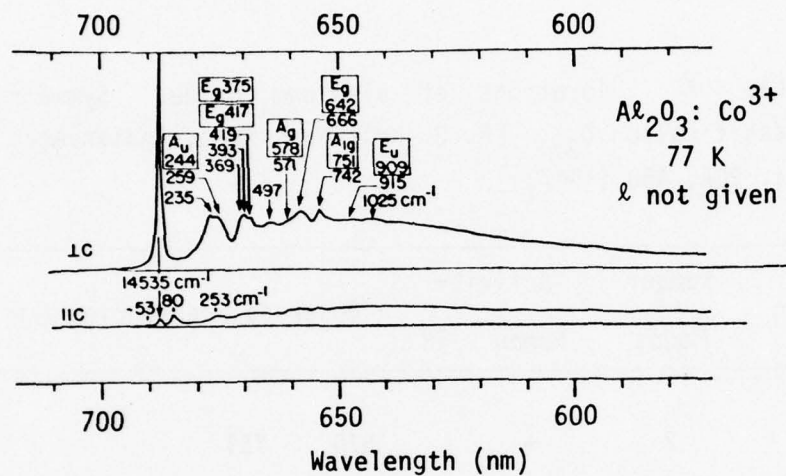
Fig. 4.50.   Vibrational structure of the first strong band of Co^{3+} in Al_2O_3. The vibrations of pure corundum and their assignments are boxed in.   [D. S. McClure, J. Chem. Phys. <u>36</u>, 2757 (1962).]
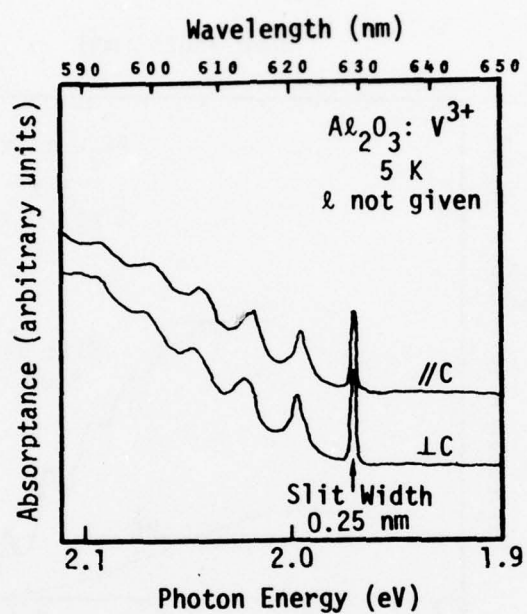
Fig. 4.51. Vibrational structure of the first strong band of V^{3+} in Al_2O_3. Peak positions of the vibrational structures are expressed in cm^{-1}.   [D. S. McClure, J. Chem. Phys. 36, 2757 (1962).]
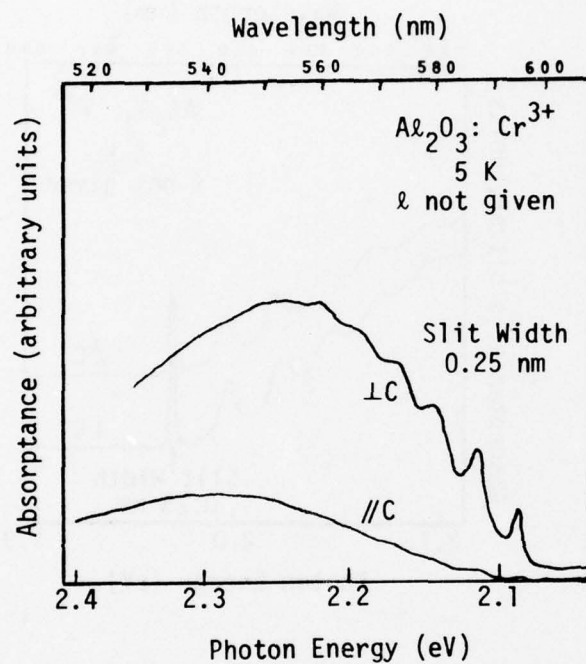
Fig. 4.52. Vibrational structure of the first strong band of Cr^{3+} in Al_2O_3. Indicated peak-position of the vibrational structures are in cm^{-1}. [D. S. McClure, J. Chem. Phys. 36, 2757 (1962).]

Co^{3+}, but the resemblance is decreased in Cr^{3+} and V^{3+} because the T_2 states are tetragonally distorted which destroys their C_3 symmetry.

Polarized absorption spectra at several temperatures between 298 and 1,300 K of Cr^{3+} and Co^{3+} in aluminum oxide are shown in Figs. 4.53 and 4.54, respectively.

The presence of transition-metal ions in aluminum oxide gives rise to additional absorptions on the high-energy side of those assigned to d-d transitions. These absorptions of various first-row transition metal ions in corundum have been measured and analyzed by Tippins,[4.24] who assigns them to a charge-transfer process whereby an electron is transferred from a non-bonding orbital, localized predominantly on the O^{--} ligands, to either the $t_{2g}(\pi^*)$ or $eg(\sigma^*)$ anti-bonding orbital localized predominantly on the transition-metal impurity. The important characteristics of the absorptions attributed to the ligand-metal charge-transfer processes are the following: (i) the peak positions are dependent on the impurity ion; (ii) the peak positions and widths are independent of temperature over the range 77-300 K; and (iii) the oscillator strengths are much higher than those associated with the d-d transitions.

Optical-absorption spectra in the region of charge-transfer transitions of Al_2O_3 doped with V^{3+}, Ti^{3+}, Cr^{3+}, Mn^{3+} (and Mn^{4+}), Fe^{3+} and Ni^{3+} are shown successively in Fig. 4.55 through Fig. 4.60.

A simple model predicts the following expression for the threshold energy of the charge-transfer process.

$$h\nu = C - I(M^{2+}) + \Delta E_d \quad , \tag{4.1}$$
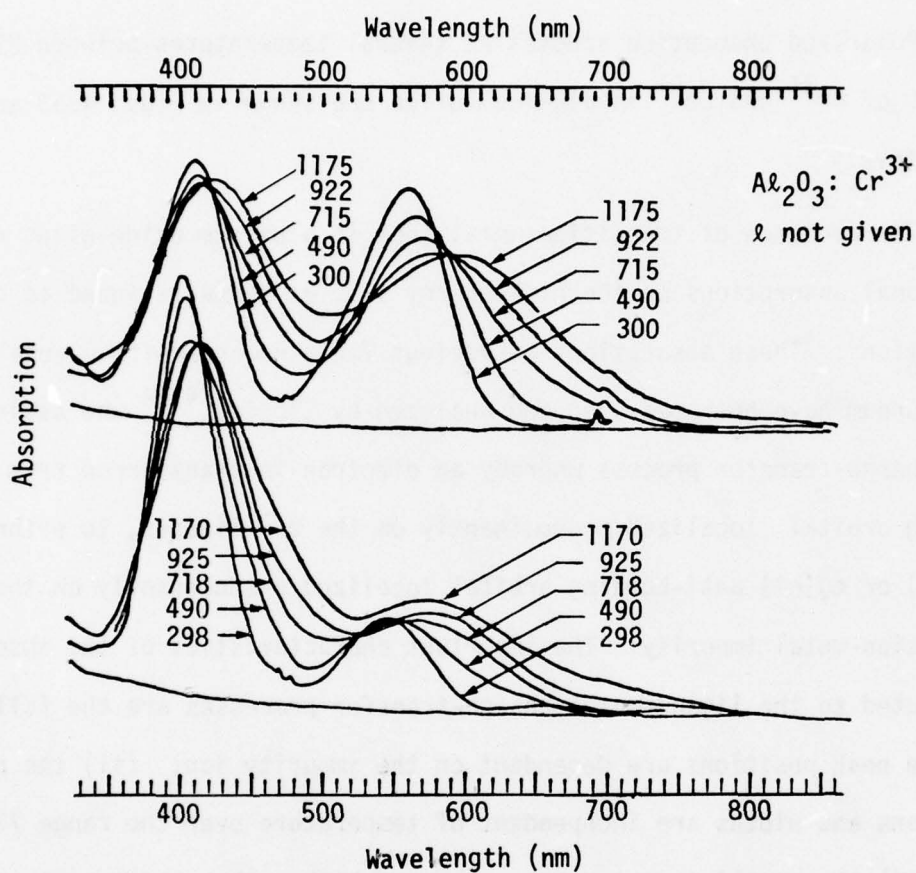
Fig. 4.53. Absorption spectra of Cr^{3+} in Al_2O_3 at various temperatures (K). Upper set $\perp$C, lower set //C. [D. S. McClure, J. Chem. Phys. <u>36</u>, 2757 (1962).]
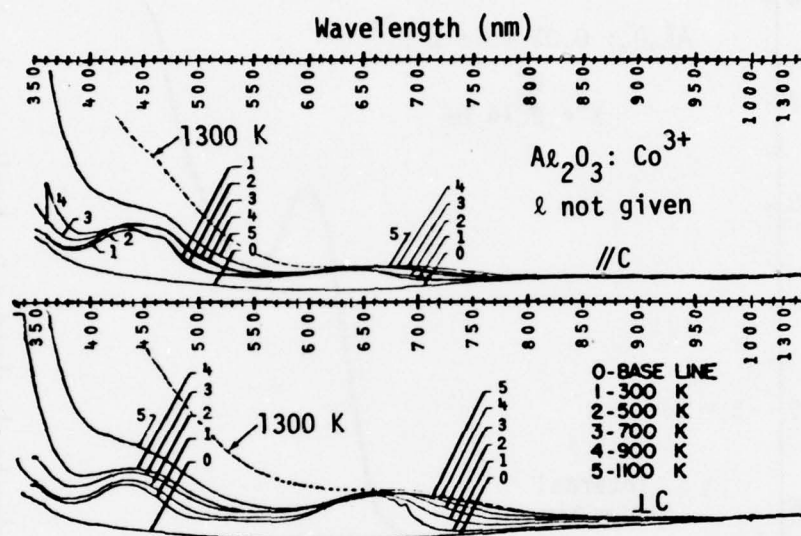
Fig. 4.54. Absorption spectra of Co^{3+} in Aℓ_2O$_3$ at various temperatures. [D. S. McClure, J. Chem. Phys. 36, 2757 (1962).]
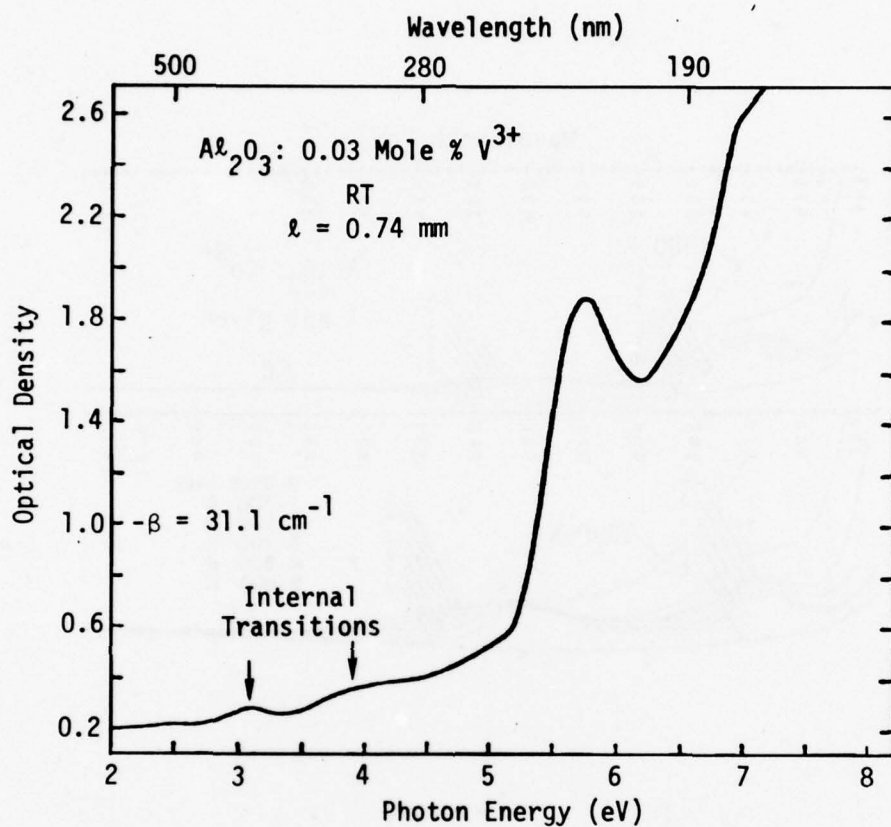
Fig. 4.55. Absorption spectrum of Aℓ$_2$O$_3$ doped with V^{3+} showing the charge-transfer threshold at 5.75 eV and the low-energy bands due to intra-d-shell transitions. [H. H. Tippins, Phys. Rev. B 1, 126 (1970).]
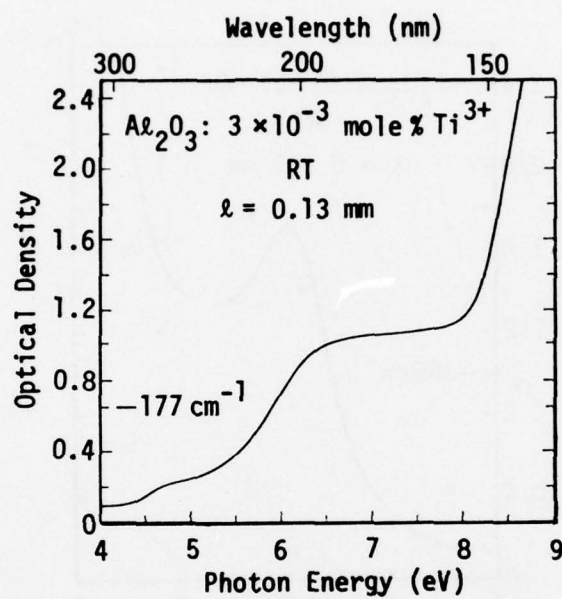
Fig. 4.56.   Absorption spectrum of Al_2O_3 doped with Ti^{3+}. The broad shoulder near 7 eV is identified as a charge-transfer transition. [H. H. Tippins, Phys. Rev. B $\underline{1}$, 126 (1970).]
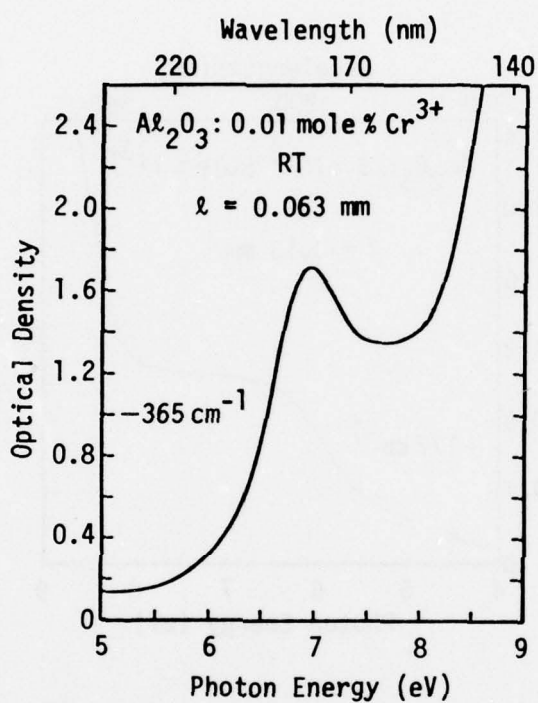
Fig. 4.57. Absorption spectrum of Al_2O_3 doped with Cr^{3+} (ruby) showing an intense charge-transfer peak at 6.94 eV.   [H. H. Tippins, Phys. Rev. B 1, 126 (1970).]
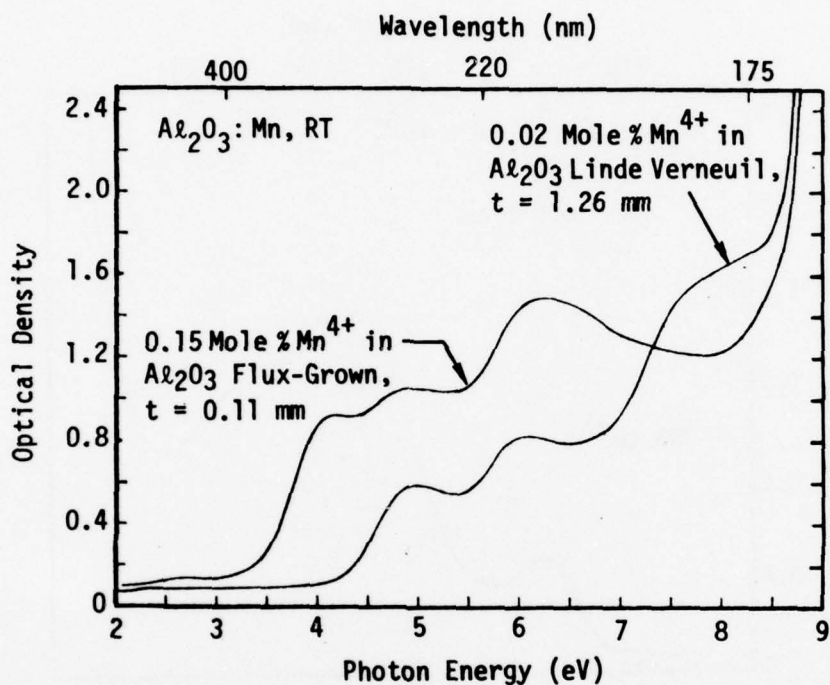
Fig. 4.58. Absorption spectra of Al_2O_3 doped with Mn^{4+}. All bands except the very weak one between 2 and 3 eV are due to charge transfer.   The peak near 4.1 eV for the flux-grown sample is believed to be the Mn^{3+} charge-transfer threshold. [H. H. Tippins, Phys. Rev. B $\underline{1}$, 126 (1970).]
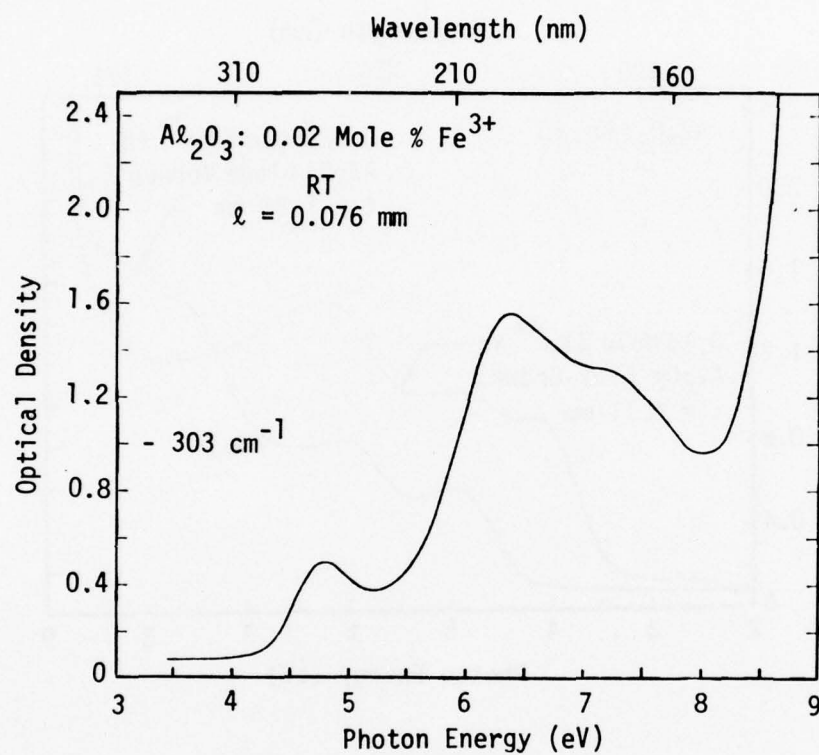
Fig. 4.59. Absorption spectrum of $A\ell_2O_3$ doped with Fe^{3+}.
At least three charge-transfer peaks are resolved. [H. H.
Tippins, Phys. Rev. B $\underline{1}$, 126 (1970).
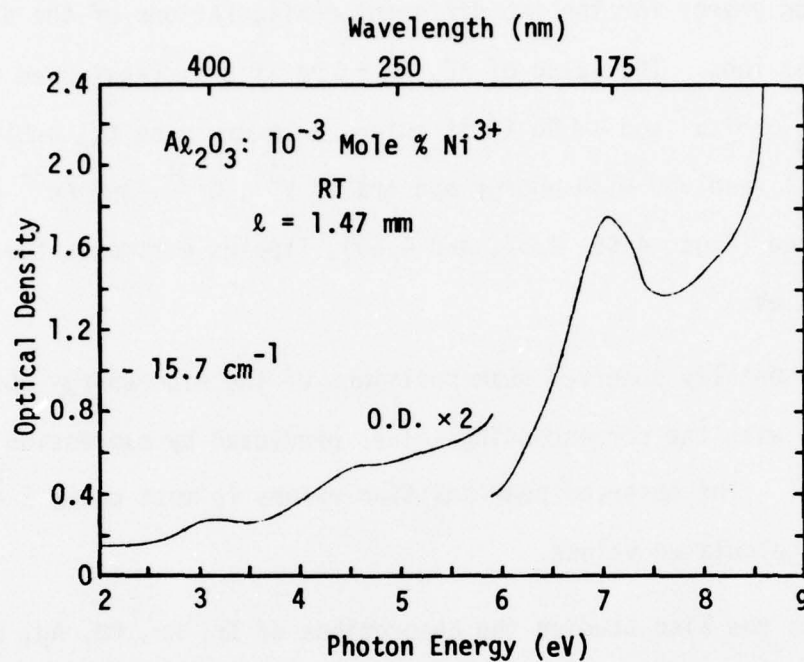
Fig. 4.60. Absorption spectrum of Al$_2$O$_3$ doped with Ni^{3+}. The low-energy tail of the band peaked at 3.2 eV extends into the visible and gives the crystal a pronounced yellow color, even for very low nickel concentration. [H. H. Tippins, Phys. Rev. B $\underline{1}$, 126 (1970).]

207

where C is an energy constant common to all impurity ions, $I(M^{2+})$ is the third ionization energy of the transition-metal impurity, and ΔE_d is the term introduced to take into consideration the difference of the d-electron stabilization energy for the two different configurations of the divalent and trivalent ions. The value of ΔE_d is $+6\,Dq$ if the transferred electron enters an e_g orbital and $-4\,Dq$ if it enters a lower-lying t_{2g} orbital. From the well resolved high-energy spectra of V^{3+}, Cr^{3+}, and Fe^{3+} in aluminum oxide (Figs. 4.55, 4.57, and 4.59), Tippins estimates the value of $C = 36.24$ eV.

Experimentally observed peak positions of the high-energy absorptions are compared with the corresponding values predicted by expression (4.1) in Table 4.7. The observed peak-position values in most cases are within 1 eV of the calculated values.

Tippins has also studied the absorptions of Zr, Ru, Pd, Ag, and Ga in Al_2O_3. Each of these elements was observed to give rise to a broad structureless shoulder on the low-energy side of the intrinsic absorption, similar to a great extent to that shown in Fig. 4.56 for the Ti^{3+}-doped aluminum oxide; no spectra were given.

In aluminum oxide containing Fe or Fe and Ti impurities, there are several observed absorption bands which cannot be assigned to d-d transitions in isolated impurities or to ligand-metal charge-transfer processes. These absorption bands fall into three classes. Two of them involve metal-to-metal charge transfer. In the first case, electron transfer takes place between the same transition-metal impurity present in two different valence states in adjacent metal sites, e.g., $Fe^{2+} \rightarrow Fe^{3+}$, and in the second case

Table 4.7.   Summary of data obtained from spectra of Figs. 4.55
to 4.60 and comparison with the threshold values predicted from
Eq. (4.1) of the text for the charge-transfer process.   All
energies are expressed in eV.   [H. H. Tippins, Phys. Rev. B $\underline{1}$,
126 (1970).]

Ion	Mole % of Dopant	Configuration	Peak Positions	36.24 $-I(M^{2+})$ $+ \Delta E_d$	$I(M^{2+})$	10 Dq
Ti^{3+}	0.003	t_{2g}	~6.9	7.82	27.47	2.36
V^{3+}	0.03	t_{2g}^2	5.75	6.06	29.31	2.17
Cr^{3+}	0.01	t_{2g}^3	6.94	6.64	30.95	2.25
Mn^{3+}	~0.01	$t_{2g}^3 e_g$	4.15(?)	4.00	33.69	2.42
Fe^{3+}	0.02	$t_{2g}^3 e_g^2$	4.78 6.38 7.2	4.78	30.64	2.05
Ni^{3+}	0.001	$t_{2g}^6 e_g$	3.16 4.6 7.04	0.48	35.16	3.04
Al^{3+}	100	...	Edge 8.8	7.8	28.44	...

the electron transfer takes place between two neighboring unlike metals in different valence states, e.g., $Fe^{2+} \rightarrow Ti^{4+}$. The third class of transition is associated with pairs of exchange-coupled Fe^{3+} ions and involves the electronic excitation of one ion of the pair or the simultaneous electronic excitation of both ions of the pair.

The energy-level diagram of Fe^{3+} and the polarized absorption spectra of natural yellow $A\ell_2O_3$, which contains Fe^{3+} impurity, are shown in Fig. 4.61.[4.28] The polarized absorption spectra of a synthetic Fe^{3+}-doped $A\ell_2O_3$ at various temperatures between 6 and 295 K are shown in Fig. 4.62.[4.28] Ferguson and Fielding[4.28] indicate that by using the Dq value of 1,430 cm^{-1} and neglecting the trigonal field, it is possible to assign single-ion states to the Fe^{3+} absorption bands near 1,031 nm (1.20 eV; $^4T_1^a$), 535 nm (2.32 eV; $^4T_2^a$), 450 nm (2.76 eV; $^4A_1, ^4E$), 391 nm (3.17 eV; $^4T_2^b$), 375 nm (3.31 eV; $^4E^b$), and 308 nm (4.03 eV; $^4T_1^b$), the observed temperature- and concentration-dependent features of the spectra can be best explained by considerations of exchange-coupled Fe^{3+} ions. According to these authors, the 450 and 375 nm bands correspond to electronic excitation of one ion of an Fe^{3+} pair, and the ones near 330, 420, and 540 nm correspond to electronic excitation of both ions of a pair.

Figure 4.63 shows the polarized absorption spectra of a sample of natural blue-green $A\ell_2O_3$, which contains Fe and Ti impurities. The absorptions seen near 562 and 704 nm (2.20 and 1.76 eV) have been assigned to $Fe^{2+} \rightarrow Ti^{4+}$ charge transfer,[4.29] and the band near 870 nm (1.43 eV) has been attributed to Fe^{2+} to Fe^{3+} charge transfer.[4.28]
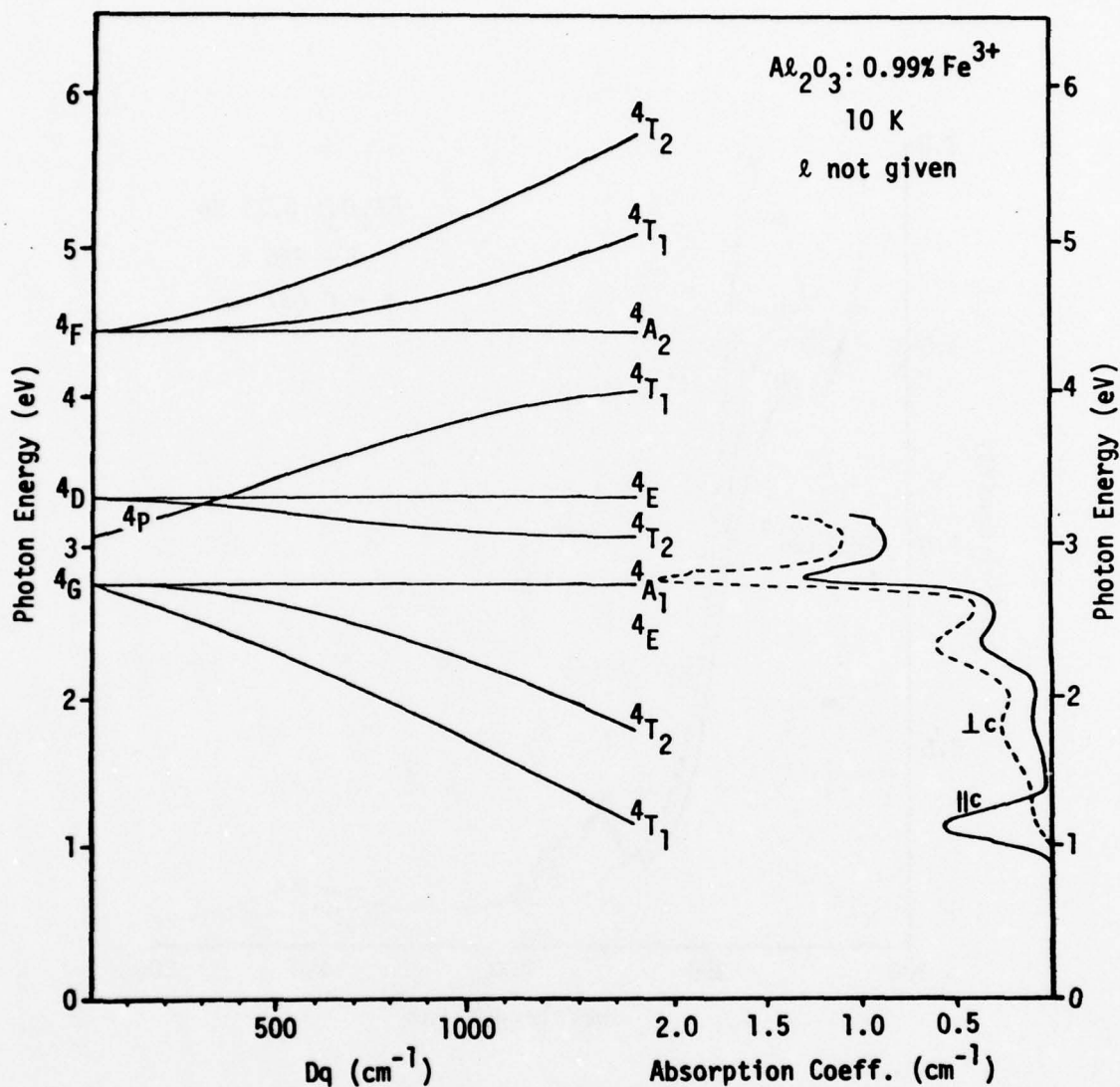
Fig. 4.61. Energy-level diagram for d^5 (left) and the absorption spectrum of a natural yellow Al_2O_3 containing 0.99% Fe^{3+}. [J. Ferguson and P. E. Fielding, Chem. Phys. Lett. 10, 262 (1971).]

211
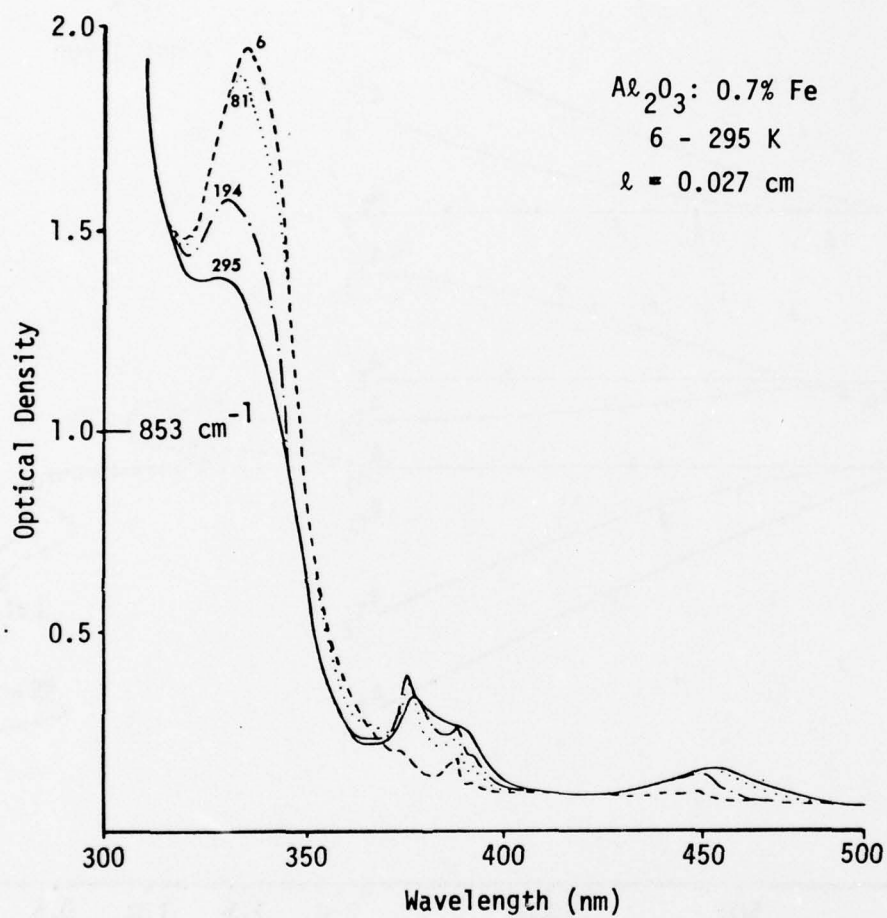
Fig. 4.62. Absorption spectrum (E perpendicular to c) of synthetic Al_2O_3 doped with 0.7% Fe at various temperatures. [J. Ferguson and P. E. Fielding, Chem. Phys. Lett. 10, 262 (1971).]
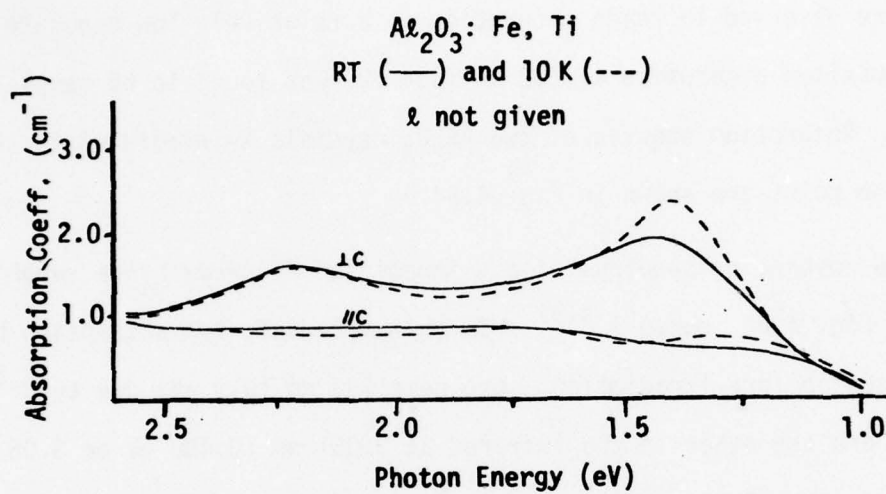
Fig. 4.63. Absorption spectrum of natural blue-green Al_2O_3 containing titanium and 0.62 percent iron. [J. Ferguson and P. E. Fielding, Chem. Phys. Lett. 10, 262 (1971).]

213

2. <u>Radiative coloration of $A\ell_2O_3$</u>. Hunt and Schuler[4.30] observed absorption bands near 230 nm (5.4 eV), 400 nm (3.1 eV), and 650 nm (1.9 eV) in X-irradiated synthetic $A\ell_2O_3$ crystals. The magnitudes of these absorptions were observed to reach saturation at a relatively low exposure level, and the maximum absorption at 230 nm (5.4 eV) was found to be sample dependent. Absorption spectra of two $A\ell_2O_3$ crystals X-irradiated to the saturation point are shown in Fig. 4.64.

The absorption spectrum of a γ-irradiated UV-grade Linde sapphire is shown in Fig. 4.65, curve 1.[4.31] In this material, two absorption bands were present before irradiation — one near 180 nm (6.9 eV) due to Cr^{3+} impurity and the other in the infrared at 3,051 nm (0.406 eV or 3.05 μm) attributed to an OH ion adjacent to a positive-ion vacancy. In the irradiated sample, in addition to the two main absorption bands seen near 227 nm (5.46 eV) and 410 nm (3.02 eV) in Fig. 4.65, a band was observed at 3,016 nm (0.411 eV or 3.016 μm) in the infrared. This band grew at the expense of 3,051 nm (0.406 eV) band and was assigned to V_{OH}- center, consisting of an OH^- ion adjacent to an aluminum vacancy which has captured a hole. It is seen in Fig. 4.65 that irradiation with 410 nm light bleaches both the 227 nm and 410 nm bands. Simultaneous bleaching of both these bands was also observed when the γ-irradiated aluminum oxide was bleached with 230 nm light. These observations, in conjunction with the studies of thermoluminescence and thermal bleaching behavior of absorptions in γ-irradiated $A\ell_2O_3$, have led Turner and Crawford[4.31] to suggest that the 410 nm (3.02 eV) band is a composite V band, one component of which is the V_{OH}- center, and that the 227 nm (5.47 eV) band

Aℓ_2O$_3$: X-rays
RT
ℓ = 5.1 mm

0.15

Optical Density

0.10 — — 0.451 cm^{-1}

0.05

0.00

300   600   900

Wavelength (nm)
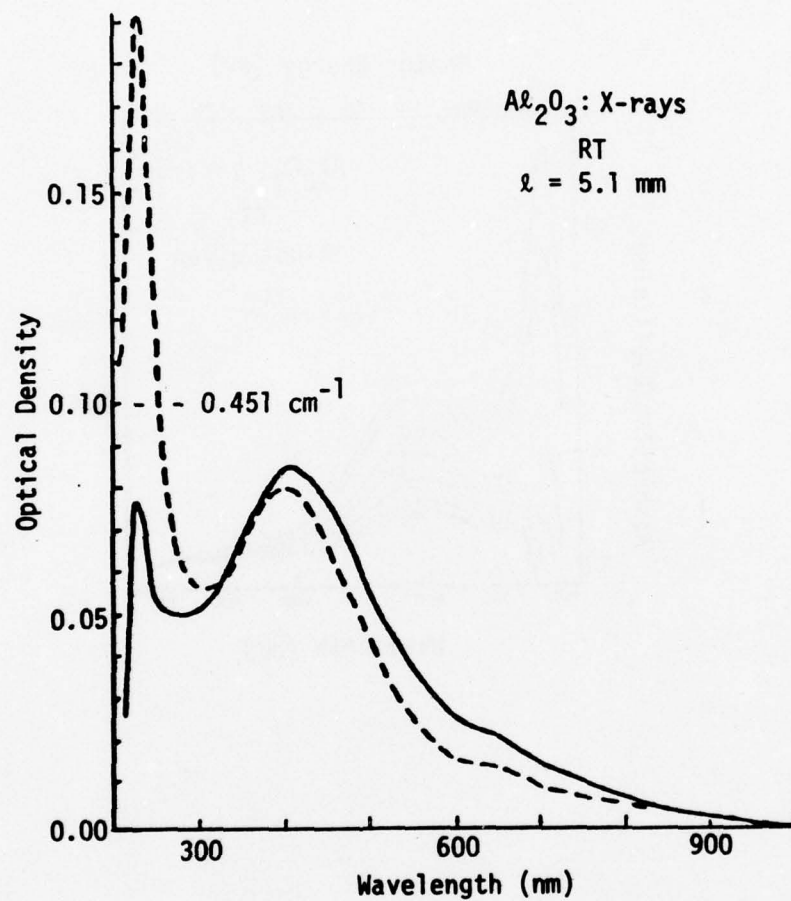
Fig. 4.64. Absorption spectra of two Aℓ_2O$_3$ crystals
X-irradiated to saturation. [R. S. Hunt and R. H.
Schuler, Phys. Rev., 89, 664 (1953).]

215
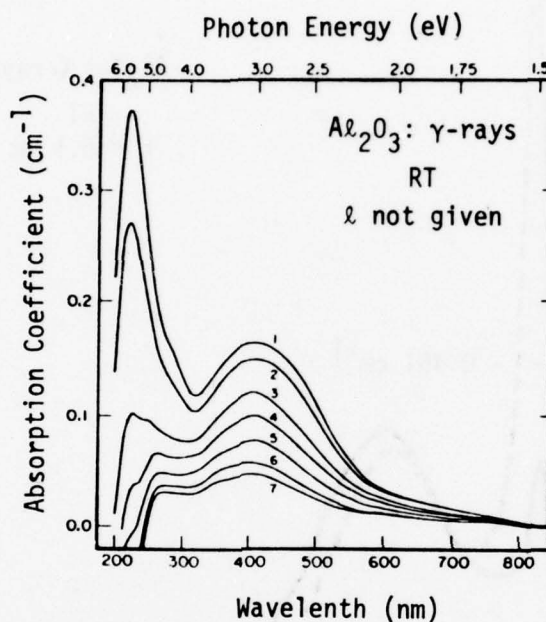
Fig. 4.65. Absorption spectrum of γ-irradiated $A\ell_2O_3$ following bleaching at 410 nm for periods of (1) 0, (2) 5, (3) 15, (4) 35, (5) 75, (6) 155, (7) 315 min. [T. J. Turner and J. H. Crawford, Jr., Solid State Commun. 17, 167 (1975).]

is due to Cr^{2+} ions, resulting from electron capture by Cr^{3+} during irradiation.

Absorption spectra at 77 K of neutron- and electron-irradiated aluminum oxide crystals are compared in Fig. 4.66.[4.32] The only band seen in the electron-irradiated sample is at 205 nm (6.05 eV); in the neutron-irradiated sample, however, additional weaker bands near 230 and 255 nm (5.4 and 5.9 eV) are also present. Since the 205 nm (6.05 eV) band can be generated by X or γ irradiation, but not by UV light, the band is presumed to arise from trapping of charges at defects which occur when atoms are displaced. Arnold and Compton[4.32] report threshold energies of 40 eV and 80 eV for the displacements of aluminum and oxygen atoms, respectively.

In another study of neutron-radiation coloration of sapphire, bands were resolved at 1.9 (653), 2.2 (564), 2.8 (443), 3.5 (354), 4.1 (302), 4.8 (258), and 6.1 eV (203 nm) at -185 C, as shown in Fig. 4.67.[4.33] Over the spectral range 2 to 6.5 eV (620 to 191 nm), only the 6.1 eV band was found to be isotropic. The anisotropy associated with other bands is shown in Fig. 4.68. For comparison, the anisotropy of absorptions induced by electron irradiation of Al_2O_3 is shown in Fig. 4.69.

While X or γ irradiation alone cannot generate the 203 nm (6.1 eV) band, a pronounced enhancement in the magnitude of the 203 nm band is observed if a neutron-irradiated Al_2O_3 sample is subsequently irradiated with X or γ rays, as illustrated in Fig. 4.70.[4.34] The effect of optical bleaching with 410 nm (3.02 eV) light on the absorptions in a neutron- and γ-irradiated Al_2O_3 sample is shown in Fig. 4.71. Since the absorption in the region of 2 to 3 eV (620 to 413 nm) has been assigned earlier to
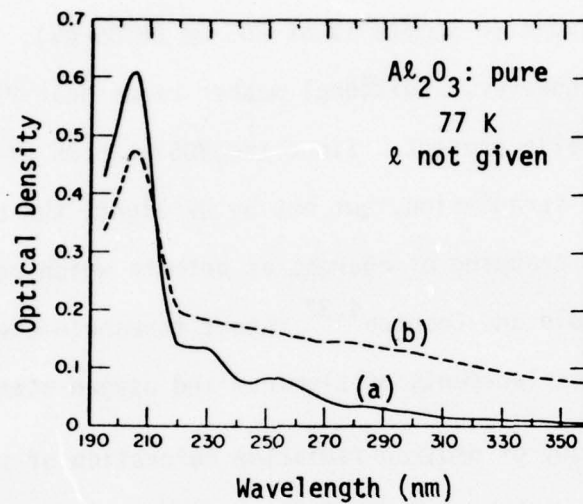
Fig. 4.66.   Absorption spectra of neutron-irradiated (a) and electron-irradiated (b) Aℓ$_2$O$_3$.   (a) 10^{17} neutrons/cm^2 (fast), pile temperature.   (b) 2 MeV electrons 9.45 × 10^{16} e/cm^2, 77 K.   Measurements made at 77 K.   [G. W. Arnold and W. D. Compton, Phys. Rev. Lett. 4, 66 (1960).]
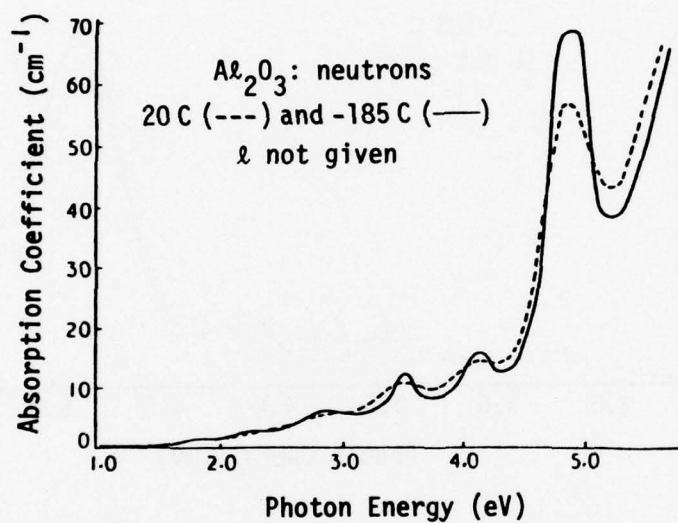
Fig. 4.67.   Absorption   spectra   at   20   and -185 C of Al_2O_3
neutron-irradiated at pile temperature.   [E. W. J. Mitchell,
J. D. Rigden, and P. D. Townsend, Phil. Mag. 5, 1013 (1960).]

219
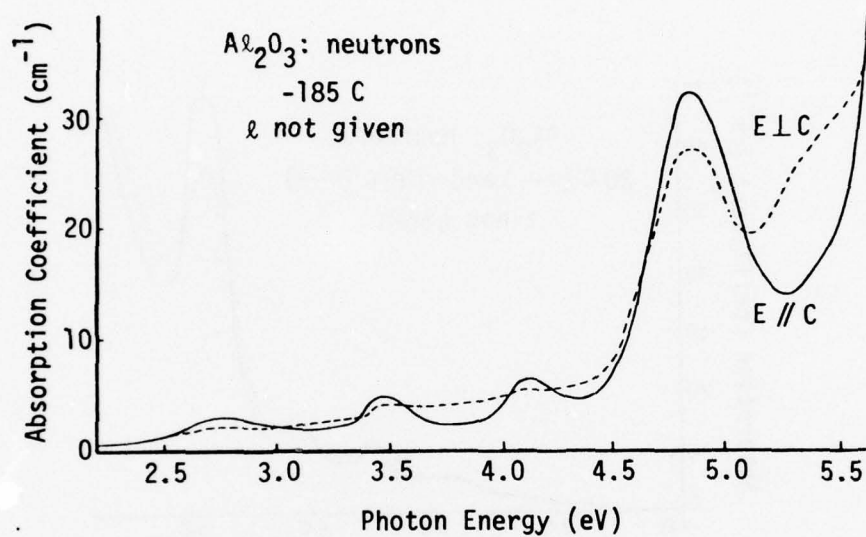
Fig. 4.68. Anisotropy of absorption induced by neutron irradiation of $A\ell_2O_3$. [E. W. J. Mitchell, J. D. Rigden, and P. D. Townsend, Phil. Mag. 5, 1013 (1960).]
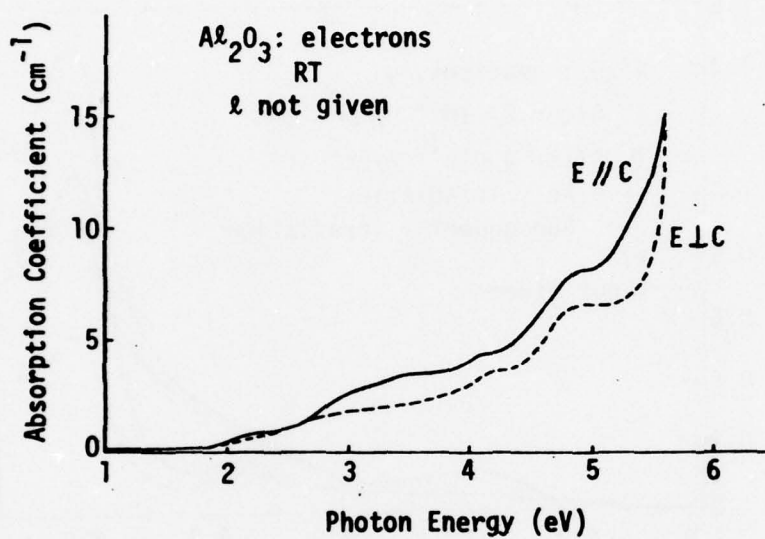
Fig. 4.69. Anisotropy of absorption induced by electron irradiation of $A\ell_2O_3$. [E. W. J. Mitchell, J. D. Rigden, and P. D. Townsend, Phil. Mag. <u>5</u>, 1013 (1960).]
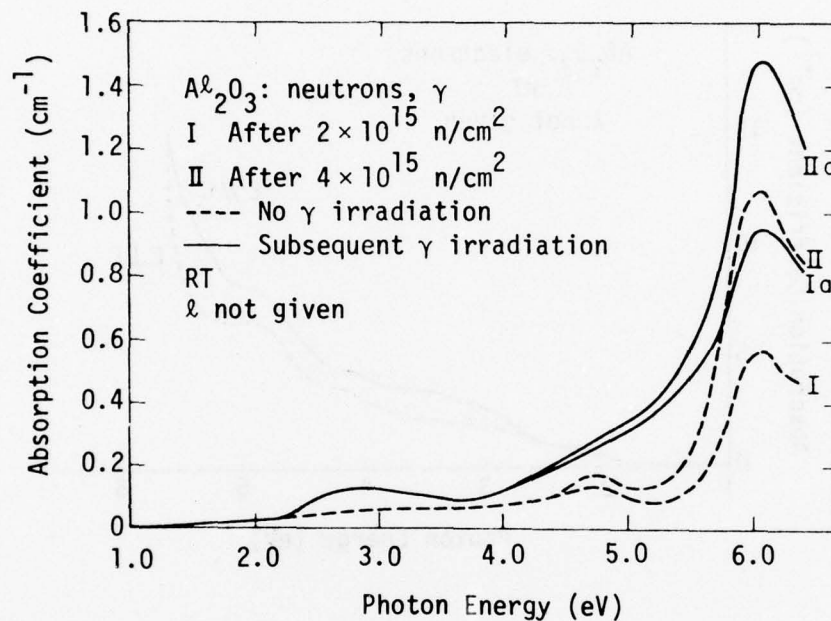
Fig. 4.70. Absorption spectra of neutron-irradiated UV-grade Aℓ$_2$O$_3$. The dashed curves were measured approximately one week after reactor exposure, the solid curve after a subsequent five-minute γ irradiation in a source of ~10^6 R/hr. [T. J. Turner and J. H. Crawford, Jr., Phys. Rev. B 13, 1735 (1976).]
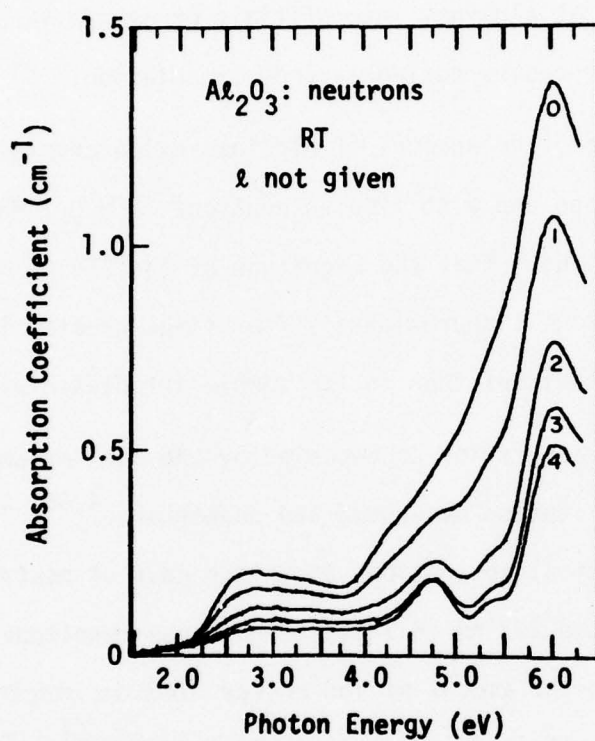
Fig. 4.71.   Effect of optical bleaching with 410 nm (3.02 eV)
light on the absorption spectrum of $A\ell_2O_3$ after neutron irra-
diation (4×10^{15} neutrons/cm^2) and γ irradiation. Bleaching
times are: 0 min - curve 0; 5 min - curve 1; 15 min - curve 2;
35 min - curve 3; 75 min - curve 4.   [T. J. Turner and J. H.
Crawford, Jr., Phys. Rev. B $\underline{13}$, 1735 (1976).]

V-type hole centers, and since the 203 nm (6.1 eV) band and the 2 to 3 eV (620 to 413 nm) absorption are bleached simultaneously during irradiation with 410 nm (3.02 eV) light, the 203 nm (6.1 eV) band has been assigned to electrons trapped at aluminum interstitials or oxygen vacancies produced by displacement processes during neutron irradiation.[4.34]

Optical absorption spectra of aluminum oxide crystals irradiated with 14 MeV neutrons and with fission neutrons (E > 0.1 MeV) are compared in Fig. 4.72.[4.35] Note that the magnitude of the 203 nm (6.1 eV) absorption per incident neutron is approximately four times greater in the sample irradiated with 14 MeV neutrons than in the sample irradiated with fission neutrons.

The optical absorption accompanied by the ion implantation of Al_2O_3 crystals has been studied by Arnold and co-workers.[4.36] The most prominent feature of the optical absorption, as in the case of neutron or electron irradiation, was the 203 nm (6.1 eV) band, whose magnitude was found to be proportional to the amount of ion energy lost in electronic processes. Absorption spectra of Al_2O_3 crystals implanted with H^+, D^+, $^4He^+$, and O^+ ions are shown in Fig. 4.73. The 260 nm (4.8 eV) band seen in this and some previous figures is believed to be associated with Al vacancies. Irradiation of Al_2O_3 often improves its UV transparency. The dip in the absorption seen near 230 nm (5.4 eV) in the case of Al_2O_3 implanted with O^+ ions is believed to have arisen from this effect. The transmittance enhancement observed near 203 nm (6.1 eV) after electron irradiation of sapphire (Fig. 4.43) was attributed to the same effect.[4.25]
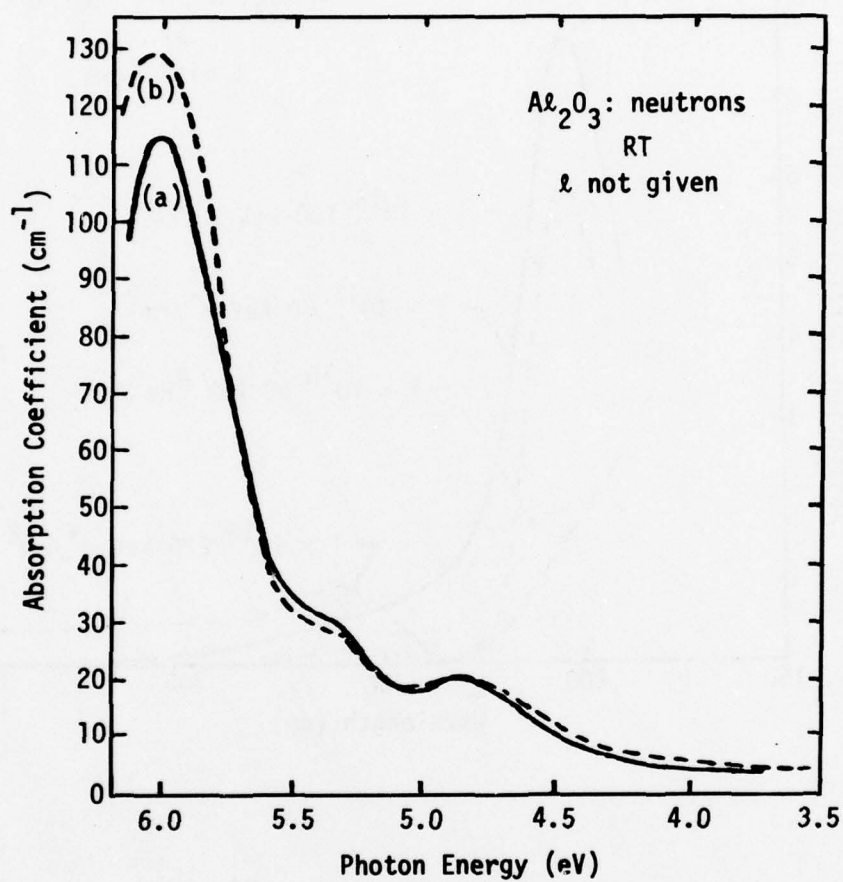
Fig. 4.72.   Absorption spectra of Al_2O_3 after irradiation by
(a) 14 MeV neutrons, 1×10^{17} n/cm^2, and (b) fission neutrons
($E_n > 0.1$ MeV), $\sim 5 \times 10^{17}$ n/cm^2.   [J. M. Bunch and F. W.
Clinard, Jr., J. Am. Ceram. Soc. 57, 279 (1974).]
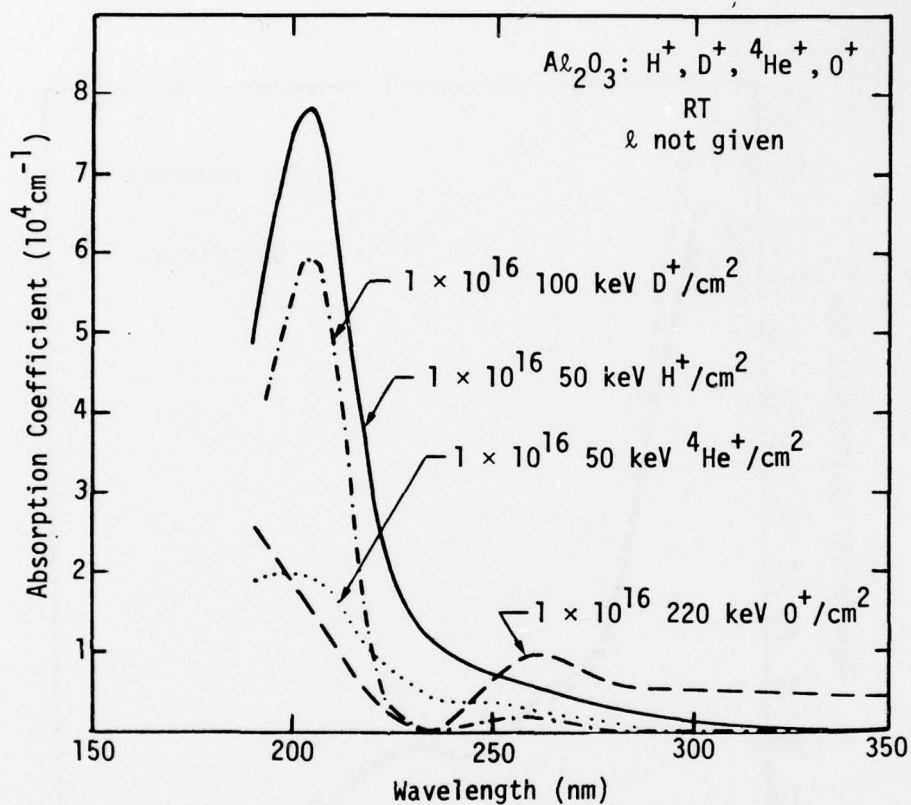
Fig. 4.73. Absorption spectra of $A\ell_2O_3$ crystals implanted with H^+, D^+, $^4He^+$ and O^+ ions. [G. W. Arnold, G. B. Krefft, and C. B. Norris, Appl. Phys. Lett. 25, 540 (1974).]

C. Magnesium Oxide[*]

Magnesium oxide (MgO) has the face-centered-cubic rock-salt (NaCℓ) structure and its binding is predominantly ionic. Because of its high melting point (2800 C) and high vapor pressure at the melting point, large MgO crystals required for commercial purposes are grown by the arc-fusion method. This technique produces badly strained crystals which contain several impurities, including hydrogen, transition metals (predominantly iron), Si, Aℓ, Zn, and foreign alkaline earths. Using a modified arc-fusion method, Butler, et al.,[4.37, 4.38] at the Oak Ridge National Laboratory have obtained high-purity MgO crystals containing a few parts per million of positive-ion impurities and a significantly lower concentration of hydrogen than the commercial crystals. The impurity analysis of an MgO boule grown at the Oak Ridge National Laboratory and of a commercial Spicer MgO crystal are given in Table 4.8.[4.39]

The room-temperature spectra of unirradiated and 3 MeV-Ne^+-bombarded Oak Ridge National Laboratory MgO crystals are shown in Fig. 4.74.[4.40] (The spectral features of the Ne^+-bombarded crystals will be discussed later.) The dashed curve near the bottom of the figure represents approximate Fresnel losses. The weak band seen near 5.7 eV (217.5 nm) in the absorption spectrum of the unirradiated crystal is ascribed to Fe^{3+} and other transition-metal impurities. The abrupt rise above 7.2 eV (172 nm) is believed to be due to the first-exciton-type transition in MgO. For a specimen 0.15 nm thick, an absorption coefficient of 5 cm^{-1} corresponds approximately to an optical density of 5 × 0.015/2.303 = 0.033. Considering the value of 0.2 for the Fresnel losses, the absorption edge corresponding to the optical density of 0.233 is seen at ~ 7.2 eV (172 nm).

---

[*]See summary Figure 1.6 of Volume I.

Table 4.8.   Impurity analyses of Oak Ridge National Laboratory and
Spicer MgO crystals.   [Y. Chen, D. L. Trueblood, O. E. Schow, and
H. T. Tohver, J. Phys. C: Solid State Phys. 3, 2501 (1970).]

Element	ORNL μg/g	Spicer μg/g
Ag	< 1	
Al	6	41
As		< 0.4
B	< 2	
Ba	< 3	< 0.6
Be	< 1	
Bi	< 3	
Ca	14	61
Co	< 10	
Cr	1	< 5
Cu	< 1	
Fe	2	3
Ge	< 5	
K	< 5	
Li	< 1	
Mn	≃ 0.06	0.3
Mo	< 1	
N	7	9
Na	0.7	0.3
Ni		< 5
P	5	2
Pb	< 5	< 0.5
Rb	< 5	
S	< 5	< 2
Sb	< 5	
Si	14	19
Sn	< 3	
Sr	< 5	
Ti	2	
V	< 3	
Zr	< 4	< 6
Zn		6

228
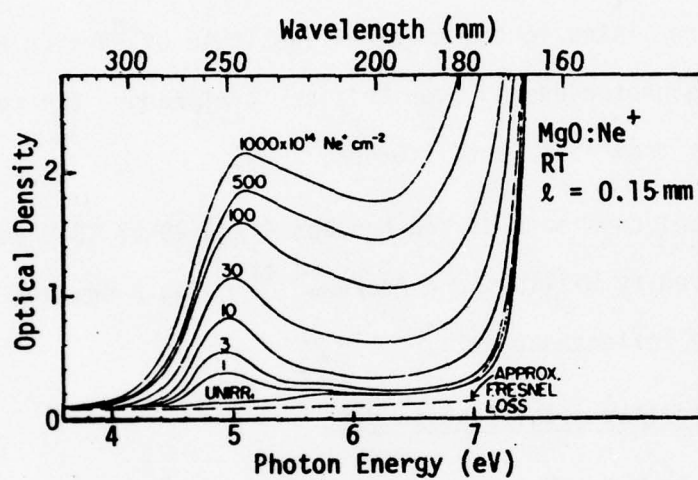
Fig. 4.74. Absorption spectra of unirradiated and
3 MeV Ne[+]-bombarded MgO crystals.   [B. D. Evans,
Phys. Rev. B 9, 5222 (1974).]

Figure 4.75 shows the reflectance of MgO measured at a 15° angle of incidence for photon energies between 4 and 29 eV (310 and 43 nm).[4.41] The optical absorption spectra of a thin film of MgO at 25 C and -170 C in the absorption edge region are shown in Fig. 4.76.[4.42]

The refractive index values of MgO between 361.2 and 5,350 nm (3.43 and 0.23 eV) are listed in the American Institute of Physics Handbook.[4.43] With decreasing photon energy over this spectral range, the refractive index decreases from 1.77318 to 1.62404.

The optical constants of MgO between 4 and 29 eV (310 and 43 nm) have been derived by Williams and Arakawa[4.41] using a Kramers-Kronig analysis of the reflectance data.

1. <u>Transition-metal ions in MgO.</u>

a. <u>V^{3+} in MgO.</u> The optical absorption spectrum of a V^{3+}-doped MgO crystal is shown in Fig. 4.77.[4.44] The two weak bands in the visible at 2 and 3 eV (620 and 413 nm) have been assigned respectively to the $^3T_1(t^2) \rightarrow {}^3T_2(et)$ and $^3T_1(t^2) \rightarrow {}^3T_1(et)$ transitions,[4.45] and the intense absorption band at 5.25 eV (236 nm) has been assigned to oxygen-to-vanadium charge transfer.[4.44] The vanadium-related absorptions in MgO are strongly influenced by the thermal history of the crystals. Fig. 4.78 illustrates the effects of annealing in various atmospheres on the UV absorption. It is seen that a 4 h treatment in hydrogen at 1400 C reduces the 5.25 eV (236 nm) absorption, apparently by converting some V^{3+} to V^{2+}, which is restored by a subsequent heat treatment in oxygen. Rapid cooling after a heat treatment in argon is seen to narrow the 5.25 eV (236 nm) band, presumably from a decreased association of the V^{3+} with
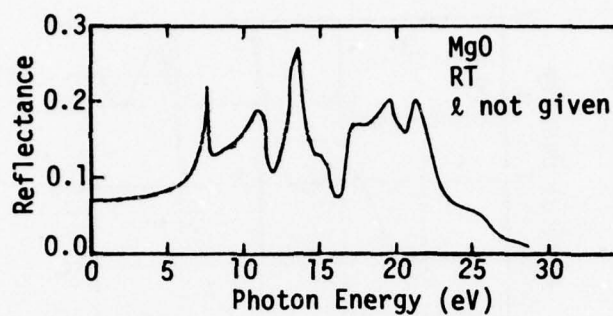
Fig. 4.75.   Reflectance spectrum of MgO for a 15 degree angle of incidence. [M. W. Williams and E. T. Arakawa, J. Appl. Phys. 38, 5272 (1967).]
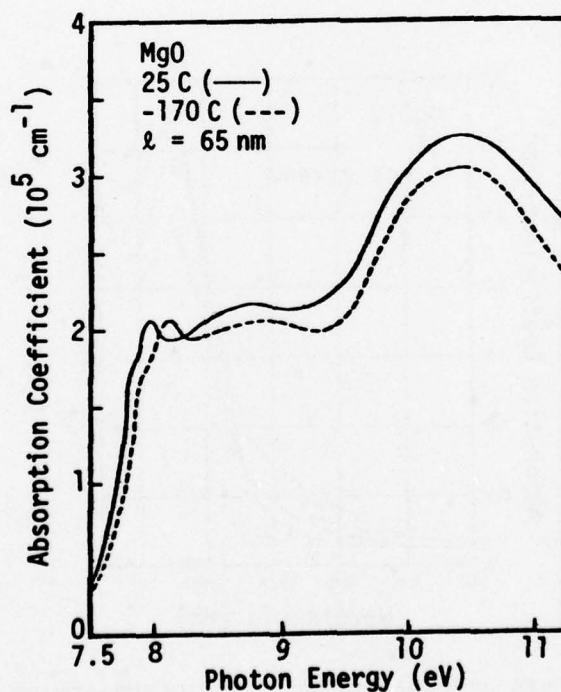
Fig. 4.76.   Optical absorption in the absorption edge region of a thin film of magnesium oxide on a lithium fluoride substrate. [G. H. Reiling and E. B. Hensley, Phys. Rev. 112, 1106 (1958).]
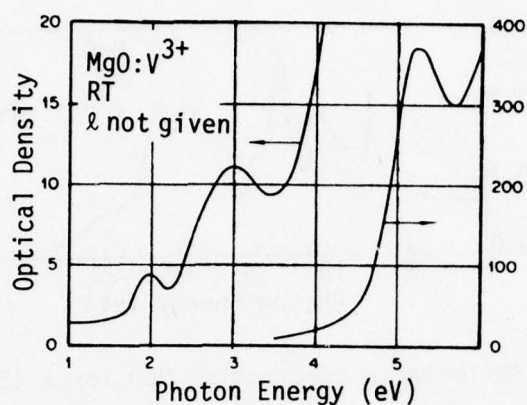
Fig. 4.77.   Absorption spectrum of V^{3+} in MgO.   [F. A. Modine, Phys. Rev. B $\underline{8}$, 854 (1973).]
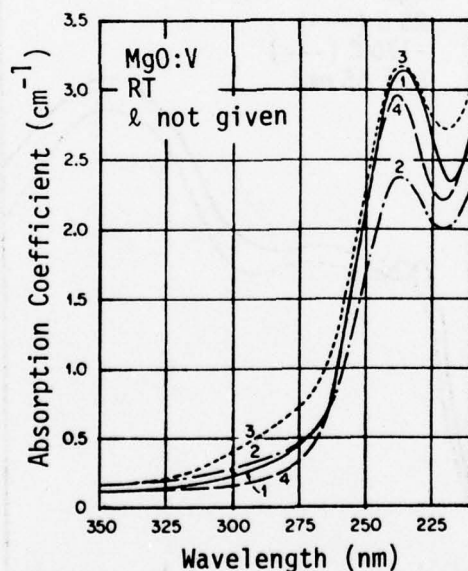
Fig. 4.78.   Effects of consecutive heat treatments on the optical absorption in V-doped MgO: (1) an untreated crystal shows only negligible change after 2 h at 1400 C in argon; (2) after 4 h at 1400 C in hydrogen; (3) after 2 h at 1400 C in oxygen; (4) after 2 h at 1000 C in argon and rapid cooling.   [F. A. Modine, Phys. Rev. B $\underline{8}$, 854 (1973).]

232

charge compensators.[4.44] A similar study of the visible absorption has been made by Sturge,[4.45] who, following a heat treatment in hydrogen, observed a decrease in the $^3T_1$ and $^3T_2$ bands which was accompanied by the appearance of three weak and narrow lines at 756 nm (1.64 eV), 743 nm (1.67 eV), and 730 nm (1.70 eV); the three lines were tentatively assigned to V^{2+}.

b. $\underline{Cr^{3+} \text{ in MgO.}}$ The optical and electron-spin-resonance studies show that the Cr^{3+} ion substitutes for Mg^{2+} in the MgO lattice and the charge compensation is achieved by the occurrence of vacancies in some cation sites.[4.46-4.50] Many chromium ions are found in sites of purely cubic symmetry where there is no local charge compensation, while others occupy non-cubic sites which are locally charge compensated. Schematic representations of the environments of Cr^{3+} ions in various non-cubic sites are shown in Fig. 4.79.[4.47] Of the non-cubic centers shown in Fig. 4.79, the tetragonal Cr-vacancy centers are encountered more often than the rhombic Cr-vacancy centers, and the Cr-vacancy-Cr centers exist in significant numbers only in MgO crystals containing relatively large concentrations of Cr impurities.

The optical absorption spectrum[4.50] in the range 1.74-4.34 eV (714-286 nm) of a Cr^{3+}-doped MgO crystal is shown in Fig. 4.80. A higher-resolution spectrum[4.48] of the same crystal in the range 672-663 nm (1.85-1.87 eV) is shown in Fig. 4.81. The positions, assignments, and the site symmetries (cubic or non-cubic) of Cr^{3+} ions responsible for the observed absorption peaks are as follows: 668.2 and 665.4 nm (1.856 and 1.863 eV), $^4A_2 \rightarrow {}^2T_1$, cubic; 613.5 nm (2.02 eV), $^4A_2 \rightarrow {}^4T_2$, cubic; 487.3 and 484.1 nm (2.544 and 2.561 eV), $^4A_2 \rightarrow {}^2T_2$, non-cubic; 452.5 nm (2.74 eV), $^4A_2 \rightarrow {}^4T_1$, cubic.[4.48] The oscillator strengths for the $^4T_2$
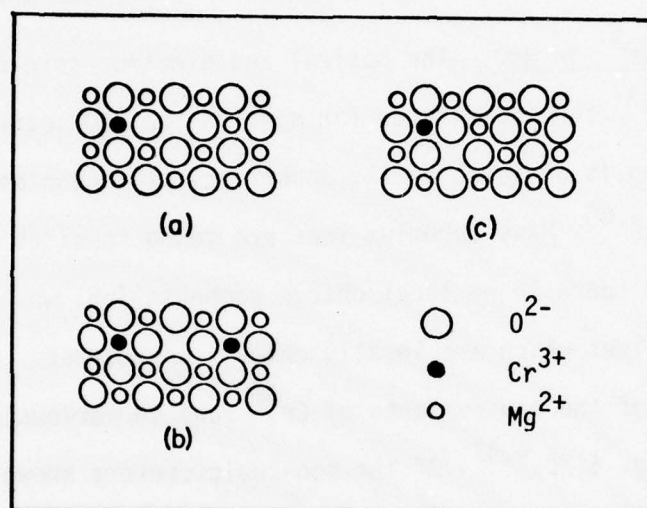
Fig. 4.79.   Representations of the (001) plane of MgO showing the environments of Cr^{3+} ions in non-cubic sites: (a) tetragonal Cr-vacancy center; (b) tetragonal Cr-vacancy-Cr center; (c) rhombic Cr-vacancy center. [J. P. Larkin, G. F. Imbusch, and F. Dravnieks, Phys. Rev. B 7, 495 (1973).]
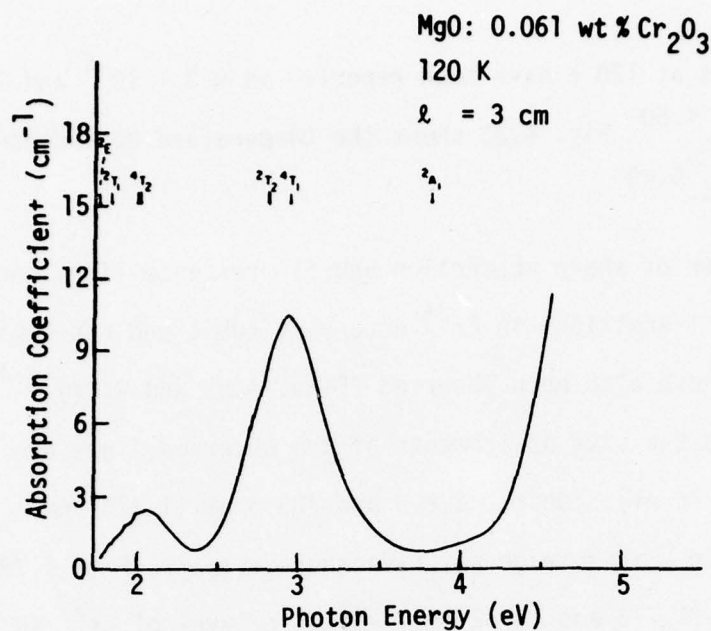
Fig. 4.80. Absorption spectrum of Cr^{3+}-doped MgO. [W. M. Fairbank, Jr., G. K. Klauminzer, and A. L. Schawlow, Phys. Rev. B 11, 60 (1975).]
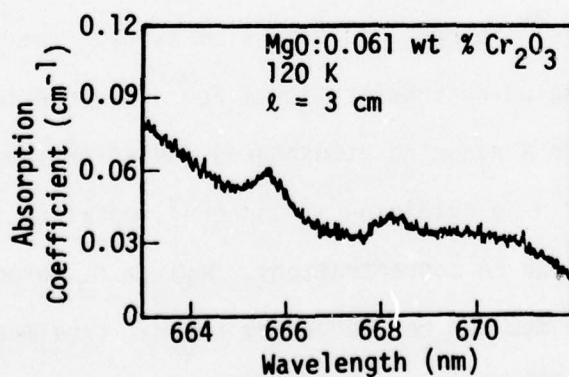
Fig. 4.81. Absorption spectrum of Cr^{3+}-doped MgO in the region of the $^4A_2 \rightarrow {}^2T_1$ transition. [W. M. Fairbank, Jr., and G. K. Klauminzer, Phys. Rev. B 7, 500 (1973).]

and $^4T_1$ bands at 120 K have been reported as 0.3×10^{-4} and 1.7×10^{-4}, respectively.[4.50] Fig. 4.82 shows the temperature dependence of the $^4T_2$ and $^4T_1$ bands.[4.49]

A number of sharp absorption and fluorescence lines corresponding to $^4A_2 \leftrightarrow {}^2E$ transitions in Cr^{3+} occupying cubic and non-cubic sites in the MgO lattice have also been observed (Figs. 4.83 and 4.84).[4.47] The peak positions and the site assignments of the observed lines are as follows: 698.1 nm (1.776 eV), cubic; 698.9 and 703.5 nm (1.774 and 1.762 eV), split ^2E level of Cr^{3+} in tetragonal Cr-vacancy-Cr pairs (Fig. 4.79b); 699.2 and 703.8 nm (1.773 and 1.762 eV), split ^2E level of Cr^{3+} in tetragonal Cr-vacancy pairs (Fig. 4.79a).[4.47]

Notice that the lines in Fig. 4.84 at 703.1 and 704.2 nm appear strong in the absorption spectrum but do not occur in the fluorescence spectrum. Larkin, et al.,[4.47] indicate that these lines may arise from chromium ions in rhombic sites or from Cr-vacancy-M centers, where M is a background impurity which might be present in MgO.

c. $\underline{Fe^{2+} \text{ and } Fe^{3+} \text{ in MgO.}}$ In magnesium oxide, iron is known to exist in various forms, including substitutional Fe^{2+} (favored in samples annealed in a vacuum or a reducing atmosphere), substitutional Fe^{3+} (favored in samples annealed in an oxidizing atmosphere), metallic iron, and in samples containing high Fe concentrations, $MgO \cdot Fe_2O_3$ precipitates.[4.51] The forms of iron in MgO can be changed by thermal treatment and by irradiation. Fig. 4.85 illustrates the influence of the thermal history on the absorption of MgO containing 5000 ppm of Fe impurity. It is seen that while the spectrum of the sample annealed in a CO atmosphere is featureless (most of the Fe in this sample is expected to be present in the divalent
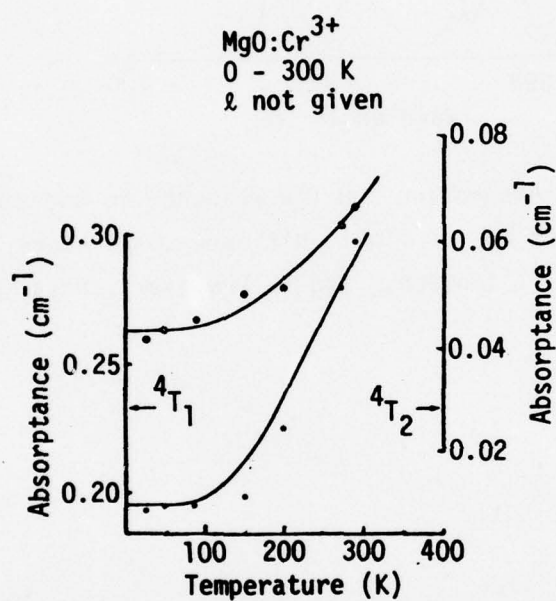
Fig. 4.82. Temperature dependence of the $^4T_2$ (open circles) and $^4T_1$ (closed circles) bands in MgO:Cr^{3+}. [K. Y. Wong, D. Sengupta, and D. J. Mackey, J. Phys. Chem. Solids $\underline{35}$, 313 (1974).]
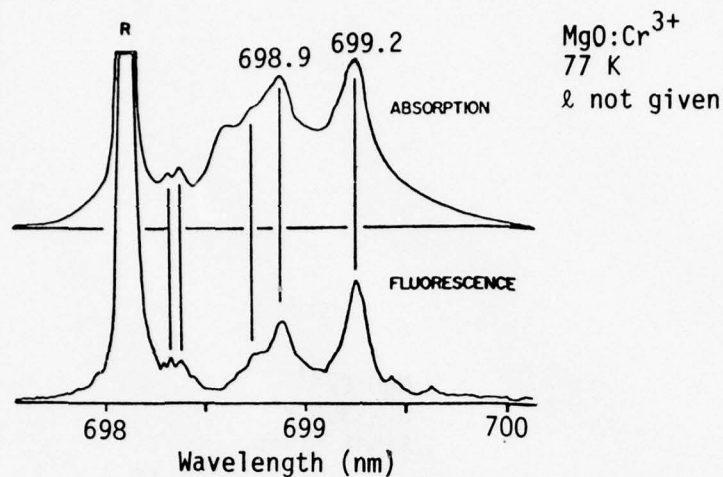
Fig. 4.83. Absorption and fluorescence in the same sample of Cr^{3+}-doped MgO at liquid-nitrogen temperature. [J. P. Larkin, G. F. Imbusch, and F. Dravnieks, Phys. Rev. B 7, 495 (1973).]
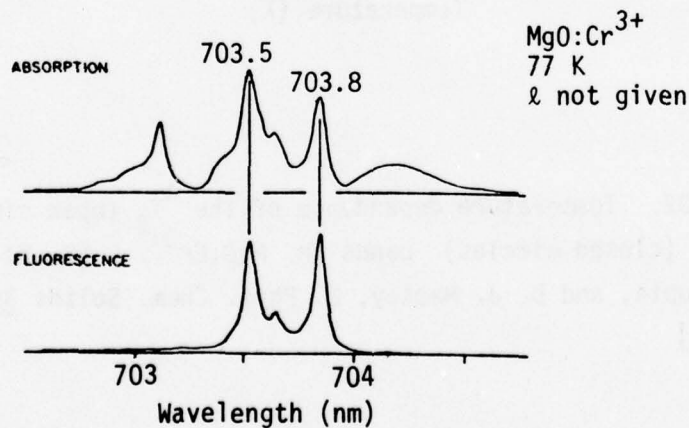
Fig. 4.84. Absorption and fluorescence in the same sample of Cr^{3+}-doped MgO at liquid-nitrogen temperature. [J. P. Larkin, G. F. Imbusch, and F. Dravnieks, Phys. Rev. B 7, 495 (1973).]

238
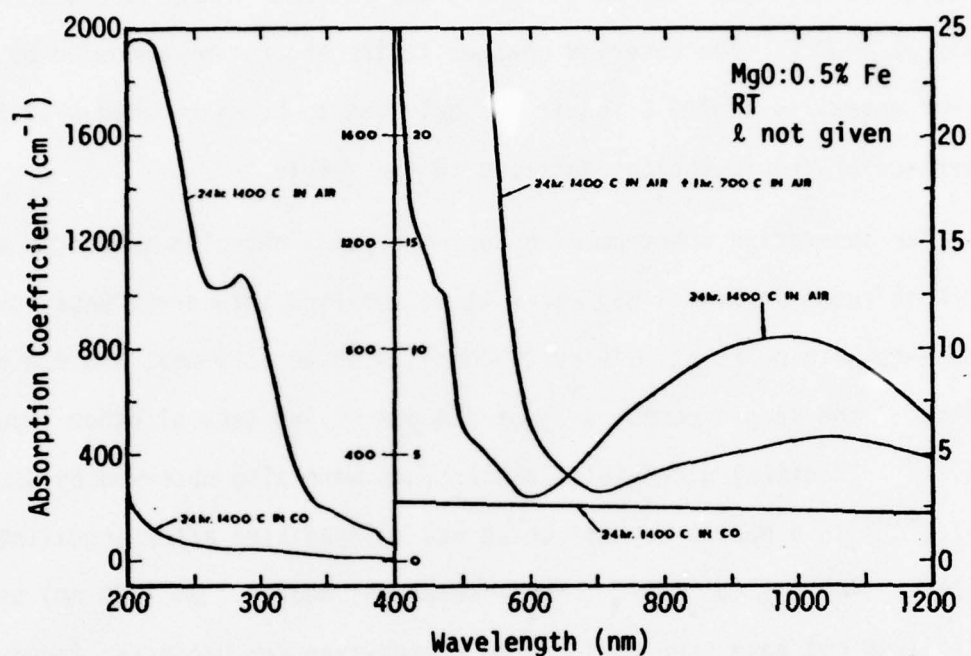
Fig. 4.85. Optical absorption spectra after three heat
treatments of an MgO crystal containing 5000 ppm Fe.
[R. W. Davidge, J. Mat. Sci. 2, 339 (1967).]

239

form), at least seven absorption bands with peaks near 210 nm (5.9 eV), 285 nm (4.35 eV), 360 nm (3.44 eV), 385 nm (3.22 eV), 460 nm (2.70 eV), 540 nm (2.30 eV), and 1000 nm (1.24 eV) are present in the sample annealed in air at 1400 C. The observed changes in the absorption produced by subsequent annealing at 700 C in air are believed to be associated with the occurrence of precipitation reactions in the sample.

The absorption spectrum of a Norton crystal annealed in oxygen at 1250 C is shown in Fig. 4.86, where it is resolved into three Gaussian components with peaks at 5.75 eV (216 nm), 4.85 eV (256 nm), and 4.3 eV (288 nm); the sample contains about 200 ppm Fe and several other impurities.[4.52] Identical ultraviolet absorptions were also observed by Soshea, et al.,[4.52] in a Norton crystal which was X irradiated after annealing in vacuum at 1400 C (Fig. 4.87). The absorptions near 5.7 eV (220 nm) and 4.3 eV (290 nm) have been assigned to charge-transfer processes involving Fe^{3+}.[4.53]

Fig. 4.88 illustrates the variation of absorption at 285 nm (4.35 eV) with iron content of MgO. The 285 nm-absorption measurements in samples containing more than 100 ppm Fe were made by Davidge,[4.51] who annealed his crystals in air at 1400 C and subsequently fast cooled them to attain saturation levels. The other data were obtained by Chen and Sibley,[4.54] who annealed their samples at 1100 C in argon and subsequently γ irradiated them to saturate the absorption at 285 nm (4.35 eV). Oscillator strengths in the range 0.04-0.1 have been reported for the 4.35 eV (285 nm) and 5.7 eV (220 nm) Fe^{3+} charge-transfer bands.[4.51,4.53]

d. <u>Co^{2+} in MgO.</u> Optical absorption spectra of Co^{2+}-doped MgO in the infrared at 290 K, and in the visible at 290 K and at 77 K are shown
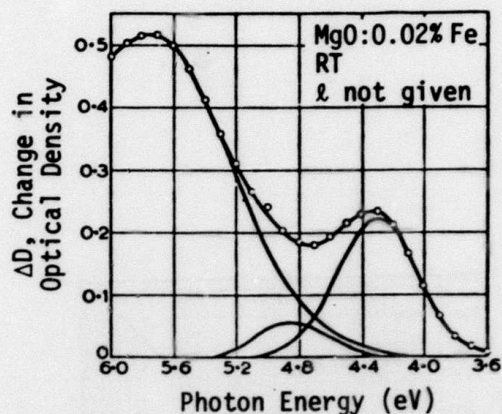
Fig. 4.86. Optical density enhancement of an MgO crystal following an annealing at 1250 C in an oxidizing atmosphere. The spectrum has been resolved into Gaussian components with peaks at 5.75, 4.85, and 4.3 eV. [R. W. Soshea, A. J. Dekker, and J. P. Sturtz, J. Phys. Chem. Solids 5, 23 (1958).]
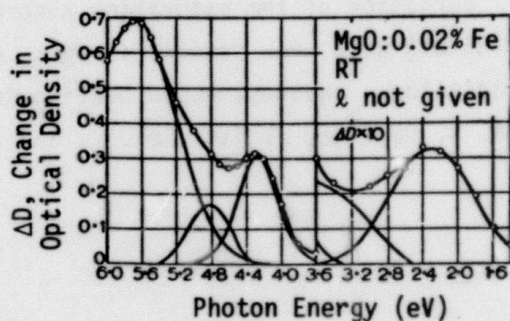
Fig. 4.87. Increase in optical absorption of an MgO crystal resulting from X irradiation at room temperature. The spectrum has been resolved into Gaussian components with peaks near 5.7, 4.8, 4.3, and 2.3 eV, and some additional absorption near 3.6 eV. [R. W. Soshea, A. J. Dekker, and J. P. Sturtz, J. Phys. Chem. Solids 5, 23 (1958).]
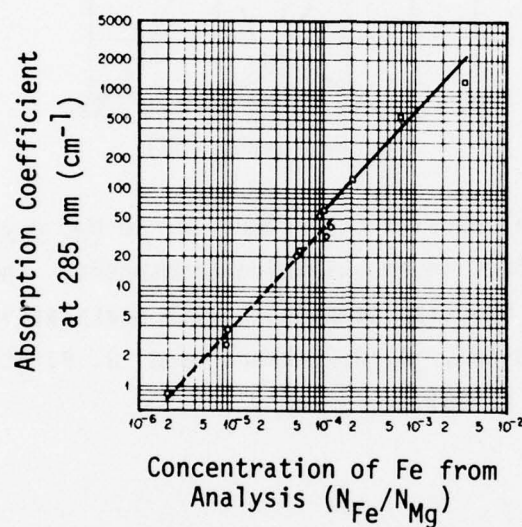
Fig. 4.88. Variation of the saturation absorption at
285 nm (4.35 eV) with Fe content in MgO: circles,
upon γ irradiation; squares, upon heating in air at
1400 C. [R. W. Davidge, J. Mat. Sci. 2, 339 (1967).]

in Figs. 4.89, 4.90, and 4.91, respectively.[4.55]   Figure 4.92 shows the energy level diagram as constructed from the observed absorption lines of Co^{2+} in MgO.

e. Ni^{2+} in MgO.   The near-infrared and visible absorption spectra of an MgO crystal diffusion-doped with NiO are shown in Fig. 4.93 and Fig. 4.94, respectively.[4.56]   The observed lines have been assinged to Ni^{2+}; their peak positions are: 1160 nm (1.07 eV), 730 nm (1.70 eV), 680 nm (1.82 eV), 464 nm (2.67 eV), 408 nm (3.04 eV), 385 nm (3.22 eV), 353 nm (3.51 eV), and 290 nm (4.28 eV).   The assignments of the observed absorptions are indicated in the energy level diagram of Ni^{2+} in MgO shown in Fig. 4.95.

The absorption spectra of $^{3}T_{2}$, $^{3}T_{1}{}^{a}$, $^{1}T_{2}$, and $^{3}T_{1}{}^{b}$ bands cf Ni^{2+} in MgO at several temperatures over the range 8 - 222 K are shown in Figs. 4.96 through 4.99, respectively.[4.57]

2. Radiation-induced absorptions in MgO.

a. V-type center in MgO.   A prominent absorption band near 2.3 eV (5.39 nm), assigned to V-type (trapped-hole) centers, is produced in MgO by ionizing radiation.   The shape of this band at 5, 78, and 295 K is shown in Fig. 4.100,[4.54] where the absorption seen on the high-energy side of the 2.3 eV (539 nm) band is primarily due to iron impurities.   (Compare the absorption spectrum in Fig. 4.87 with that in Fig. 4.86.)   The 2.3 eV (539 nm) band typically reaches saturation at an exposure level of the order of 10^{7} R.   Chen and Sibley[4.54] found that the saturation value and the room temperature decay rate of the 2.3 eV (539 nm) band were dependent on the sample purity and quenching temperature (Figs. 4.101 and 4.102).
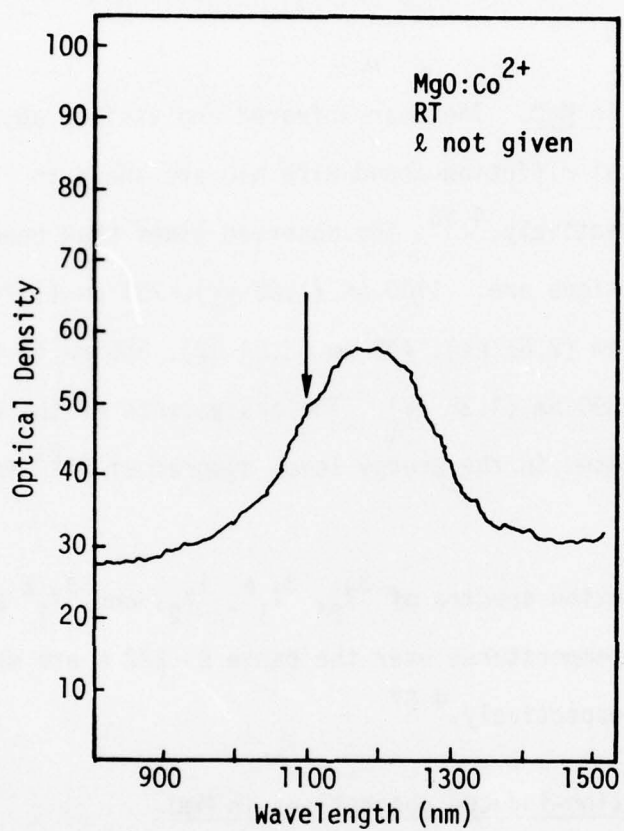
Fig. 4.89. Infrared spectrum of Co^{2+} in MgO. An additional
small peak is located at 1100 nm.   [W. Low, Phys. Rev. 109,
256 (1958).]
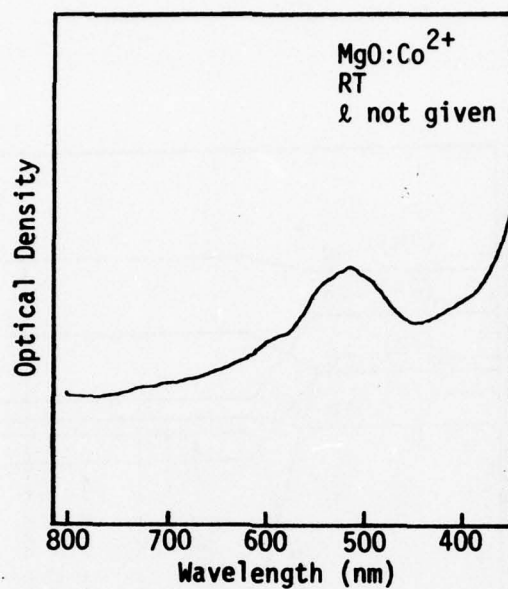
Fig. 4.90. Visible spectrum of Co^{2+} in MgO. [W. Low, Phys. Rev. 109, 256 (1958).]
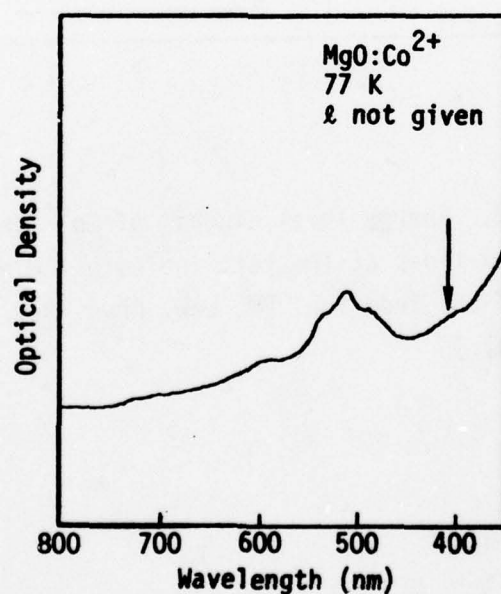
Fig. 4.91. Visible spectrum of Co^{2+} in MgO. The line at 407 nm becomes noticeable at this temperature. [W. Low, Phys. Rev. 109, 256 (1958).]
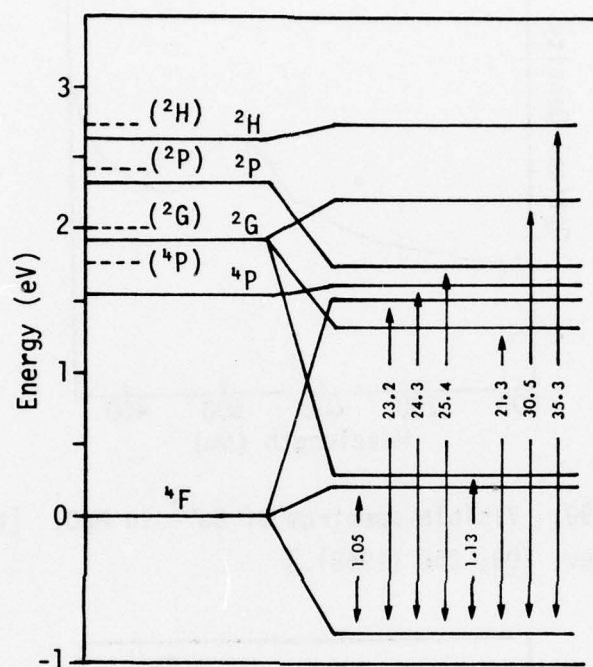
Fig. 4.92. Energy level diagram of Co^{2+} in MgO.
The dotted lines at the left indicate the energy
levels of the free ion. [W. Low, Phys. Rev. 109,
256 (1958).]
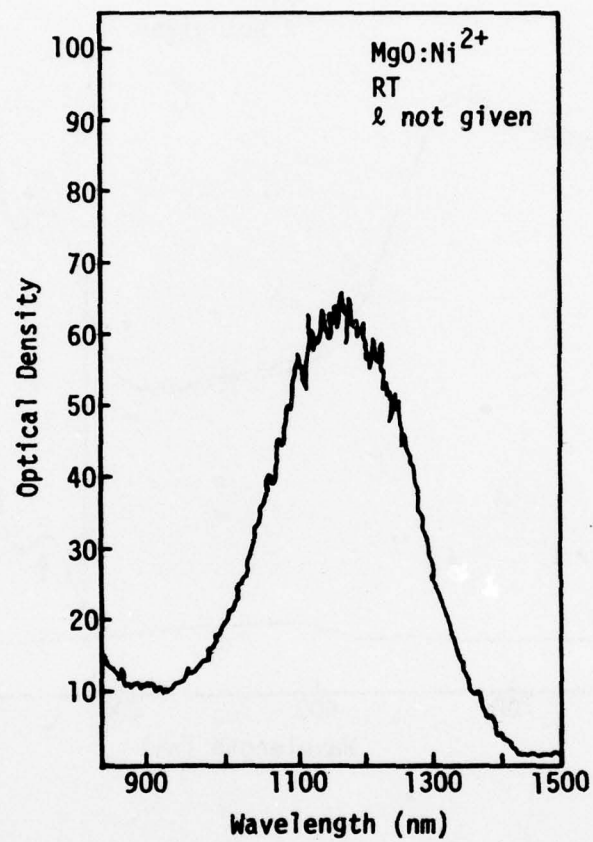
Fig. 4.93. Near-infrared spectrum of Ni^{2+} in MgO.
[W. Low, Phys. Rev. 109, 247 (1958).]
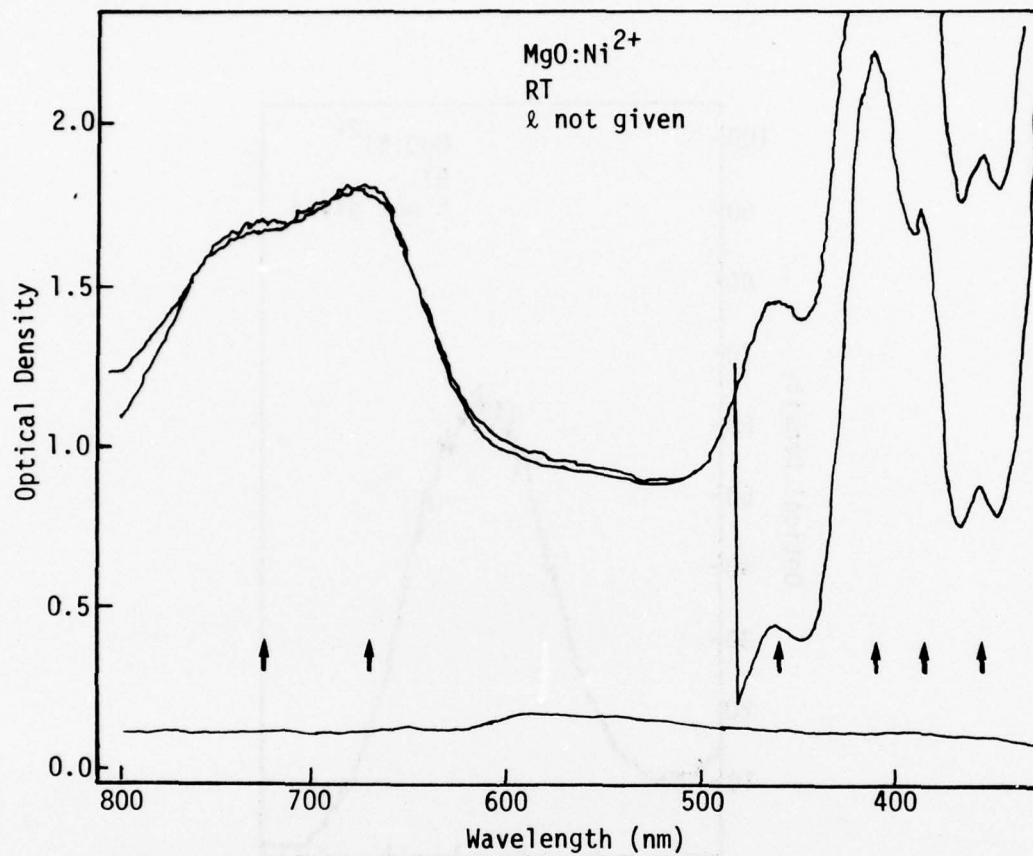
Fig. 4.94. Visible spectrum of Ni^{2+} in MgO. The intense line at 410 nm went off the scale;   its tracing without any change in amplification is shown on the lower right-hand corner. [W. Low, Phys. Rev. 109, 247 (1958).]
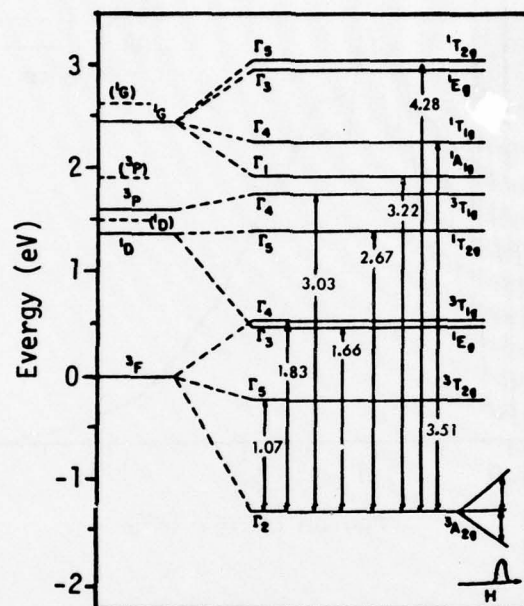
Fig. 4.95. Energy level diagram showing the assignments of the observed optical transitions of Ni^{2+} in MgO. [W. Low, Phys. Rev. 109, 247 (1958).]
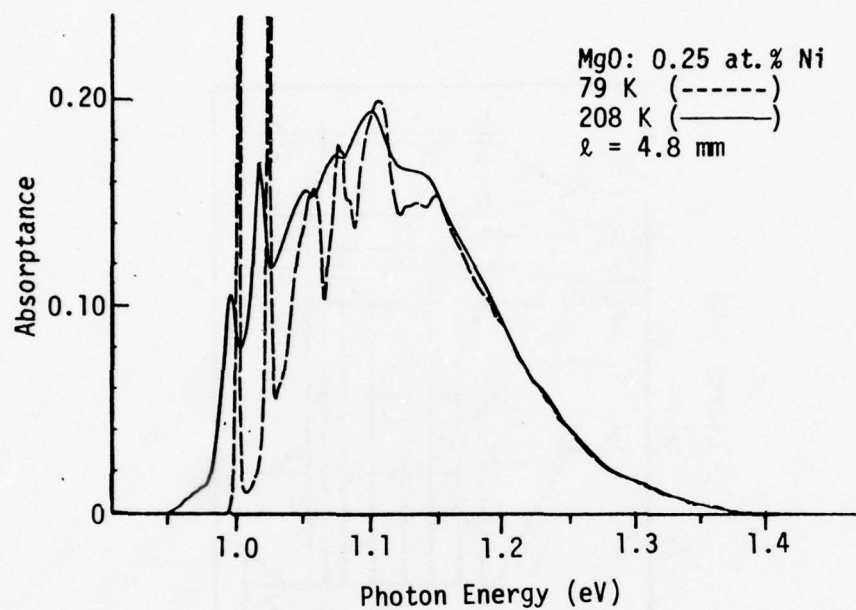
Fig. 4.96.   Absorption spectrum of $^3T_2$ band of MgO:Ni at 79 and 208 K. [B. D. Bird, G. A. Osborne, and P. J. Stephens, Phys. Rev. B <u>5</u>, 1800 (1972).]
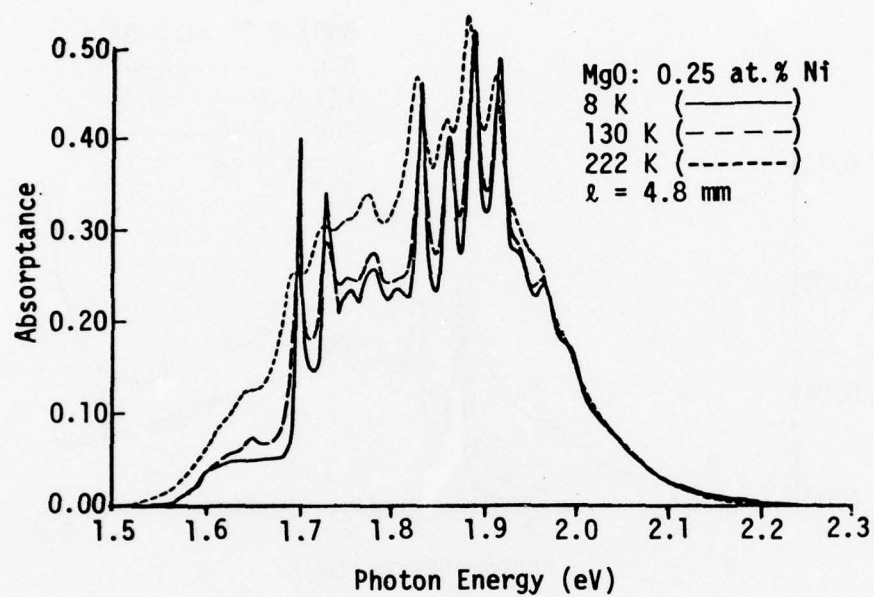
Fig. 4.97.   Absorption   spectrum   of $^3T_1^a$ band of MgO:Ni at 8, 130, and 222 K. [B. D. Bird, G. A. Osborne, and P. J. Stephens, Phys. Rev. B $\underline{5}$, 1800 (1972).]
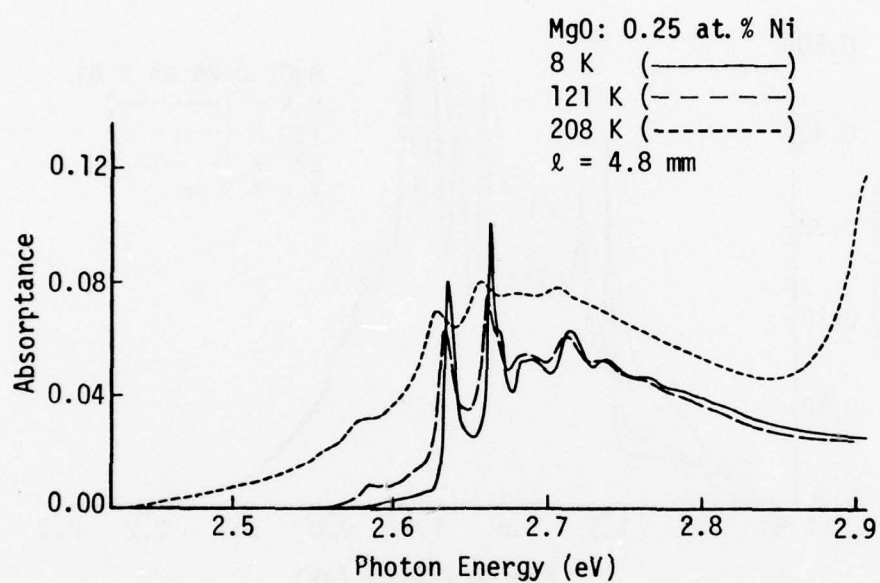
Fig. 4.98. Absorption spectrum of $^{1}T_{2}$ band of MgO:Ni at 8, 121, and 208 K. [B. D. Bird, G. A. Osborne, and P. J. Stephens, Phys. Rev. B $\underline{5}$, 1800 (1972).]
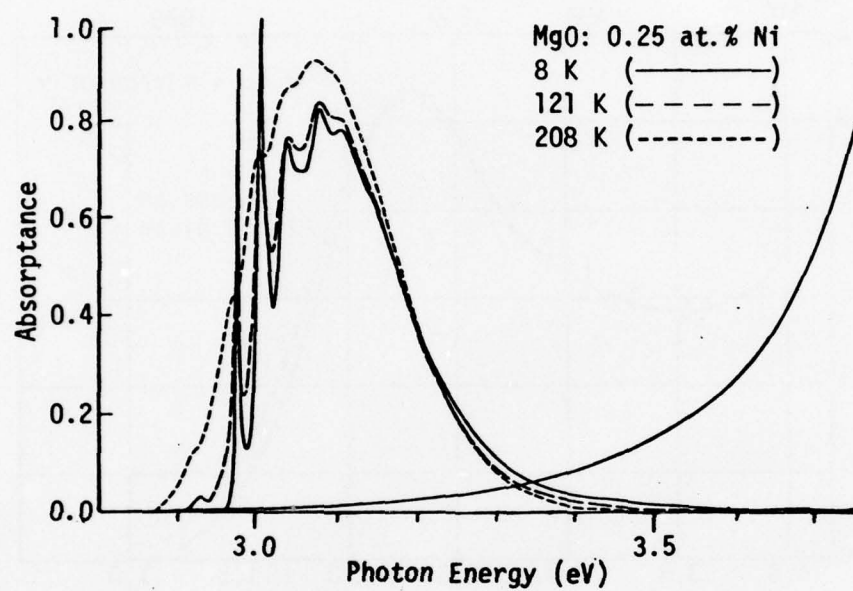
Fig. 4.99. Absorption spectrum of $^3T_1^b$ band of MgO:Ni at 8, 121, and 208 K. Baselines have been subtracted.   The smoothly rising curve represents the baseline at 8 K. [B. D. Bird, G. A. Osborne, and P. J. Stephens, Phys. Rev. B $\underline{5}$, 1800 (1972).]
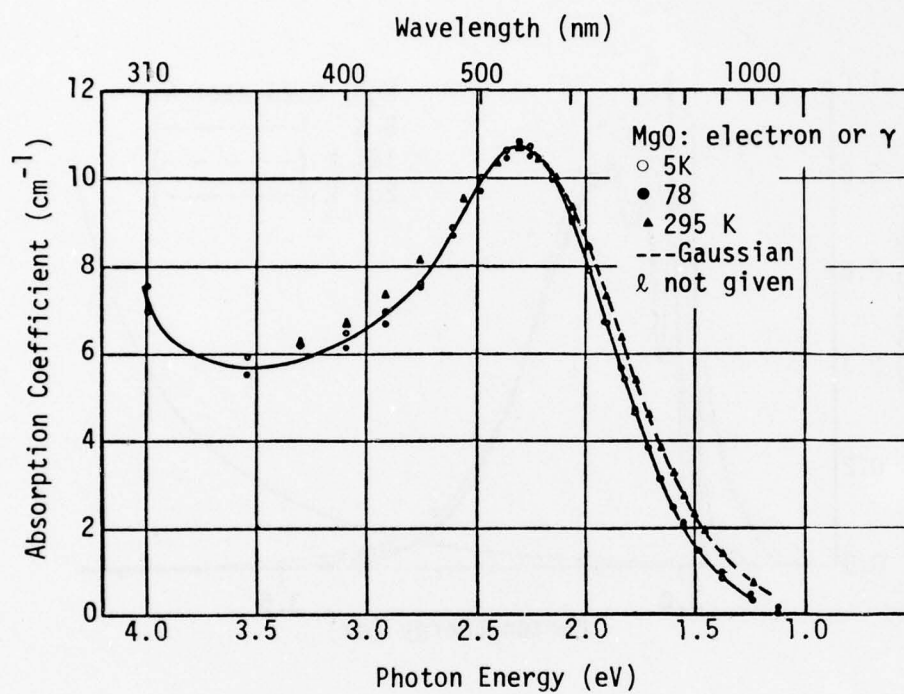
Fig. 4.100.   The 2.3 eV (539 nm) band in MgO resulting from gamma
or electron irradiation at 5, 78, and 295 K.   [Y. Chen and W. A.
Sibley, Phys. Rev. 154, 842 (1967).]
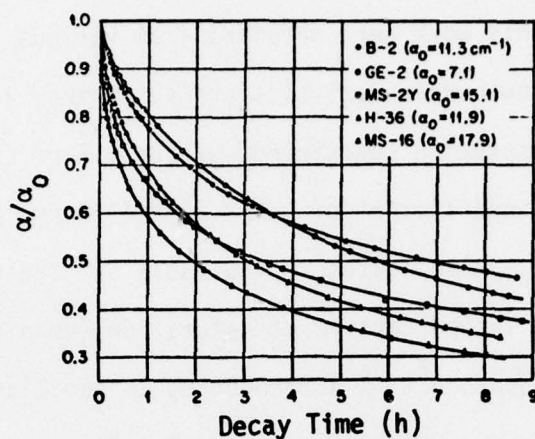
Fig. 4.101. Room-temperature decay rates of the 2.3 eV (539 nm) band in different MgO crystals irradiated to saturation by a gamma source. The saturation value α_0 obtained in various crystals is indicated in the inset. α/α_0 is the fraction of the 2.3 eV absorption that has not decayed. See also Table 4.9. [Y. Chen and W. A. Sibley, Phys. Rev. 154, 842 (1967).]
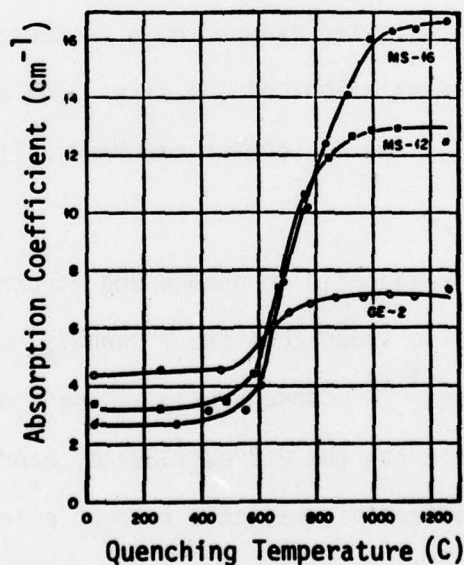
Fig. 4.102. Absorption coefficient of the 2.3 eV (539 nm) band resulting from γ-irradiation to saturation in MgO crystals quenched from various temperatures. The samples were obtained from different commercial sources — see Table 4.9. [Y. Chen and W. A. Sibley, Phys. Rev. 154, 842 (1967).]

The samples used in this work were obtained from various sources. Their designations and various characteristics are summarized in Table 4.9, where α_{OH} represents the absorption coefficient of the 3.3 μm (0.38 eV) OH band and α_V the absorption coefficient of the 2.3 eV (539 nm) band in a quenched crystal at saturation. Also listed in the table are the estimates of the concentrations of the V-type centers at saturation (obtained using a Gaussian form of the Smakula equation[4.57a] and choosing an oscillator strength of 0.15, half-width of 0.96 eV, and refractive index of 1.74).

In recent years several studies of radiation-induced defects in MgO have been made, involving optical absorption and electron spin resonance techniques alone[4.58-4.61] or in conjunction with the electron-nuclear double-resonance technique.[4.62,4.63] These studies indicate that the absorption in the vicinity of 2.3 eV (539 nm) in irradiated MgO is associated with one or more of the following trapped-hole centers: V^-, V^0, V_{OH}, V_F, and $V_{A\ell}$. Schematic representations of the first four of these centers are shown in Fig. 4.103;[4.64] the $V_{A\ell}$ center has the configuration $O^- - (Mg^{2+}$ vacancy$) - O^{--} - A\ell^{3+}$.

Recent electron paramagnetic resonance and electron-nuclear double-resonance studies have also shown that the V^- and $V_{A\ell}$ centers absorb microwave power at the same g value.[4.62] Consequently, in many of the earlier studies of the defects responsible for the 2.3 eV (539 nm) band, which were made using only the optical and electron paramagnetic resonance techniques, no distinction between the V^- and $V_{A\ell}$ centers was made.

The thermal stability of the various trapped-hole centers in MgO decreases in the order V^-, $V_{A\ell}$, and V_{OH}. At room temperature, the half-lives of V_{OH} and $V_{A\ell}$ centers are of the order of hours, while the V^- center

Table 4.9. Designations, impurity concentrations, and the colorability of the 2.3 eV (539 nm) V band in MgO crystals from various sources. [Y. Chen and W. A. Sibley, Phys. Rev. 154, 842 (1967).]

Sample	Thickness (cm)	Source	α_V (cm^{-1})	Estimated V conc. (cm^{-3})	α_{OH} (cm^{-1})	Fe (ppm)	Cr (ppm)
H-36	0.167	Harwell	11	4×10^{17}	0.8	5	<1
H-4	0.145	Harwell	8	3×10^{17}	1.6	80	<1
GE-2,4,5,	0.082 0.167 0.186	General Electric	7	3×10^{17}	1.6	5	<1
MS-12,15 16,19	0.051 0.140 0.122 0.213	Muscle-Shoals	11–17	4–6×10^{17}	0.3	52	20
B-2,3,4	0.149 0.135 0.134	Bristol	10–11	3×10^{17}	0.8	10	2
N-13-Mn	0.121	Norton	0	0	2.9	...	...
MS-2Y	0.121	Muscle-Shoals	14	5×10^{17}	0	100	15
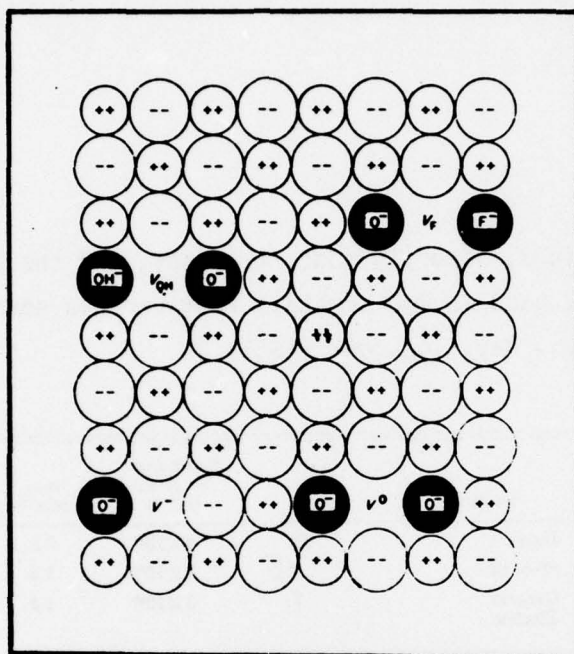
Fig. 4.103.   Schematic representations of the structures of V_{OH}, V^-, V^0, and V_F centers in alkaline-earth oxides.   F and H designate fluorine and hydrogen impurities, respectively. [E. Sonder and W. A. Sibley, in Point Defects in Solids, Vol. 1 of General and Ionic Crystals, edited by J. W. Crawford, Jr. and L. M. Slifkin, (Plenum, New York, 1972), Chapter 4.]

has a half-life of several months.[4.65] The differences in the decay characteristics of the various V-type centers enabled Kappers, et al.,[4.58] to deduce the contribution of the V_{OH} centers to the 2.3 eV (539 nm) absorption, as illustrated in Fig. 4.104. In the figure, all the absorption bands shown were recorded at 77 K; curve (a) represents absorption immediately after X irradiation at 77 K, and curve (b) shows the absorption in the same crystal following an annealing treatment at 25 C for 68 hours. Since the parallel electron spin resonance studies indicated that the annealing treatment had completely bleached the V_{OH} centers without significantly affecting the concentrations of other trapped-hole centers, the curve (c), obtained by subtracting curve (b) from curve (a) in Fig. 4.104, was assigned to V_{OH} centers.

Using a somewhat more involved procedure, Kappers, et al.,[4.60] were also able to determine the peak positions, half-widths, and oscillator strengths of V^0, V^-, and V_{OH} centers at various temperatures between 4 and 298 K (Table 4.10). Optical absorption bands arising from V_{OH}, V^0, and V^- centers are shown in Fig. 4.105, where they are normalized to the same peak height for comparison.

b. <u>Na in MgO.</u> In MgO containing substitutional sodium ions, a trapped-hole center with the configuration $O^{--} - Na^+ - O^-$ has been identified. The center is named $[Na]^0$; it absorbs near 1.58 eV (785 nm) as shown in Fig. 4.106.[4.66]

c. <u>F and F^+ centers in MgO.</u> Since the oxygen is divalent, one or two electrons can be trapped by a vacant anion site in the MgO lattice; the centers thus formed are designated F^+ and F, respectively.
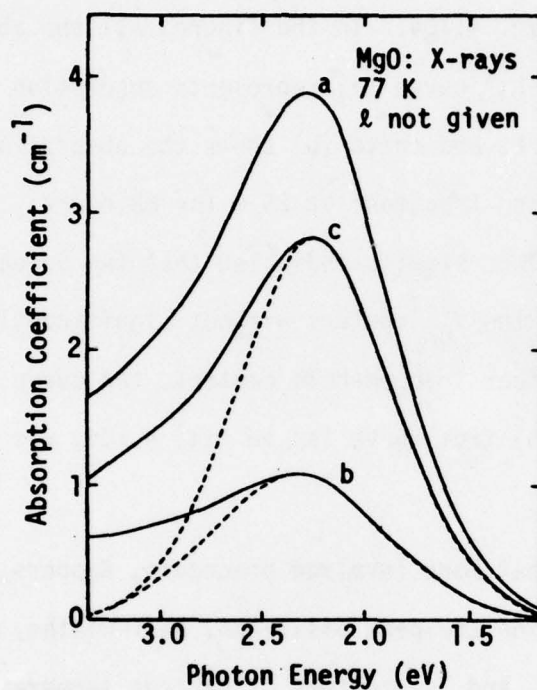
Fig. 4.104. Induced optical absorption spectra of X-irradiated MgO crystal at 77 K. (a) Absorption spectrum observed immediately following a 20 min X-ray exposure at 77 K. (b) Absorption spectrum observed after 68 hr heat treatment at 25 C in the dark. (c) Optical absorption band assigned to the V_{OH} center in MgO, obtained from difference between absorption curves a and b. [L. A. Kappers, F. Dravnieks, and J. E. Wertz, Solid State Commun. 10, 1265 (1972).]

Table 4.10. Optical parameters for V^0, V^-, and V_{OH} centers in MgO. [L. A. Kappers, F. Dravnieks, and J. E. Wertz, J. Phys. C: Solid State Phys. 7, 1387 (1974).]

Centre	Peak position (eV)			Half-width (eV)			Oscillator strength
	4 K	77 K	298 K	4 K	77 K	298 K	
V^0	2·37	2·37	2·36	0·95	0·95	1·04	0·24
V^-	2·33	2·33	2·33	0·97	0·97	1·10	0·15
V_{OH}	2·23	2·23	2·21	0·88	0·88	0·94	0·10
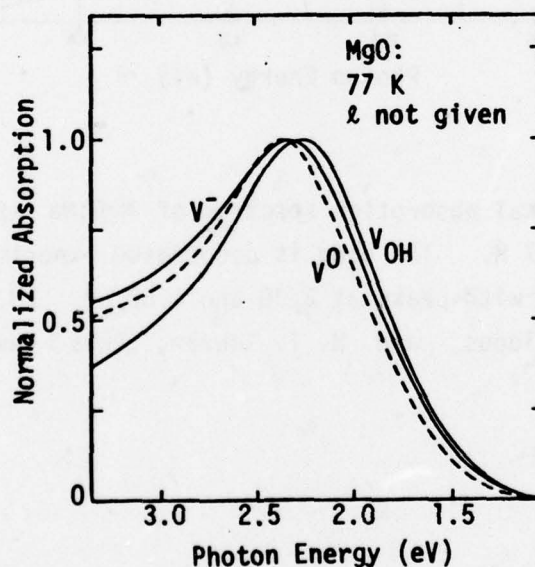
Fig. 4.105. Comparison of the optical absorption bands assigned to the V^-, the V_{OH}, and the V^0 centers in MgO. [L. A. Kappers, F. Dravnieks, and J. E. Wertz, J. Phys. C: Solid State Phys. 7, 1387 (1974).]
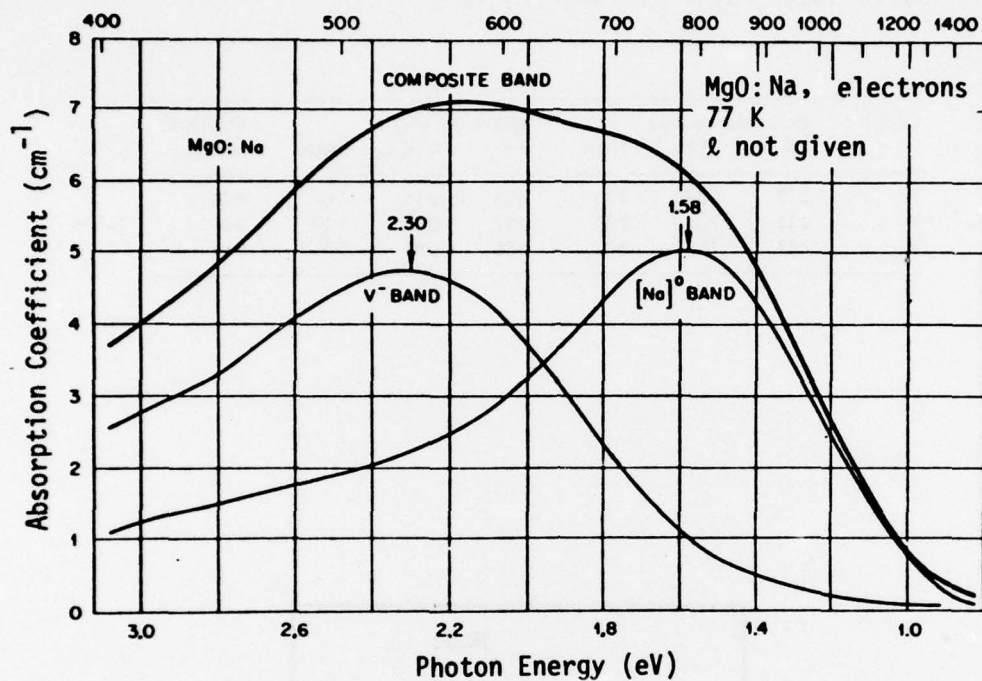
Fig. 4.106. Optical absorption spectrum of MgO:Na after electron irradiation at 77 K. The band is decomposed experimentally into two separate bands with peaks at 2.30 and 1.58 eV. [M. M. Abraham, Y. Chen, J. L. Kolopus, and H. T. Tohver, Phys. Rev. B 5, 4945 (1972).]

An absorption band near 250 nm (5.0 eV) is observed in MgO crystals
irradiated with fast neutrons. Parallel electron spin resonance and optical
absorption studies on neutron-irradiated MgO crystals indicate that the band
is due to F^+ centers.[4.67] Figure 4.107 shows the absorption spectra of MgO
crystals irradiated with doses of fast neutrons (E > 1 MeV) in the range
5×10^{16} to 10^{20} cm^{-2}. It can be seen that the F^+-center concentration
reaches a maximum at a dosage of $\sim 9 \times 10^{18}$ cm^{-2}. The shape of the F^+ band
at 4, 298, and 473 K is shown in Fig. 4.108.[4.68]

MgO crystals have been additively colored by heating them in Mg vapor
at temperatures between 1600 and 1800 C.[4.68] An absorption band nearly
identical in peak position and half-width with the F^+ band is observed in
additively colored MgO (Fig. 4.109). Electron spin resonance studies indi-
cate that the 250 nm (4.96 eV) band in additively colored MgO is due to F
centers.[4.68] (While an F center and an F^+ center absorb light of nearly the
same wavelength, the distinction between the two centers can be made by
electron spin resonance because the F center in the ground state does not
absorb microwave power.)

The $F \rightarrow F^+$ photoconversion process in MgO is illustrated in
Fig. 4.110,[4.68] where curve (1) represents the spectrum of an additively
colored crystal, while curve (2) shows the shift in the absorption as a
result of irradiation with 250 nm (5.0 eV) light. The shift occurs because
the 250 nm (5.0 eV) light releases electrons from several F centers and
converts them into F^+ centers. The released electrons are apparently
trapped by impurities in the crystal since the subsequent heating to 800 C
is seen to destroy the F^+ band and simultaneously restore the F band,
curve (c). The observed increase in the absorption near 5 eV upon optical
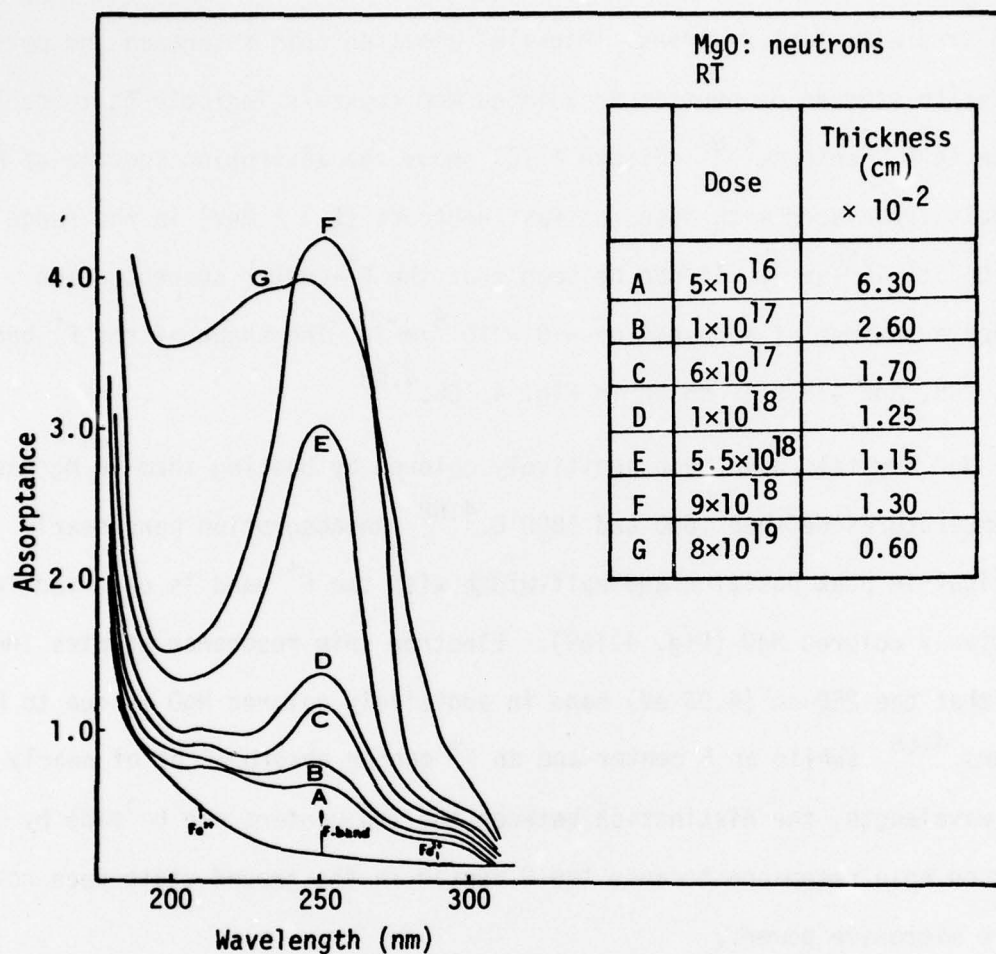
Fig. 4.107. The growth of the 250 nm (5.0 eV) band as a function of 1 MeV neutron dose in MgO. The sample contained 50 ppm of Fe impurity; the positions of the Fe^{3+} absorptions are indicated. [B. Henderson and R. D. King, Phil. Mag. 13, 1149 (1966).]

264
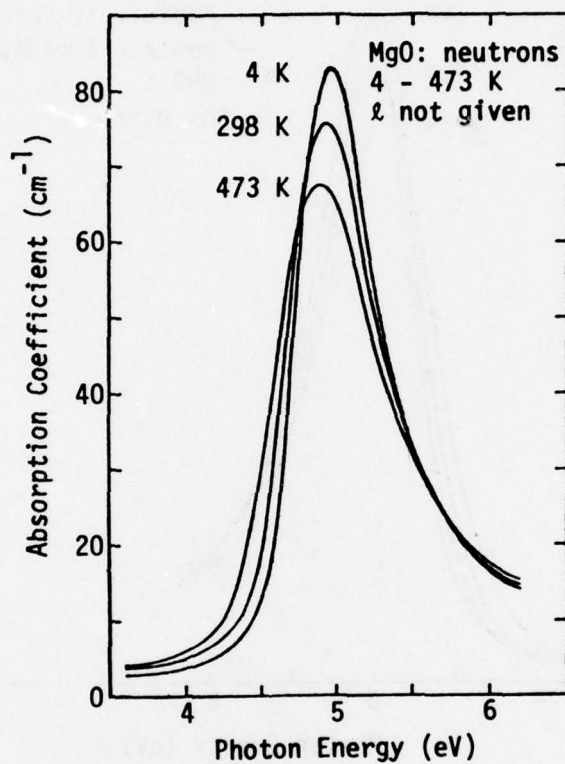
Fig. 4.108. Optical absorption spectra of a neutron-irradiated MgO crystal measured at three different temperatures. The fast neutron (> 1 MeV) dose was 7×10^{17} cm^{-2}. [L. A. Kappers, R. L. Kroes, and E. B. Hensley, Phys. Rev. B $\underline{1}$, 4151 (1970).]
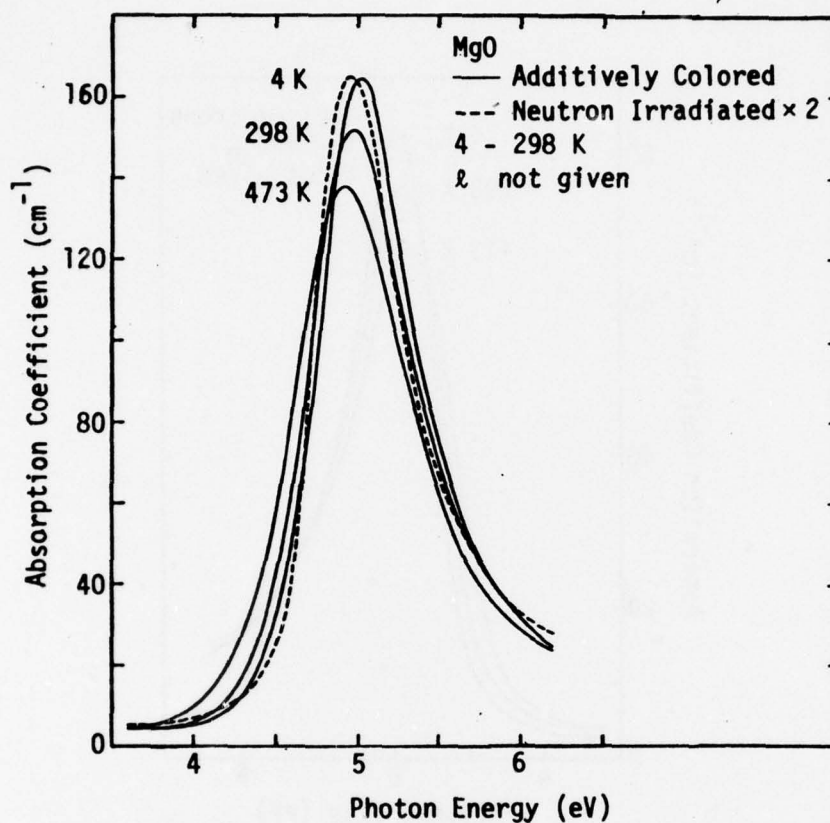
Fig. 4.109. Absorption spectra of an additively colored MgO crystal. The crystal was additively colored in Mg vapor at 1800 C at a pressure of 1300 torr for 1 h. The band is attributed to absorption by F centers. For comparison the dashed curve is the 4 K curve of a neutron-irradiated crystal which is attributed to absorption by F^+ centers. [L. A. Kappers, R. L. Kroes, and E. B. Hensley, Phys. Rev. B $\underline{1}$, 4151 (1970).]
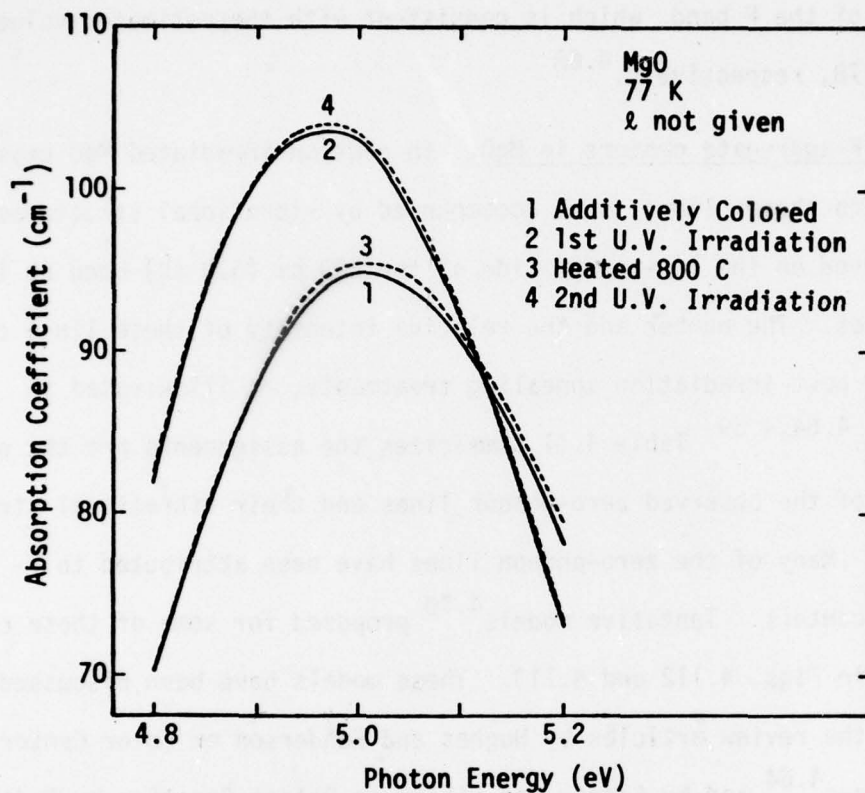
Fig. 4.110. Absorption spectra illustrating the reproducibility of the $F \rightarrow F^+$ photoconversion process. Curve 1 shows the upper portion of the F band of the initial additively colored crystal. Curve 2 shows the shift in the absorption spectra as a result of irradiation with 250 nm light. Heating to 800 C restores the spectra to its original state as shown by curve 3. The result of a second ultraviolet irradiation is shown by curve 4. [L. A. Kappers, R. L. Kroes, and E. B. Hensley, Phys. Rev. B 1, 4151 (1970).]

bleaching suggests that the oscillator strength of the F^+ band is greater than that of the F band, which is consistent with the estimated values of 1.1 and 0.78, respectively.[4.68]

  d. <u>F-aggregate centers in MgO.</u> In neutron-irradiated MgO crystals, several zero-phonon lines, some accompanied by vibrational structures, have been observed on the low-energy side of the 250 nm (5.0 eV) band at low temperatures. The number and the relative intensity of these lines can be changed by post-irradiation annealing treatments, as illustrated in Fig. 4.111.[4.64,4.69] Table 4.11 summarizes the assignments and the peak positions of the observed zero-phonon lines and their vibrational structures.[4.64] Many of the zero-phonon lines have been attributed to F-aggregate centers. Tentative models[4.70] proposed for some of these centers are shown in Figs. 4.112 and 4.113. These models have been discussed in detail in the review articles by Hughes and Henderson on Color Centers in Simple Oxides[4.64] and by Sonder and Sibley on Defect Creation by Radiation in Polar Crystals.[4.64]

  Figure 4.114 compares the spectra of MgO irradiated by 2 MeV electrons with that of MgO irradiated by neutrons to attain nearly the same concentrations of F-type centers.[4.64] Figure 4.115 shows the absorption spectrum of an MgO crystal irradiated with 29 MeV electrons, curve (a), and the changes produced in this spectrum by successive bleaching with 254 nm (4.88 eV) and 540 nm (2.30 eV) light, curves (b) and (c), respectively. Since the bleaching with 254 nm (4.88 eV) light, which is expected to release electrons from the F-type centers, maximizes the intensities of the zero-phonon lines at 361.5 nm (3.430 eV), 1044.5 nm (1.187 eV), and 1342.5 nm (0.9235 eV); and since the bleaching into the 2.30 eV (540 nm) band, which is expected
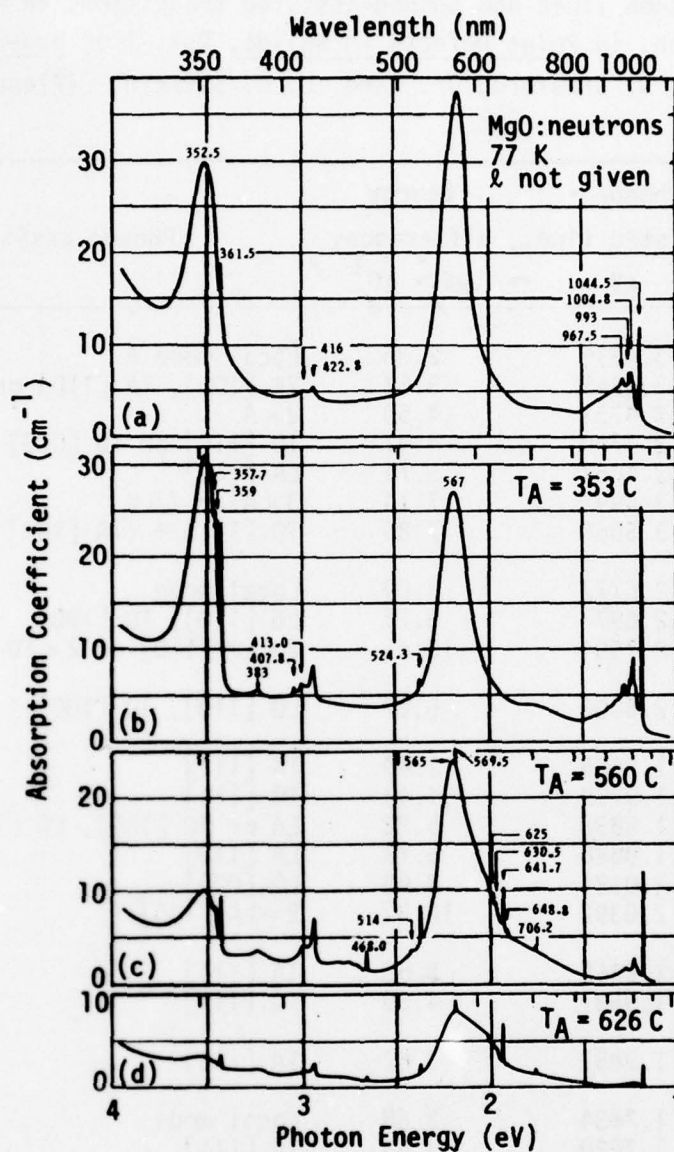
Fig. 4.111. Absorption spectra of MgO crystal irradiated with 2.2×10^{18} neutrons/cm^2 and annealed for 10 min at the temperatures indicated. [Y. Chen and W. A. Sibley, Phil. Mag. 20, 217 (1969).]

Table 4.11. Zero-phonon lines and phonon-assisted transitions in MgO. [A. E. Hughes and B. Henderson, in <u>Point Defects in Solids</u>, Vol. 1 of <u>General and Ionic Crystals</u>, edited by J. W. Crawford, Jr. and L. M. Slifkin, (Plenum, New York, 1972), Chap. 7.]

| Zero-phonon line | | Phonon-assisted line, | Energy difference, | Phonon assignment |
nm	eV	eV	eV $\times$ 10^2	
361.8	3.4283	3.4516	2.33	Local mode A
		3.4645	3.62	TA [100], TA [110] or TA [111] (B)
		3.4733	4.50	2 × A
		3.4780	4.97	TO [110] or TO [000]
		3.4857	5.74	LA [110]
		3.4997	7.14	3 × A or 2 × B
		3.5069	7.86	TO [111] + (TA [100] or TA [110])
468.5	2.6465	2.6773	3.09	Local mode
		2.6977	5.12	LO [110], TO [100]
		2.7504	10.4	2 × LO [110] or 2 × TO [100]
470.0	2.6379	2.6906	5.27	LO [110], TO [100]
642.0	1.9316	1.9655	3.40	TA [111]
		1.9758	4.43	TO [111]
		1.9838	5.22	LA or TO [100], LO [110]
		1.9888	5.73	LA [110]
		2.0184	8.68	LO [000]
		2.0392	10.8	2 × LA [100]
649.0	1.9101	1.9455	3.53	TA [111]
		1.9531	4.30	TO [111]
670.6	1.8489	1.8851	3.62	TA [110]
705.8	1.7566	1.7834	2.68	Local mode
		1.7920	3.53	TA [111]
		1.8005	4.39	TO [111]
		1.8047	4.75	TO [110]
993.1	1.2485	1.2956	4.71	TO [110]
		1.3440	9.55	2 × TO [110]
		1.3700	12.2	2 × (LO [100] or LA [111])
		1.3899	14.1	3 × TO [110]
		1.4320	18.3	3 × LO [100]
		1.4915	24.3	4 × LO [100]
1045.0	1.1865	1.2213	3.47	TA [111] or TA [110]
		1.2337	4.71	TO [110]
		1.2659	7.94	TA [111] + TO [110]
		1.2808	9.42	2 × TO [110]
		1.3254	13.9	3 × TO [110]
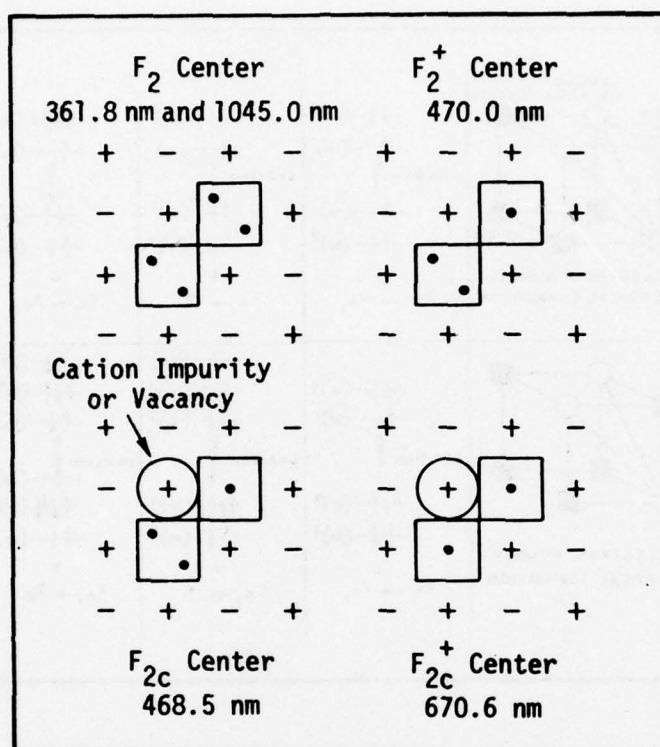
Fig. 4.112. Some models for orthorhombic F-aggregate centers and their possible assignments to zero-phonon lines in MgO.   [B. Henderson and J. E. Wertz, Advan. Phys. 17, 749 (1968).

271
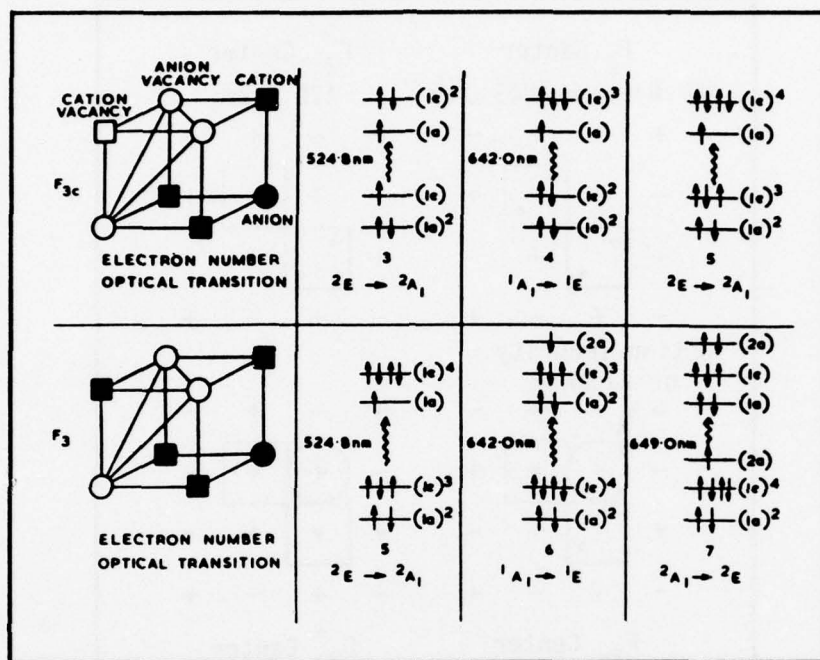
Fig. 4.113.   Models and molecular orbital schemes for trigonal
F-aggregate centers and their possible assignments to zero-phonon
lines in MgO.   [B. Henderson and J. E. Wertz, Advan. Phys. 17,
749 (1968).]
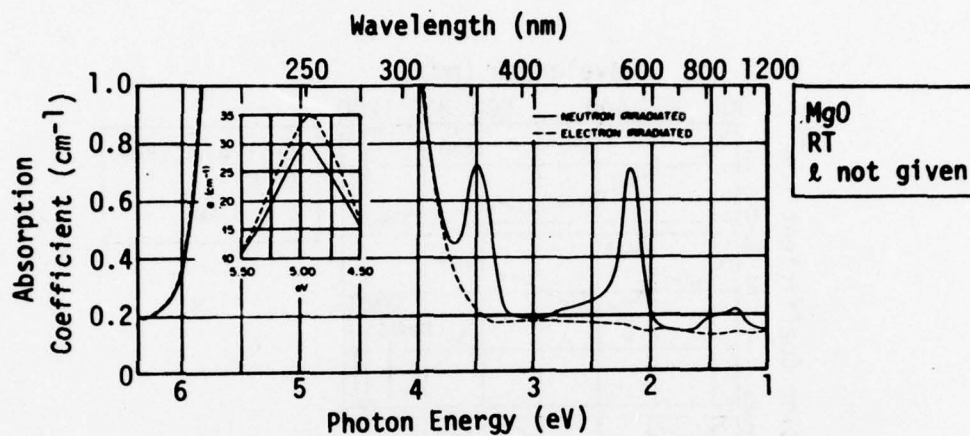
Fig. 4.114. Comparison of the absorption spectra of MgO
crystals irradiated with 2 MeV electrons or neutrons.
[E. Sonder and W. A. Sibley, in Point Defects in Solids,
Vol. 1 of General and Ionic Crystals, edited by J. W.
Crawford, Jr., and L. M. Slifkin, (Plenum, New York,
1972), Chap. 4.]
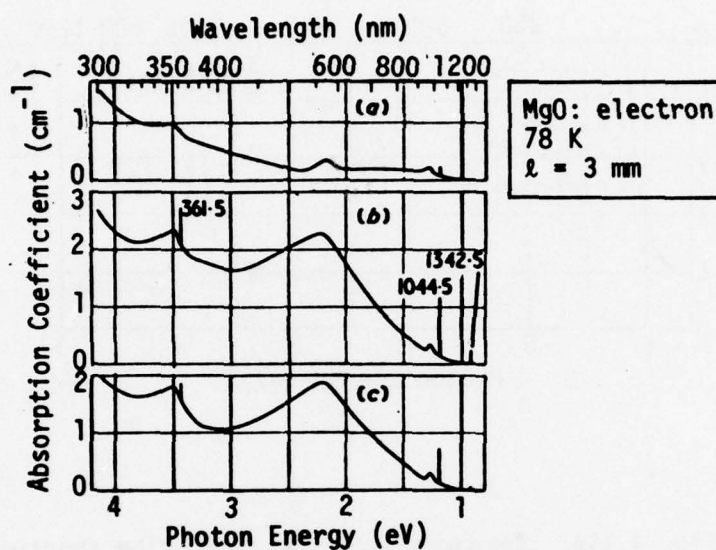
Fig. 4.115. Spectra of MgO crystal irradiated with 29 MeV electrons, measured at 78 K after (a) prolonged period in the dark; (b) bleaching with 254 nm light at 295 K, V⁻ band (540 nm) appears; (c) bleaching with 540 nm light. Step (b) maximizes zero-phonon-line intensities. [Y. Chen, D. L. Trueblood, O. E. Schow, and H. T. Tohver, J. Phys. C: Solid State Phys. 3, 2501 (1970).]

to release holes from the V-type centers, is accompanied by a decrease in the intensities of all the zero-phonon lines, the results of bleaching experiments indicate that all the zero-phonon lines are associated with trapped electron centers.[4.39]

Figure 4.116 compares the thermal stabilities of the 250 nm (5.0 eV) band in electron-irradiated, neutron-irradiated, and additively colored MgO crystals.[4.64,4.71]

e. Ne^+ irradiation of MgO. Optical absorption spectra[4.40] of MgO crystals implanted with 3 MeV-Ne^+ in the dose range from 10^{14} to 10^{17} ions/cm^2 are shown in Fig. 4.74. Evans[4.40] shows that much of the observed absorption arises from displacement-type lattice damage and that the spectrum can be decomposed into three regions near 5.0 eV (250 nm), 5.8 eV (210 nm), and 7.0 eV (180 nm). His electron-spin-resonance data indicate that the absorption in the region of 5.0 eV (250 nm), as in the case of neutron-irradiated MgO, arises predominantly from F^+ centers.

Figure 4.117 compares the room-temperature spectra of MgO implanted at 77 K and at 300 K with a 3 MeV-Ne^+ ion fluence of 10^{14} cm^{-2}. The absorption near 5.0 eV (250 nm) is seen to be higher by about a factor of two in the sample irradiated at 77 K; apparently the implantation-induced Frenkel pairs recombine at a lower rate at this temperature as compared to 300 K.

Optical absorption spectra of MgO crystals taken at 100 K and at 300 K before and after 3 MeV-Ne^+ implantation are shown in Fig. 4.118. Absorption spectra of an Ne^+-implanted MgO after isochronal (12 min.) annealing at various temperatures in the range 25-1250 C are shown in Fig. 4.119. Notice that the 5.8 eV (210 nm) band becomes very prominent in the sample annealed
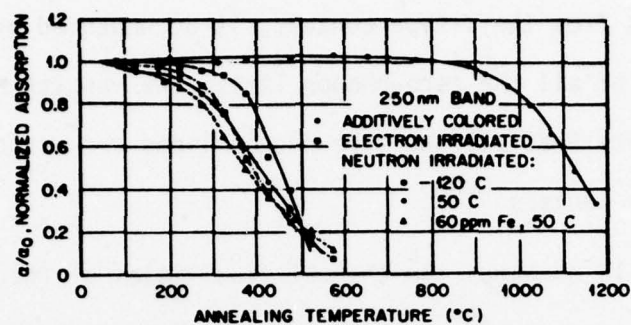
Fig. 4.116. Normalized absorption coefficient at the peak of the F band (5.0 eV) versus annealing temperature (10 min at temperature) for electron-irradiated, neutron-irradiated, and additively colored MgO crystals.   [Y. Chen, R. T. Williams, and W. A. Sibley, Phys. Rev. 182, 960 (1969).]
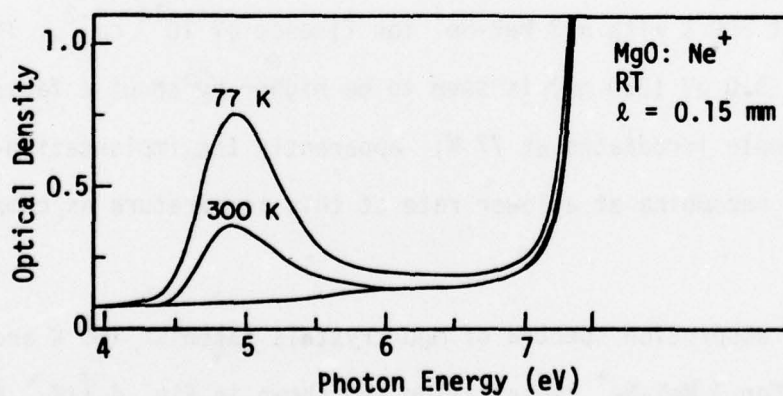
Fig. 4.117.   Room-temperature spectra of MgO bombarded with 3 MeV Ne$^+$ at 77 K and at 300 K to a fluence of 10^{14} cm^{-2}.   [B. D. Evans, Phys. Rev. B 9, 5222 (1974).]
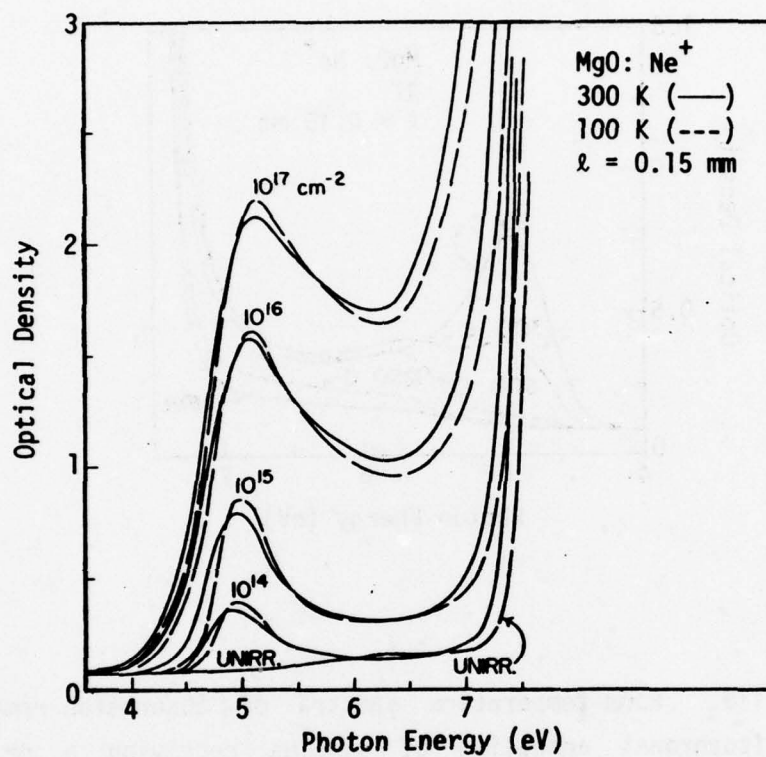
Fig. 4.118.   Temperature and dose dependence of the absorption
spectrum of MgO before irradiation with Ne[+] ions. [B. D. Evans,
Phys. Rev. B <u>9</u>, 5222 (1974).]
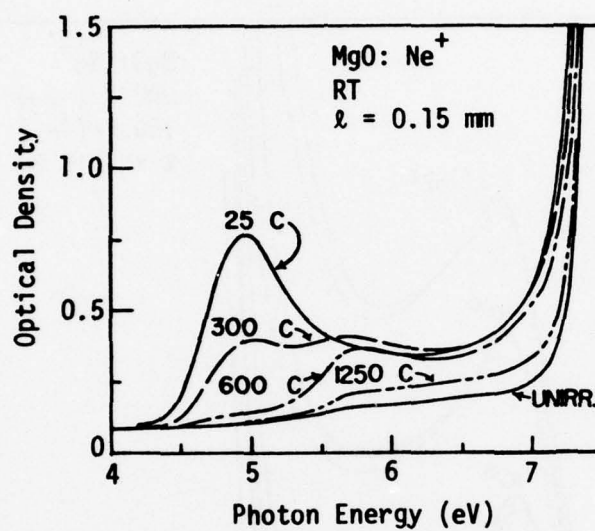
Fig. 4.119. Room-temperature spectra of absorption remaining after isochronal annealing of samples receiving a dose of 10^{15} 3 MeV-Ne$^+$ cm^{-2}. [B. D. Evans, Phys. Rev. B 9, 5222 (1974).]

at 600 C.   Figure 4.120 shows that the 5.8 eV (210 nm) band has almost
identical spectral position and half-width as the deformation-induced ab-
sorption band in MgO.   Evans attributes the 5.8 eV (210 nm) band to the
bombardment-induced deformation and suggests that the band could be
associated with an anion-cation vacancy pair containing two trapped holes
or electrons in the vicinity.

Absorption spectra of 3 MeV proton bombarded, 3 MeV-Ne[+] bombarded,
and fast-neutron irradiated MgO crystals are compared in Fig. 4.121.   The
observed similarity in the spectral features indicates that the defect
structures produced in MgO by light-particle irradiation do not differ
significantly from those produced by Ne[+] bombardment.
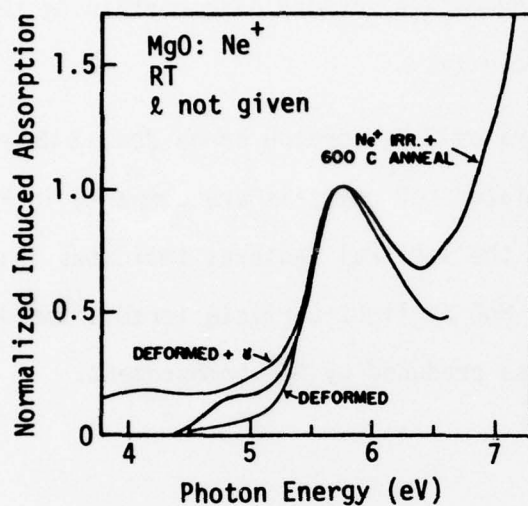
Fig. 4.120. Normalized absorption spectra comparing the 5.8 eV (214 nm) band in MgO resulting from (a) Ne$^+$ bombardment, to a fluence of 10^{15} cm^{-2} followed by a 12 min anneal at 600 C, (b) deformation, and (c) deformation followed by γ-irradiation. [B. D. Evans, Phys. Rev. B $\underline{9}$, 5222 (1974).]
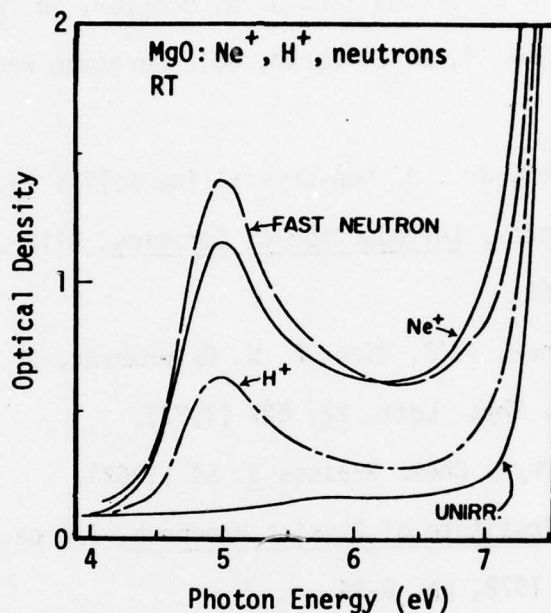
Fig. 4.121. Room-temperature absorption induced by 3 MeV
^{20}Ne$^+$, to a fluence of 3×10^{15} cm^{-2} (solid line), by 3 MeV
H$^+$ to a fluence of 8×10^{16} cm^{-2} (dash-dot line), and by
fast neutrons (E > 1 MeV) to a fluence of approximately
5×10^{17} cm^{-2} (broken line). The neutron sample is 0.08 mm
thick; the others including the unirradiated sample are
0.23 mm thick. [B. D. Evans, Phys. Rev. B 9, 5222 (1974).]

281

REFERENCES

4.1   J. I. Slaughter, in Ceramics for Advanced Technologies, J. E. Hove
        and W. C. Riley, eds., Wiley, New York, 1965, pp. 218-250.

4.2   E. Lell, N. J. Kreidl, and J. R. Hansler, in Progress in Ceramic
        Science, Vol. 4, J. E. Burke, ed., Pergamon Press, New York, 1966,
        pp. 1-93.

4.3   G. H. Sigel, Jr., J. Non-Crystalline Solids 13, 372 (1973/74).

4.4   W. D. Kingery, Introduction to Ceramics, Wiley, New York, 1960,
        pp. 140-160.

4.5   D. A. Pinnow, T. C. Rich, F. W. Ostermayer, Jr., M. DiDomenico,
        Jr., Appl. Phys. Lett. 22, 527 (1973).

4.6   E. Lell, Phys. Chem. Glasses 3, 84 (1962).

4.7   American Institute of Physics Handbook, 3rd ed., McGraw-Hill,
        New York, 1972, pp. 6-94.

4.8   R. J. Ginther and R. D. Kirk, J. Non-Crystalline Solids 6, 89
        (1971).

4.9   P. W. Levy, J. Phys. Chem. Solids 13, 287 (1960).

4.9a   E. Lell, N. J. Kreidl, and J. R. Hansler, in Progress in Ceramic
        Science, Vol. 4, J. E. Burke, ed., Pergamon Press, New York, 1966,
        pp. 1-94; the data from P. W. Levy, J. Phys. Chem. Solids 13,
        287 (1960).

4.10   R. A. Weeks and C. M. Nelson, J. Appl. Phys. 31, 1555 (1960).

4.11   R. A. Weeks, J. Appl. Phys. 27, 1376 (1956).

4.12   R. A. Weeks, Phys. Rev. 130, 570 (1963).

4.13   C. M. Nelson and J. H. Crawford, Jr., J. Phys. Chem. Solids 13,
        296 (1960).

4.14   R. A. Weeks, J. Am. Ceram. Soc. 53, 176 (1970).

4.15   D. F. Heath and P. A. Sacher, Appl. Opt. 5, 937 (1966).

4.16   P. N. Mace and D. H. Gill, IEEE Trans. Nucl. Sci. 14, 62 (1967).

4.17   J. F. Holzrichter and J. L. Emmett, J. Appl. Phys. 40, 159 (1969).

4.18   G. W. Arnold, IEEE Trans. Nucl. Sci. 20, 220 (1973).

4.19   A. J. DeLai, C. P. Gazzara, and R. N. Katz, Proceedings of the
         Fourth Annual Conference on Infrared Laser Window Materials,
         Tucson, Arizona, 1974, p. 475.

4.20   American Institute of Physics Handbook, 3rd ed., McGraw-Hill,
         New York, 1972, pp. 6-40.

4.21   V. Chandrasekharan and H. Damany, Appl. Opt. 7, 939 (1968).

4.22   V. Chandrasekharan and H. Damany, Appl. Opt. 8, 671 (1969).

4.23   T. F. Deutsch, J. Phys. Chem. Solids 34, 2091 (1973).

4.24   H. H. Tippins, Phys. Rev. B 1, 126 (1970).

4.25   D. F. Heath and P. A. Sacher, Appl. Opt. 5, 937 (1966).

4.26   D. S. McClure, J. Chem. Phys. 36, 2757 (1962).

4.27   R. S. Krishnan, Proc. Indian Acad. Sci. 26A, 450 (1947).

4.28   J. Ferguson and P. E. Fielding, Chem. Phys. Lett. 10, 262 (1971).

4.29   M. G. Townsend, Solid State Commun. 6, 81 (1968).

4.30   R. A. Hunt and R. H. Schuler, Phys. Rev. 89, 664 (1953).

4.31   T. J. Turner and J. H. Crawford, Jr., Solid State Commun. 17,
         167 (1975).

4.32   G. W. Arnold and W. D. Compton, Phys. Rev. Lett. 4, 66 (1960).

4.33   E. W. J. Mitchell, J. D. Rigden, and P. D. Townsend, Phil. Mag. 5,
         1013 (1960).

4.34   T. J. Turner and J. H. Crawford, Jr., Phys. Rev. B 13, 1735 (1976).

4.35   J. M. Bunch and F. W. Clinard, Jr., J. Am. Ceram. Soc. 57, 279
        (1974).

4.36   G. W. Arnold, G. B. Krefft, and C. B. Norris, Appl. Phys. Lett.
        25, 540 (1974).

4.37   C. T. Butler, B. J. Sturm, and R. B. Quincy, Jr., J. Cryst.
        Growth 8, 197 (1971).

4.38   M. M. Abraham, C. T. Butler, and Y. Chen, J. Chem. Phys. 55,
        3752 (1971).

4.39   Y. Chen, D. L. Trueblood, O. E. Schow, and H. T. Tohver, J.
        Phys. C: Solid State Phys. 3, 2501 (1970).

4.40   B. D. Evans, Phys. Rev. B 9, 5222 (1974).

4.41   M. W. Williams and E. T. Arakawa, J. Appl. Phys. 38, 5272 (1967).

4.42   G. H. Reiling and E. B. Hensley, Phys. Rev. 112, 1106 (1958).

4.43   American Institute of Physics Handbook, Third Edition, McGraw-
        Hill, New York, 1972, p. 6-36.

4.44   F. A. Modine, Phys. Rev. B 8, 854 (1973).

4.45   M. D. Sturge, Phys. Rev. 130, 639 (1963).

4.46   W. Low, Phys. Rev. 105, 801 (1957).

4.47   J. P. Larkin, G. F. Imbusch, and F. Dravnieks, Phys. Rev. B 7,
        495 (1973).

4.48   W. M. Fairbank, Jr. and G. K. Klauminzer, Phys. Rev. B 7, 500
        (1973).

4.49   K. Y. Wong, D. Sengupta, and D. J. Mackey, J. Phys. Chem. Solids
        35, 313 (1974).

4.50   W. M. Fairbank, Jr., G. K. Klauminzer, and A. L. Schawlow, Phys.
        Rev. B 11, 60 (1975).

4.51   R. W. Davidge, J. Mat. Sci. $\underline{2}$, 339 (1967).

4.52   R. W. Soshea, A. J. Dekker, and J. P. Sturtz, J. Phys. Chem.
        Solids $\underline{5}$, 23 (1958).

4.53   J. C. Cheng and J. C. Kemp, Phys. Rev. B $\underline{4}$, 2841 (1971).

4.54   Y. Chen and W. A. Sibley, Phys. Rev. $\underline{154}$, 842 (1967).

4.55   W. Low, Phys. Rev. $\underline{109}$, 256 (1958).

4.56   W. Low, Phys. Rev. $\underline{109}$, 247 (1958).

4.57   B. D. Bird, G. A. Osborne, and P. J. Stephens, Phys. Rev. B $\underline{5}$,
        1800 (1972).

4.57a   J. H. Schulman and W. D. Compton, Color Centers in Solids (the
        Macmillan Company, New York, 1962).

4.58   L. A. Kappers, F. Dravnieks, and J. E. Wertz, Solid State
        Commun. $\underline{10}$, 1265 (1972).

4.59   W. C. O'Mara and J. E. Wertz, J. Magn. Reson. $\underline{8}$, 366 (1972).

4.60   L. A. Kappers, F. Dravnieks, and J. E. Wertz, J. Phys. C:
        Solid State Phys. $\underline{7}$, 1387 (1974).

4.61   O. F. Schirmer, P. Koidl, and H. G. Reik, Phys. Stat. Sol. (b)
        $\underline{62}$, 385 (1974).

4.62   M. M. Abraham, Y. Chen, and W. P. Unruh, Phys. Rev. B $\underline{9}$, 1842
        (1974).

4.63   Y. Chen, M. M. Abraham, L. C. Templeton, and W. P. Unruh,
        Phys. Rev. B $\underline{11}$, 881 (1975).

4.64   E. Sonder and W. A. Sibley, in Point Defects in Solids, Vol. 1
        of General and Ionic Crystals, edited by J. W. Crawford, Jr.
        and L. M. Slifkin (Plenum, New York, 1972), Chap. 4; A. E.
        Hughes and B. Henderson, ibid., Chap. 7.

4.65   W. P. Unruh, Y. Chen, and M. M. Abraham, Phys. Rev. Lett. $\underline{30}$, 446 (1973).

4.66   M. M. Abraham, Y. Chen, J. L. Kolopus, and H. T. Tohver, Phys. Rev. B $\underline{5}$, 4945 (1972).

4.67   B. Henderson and R. D. King, Phil. Mag. $\underline{13}$, 1149 (1966).

4.68   L. A. Kappers, R. L. Kroes, and E. B. Hensley, Phys. Rev. B $\underline{1}$, 4151 (1970).

4.69   Y. Chen and W. A. Sibley, Phil. Mag. $\underline{20}$, 217 (1969).

4.70   B. Henderson and J. E. Wertz, Advan. Phys. $\underline{17}$, 749 (1968).

4.71   Y. Chen, R. T. Williams, and W. A. Sibley, Phys. Rev. $\underline{182}$, 960 (1969).

CONTENTS OF PRESENT AND PREVIOUS REPORTS

First Technical Report, March 1972

1. Introduction
2. Calculation of Multiphonon Absorption Coefficients
3. Calculation of Extrinsic Absorption Coefficient
4. Effects of Pressure on Operation of Windows
5. Recommendations for an Experimental Program
6. Experimental Data from the Literature
7. Nonlinear Processes
App. A — Elementary Introduction to the Theory of Infrared Absorption Spectra

Second Technical Report, June 1972

1. Introduction
2. Calculation of Multiphonon Absorption Coefficient
3. Green's Function Analysis and Sjolander-Type Approximations
4. Rigid-Ion, Next-Near-Neighbor Model for the Scattering Hamiltonian
5. Pressure-Induced Optical Distortion in Laser Windows
6. Plans for Continued Research
App. A — Tabulation of Pressure-Induced Optical-Distortion Results
App. B — Eigenvectors for the Rigid-Ion, Next-Near-Neighbor Model

Final Technical Report, December 1972

A. Introduction
B. Theory of Multiphonon Infrared Absorption
C. Theory of Infrared Absorption and Material Failure in Crystals
   Containing Inclusions
D. Collection of Experimental Results for $\beta(\omega)$
E. References to Previous Multiphonon Calculations

First Technical Report, June 1973

A. Introduction
B. Theory of Infrared Absorption and Material Failure in Crystals
   Containing Inclusions
C. Theory of Multiphonon Absorption in Insulating Crystals
D. Temperature Dependence of Multiphonon Infrared Absorption
E. Theory of Infrared Absorption by Crystals in the High Frequency
   Wing of Their Fundamental Lattice Absorption
F. Temperature Dependence of the Absorption Coefficient of Alkali
   Halides in the Multiphonon Regime
G. Temperature and Frequency Dependence of Infrared Absorption as a
   Diagnostic Tool
H. Short-Pulse Operation of Infrared Windows without Thermal Defocusing

Second Technical Report, December 1973

A. Introduction
B. Extrinsic Absorption
C. Extrinsic Absorption in 10.6 μm Laser Window Materials Due to Molecular-Ion Impurities
D. Very High-Intensity Effects
E. Explanation of Laser-Damage Cone-Shaped Surface Pits
F. Nonlinear Infrared Absorption from Parametric Instabilities of Phonons
G. High-Power 2-6 μm Window-Material Figures of Merit with Edge Cooling and Surface Absorption Included
H. High-Power 10.6 μm Window-Material Figures of Merit with Edge Cooling and Surface Absorption Included
I. Explicit Exponential Frequency Dependence of Multiphonon Infrared Absorption
J. Quasiselection Rule for Infrared Absorption by NaCℓ-Structure Crystals
K. The Absorption Coefficient of Alkali Halides in the Multiphonon Regime: Effects
L. Vertex Corrections for Multiphonon Absorption
M. Negligible Intrinsic-Absorption Processes
N. Summary of Publications and Results
App. — Simple Pendulum Instability

Third Technical Report, June 1974

A. Introduction and Summary
B. Intensity Limits of High-Intensity Vacuum Ultraviolet Materials
C. Multiphoton Absorption
D. Calculated Reflectance of Aluminum in the Vacuum Ultraviolet
E. Total-Internal-Reflection Devices
F. The Scattering and Absorption of Electromagnetic Radiation by a Semi-Infinite Crystal in the Presence of Surface Roughness
G. Infrared Absorption by the Higher-Order-Dipole-Moment Mechanism
H. Stimulated Raman and Brillouin Scattering: Parametric Instability Explanation of Anomalies
I. Extrinsic Absorption in 10.6 μm Laser Window Materials
J. Erratum, High-Power 2- to 6-μm Window-Material Figures of Merit with Edge Cooling and Surface Absorption Included
K. List of Recent Publications

Fourth Technical Report, December 1974

A. Introduction and Summary
B. Stimulated Raman Scattering: Enhanced Stokes Gain and Effects of Anti-Stokes and Parametric Phonon Processes
C. Enhanced Stimulated Raman Scattering and General Three-Boson Parametric Instabilities
D. Theory of Laser-Materials Damage by Enhanced Stimulated Raman Scattering

LIST OF PUBLICATIONS

All publications of this program and the previous programs are included in the following list:

1. M. Sparks, Immediate Needs of the High-Power Infrared Window Program and Methods of Reducing Thermally Induced Optical Distortion, Rand Corporation Report WN-7243-PR, June 1971.

2. M. Sparks, Stress and Temperature Analysis for Surface Cooling or Heating of Laser Window Materials, Parke Mathematical Laboratories TM-1, July 1971.

3. M. Sparks, Temperature and Stress Analysis for Bulk- and Surface-Heated Slabs, Parke Mathematical Laboratories TM-2, August 1971.

4. M. Sparks, Optical Distortion by Heated Windows in High-Power Laser Systems, Rand Corporation Report R-545-PR, September 1971.

5. M. Sparks, Calculated Temperature Distributions in Slabs Heated in a Thin Surface Layer, Parke Mathematical Laboratories TM-3, September 1971.

6. M. Sparks, "Optical Distortion by Heated Windows in High-Power Laser Systems," J. Appl. Phys. 42, 5029 (1971).

7. M. Sparks, "Introduction to the High-Power Infrared Window Material Problem," AFCRL Conference on High-Power IR Laser Window Materials, December 1971.

8. M. Sparks, "Engineering Approaches to High-Power Infrared Window Problems," AFCRL Conference on High-Power IR Laser Window Materials, December 1971.

9. M. Sparks and T. Azzarelli, Theoretical Studies of High-Power Infrared Window Materials, Xonics Quarterly Technical Progress Report No. 1, Contract DAHC15-72-C-0129, March 1972.

10. M. Sparks, "Recent Developments in High-Power Infrared Window Research," NBS Spec. Publ. 372, 4th ASTM Symposium on Laser Induced Damage in Optical Materials, Boulder, Colo., June 14-15, 1972.

11. M. Sparks and T. Azzarelli, Theoretical Studies of High-Power Infrared Window Materials, Xonics Quarterly Technical Progress Report No. 2, Contract DAHC15-72-C-0129, June 1972.

12. M. Sparks and L. J. Sham, "Theory of Multiphonon Infrared Absorption," AFCRL Conference on High-Power IR Laser Window Materials, Hyannis, Mass., Oct. 30 - Nov. 1, 1972.

13. M. Sparks and M. Cottis, "Pressure-Induced Optical Distortion in Infrared Windows," AFCRL Conference on High-Power Infrared Laser Window Materials, Hyannis, Mass., Oct. 30 - Nov. 1, 1972.

14. M. Sparks, Theoretical Studies of High-Power Infrared Window Materials, Xonics Final Report, Contract DAHC15-72-C-0129, December 1972.

15. M. Sparks and L. J. Sham, "Exponential Frequency Dependence of Multi-phonon Summation Infrared Absorption," Solid State Commun, 11, 1451 (1972).

16. C. J. Duthler and M. Sparks, "Theory of Material Failure in Crystals Containing Infrared Absorbing Inclusions," NBS Spec. Publ. 387, 5th ASTM-ONR-NBS Symposium on Laser Induced Damage in Optical Materials, Boulder, Colo., May 15-16, 1973.

17. M. Sparks, Theoretical Studies of High-Power Infrared Window Materials, Xonics First Technical Report, Contract DAHC15-73-C-0127, June 30, 1973.

18. M. Sparks, Physical Principles, Materials Guidelines, and Materials List for High-Power 10.6 μ Windows, Rand Corporation Report R-863-PR, September 1973.

19. M. Sparks, C. J. Duthler, H. C. Chow, L. J. Sham, A. A. Maradudin, and D. L. Mills, "Theoretical Studies of High-Power Infrared Window Materials," AFCRL Conference on High-Power Infrared Laser Window Materials, Hyannis, Mass., Nov. 12-14, 1973.

20. M. Sparks and H. C. Chow, "High-Power 10.6 μm Window Material Figures of Merit with Edge Cooling and Surface Absorption Included," AFCRL Conference on High-Power Infrared Laser Window Materials, Hyannis, Mass., Nov. 12-14, 1973.

21. M. Sparks and C. J. Duthler, Theoretical Studies of High-Power Infra-red Window Materials, Xonics Second Technical Report, Contract DAHC15-73-C-0127, Dec. 6, 1973.

22. M. Sparks, "Short-Pulse Operation of Infrared Windows without Thermal Defocusing," Appl. Opt. 12, 2033 (1973).

23. M. Sparks, "Temperature and Frequency Dependence of Infrared Absorption as a Diagnostic Tool," Appl. Phys. Lett. 23, 368 (1973).

24. M. Sparks and M. Cottis, "Pressure-Induced Optical Distortion in Laser Windows," J. Appl. Phys. 44, 787 (1973).

25. M. Sparks and C. J. Duthler, "Theory of Infrared Absorption and Material Failure in Crystals Containing Inclusions," J. Appl. Phys. 44, 3038 (1973).

26. M. Sparks, "Stress and Temperature Analysis for Surface Cooling or Heating of Laser Window Materials," J. Appl. Phys. 44, 4137 (1973).

27. D. L. Mills and A. A. Maradudin, "Theory of Infrared Absorption by Crystals in the High Frequency Wing of Their Fundamental Lattice Absorption," Phys. Rev. B 8, 1617 (1973).

28. M. Sparks and L. J. Sham, "Theory of Multiphonon Absorption in Insulating Crystals," Phys. Rev. B 8, 3037 (1973).

29. M. Sparks and L. J. Sham, "Temperature Dependence of Multiphonon Infrared Absorption," Phys. Rev. Lett. 31, 714 (1973).

30. A. A. Maradudin and D. L. Mills, "Temperature Dependence of the Absorption Coefficient of Alkali Halides in the Multiphonon Regime," Phys. Rev. Lett. 31, 718 (1973).

31. C. J. Duthler and M. Sparks, "Extrinsic Absorption in Laser Window Materials," NBS Spec. Publ. 414, 6th ASTM-ONR-NBS Symposium on Laser Induced Damage in Optical Materials, Boulder, Colo., May 22-23, 1974.

32. M. Sparks and C. J. Duthler, Theoretical Studies of High-Power Ultraviolet and Infrared Materials, Xonics Third Technical Report, Contract DAHC15-73-C-0127, June 30, 1974.

33. M. Sparks and C. J. Duthler, "Current Status of High-Intensity Vacuum Ultraviolet Materials," 4th ARPA Conference on Infrared Laser Window Materials, Tucson, Ariz., Nov. 18-20, 1974.

34. C. J. Duthler, "Impurity Absorption in Halide Window Materials," 4th ARPA Conference on Infrared Laser Window Materials, Tucson, Ariz., Nov. 18-20, 1974.

35. M. Sparks and C. J. Duthler, Theoretical Studies of High-Power Ultraviolet and Infrared Materials, Xonics Fourth Technical Report, Contract DAHC15-73-C-0127, Dec. 6, 1974.

36. C. J. Duthler, "Explanation of Laser-Damage Cone-Shaped Surface Pits," Appl. Phys. Lett. 24, 5 (1974).

37. M. Sparks and H. C. Chow, "High-Power 2-6 µm Window-Material Figures of Merit with Edge Cooling and Surface Absorption Included," J. Appl. Phys. 45, 1510 (1974).

38. C. J. Duthler, "Extrinsic Absorption in 10.6 µm Laser Window Materials Due to Molecular-Ion Impurities," J. Appl. Phys. 45, 2668 (1974).

39. L. J. Sham and M. Sparks, "Explicit Exponential Frequency Dependence of Multiphonon Infrared Absorption," Phys. Rev. B 9, 827 (1974).

40. C. J. Duthler and M. Sparks, "Quasiselection Rule for Infrared Absorption by NaCl-Structure Crystals," Phys. Rev. B 9, 830 (1974).

41. M. Sparks and H. C. Chow, "Parametric Instabilities of Phonons: Nonlinear Infrared Absorption," Phys. Rev. B 10, 1699 (1974).

42. D. L. Mills and A. A. Maradudin, "The Absorption Coefficient of Alkali Halides in the Multiphonon Regime: Effects of Nonlinear Dipole Moments," Phys. Rev. B 10, 1713 (1974).

43. M. Sparks, "Infrared Absorption by the Higher-Order-Dipole-Moment Mechanism," Phys. Rev. B 10, 2581 (1974).

44. M. Sparks, "Stimulated Raman and Brillouin Scattering: Parametric Instability Explanation of Anomalies," Phys. Rev. Lett. 32, 450 (1974).

45. M. Sparks and C. J. Duthler, Theoretical Studies of High-Power Ultraviolet and Infrared Materials, Xonics Fifth Technical Report, Contract DAHC15-73-C-0127, June 30, 1975.

46. M. Sparks, "Current Status of Electron-Avalanche-Breakdown Theories," NBS Spec. Publ. 435, 7th ERDA-ASTM-ONR-NBS Symposium on Laser Induced Damage in Optical Materials, Boulder, Colo., July 29-31, 1975.

47. C. J. Duthler and M. Sparks, "Irradiance Limits for Vacuum Ultraviolet Material Failure," NBS Spec. Publ. 435, 7th ERDA-ASTM-ONR-NBS Symposium on Laser Induced Damage in Optical Materials, Boulder, Colo., July 29-31, 1975.

48. C. J. Duthler, J. Harrington, F. Patten, and M. Hass, "Multiphonon Absorption of Alkali Halides and Quasiselection Rules," 5th DARPA Conference on Infrared Laser Window Materials, Las Vegas, Nevada, Dec. 1-4, 1975.

49. M. Sparks, Theoretical Studies of Materials for High-Power Infrared Coatings, Xonics Sixth Technical Report, Contract DAHC15-73-C-0127, Dec. 31, 1975.

50. H. C. Chow and M. Sparks, "Calculated Reflectance of Aluminum in the Vacuum Ultraviolet," J. Appl. Phys. 46, 1307 (1975).

51. M. Sparks, "Theory of Laser-Materials Damage by Enhanced Stimulated Raman Scattering," J. Appl. Phys. 46, 2134 (1975).

52. M. Sparks, "Stimulated Raman Scattering: Enhanced Stokes Gain and Effects of Anti-Stokes and Parametric Phonon Processes," Phys. Rev. A 11, 595 (1975).

53. A. A. Maradudin and D. L. Mills, "The Scattering and Absorption of Electromagnetic Radiation by a Semi-Infinite Crystal in the Presence of Surface Roughness," Phys. Rev. B 11, 1392 (1975).

54. D. L. Mills and A. A. Maradudin, "Surface Roughness and Optical Properties of a Semi-Infinite Material: The Effect of a Dielectric Overlayer," Phys. Rev. B 12, 2943 (1975).

55. M. Sparks and J. H. Wilson, "Enhanced Stimulated Raman Scattering and General Three-Boson Parametric Instabilities," Phys. Rev. B $\underline{12}$, 4493 (1975).

56. M. Sparks and C. J. Duthler, Theoretical Studies of High-Power Ultraviolet and Infrared Materials, Xonics Seventh Technical Report, Contract DAHC15-73-C-0127, June 30, 1976.

57. M. Sparks, "Overview of Materials of High-Power Visible and Ultra-violet Lasers," DARPA Infrared Laser Window Materials Meeting, Boulder, Colo., July 12, 1976.

58. M. Sparks, "Materials for High-Power Window and Mirror Coatings and Multilayer-Dielectric Reflectors," NBS Spec. Publ. 462, 8th NBS-ASTM-ONR-ERDA-DARPA Symposium on Laser Induced Damage in Optical Materials, Boulder, Colo., July 13-15, 1976.

59. C. J. Duthler, "Quasiselection Rules for Multiphonon Infrared Absorption in Alkali Halides," American Physical Society Meeting, Atlanta, Ga., Mar. 29 - Apr. 1, 1976. Abstract published: Bull. Am. Phys. Soc. $\underline{21}$, 419 (1976).

60. M. Flannery, C. J. Duthler, and M. Sparks, Research on Crystal Chemistry Studies, Xonics Final Report, Contract F19628-75-C-0123, Nov. 30, 1976.

61. C. J. Duthler, "Simplified Method for Calculating Multiphonon Infrared Absorption in Alkali-Halide Window Materials," Topical Meeting on Optical Phenomena in Infrared Materials, Annapolis, Md., Dec. 1-3, 1976.

62. M. Sparks and C. J. Duthler, Theoretical Studies of High-Power Ultra-violet and Infrared Materials, Xonics Eighth Technical Report, Contract DAHC15-73-C-0127, Dec. 31, 1976.

63. M. Sparks, "Theory of Laser Heating of Solids: Metals," J. Appl. Phys. $\underline{47}$, 837 (1976).

64. C. J. Duthler, "Quasiselection Rules for Multiphonon Absorption in Alkali Halides," Phys. Rev. B $\underline{14}$, 4606 (1976).

65. J. A. Harrington, C. J. Duthler, F. W. Patten, and M. Hass, "Multi-phonon Absorption of Alkali Halides and Quasiselection Rules," Solid State Commun. $\underline{18}$, 1043 (1976).

66. M. Sparks, "A Simple Method for Calculating the Optical Properties of Multilayer-Dielectric Reflectors," J. Opt. Soc. Am. $\underline{67}$, 1590 (1977).

67. H. Vora, M. Flannery, and M. Sparks, Tabulation of Impurity Absorption Spectra - Ultraviolet and Visible, Volume I, Xonics Ninth Technical Report, Contract DAHC15-73-C-0127, June 30, 1977.

68. M. Flannery and M. Sparks, "Extrinsic Absorption in Infrared Laser-Window Materials," Ninth Damage Symposium on Optical Materials for High Power Lasers, Boulder, Colo., Oct. 4, 1977.

69. M. Sparks, "Optical Distortion and Failure in High-Power Reflectors," NBS High Power Laser Optical Components and Component Materials Meeting, Boulder, Colo., Oct. 4, 1977.

70. M. Sparks and P. Sen, "Possible Reduction of Laser-Fusion Target Illumination by Enhanced Stimulated Raman Plasmon Scattering," Phys. Rev. Lett. 39, 751-753 (1977).

71. H. Vora, M. Flannery, and M. Sparks, Tabulation of Impurity Absorption Spectra - Ultraviolet and Visible, Volume II, Xonics Tenth Technical Report, Contract DAHC15-73-C-0127, 31 December 1977.

72. M. Flannery and M. Sparks, "Polymer Coatings for Protection of Optical Components," submitted for publication.

73. M. Flannery, M. Sparks, and E. Loh, Jr., "Theory of Nearly Perfect Multilayer Dielectric Reflectors," submitted to Applied Optics.

74. M. Sparks and E. Loh, Jr., "Theoretical Thresholds for Damage to High-Power Metallic Reflectors," to be published.

75. M. Sparks and E. Loh, Jr., "Theory of Badly Degraded Optics," to be published.

76. P. N. Sen and M. Sparks, "Theory of the Time Dependence of Raman Scattering," to be published.

77. P. N. Sen and M. Sparks, "Ferromagnetic Instability Results from the Mode-Amplitude Equations; Relation to Enhanced Raman Scattering," to be published.

78. M. Sparks, "Thermal Stresses and Expansion in Multilayer Dielectric Reflectors," to be published.

79. M. Sparks and E. Loh, Jr., "Damage Criteria and Temperature Dependence of Absorptance in Laser Damage of Metallic Reflectors," to be published.

80. M. Sparks and P. N. Sen, "Enhancement in Stimulated Raman Scattering," Xonics SM-WN-772, 1977.